SOLID ISOTROPIC MATERIAL WITH THICKNESS PENALISATION – AN ADDITIVE MANUFACTURING-ORIENTED STRUCTURAL TOPOLOGY OPTIMISATION METHOD WITH A 2.5D APPROACH

TEJESWAR YARLAGADDA

PhD

The Hong Kong Polytechnic University

2023

The Hong Kong Polytechnic University

Department of Building Environment and Energy Engineering

Solid Isotropic Material with Thickness Penalisation – An Additive Manufacturing-Oriented Structural Topology Optimisation Method with a 2.5D Approach

Tejeswar Yarlagadda

A thesis submitted in partial fulfillment of the requirements for the degree of Doctor of Philosophy

August 2022

CERTIFICATE OF ORIGINALITY

I hereby declare that this thesis is my own work and that, to the best of my knowledge and belief, it reproduces no material previously published or written, nor material that has been accepted for the award of any other degree or diploma, except where due acknowledgement has been made in the text.

Tejeswar Yarlagadda
(Name of the student)

“No language in this world can describe you.”

In the loving memory of my father, Shri Purna Chandra Rao Yarlagadda

Abstract

Climate change is a pressing global issue, and there is a growing demand for carbon-neutral manufacturing processes and sustainable products. However, the construction industry has been slow to adapt its traditional, polluting, and wasteful practices. Compared to other manufacturing industries, the construction industry has been resistant to change and has not embraced the use of templates, prototypes, and economies of scale. This has resulted in a predominantly one-off construction process that is environmentally damaging.

Architects and designers often propose highly personalised and ambitious designs that can pose challenges for engineers responsible for structural and building systems design. To address this issue, engineers have proposed precast, prefabricated, or modular construction, but this severely limits architectural expression. As a result, the construction industry has not fully embraced this approach, and it remains a fringe segment of the industry.

To provide a novel and alternative solution to the traditional structural design process, this thesis proposes an additive manufacturing-oriented optimisation strategy. This approach aims to optimise material usage, provide greater freedom for architectural creativity and expression, and reduce the environmental impact of construction. The optimisation tool used in this thesis is inspired by the widely accepted SIMP method.

SIMP is a commonly used topology optimisation method for minimising material utilisation in structural components using element densities as a design variable. However, this approach has limitations when it comes to additive manufacturing, as it requires voxels instead of pixels. The density design variable restricts the shape outcomes to pixels, making it difficult to use SIMP for additive manufacturing. Additionally, the use of density as a design variable can cause issues with the stiffness matrix's positive definiteness. A possible alternative to the density design variable is a geometric parameter (such as web thickness in beams), which could avoid the limitations of the former. Accordingly, a new optimisation methodology called Solid Isotropic Material with Thickness Penalisation “SIMTP” is developed using thickness as a design variable. To explore the designs with finite element analysis, a 2.5D element has been introduced. The 2.5D element is based on a 2D planar transformation with varying nodal thicknesses, which allows 2D strain energy to be projected onto a 3D space.

The 2.5D SIMTP approach includes a 2.5D element that allows exploration of a variety of design models, including cantilever, MBB, and L-beams, without experiencing issues related to checkerboarding or other topology-related problems. An adaptive refinement strategy has also been implemented to refine elements with high-thickness gradients and negative energies. However, it was found that this alone can lead to the islanding phenomenon, which was not observed until after filtering. Overall, 2.5D SIMTP provides a more efficient and cost-effective way to achieve desired design outcomes with fewer elements, reducing computational costs. Additionally, it can bridge the design coordination gap between architects and structural engineers by using the architect's vision as the foundation for the design process.

This thesis draws inspiration from the renowned architecture of Antoni Gaudi in Barcelona to create a framework that allows for greater freedom in raw architectural expression. The framework involves optimising the structural component shapes imagined by architects for cost, weight, structural function, sustainability, and aesthetic appearance. By doing so, buildings can be constructed with structural components of distinct non-prismatic and even organic shapes, resulting in a spectacular range of architectural styles that can be fabricated using additive manufacturing. In this thesis, an application of this process is demonstrated using 2.5D SIMTP, where an optimised MBB beam prototype is 3D printed at PolyU's U3DP laboratory using ABS M30i material. Additionally, in an effort to explore practical aspects of 3D printed concrete structures, 2.5D SIMTP has been extended to optimise prestressed beams, where the cable and concrete shapes are simultaneously optimised. Several prestressed problems have been explored using 2.5D SIMTP, including single, two, and three-span beams.

To aid in education and future research, MATLAB codes developed throughout the project are presented at the end of this thesis. Overall, this framework provides a new way to approach architectural design and construction, pushing the boundaries of what is possible and allowing for greater creativity and expression in building design.

Publications Arising from the Thesis

Yarlagadda T, Zhang Z, Jiang L, Bhargava P, Usmani A. Solid isotropic material with thickness penalisation – A 2.5D method for structural topology optimisation. Computers & Structures 2022;270:106857. https://doi.org/10.1016/j.compstruc.2022.106857

Other Publications

Yarlagadda T, Hajiloo H, Jiang L, Green M, Usmani A. Preliminary Modelling of Plasco Tower Collapse. International Journal of High-Rise Buildings 2018;7:397-408. https://doi.org/10.21022/IJHRB.2018.7.4.397

Zhang Z, Yarlagadda T, Zheng Y, Jiang L, Usmani A. Isogeometric analysis-based design of post-tensioned concrete beam towards construction-oriented topology optimisation. Structural and Multidisciplinary Optimisation 2021. https://doi.org/10.1007/s00158-021-03058-z

Orabi MA, Khan AA, Jiang L, Yarlagadda T, Torero J, Usmani A. Integrated nonlinear structural simulation of composite buildings in fire. Engineering Structures 2022;252:113593. https://doi.org/10.1016/j.engstruct.2021.113593

Project Funding Obtained Based on this Thesis

The Research Institute for Advanced Manufacturing (RIAM) based at PolyU is offering funding for the development and manufacturing of concrete systems based on the research and findings presented in this thesis.

Acknowledgements

I am immensely grateful to my chief supervisor, Prof. Asif Usmani, for his invaluable vision, guidance, and support throughout my PhD journey. His mentorship, patience, and kindness have been instrumental in shaping the contents of this thesis. I am also fortunate to have Prof. Pradeep Bhargava as my mentor, who has provided me with professional and emotional support since my post-graduation.

I would like to express my sincere thanks to Dr Liming Jiang and Mr Zixin Zhang for their guidance and assistance in my thesis topic of "Solid Isotropic Material with Thickness Penalisation – An Additive Manufacturing-Oriented Structural Topology Optimisation Method with A 2.5D Approach." I am also grateful to the general staff and DRC of BEEE for their cooperation in providing the required material and services.

I extend my gratitude to Ms Sailja, Ms Jyothsna Rani, Ms Vandana, Ms Bharati, and Mr Sukesh for their unwavering moral, emotional, and financial support throughout the process. I would also like to thank all of my friends whose encouragement and cooperation have helped me in completing this thesis. Any omission in this brief acknowledgement does not mean a lack of gratitude. Finally, I dedicate this thesis to my late father, Shri Purna Chandra Rao Yarlagadda, who has been my inspiration and strength to pursue my dreams. I am grateful for his unwavering support and guidance, which has helped me to achieve my goals.

Table of Contents

Abstract **i**

Publications Arising from the Thesis **iv**

Acknowledgements **vi**

List of Figures **x**

List of Tables **xiii**

List of Abrevations and Notations **xiv**

1 Introduction **1**

1.1 Background..1
1.2 Automation in Construction 3
1.3 Aesthetic Sense in Routine Construction 4
1.4 Optimisation as a Tool to Integrate Form and Function.......5
1.5 Research Objectives..7
1.6 Research Questions...8
1.7 Research Methods...9

1.8 Organisation of the Thesis 12

2 Literature Review **15**

2.1 Automation in onstruction 16
2.2 Optimisation 23
2.3 Conclusions 34

3 Introduction to 2.5D Element **37**

3.1 Element Stability and Accuracy 41
3.2 The Computational Efficiency of the 2.5D Element 47
3.3 Remarks 50

4 Introduction to SIMTP **52**

4.1 Definition of SIMTP 53
4.2 Thickness Optimisation Problem 55
4.3 Comparison of Pixels 61
4.4 Remarks 69

5 Adaptive Refinement **71**

5.1 Refinement Strategy and Thickness Mapping 72
5.2 Element Marking, Refinement and Treatment of Hanging Nodes 76
5.3 Refinement Algorithm and Comparison of Pixels 80
5.4 Remarks 86

6 3D Printing and Surface Fetching **89**

6.1 Comparison of Surface and Voxels 91
6.2 Prototype 3D Printing 98
6.3 Remarks 102

7 Optimisation of Prestressed Concrete Beams **105**

7.1 Tendon Geometry and Transfer of Prestress to Concrete................. 106
7.2 Validation of the Modelling Strategy 109
7.3 Optimisation Methodology 112
7.4 Prestressed Beam Design and Optimisation Results 122
7.5 Remarks 130

8 Conclusions and Future Work 133

8.1 Conclusions... 135
8.2 Future Work 139

References 141

Appendix A 162

Appendix B 169

Appendix C 174

Appendix D 180

Appendix E 184

List of Figures

2.1 3D printed structures ... 18

2.2 OptiBridge project ... 20

2.3 Bridge project ... 20

2.4 External reinforcement ... 21

2.5 Internal reinforcement ... 22

2.6 Fibre-reinforced concrete concept ... 22

3.1 Degeneration of 3D serendipity element ... 38

3.2 Geometric models and thickness data ... 43

3.3 Surface load to UVL ... 44

3.4 Flexural stresses at extreme fibres ... 45

3.5 Deformed stress contours for prismatic beam ... 46

3.6 Deformed stress contours for non-prismatic beam ... 47

3.7 Elements geometry ... 48

4.1 Boundary representation of a 3D solid body ... 53

4.2 Energy regularisation ... 60

4.3 2.5D SIMTP algorithm ... 62

4.4 Benchmark problems ... 63

4.5 Pixels of cantilever beam ... 64

4.6 Cantilever beam - performance comparison 65

4.7 Magnified boundaries 66

4.8 Pixels of MBB beam 66

4.9 Pixels of L- beam 68

5.1 1-Irregular rule for Q4 element 73

5.2 Element refinement 74

5.3 Surface plots of Franke's functions 74

5.4 Thickness mapping and error estimate 75

5.5 Refinement and hanging nodes 77

5.6 Continuous field 77

5.7 Discontinuous field 78

5.8 Irregular edge of a 2.5D element 79

5.9 Adaptive 2.5D SIMTP algorithm 81

5.10 Benchmark problems 82

5.11 Comparison of adaptive meshes and pixels 83

5.12 Comparison of performance and discretisation 84

5.13 Pixels of MBB 85

5.14 Pixels of L- beam 86

6.1 Modifications of top211 for non-prismatic surfaces 90

6.2 Design space and material properties 90

6.3 Initial design 93

6.4 Solid volume from a surface boundary 94

6.5 Comparison of material occupancy 95

6.6 Optimised profiles 95

6.7 Performance comparison 96

6.8 Surface boundary inspection 99

6.9 STL model of beam prototype 99

6.10 Ultimate displacement analysis and stresses 100
6.11 3D printed beam prototype 101
6.12 2.5D SIMTPs ecosystem 102
7.1 Transfer of prestress to concrete 107
7.2 Modelling of prestressed beams 108
7.3 Beam properties 110
7.4 Recovered stress contours 111
7.5 Filtering scheme 113
7.6 Tendon to concrete filter 114
7.7 Tendon layout 120
7.8 Prestressed beam optimisation algorithm 122
7.9 Beam properties for test case I 124
7.10 Tendon layout comparison 124
7.11 Load to prestress ratio - comparison of optimised profiles 125
7.12 Case I with UDL 126
7.13 Beam properties for test case II 126
7.14 Shape comparison of Case I with UDL 127
7.15 Shape comparison of Case II 127
7.16 Case II with three-span 127
7.17 Optimised three-span beam 128
7.18 Optimised prestressed beams with UDL and dead loads 128
7.19 Surface optimisation - prestressed concrete beams 129

List of Tables

3.1 Comparison of midspan downward deflections....................................46

4.1 Cantilever beam results....................................64

4.2 MBB beam results....................................66

4.3 L- beam results....................................68

5.1 Case studies, parameters, and outcomes....................................82

6.1 Model discretisation, parameters, and outcomes....................................94

7.1 Comparison of midspan upward deflections....................................110

7.2 Comparison of top and bottom stresses at midspan....................................110

7.3 Prestressed beam optimisation parameters....................................123

List of Abrevations and Notations

3DCP	:	3D construction printing
3DP	:	3D printing
AM	:	Additive manufacturing
CAD	:	Computer-aided design
CAMD	:	Continuous Approximation of Material Distribution
CC	:	Contour crafting
CM	:	Compliant mechanisms
cm	:	Coarse mesh
CNC	:	Computer numerical controls
DF	:	Digital fabrication
DO	:	Density-based optimisation
EDV	:	Element density variables
ESO	:	Evolutionary Structural Optimisation
FE	:	Finite element
FEM	:	Finite element method
fm	:	Fine mesh
GBA	:	Greater Bay Area
HDM	:	Homogenisation design method

HPM	:	Heaviside projection method
LSM	:	Level set methods
MMC	:	Moving Morphable Components
MOLE	:	MOnotonicity based minimum LEngth scale
MTOP	:	Multiresolution Topology Optimisation
NDV	:	Nodal density variables
OC	:	Optimality criteria
PFM	:	Phase field methods
PM	:	Point mass
RAMP	:	Rational Approximation of Material Properties
RIAM	:	Research Institute for Advanced Manufacturing
SIMP	:	Solid Isotropic Material/Microstructure with Penalisation
SIMTP	:	Solid Isotropic Material with Thickness Penalisation
SINH	:	Hyperbolic Sinusoidal Function
SRV	:	Sum of the Reciprocal Variables
STL	:	Stereolithography
TF	:	Thickness factor
TO	:	Topology optimisation
UVL, UDL	:	Uniformly varying and Distributed loads
(ξ,η,ζ)	:	Isoparametric directions
(w_l,w_m,w_n)	:	Gauss weights of a sampling point (l,m,n)

(x,y,z)	:	Global coordinate system
$[F_1\ F_2\ F_3]$	:	Nodal loads of a quadratic line element
$[L_1\ L_2\ L_3]$	:	2D Quadratic shape functions of a line element
$[P_1\ P_2\ P_3]$	:	Equivalent prestressing forces of a quadratic line element
$[Q_1\ Q_2\ Q_3]$	:	UVL matrix
$[t_1\ t_2\ t_3]$	:	Noda thicknesses of a quadratic line element
A, B, C, D, E	:	Area, Strain matrix, Compliance, Constitutive matrix and Elastic modulus
C_{eq}, e, G, Z	:	Set of constraint equations, eccentricity, shear modulus and section modulus
c_e, β, β_{HS}, μ	:	Effective cover, tendon cover and smoothness controller of void-solid phase and sharpness control
$d_{i,j}$	:	Shortest distance between node *i* and *j*
$\partial C/\partial f_i$, $\partial K/\partial f_i$, $\partial V/\partial f_i$	:	Rate of change of compliance, stiffness and volume w.r.t TF
$\partial C/\partial R_{y,i}$, $\partial K/\partial R_{y,i}$, $\partial V/ R_{y,i}$	:	Rate of change of compliance, stiffness and volume w.r.t vertical position of control point *i*
e_z, r_z, Δp	:	Element size, ratio of $r_{I,i}$ to e_z and penalty increment
η_{ero}, η_{dil}	:	Projection thresholds of eroded and dilated layouts
f(x,y)	:	Dimensionless parameter called TF
f_i, $\hat{f}_i$	:	Filtered and actual TF of node *i* in Chapter 4
f_i, $f_{r,i}$, $f_{tc,i}$, $f_{ero,i}$, $f_{dil,i}$	:	Actual, regularised, tendon-concrete filtered, eroded and dilated TF of node *i* in Chapter 7

f_{min}, f_{max}	:	Minimum and maximum TF
$\hat{f}_i$	:	Design variables, TF in traditional beam problems
f_i, $R_{y,j}$	:	Design variables, TF and vertical position of tendon control points in prestressed beam optimisation
F_{LL}, F_{DL}, F_P	:	Force matrices of live loads, dead loads and prestressing forces
K, V, F, u	:	Global stiffness, Force and deformation matrices
$K_{e,i}$, $V_{e,i}$	:	Stiffness and volume of element *i*
λ	:	Lagrangian multiplier
l, d, b	:	Dimensions of a design space (length, depth, width)
nc, ns, ne	:	Number of control points, segments and set of nodes in an element
N_i^{3D}	:	3D shape functions of a node *i* for geometric approximation
$N_{ni}^{2.5D}$	:	2.5D shape functions of a node *ni* for planar transformation
N_e, N_n, $N_{I,i}$, N_h	:	Set of elements, nodes, influencing nodes of node *i* and hanging nodes
Ω, Ω^m, Ω_e	:	Design, Material occupancy and element spaces
p	:	Penalty to avoid intermediate design candidates
r_i, t_i	:	Tendon coordinates, and scaling factor for Bezier definition
$r_{I,i}$, $r_{i,j}$	:	Influence radius of node *i*, and distance of node *j* from node *i*
R	:	Set of real numbers

R_i, $R_{y,i}$	:	Coordinate and vertical position of control point *i*
σ, δ	:	Stress and displacement
$t(x,y)$	:	Characteristic thickness
$th_{k,i}$, $th_{v,i}$	:	Thicknesses of node *i* for stiffness and volume estimations
V, V_o, V_r	:	Volume of material space, design space and volume ratio
w_i	:	Inverse distance wight of node *i*
W_c, P_{ext}	:	Concentrated load and external prestressing

Chapter 1

Introduction

1.1 Background

Concrete is a widely used building material around the world due to the abundance of its constituent materials and relatively cheap production costs. Concrete can be moulded to any desired shape due to its workability, and myriad structural forms can be achieved. However, the shape of the concrete structures is often associated with pre-cast moulds (formwork) in traditional constructions. In current design practice, only a limited range of structural shapes are available due to using formwork in construction. New formwork must be manufactured often to achieve new-fashioned forms into which ready mixed concrete can be poured after adequate steel reinforcement is appropriately placed and anchored. Structurally optimised geometries could reduce material usage and, potentially, construction costs. Despite the potential of concrete that can be moulded to any complex geometry, relative formwork and the requisite skilled labour can be expensive and difficult to procure. The requirement of highly skilled labour and increasing complex formwork leads to extended construction times, thereby severely constraining the degree of optimisation that is practically possible. Therefore, traditional construction practices are not equipped to take full advantage of the potential of concrete construction by its ability to be moulded into an infinite number of shapes.

Besides cement sector is ranked 3rd in the industrial source of pollution. Construction is among the most polluting industries on the planet, and its contribution to global emissions is categorised into (a) material production and construction-related activities and (b) operation of constructed environments. The former accounts for 10% of the global carbon dioxide emissions [1], consuming 40-50% of globally available raw material resources and 40% of the waste in landfills. Manufacturing construction materials itself consumes 5% of global energy and contributes to 5% of global greenhouse emissions. Reportedly 10-15% of material is wasted at the time of construction. Green and sustainable construction management practices can also be adopted to reduce construction waste [2-3]. Further, replacing cement with fly ash in the concrete mix can help [4], but with prevailing practices, the carbon footprint of construction will remain high.

The intensive use of the material in chunky constructions, the inability to use the potential of design-based structural optimisation and the large requirement of labour is making construction expensive in terms of money, resources, and environment. Most traditional constructions involve 70% labour and 30% material costs, with an average profit of 10-25% depending on the scale of construction [5-6]. With the ability to mould cement to any shape and manufacturing of design-based optimised systems quantitatively requires less material and little labour and reduces material wastage, this further impacts the production of construction materials, thereby reducing the environmental impact of the construction industry. Therefore, automating the construction process and optimising the material usage could help save labour and material costs, including material wastes and these savings are estimated to be approximately 50% of conventional construction costs [6-7].

1.2 Automation in Construction

In her 2020 policy address, the HK Chief Executive set the target of peak carbon by 2030 and carbon neutrality by 2050. To achieve this ambitious target, a circular economy in the context of climate and carbon-neutral urbanism is the only way forward for Hong Kong and the Greater Bay Area (GBA). GBA ranked second among the world's top 100 innovation clusters in 2020 (by scientific publications and patent applications), rapidly becoming an economy with a growing reliance on technological innovation and high-value manufacturing based on robotics and automation. This, however, is not the case in the construction industry, both locally and globally. Although automation in construction has been spoken about for a long time, the pace of change in construction practices has been much slower. Precast, prefabricated, and modular construction have been around for a long time, having promised much but delivered a lot less, seemingly unable to capture the imagination of engineers and architects in the same way that automation has transformed automotive manufacturing, for instance. In addition to environmental concerns, skills shortages and an ageing workforce is plaguing construction in most developed economies, including Hong Kong. Therefore, automation in construction is increasingly the only option available, and satisfactory alternatives must be found to reduce reliance on traditional construction processes that are slow, expensive, polluting, dangerous, labour-intensive, and wasteful of material and energy resources and, therefore, unsustainable. While precast or prefab reinforced concrete construction can be faster, cleaner, less labour-intensive, and less dangerous, it is still be wasteful of material and energy resources. However, the lack of widespread adoption and acceptance of traditional prefab construction has more to do with its limitations in offering architecturally and aesthetically interesting options. Traditional prefab construction is based on largely uniform and prismatic structural components assembled to create boring and boxy architectural forms. Therefore, just as traditional in-situ construction, traditional prefab construction also presents significant hurdles against achieving a harmonious balance between form and function and imposes severe limitations upon the architect's vision of the practicalities of engineering and the constraints of what is technically and economically feasible.

1.3 Aesthetic Sense in Routine Construction

What if judicious exploitation of modern technologies in construction could open up new opportunities in this context: where ostensibly conflicting requirements could lead to novel synergies [8-10]; so that mathematically optimised forms of structural components could also satisfy aesthetic concerns; while other functional, engineering, economic and sustainability imperatives may be addressed by the optimum placement of materials through additive manufacturing (AM). These components could then be prefabricated using techniques such as 3D printing (3DP) in a smart and automated manufacturing facility, followed by transport and assembly on-site. Mass production of customised components using AM techniques as described here should significantly reduce resource requirements lowering embodied energy of constructed facilities while also enabling much greater leeway in accommodating the architect's vision, thereby promoting more widespread adoption of prefab construction. Such a view of future construction has a natural synergy with engineering idealisations traditionally made for analysing structural components where hidden internal structures are visualised inside the usually prismatic shape of a structural component. Form finding is a common technique used in tension structures and famously even for renaissance architecture, such as Gaudi's use of chains in tension to obtain the ideal form of the Gothic spires of the Sagrada Familia. The organic forms of Gaudi's architecture has made Barcelona a must-see international tourism destination. Architects such as Eladio Dieste and Félix Candela have exploited the tremendous strength of the shell and folded plate forms to create impossibly slender and long-span enclosures without internal supports [11-12]. However, these human endeavours pale into insignificance against the sheer fecundity of nature in the diversity of forms and their constant evolution in order to better adapt to their environment. Examples of such evolution are also found in vernacular architecture, where constructions that survive natures tests, such as earthquakes, proliferate (e.g. "Dhajji Diwari" type construction in the Himalayan region of Kashmir). The increasing complexity of modern architectural designs that primarily draw their inspiration from art and human imagination and creativity could potentially benefit from a shape optimisation methodology leading to sustainable and robust structural forms that remain architecturally intriguing and aesthetically pleasing. This thesis is intended to explore the feasibility of using a relatively quick and computationally efficient visualisation approach coupled with an efficient shape optimisation technique to achieve the aforementioned objective. The same approach could then be adapted to guide the fabrication process using AM technologies. Such an approach can only be established if engineers and architects collaborate more closely and have access to tools that allow them to examine and explore novel of forms and structural members that they design and subsequently refine iteratively for form and function.

1.4 Optimisation as a Tool to Integrate Form and Function

The concept of form and function flexibility in construction has gained increasing interest in the commercial sector and among engineers [13]. While modern construction practices and construction-oriented optimisation [14] have been explored, the intersection of this with architecturally appealing structures has yet to be fully realised. Topology optimisation (TO) in structural, aerospace and mechanical engineering fields has been conceptually investigated [15-26] but manufacturing the optimised components is still a complicated process due to (a) the manufacturing burden of formwork and (b) the difficulty in achieving the standards of limit-state design. Recently growing AM/3DP process is stepping forward to form-free construction, but (a) achieving tensile strength and (b) printing the entire structure are still questionable. Aesthetical appearance is one of the major aspects of iconic constructions, but severe limitations are usually imposed upon an architect's vision by the practicalities of engineering and economics. An architecture made routinely and economically without wasting material is achievable by a marriage of form and function, e.g., manufacturing aesthetically inspired and optimised components using 3DP. In recent years, researchers at the UK EPSRC Centre for Innovative Manufacturing in Additive Manufacturing have made valuable efforts to deliver an AM process capable of producing full-scale construction and architectural components [27-30]. However, the enormous potential of these ideas has not been fully explored, particularly with reference to learning from natural systems or as part of a systematic mathematical approach to optimise form and function. The traditional linear approach to civil engineering construction inhibits architectural flair and creativity as a result of the aforementioned limitations. The approach proposed here will take advantage of modern software tools for geometry modelling and visualisation, shape optimisation and computational simulation in order to substantially expand the engagement between architects and engineers in order to conceive hitherto unimaginable designs for fabrication using AM technologies. This paradigm already exists in manufacturing mechanical components. However, the approaches to structural shape optimisation in this field can be highly computationally intensive because of the complexity of the shapes involved. This can be justified for mechanical parts that, once designed, may be produced in their thousands or even millions but are unlikely to be cost-effective for a building made of 100s or 1000s of individually customised structural members in the context of the proposed paradigm. This is where AM technology promises great potential to serve the architect's imagination. Modern AM processes are already capable of producing full-scale construction and architectural components. Thus, customising structural components could benefit from the shape-optimised design, which not only offers structurally efficient and sustainable designs but can also satisfy aesthetic aspirations.

The overview of the above aspects inspired the author to explore the ultimate vision of creating a new cross-disciplinary architectural design framework that facilitates concurrent engagement of architects and engineers at all stages of the process of a building, from the earliest stages of conceptualisation through to construction. The aim of this framework is to bridge the gap between form and function by providing designers with a tool that can be used for generating highly customised designs optimised for cost, function and aesthetic appearance while establishing a suitable modelling and structural analysis approach and developing the necessary software tools for implementing the new design framework that offers not only functionally efficient and sustainable structural designs but also aesthetically pleasing results. This further requires a practical demonstration of a series of increasingly complex use cases through unlocking the potential of AM in the field of engineering and construction in consultation with the professional network of engineers and architects who have pledged contributions to this vision, thereby the output is directly adaptable by industry and can be integrated into other areas of architectural design. Despite the potential benefits of form and function flexibility in construction, there are still significant challenges that must be overcome before this vision can become a reality. Due to the limited size and scope of this thesis, it can only begin to address some of the most pressing challenges that are relevant to advancing this vision.

The main aim of this thesis will be to flesh out the above-proposed design framework that allows an architectural expression into engineering design. In this context, structural components such as beams are planned to explore, and the contents of this thesis are believed to help develop a new architectural paradigm that enables highly customised and automated prefab construction process optimised for form, function, cost and performance. The afore-discussed and outlined solutions for the highlighted issues or foreseen advancements, possibilities and limitations helped to form the objectives of this thesis which will be pointed out in the following section.

1.5 Research Objectives

The above discussion provides clear guidance for this thesis in introducing a new optimisation procedure in the context of 3DP and aesthetic design. The supposition is that optimising a structural component will result in non-prismatic shapes. The primary objectives of this research are to develop a novel element that can effectively characterise these non-prismatic shapes for structural analysis and to create an innovative optimisation module that can efficiently retrieve and track the shapes of structural components.

I. The first objective aims to develop an element that can accurately describe the non-prismatic shapes of structural components. This element will be used for structural analysis and will be developed based on mathematical and computational models. The goal is to create a new element that can accurately represent the complex geometries of non-prismatic shapes.

II. The second objective aims to develop an optimisation module that can efficiently retrieve and track the shapes of structural components. This module will be designed to work with the new element developed in the first objective and will be capable of fetching the shapes of the structural components. This process will involve exploring the widely-used optimisation method TO.

By achieving these objectives, this research intends to contribute to the field of structural engineering and 3DP by providing a new approach to designing and optimising structural components that can enhance both their functional and aesthetic properties. Although this research will not include the evaluation of the aesthetic properties of the optimised shapes and their contribution to the overall design of the structural component, these factors will be explored in future research by developing an assessment tool for visual appeal, uniqueness, and functionality, as well as how the optimised shapes fit within the broader design context.

This research may have practical applications in various fields, such as architecture, product design, and engineering, where the use of 3DP is growing rapidly. The potential impact of this research will be significant, and it may pave the way for further developments in the field of structural engineering and 3DP.

1.6 Research Questions

There are many challenging questions to be answered while achieving the above objectives. In this context, the most important and fundamental research questions to be addressed in the thesis are:

I. Can the new element accurately represent the complex geometries of non-prismatic shapes, including curvy profiles and varying cross-sections, for structural analysis?

II. Can the new element provide efficient results comparable to traditional finite elements while accurately representing non-prismatic shapes?

III. Can the proposed optimisation tool effectively address the shortcomings of TO and produce optimised profiles like the famous Solid Isotropic Material/Microstructure with Penalisation (SIMP) [16-18] method for non-prismatic shapes?

IV. Do the optimised shapes generated by the proposed optimisation tool offer the necessary safety and stability required for structural components?

V. Can the proposed optimisation tool generate smooth shapes that require minimal or no post-processing efforts?

Addressing these fundamental research questions will require a thorough investigation of various mathematical and computational models and optimisation techniques. Overall, the above task will contribute to creating an innovative optimisation module that can efficiently retrieve and track the shapes of structural components.

1.7 Research Methods

The present thesis aims to develop a tool that bridges aesthetics, structural design, and manufacturing with the primary goal of enhancing the functional and aesthetic properties of structural components. Any architectural expression will serve as the initial design candidate, while manufacturing will play a critical role in the final phase of building the tool. The tool will involve processes such as numerical modelling, simulation, and optimisation, which will be developed in various phases while addressing the above research questions. The phases of development are listed as follows:

I. Development of a novel element: The development of a novel element will involve a thorough investigation of various mathematical and computational models to accurately represent non-prismatic shapes.

The accuracy and efficiency of the new element will be evaluated using established engineering principles and testing methods. The development process will involve the following steps:

(i) Review and analysis of existing literature on mathematical and computational models for TO techniques and the element classes used.

(ii) Selection of appropriate models based on their accuracy and efficiency.

(iii) Implementation of the selected models to develop the new element.

II. Evaluation of accuracy and efficiency of the new element: The accuracy and efficiency of the new element will be evaluated using established engineering principles and testing methods. The evaluation process will involve the following steps:

(i) Selection of appropriate test cases and benchmark problems to evaluate the accuracy and efficiency of the new element.

(ii) Implementation of the new element to solve the selected test cases and benchmark problems.

(iii) Comparison of the results obtained using the new element with those obtained using traditional finite element methods. Factors such as displacements, stresses, and computational resources will be compared.

(iv) Evaluation of the accuracy and efficiency of the new element based on the comparison of the results obtained.

III. Development of an innovative optimisation module: The development of an innovative optimisation module will involve exploring various TO techniques and evaluating their effectiveness in generating optimised profiles. The optimisation module will be designed to ensure that the optimised shapes offer the necessary safety and stability required for structural components while requiring minimal post-processing efforts to produce non-prismatic shapes. The development process will involve the following steps:

(i) Review and analysis of existing literature on various TO techniques (pathologies, limitations and advantages).

(ii) Selection of appropriate theories to develop an optimisation technique based on their effectiveness in generating optimised profiles for non-prismatic shapes.

IV. Evaluation of the effectiveness of the innovative optimisation module: The effectiveness of the innovative optimisation module will be evaluated using established engineering principles and testing methods. The evaluation process will involve the following steps:

(i) Identification and selection of appropriate test cases and benchmark problems to evaluate the effectiveness of the optimisation module.

(ii) Implementation of the optimisation module to solve the selected test cases and benchmark problems using the widely-used optimisation method TO.

(iii) Comparison of the results obtained using the optimisation module with those obtained using traditional optimisation techniques. Factors such as computation time, optimised shape resolution, and energy minimisation will be compared to assess the performance of the optimisation module.

(iv) Evaluation of the effectiveness of the optimisation module based on the comparison of the results obtained. The findings will be analysed to determine the strengths and limitations of the optimisation module and to identify potential areas for improvement.

(v) Application of ultimate loads to one of the test cases to assess the stress state of the component beyond its designed loading capacity. This will provide insights into the structural behaviour and robustness of the optimised shapes.

V. Demonstration of the practical application of the optimisation module by manufacturing one of the test cases: The optimised shape from the ultimate displacement analysis will be manufactured using 3D printing for display purposes. The manufacturing process will be documented to evaluate the feasibility and practicality of the optimisation module for real-world applications.

VI. Demonstration of surface fetching into the optimisation module: In this phase, a demonstration is presented on how the tool can efficiently retrieve and track the shapes of structural components.

VII. Extension of the capabilities of the optimisation module to deal with practical applications of concrete constructions: This phase will involve expanding the optimisation module's capabilities to enhance the design of concrete constructions.

Overall, the research methodology for this thesis will involve a combination of literature review, mathematical and computational modelling, implementation, and evaluation using established engineering principles and testing methods. Apart from the above methods or questions, many technical issues might arise while dealing with mathematical modelling. Most of these issues might be technical and will be addressed with swift logic.

1.8 Organisation of the Thesis

This thesis is structured in a traditional chapter-wise manner, with each chapter covering a specific aspect related to the central focus of the thesis, which is the creation of a novel tool that merges aesthetics, structural design, and manufacturing to enhance the functional and aesthetic properties of structural components.

The thesis is highly technical and requires the reader to have a fundamental understanding of several fields, including AM, free body mechanics, calculus, finite element modelling and simulation, structural engineering, and optimisation techniques. Additionally, prior knowledge of MATLAB command language and visualisation is necessary.

The chapters are organised as follows:

Chapter 2 - Discusses the history of automation, the evolution of AM, and the evolution of structural optimisation in line with the thesis's objectives.

Chapter 3 - Development and testing of a new 2.5D element to represent the non-prismatic nature of structural components and integrate architecturally inspired shapes into the optimisation module.

Chapter 4 - Presentation of a new optimisation setup called Solid Isotropic Material with Thickness Penalisation (SIMTP) to scale the geometric design variables and perform parametrisation within the structural design code conditions. Testing of the SIMTP method on cantilever MBB and L-beams using 2.5D elements.

Chapter 5 - This chapter explores adaptive refinement with SIMTP and revisits the test cases demonstrated in Chapter 4, using different mesh setups for design and analysis modules with 2.5D elements.

Chapter 6 - Comparison of optimised profiles using 2.5D SIMTP with a beam optimised using a 3D optimisation module. Practical application of 2.5D SIMTP in digital manufacturing using thermoplastic material after performing ultimate load analysis.

Chapter 7 - Extension of 2.5D SIMTP to prestressed concrete systems and exploration of various test case scenarios. Use of load balancing concept to identify optimal tendon profile and concrete geometry and modeling of prestresses using the equivalent load method. Use of Bezier representation to build tendon geometry.

Chapter 8 - Conclusion and future work, outlining remarks and conclusions from Chapters 2 through 7 and paving the way for future research. The thesis presents a novel approach to structural design and manufacturing, highlighting the possibilities of bridging architectural design, structural design, and manufacturing aspects using the 2.5D SIMTP tool.

Overall, the thesis provides an in-depth exploration of 2.5D elements and the development of the SIMTP optimisation setup, presenting a fascinating and innovative approach to structural design and manufacturing. The detailed organisation of the thesis offers an engaging and informative read for anyone interested in the field.

Chapter 2

Literature Review

The primary objectives of this thesis were discussed in the previous chapter, which emphasised the significance of exploring the fascinating topics of automation in construction, AM, and structural optimisation. This chapter aims to comprehensively review the latest research in these fields, contributing to the growing body of knowledge on AM and optimisation. By examining advancements in these areas, this thesis hopes to identify new opportunities for innovation and improvements in manufacturing efficiency and effectiveness. To fully comprehend the contents and terminology in this chapter, readers should have a fundamental understanding of these subjects. This literature review serves as a crucial foundation for the remainder of the thesis, which will delve deeply into the latest advancements and challenges in the automation and manufacturing of optimised components. In summary, this chapter will review a diverse range of articles related to automation in construction, AM, and structural optimisation, highlighting key findings and insights that can inform future research and development in these fields.

2.1 Automation in onstruction

Automation in construction is seen as the future of technology and engineering in the construction industry. The concept of robotic construction has been around since the 1950s, with early developments focused on laying bricks, fabricating building units, and assembling building components [31]. However, these approaches were limited in meeting the needs of contemporary architecture. Since then, this concept has been extended to include the idea of depositing materials through unmanned actions, leading to the development of various terms such as AM, rapid prototyping, 3DP, digital fabrication (DF), and freeform construction, with AM becoming the most commonly used.

Additive manufacturing, also known as 3D printing, had its roots in the 1980s when the basic idea of robotic material deposition to create 3D solid objects from computer-aided design (CAD) models were first explored [32]. The robotic movements are directed by computer numerical controls (CNC), allowing for precise placement of the material in accordance with the geometrical coordinates [33]. The first patented process for AM was stereolithography (STL), filed on July 16, 1984 [34]. STL stores volumetric data in a surface mesh format, which is used by 3D printers to deposit material in a layer-by-layer fashion to form required geometrical models and prototypes. Since then, various additive processes have been proposed and brought into practice, including fused deposition modelling [35], rapid prototyping [36], and contour crafting (CC) [37], primarily used for building printing using concrete. Another advancement in AM technology is voxel-based printing, which enables greater control and customisation of printed objects [38]. Unlike traditional 3D printing methods, which rely on layer-by-layer deposition of materials, voxel-based printing divides a 3D object into small cubic units known as voxels, allowing for the creation of complex geometries and customised internal structures [39].

Voxel-based printing has shown potential in various fields, including medicine, where 3D printed organs and tissues can be customised to match the specific needs of individual patients [38]. For example, using voxel-based printing, doctors can create patient-specific implants that precisely fit the shape and size of the patient's bone or tissue, reducing the risk of complications and improving the patient's outcome [40].

Moving on to 3D construction printing (3DCP), this technique uses large-scale 3D printers to create building structures and is gaining popularity due to its speed, cost-effectiveness, and sustainability. 3DCP could revolutionise the building industry by reducing construction time and waste while enabling architects to create more complex and intricate designs [37]. Overall, the STL patent and subsequent advances in AM technology, including voxel-based printing, have opened up new possibilities for customisation and complexity in manufacturing, with applications ranging from medicine to construction.

2.1.1 3D Construction Printing

The construction industry has seen the emergence of 3DCP, a type of AM that can produce structural components without the use of formwork or moulds. The use of 3DP in construction has been under development since the mid-1990s [41], with CC and selective laser sintering [42] being two techniques that can be used to print concrete and steel, respectively. CC was the first patented 3DCP technique developed by Dr Behrokh Khoshnevis at the University of Southern California in 1995 [37]. CC uses a large-scale 3DP system with a computer-controlled gantry system and a specially designed extrusion nozzle to deposit concrete in a precise and controlled manner, allowing for the rapid construction of large structures. CC has the potential to revolutionise the construction industry by reducing the time and cost of building construction and enabling more complex designs. Although still in the early stages of development, CC has already been used to construct small buildings and is being explored for larger-scale projects.

In 2000, model-scale 3DP of construction materials was tested at the laboratory level. Various deposition strategies were proposed between 2000 and 2010, including freeform fabrication [43], which includes D-shape and gantry-based techniques. In mid-2014, the first 3D-printed concrete castle was completed by Total Kustom [44] and in the same year, WinSun Decoration Design Engineering Co., a China-based construction company, allegedly constructed a group of houses in a day. In early 2015, the company completed the construction of a 6-storey building and a villa in China [45], stating that this construction method saved 60% materials, 70% time, and 80% labour compared to traditional construction practices.

Figure 2.1: 3D printed structures. (a) Concrete Castle in Minnesota [44]; (b) Six-storey building in China [45]; (c) Bikers bridge in Netherlands [46]; (d) Office building in Dubai [47]; (e) Two storey house in China [48]; (f) MX3D bridge in Eindhoven [49]

Various 3D-printed structures are presented in Fig. 2.1. One notable example is the 3D-printed pre-stressed concrete bridge installed and opened for cyclists in the Netherlands by TU/e and BAM Infra in 2015 [46]. The bridge underwent safety testing and can withstand loads of up to two tons. The construction process involved segmental printing, with individual end blocks designed and printed separately, then later assembled to form the bridge. Other impressive 3D printing projects include the 3D-printed hotel completed in the Philippines in 2015 [50], an office building in Dubai constructed using 3DP in 2016 [47], and a two-story building in China also built using 3DP in the same year [48]. The MX3D bridge project, which began in 2015, was completed in 2018 and demonstrated that AM is applicable to massive constructions [49]. These examples demonstrate the potential of 3DP in the construction industry and have spurred further research and development in the field. Many organisations are adopting 3DP technology, and there is a growing interest in this area [51].

Through the use of 3DCP, it is possible to construct complex and intricate structures with a high degree of precision and accuracy. This has the potential to revolutionise the construction industry by reducing costs and construction times [6-7], while also enabling the creation of more unique and innovative designs. 3DCP has been utilised to construct a variety of structures, including houses, bridges, and other infrastructure projects. However, the technology is still in the early stages of development for building large-scale structures due to limited strategies for the simultaneous printing of concrete and steel.

2.1.2 Available Printing Strategies and Technologies

The construction industry is gradually evolving with the integration of innovative manufacturing technologies, and 3DP is at the forefront of this revolution [52]. The potential of 3DP to liberate construction processes from rigid form-dependencies is promising, offering limitless opportunities for aesthetic expression and free exploration of architectural form. Beyond the aesthetic benefits, 3DP has the potential to significantly reduce the carbon footprint of construction [5-7], while also facilitating the manufacture of optimised components for functional objectives, such as weight reduction and efficient use of materials [13].

Despite its potential, 3DP technology is still developing and faces significant challenges before it can be widely adopted as a viable alternative to traditional construction practices. One of the main challenges is the incompatibility of 3DP technologies for steel and concrete, which is a critical limitation for reinforced concrete systems [41,52-53]. This severely limits the ductility of digitally fabricated concrete components and results in an immediate fracture under tensile loads. To overcome this limitation, prestressing is found to be a better alternative. Projects such as "OptiBridge" by Ghent University [54] (Fig. 2.2) and the "Bridge Project" by TU Eindhoven [55] (Fig. 2.3)) have successfully produced 3D printed prestressed concrete bridges. With ongoing research and development, researchers and industry experts are working tirelessly to devise a strategy that can unlock the full potential of 3DP in construction.

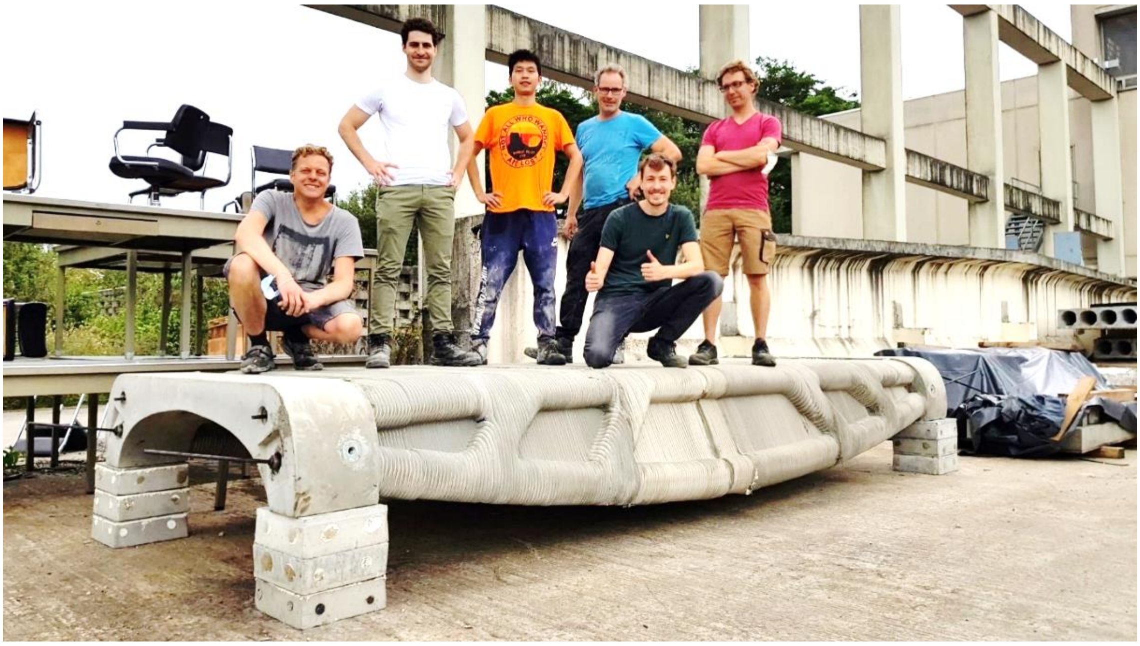

Figure 2.2: OptiBridge project [54]

Figure 2.3: Bridge project [55]

As highlighted in Fig. 2.4 to Fig. 2.6, various techniques have been developed to digitally fabricate reinforced concrete structures. These techniques include external reinforcement [56-59], internal reinforcement [59-61], and fibre reinforcement [62-66].

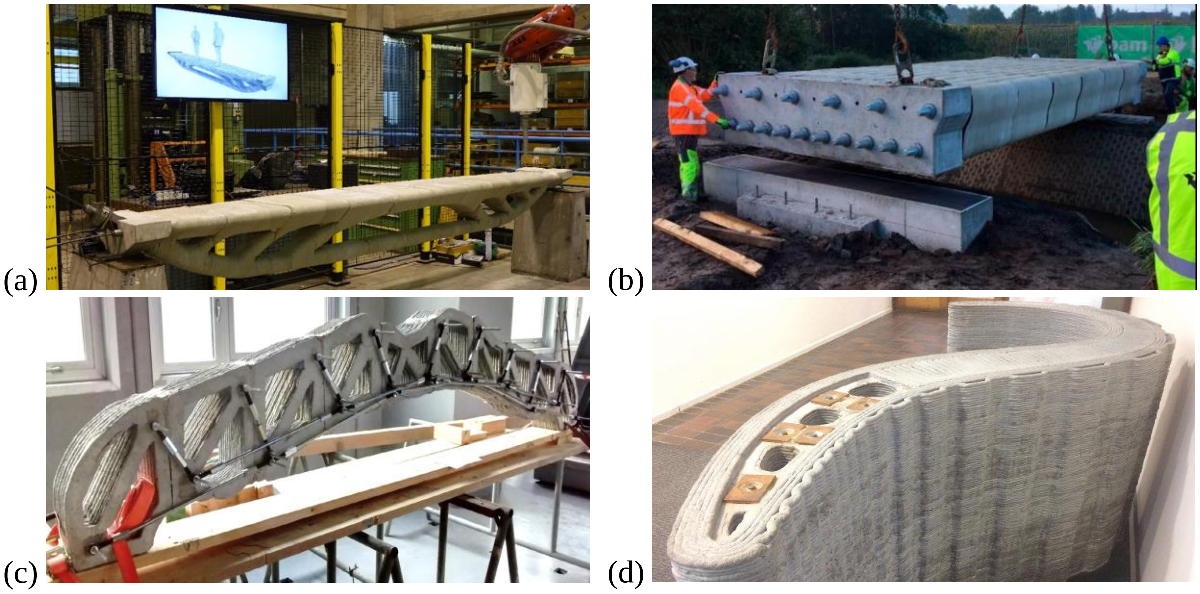

Figure 2.4: External reinforcement. (a) optimised and prestressed beam [56]; (b) prestressed bridge [57]; (c) external rebar [58]; (d) post-tensioned wall [59]

External reinforcement, as presented in Fig. 2.4(b), involves prestressing by post-tensioning and has been successfully used in the construction of a bridge for cyclists in the Netherlands [57]. While this technique has proven effective, it may not always be practical and imposes restrictions on the form. On the other hand, the direct placement of reinforcement [58] can be flexible for small-scale components but poses severe constraints on form and practicality, as shown in Fig. 2.4(c). To mitigate the risks from exposure to the structural elements, it is essential to cover the reinforcement.

Internal reinforcement techniques, as presented in Fig. 2.5(a), use the direct placement of workable concrete, while 3DP requires non-slump and fast-setting concrete, which may result in a cold bond between concrete and steel. However, the use of non-concrete formworks, as shown in Fig. 2.5(b), can increase production costs, and the use of concrete formworks, as shown in Fig. 2.5(d), can result in a cold joint with infilled concrete.

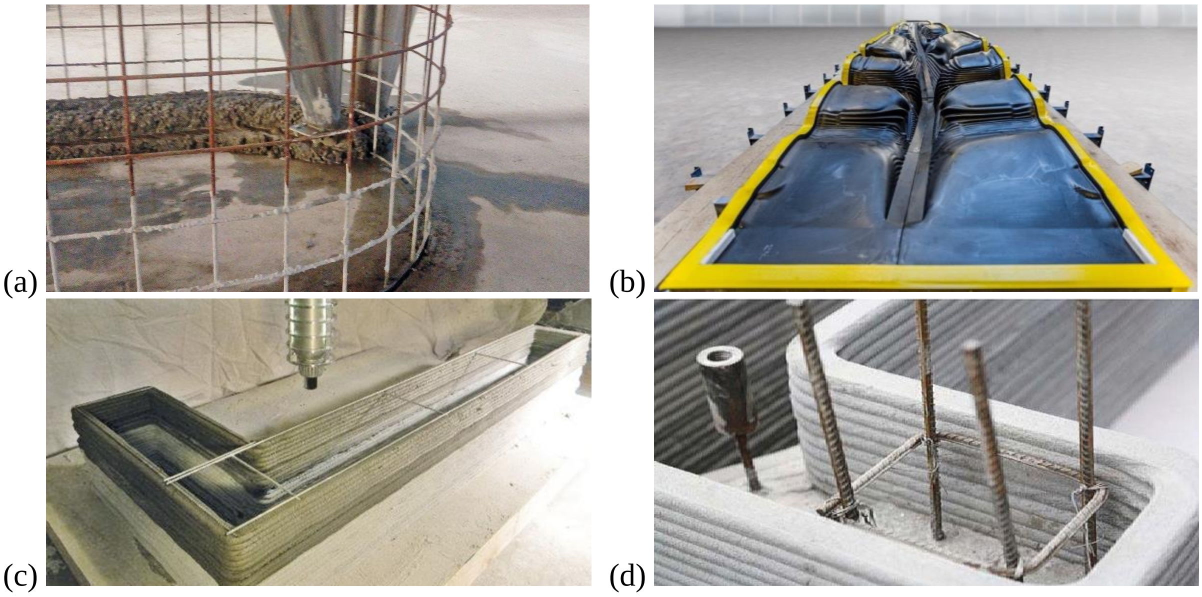

Figure 2.5: Internal reinforcement. (a) simultaneous concrete laying [59]; (b) non-concrete printed formwork [60]; (c) placing while laying concrete layers [61]; (d) concrete formwork [61]

Fig. 2.6 shows an alternative technique to significantly improve the ductility of the concrete by using steel wires or fibres in the concrete mix [62]. This technique has shown great promise and has the potential to revolutionise the way we construct buildings and infrastructure. However, fibre reinforcement usually underperforms relative to rebars [53,63], and further research is needed to study the rheology of fibre-reinforced printed concrete in the context of 3DP.

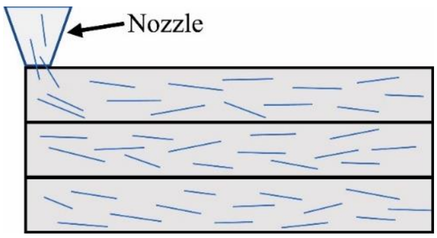

Figure 2.6: Fibre-reinforced concrete concept [62]

Despite the above challenges, one of the main limitations of 3DCP is the lack of design codes and standards, which can make it difficult to ensure the structural integrity of the reinforced structure. In addition, the long-term performance of 3D printed structures under different environmental conditions is not yet fully understood.

In conclusion, the development of these new techniques for digitally fabricating reinforced concrete structures is a testament to the innovation and dedication of researchers and industry experts in this field. Despite the remaining challenges, 3DP technology is rapidly gaining worldwide appeal as a solution for digitally fabricating reinforced concrete structures. With continued innovation and development, it has the potential to revolutionise the construction industry, providing cost-effective, durable, and safe solutions.

The evolution of optimisation techniques over the decades, as discussed in the following section, further highlights the potential for creating sustainable and efficient structures by integrating 3DP with structural optimisation principles. As new techniques are developed, and existing methods are refined, future construction will hold endless possibilities for digitally fabricating structurally optimised reinforced concrete structures.

2.2 Optimisation

Optimising the material distribution in a design domain is gaining traction with newly emerging technologies [56], especially in the context of 3DP processes. Various mathematical formulations have been developed to optimise the size, shape, and topology of a component to achieve optimal stiffness and strength while minimising the overall weight of the structure. Early in the 1980s, optimisation was limited to sizing (cross-section) and shaping (geometry), making it challenging to generate holes in topology for various reasons. TO methods were the first to introduce holes in a design space by gradually removing the material.

2.2.1 Topology Optimisation

TO came to the limelight after Bendsøe and Kikuchi [15] developed the homogenisation design method (HDM). HDM fundamentally describes the body as many microstructures that have void and solid phases, providing a basis for the development of several density-based optimisation (DO) methodologies. These include SIMP [16-18], RAMP: Rational Approximation of Material Properties [19], SINH: Hyperbolic Sinusoidal Function [20], and SRV: Sum of the Reciprocal

Variables [21]. Additionally, researchers have explored geometric representation methods such as LSM: level set methods [22], PFM: phase field methods [23], MMC: Moving Morphable Components [24], cellular methods [25], and ESO: Evolutionary Structural Optimisation models [26], to investigate the optimal material distribution. SIMP, in particular, has become a widely used DO method and is a standard tool for optimising lightweight components in the aerospace and automotive industries. The essence of SIMP is to optimise the material distribution by minimising the compliance of the structure subjected to certain constraints such as volume fraction, stress, and displacement.

However, every mathematical expression and implementation strategy comes with limitations that must be understood to enhance existing strategies. One of the limitations of SIMP is the presence of numerical instabilities in the limit state. This instability occurs when the material density approaches zero, leading to a singularity in the problem. Another limitation of SIMP is the presence of checkerboard patterns in the material distribution. This pattern arises due to the discrete nature of the optimisation problem, causing alternate regions of high and low densities in the optimised structure. To overcome the limitations of SIMP, researchers have proposed several modifications, including adding a penalisation term to the objective function, introducing filters to eliminate checkerboard patterns, and using a material interpolation scheme such as the power-law or exponential law.

The subsequent section of this study will focus on discussing the limitations and instabilities of SIMP, as well as the modifications proposed to overcome them. This discussion aims to provide valuable insights into the challenges associated with optimising material distribution using SIMP and the various methods that have been proposed to enhance its effectiveness.

2.2.2 Limitations and Numerical Instabilities of SIMP

SIMP has been widely used for over two decades to optimise structural components in the finite element method (FEM), and it has been implemented in most commercial software due to its simplicity and efficiency. In conventional FEM, density is used as a design variable to yield stiffness-based solutions under given load and boundary conditions. Density as a design variable conventional FEM delivers stable solutions until the material remains within its elastic limits. However, material non-linearity and geometric non-linearity with incremental strain analysis can add complexity to this process, as stiffness becomes a function of density and strain. This complexity is exacerbated by low-density design values resulting from the optimisation process, which can cause the loss of positive definiteness of the stiffness matrix.

To deal with material and geometric non-linearity in TO, several methods are available in the literature. One of the most popular methods is the element removal approach, such as ESO [67]. However, TO problems can also suffer from (a) checkerboarding, (b) mesh dependency, (c) point flexure or hinge formation (one-node and de-facto) in compliant mechanisms (CM), (d) pixelated (low resolution) images, grayscaling, (e) sharp boundaries and thin member formations, (f) layering or islanding phenomenon. There are many alternatives in the literature to avoid the issues mentioned above, such as (a) using higher-order elements, (b) regularisation techniques implemented either by filtering or adding extra constraints (sensitivity and density filters, MOLE constraint method: MOnotonicity-based minimum LEngth scale), (c) projection methods (Heaviside and Morphology filters), (d) non-conforming finite elements and adaptive refinement, (e) nodal design variables (CAMD: Continuous Approximation of Material Distribution) and Multiresolution methods (MTOP: Multiresolution Topology Optimisation).

Rigid mechanisms: Articles on TO typically focus on determining the optimal material distribution for various beam designs, including cantilevers, MBBs, and L-beams. This optimisation process is based on the FEM, which utilises 2D plane stress elements with a unit thickness to model the beams' behaviour under load. While most studies rely on element-based density as design variables (EDV) with a constant or uniform material distribution within the element, some investigated material distribution using nodal density variables (NDV). However, research has shown that many TO issues are associated with EDV, including checkerboarding and mesh dependency issues. Regularisation methods such as sensitivity filters [68-69] and density filters [70-71] can address these issues, but solutions often result in grayscaling. Higher-order elements have also been explored, but they cannot entirely suppress checkerboarding issues [72-73]. A Heaviside projection method (HPM), introduced by Guest et al. [74], is an effective alternative for suppressing grayscaling while producing smooth boundaries. Non-conforming elements have also been used to eliminate checkerboarding issues, with Jang et al. [75-76] utilising these elements in 2D and 3D with perimeter control [77] / slope control [78] / local slope (density) control [79] to solve numerical instabilities. However, thin members were observed in optimised results using non-conforming elements.

Flexible mechanism: Flexible mechanisms, also known as compliant mechanisms, are prone to pathologies such as checkerboarding and point flexures, specifically one-node and de-facto hinges. Studies have shown that checkerboarding and point flexure occur due to overestimated element stiffness or lower spring stiffness [80-83]. While one-node connected hinges are an advanced form of checkerboarding, checkerboarding is reported during the optimisation process, especially when using EDV, whereas hinge formations in CM result from mathematical modelling. Filtering methods that can eliminate checkerboarding can also eliminate one-node hinges, but de-facto hinges are inevitable. Even when one-node hinges are eliminated using filtering methods, it results in lumped compliance or ultra-thin membered hinges. Alternatively, some studies have attempted to eliminate hinge formations through distributed compliance. For instance, Poulsen [84] developed the MOLE method to eliminate checkerboard problems and converted one-node hinges to distributed hinges, resulting in persistent grayscaling. A recent review paper by Zhu et al. [85] also reported that point flexures require attention beyond existing methods. However, the pathologies that arise during the optimisation of CM are beyond the scope of the present study and will be evaluated in future studies.

Given the issues associated with EDV, such as pixelation and low resolution, the development of alternative methods for TO has become an active area of research. NDV has emerged as a promising alternative, and recent studies have explored its potential to achieve higher resolution and smoother results. Therefore, the next section will provide an overview of the latest developments in TO, with a particular emphasis on the research findings regarding the effectiveness of NDV in addressing the limitations of EDV.

2.2.3 Non-uniform Density Distribution

TO is a powerful tool for designing structures and systems, and the use of nodal densities is an approach that has been explored in various studies to enhance its effectiveness. Kumar and Gossard [86] introduced an approach for TO that utilises nodal densities to represent the shape of the design domain. This approach ensures C^0 continuity, which improves the smoothness of the final design. By assigning nodal densities at each node of the finite element mesh, the distribution of material within each element can be determined, resulting in a high-resolution design. Hammer [87] proposed using NDV to determine the element densities for TO. NDV can be defined at each node of the finite element mesh, and the element densities can be obtained by averaging the nodal densities. By using element densities that depend on neighbouring elements, checkerboarding and mesh dependency can be eliminated. However, Bendsøe and Sigmund [88] cited the former approach in their monography and stated that it could create zig-zag boundaries, which can be prevented using filtering schemes. Despite its limitations, the use of NDV has been explored in several studies, and researchers have proposed various ways to address the challenges associated with this method.

Belytschko et al. [89] proposed an NDV method that controls the shape by using implicit functions, which eliminates checkerboarding. Matsui and Terada [90] introduced the CAMD method, which uses bilinear shape functions to ensure material distribution and continuity for both standard-linear and higher-order elements, and reported no numerical instabilities during the process. However, Rahmatalla and Swan [91] found the "islanding" phenomenon while using Q4/Q4 elements with coarse meshes, which refers to the unwanted placement of material in the design domain. Although the Q4/Q4 implementation intended to revisit the problem of checkerboarding, the other goal was to explore the instabilities of the Q4 element indicated in Jog and Haber [73].

Islanding is a phenomenon in the TO where the material is placed in a layered manner within the design domain, leading to impractical designs due to the creation of thin layers of material. To address this issue, researchers have proposed various methods. Paulino and Le [92] proposed a modified Q4/Q4 method that generates high-resolution topologies and uses an internal averaging technique to eliminate islanding, which was successfully achieved. Additionally, the authors reported that CAMD [90] also suffers from islanding.

Kang and Wang [93,94] successfully demonstrated the elimination of islanding, mesh-dependency, and checkerboarding using higher-order elements (Q8) and nodal densities. Higher-order elements provide a higher degree of freedom and better approximation of the shape. They used local [94] and non-local [93] Shepard interpolants to interpolate the nodal densities since interpolation using regular Q8 shape functions may cause negative density values. Moreover, non-local Shepard interpolants introduced in [93] have the flexibility of separating the design variable points from the finite element mesh [95] and thus can be positioned at freely chosen points other than element nodes, facilitating design variable refinement to achieve a higher quality of the boundary description.

Further to the NDV methods in TO, Guest et al. [74] implemented a minimum length scale using linear and non-linear projections (HPM) on nodal densities to address potential numerical instabilities and improve the smoothness of designs. However, the authors identified that using a reduced length scale could lead to the development of thinner members and the possible appearance of point flexures - areas of high stress concentration that can lead to structural failure. To address these issues and manufacturing constraints (such as sharp corners), Guest [96] proposed multiphase projections using a minimum length scale on both void and solid phases. Guest and Genut [97] also incorporated adaptive design variables into the methodology by separating the density field from the analysis field to reduce dimensionality. Despite using Q4 elements, Guest's work [74,96-97] did not report any numerical instabilities, including the islanding phenomenon.

Nguyen et al. [98] proposed MTOP, a method similar to NDV, which produces high-resolution images without changing discretisation and reducing computational costs. Other studies have explored the use of nodal densities in conjunction with various techniques, such as functionally graded materials, which involve varying the material properties across the design domain [99]. The classical Newton-Raphson solution is another technique that can be used to improve the convergence of the optimisation process [100]. Adaptive mesh refinement, Isogeometric analysis, meshfree methods, and virtual element methods are all numerical techniques that can be used in conjunction with nodal densities to improve the efficiency of TO [95,101-116]. Other approaches, such as stress-constrained TO, geometric non-linearity, ESO, CM, design-dependent surface loading, and piezoelectric actuators, have also been explored in combination with nodal densities to address specific design challenges [80-83,110,117-123]. Additionally, MTOP has been further developed and refined by other researchers to improve its effectiveness in TO [124].

In summary, nodal density-based TO has the potential to produce high-resolution and smooth designs, but careful consideration must be given to the choice of nodal density scheme and the potential for numerical instabilities and islanding. Researchers have proposed various methods to address these challenges, including using higher-order elements, implementing minimum length scales, and using filtering schemes. Additionally, the use of other techniques in conjunction with nodal densities, such as adaptive refinement, can further improve the effectiveness of TO. The following section will focus specifically on the introduction and advancement of adaptive refinement in TO.

2.2.4 Adaptive Refinement

Adaptive techniques in TO have been an active area of research since their introduction in 1994 [125-126] and have since been extended to shells [127] and elastoplastic structures [128]. Maute and Ramm [125] found that conventional mesh refinement techniques yield unsatisfactory results and are among the first researchers to propose an adaptive isoline-based material distribution using Cubic or Bezier splines, which achieved satisfactory results compared to conventional mesh refinement techniques. Lambe and Czekanski [104-105] studied h-refinement on analysis and design meshes with a continuous density field method CAMD [90] to trace the precise boundary description. Mesh refinement is used to generate high-resolution images and eliminate checkerboard patterns while generating continuous density distribution [95,97,101-105]. However, the computational costs associated with these techniques have been a major concern while leading to discontinuous density distribution and form ultra-thin members [95,102]. Since then, several researchers have explored various adaptive processes [129-131] in TO, including r-refinement, and adaptive projection methods, to achieve high-resolution boundaries while also reducing computational costs.

Efforts were made to develop adaptive projection methods. These methods are based on separating the design field from the analysis domain. This allows the design variables to be refined or coarsened independently of the finite element mesh. The design field is then projected onto the analysis field using a filtering or smoothing operator that preserves the boundary information while eliminating spurious features and enhancing computational efficiency. Guest and Genut [97] explored these adaptive design variables using HPM [74], while Wang et al. [95] used refinement on separated density fields to reduce the computational burden and capture high-resolution boundary profiles.

Mesh adjustment, also known as moving mesh or r-refinement, is a technique that moves mesh nodes while keeping the number of elements constant. This method is relatively computation-friendly since it does not require independent design and analysis fields. However, maintaining the quality of the mesh during node movement can be challenging and may result in numerical errors or convergence difficulties. Additionally, ensuring that the boundary nodes match the optimal material distribution obtained from TO is another challenge. Wang et al. [101] and Liu and Korvink [103] used the moving mesh method to trace boundaries and addressed these challenges by employing adaptive node movement strategies based on element shape or density gradient, as well as smoothing or projection techniques to align the nodes with the desired boundary shape. Mesh adjustment methods can achieve high-resolution boundaries with low computational costs, but they may introduce inaccuracies or artefacts due to the node movement and boundary alignment procedures. Although the cited studies show promising results in achieving smoother resolution, this technique remains underexplored in the literature and requires further attention.

In summary, the TO commonly uses two approaches: element design variables and nodal design variables, each with its own advantages and disadvantages. Adaptive refinement techniques, such as r-refinement and adaptive projection methods, have been explored to achieve high-resolution boundaries while reducing computational costs, showing the potential to significantly improve the efficiency of TO. However, all of these approaches use densities as design variables (DO), and DO has its limitations. The next section will explore another important aspect of optimisation: using thickness as a design variable. By combining these different techniques, it is possible to achieve more comprehensive and optimal designs that meet multiple performance criteria.

2.2.5 Thickness Optimisation

Using thickness as a design variable is not a new idea in optimisation. Rossow and Taylor [132] proposed variable thickness sheet optimisation, but this approach cannot generate holes since the thickness is a dimensional variable that cannot be penalised, which is a primary advantage of DO. The thickness optimisation background until the 1990s and its examples can be found in Bendsøe [133]. Bendsøe [16] also stated that the basic formulation of the SIMP method excluding penalty, represents the variable thickness sheet problem. Li et al. [134,135] proposed a thickness-based ESO method where the material with lower thickness was systematically removed to create holes. Li et al. [136] also proposed a smoothing algorithm to avoid checkerboarding in ESO and demonstrated a few examples. Makrodimopoulos et al. [137,138] also proposed a smoothing algorithm to avoid checkerboarding in ESO and demonstrated a few examples. Kennedy [139] proposed a discrete thickness optimisation (DTO) method that converts discrete thickness into a continuous variable using an interpolation parameter similar to the density variable in TO. This interpolation parameter with intermediate designs was then penalised piecewise and subjected to a constraint function based on SIMP/RAMP. The cases presented in the above study are promising, and the formulation could generate holes.

However, the methods discussed above have limitations and drawbacks. For instance, the variable thickness sheet problem assumes that the thickness is uniform within each element, which may not be realistic for complex structures. The ESO method requires a predefined number of iterations and removal ratios, which may affect the convergence and optimality of the solution. The DTO method introduces additional variables and constraints, which increase the computational cost and complexity of the problem. Moreover, these methods do not consider the manufacturability of the designs, which may result in impractical or unrealistic solutions. It is worth noting that most of the approaches covered so far are conceptual, and practical cases of structural elements involved in construction are rarely presented. The following section will provide an overview of the optimisation of prestressed concrete systems, which may contribute to the idea of the practical application of the contents of this thesis.

2.2.6 Prestressed Systems

Construction-oriented optimisation [14] has the potential to be a game-changer in the construction industry, reducing material usage, promoting economic construction, and mitigating the environmental impact of construction materials. However, the optimisation of prestressed components has not been deeply explored in terms of topological derivatives, leaving a significant opportunity for innovation and advancement. Since the 1980s, research articles have made strides in the optimisation of prestressed concrete setups, albeit with limitations due to manufacturability constraints. These studies have focused on limiting design variables to cross-sectional dimensions while avoiding complex topologies, such as voids or holes. The results have been impressive, with optimal tendon configurations for multi-supported prestressed bridges demonstrated by Kirsch [140] and computer programs for optimising prestressed concrete beams using cross-sectional dimensions, reinforcement, and prestressing cable areas as design variables presented by Cohn and MacRae [141].

Despite the progress made in the field of topologically optimised prestressed components, there is still significant scope for further exploration and discovery, particularly in the area of topological derivatives. Quiroga and Arroyo [142] investigated the optimal cable size and position inside a fixed bridge deck geometry to counteract transverse loading stresses, and Erbatur et al. [143]

developed an interactive microcomputer program for optimising prestressed beams based on section adequacy, Magnel diagrams, deflections, and buckling. Lounis and Cohn [144] extended their work on multiobjective optimisation to optimal limit design for prestressed structures with fully or partially prestressed members, considering ultimate and serviceability limit states [145]. Al-Gahtani et al. [146] developed an experimental software for optimisation and structural analysis of partially prestressed continuous concrete beams with design variables including cross-sectional dimensions of the standard unsymmetrical flanged sections, area of reinforcement and tendon geometry. Han et al. [147-148] studied the minimum cost optimisation of the multi-span partially prestressed concrete beams, while Fontan et al. [149] presented a formulation for optimising the launching nose of a bridge to minimise bending moments. Despite the progress made, the majority of articles on the design optimisation of prestressed systems are similar to the above citations, with only moderate advancements such as reliability-based optimisation [150-151], algorithmic enhancements [152-156] and composite sections [157].

While continuum-based TO [15] procedures have evolved significantly, previous articles on prestressed component optimisation have generally been based on sectional analysis with a limited number of design variables due to computational constraints. This limitation arises from the need to solve a large number of inequality constraints (limit state) for each design variable, which increases the computational cost. Optimality criteria (OC) has been used to reduce the computational burden by solving the optimisation problem without explicit constraints [158], but they have limitations in terms of multi-constraint problems involving stress, displacement and frequency constraints [159-160]. Moreover, practical engineering aspects have prevented many researchers from exploring topologically optimised prestressed components fully.

Despite these limitations, some researchers have made significant progress in this area. Qing Quan Liang and Grant [161] explored performance-based optimisation of prestressed concrete beams by applying prestressing forces as external forces and converting topologically optimised beams into strut-and-tie models. Eurviriyanukul and Askes [162-163] predicted tendon position by vanishing configuration forces using the FEM, while Amir and Shakour [164] simultaneously optimised tendon geometry and concrete domain using SIMP (a density-based TO). The contents of their study were later 3D printed after the design processing of the beam [56]. Officially, this was the first optimised and 3D printed beam. However, the fabricated beam is not the direct outcome of the TO as the process is limited to producing pixel-based images, which must be extruded and post-processed for 3DP purposes. Zhang et al. [14] extended the above work to an Isogeometric analysis, idealised the tendon profile with NURBS, and imposed stress constraints on tension and compressions using the Drucker–Prager criterion. A source code for the above implementation can be found at [165]. Their study paved the way to include design criteria (limit state) into topologically optimised prestressed concrete beams. However, the above-cited articles (based on TO) are limited to elastic analysis, use element densities as design variables, and require extrusion techniques and post-processing for 3DP.

To summarise, TO is a promising approach for optimising structural components, but its full potential is yet to be realised due to computational constraints and practical engineering limitations. Despite these challenges, researchers have made significant progress in this area, with some exploring performance-based optimisation of various structural components, including prestressed concrete beams. To further advance the field, review articles on structural topology optimisation [166-169], LSM [170], aircraft and aerospace structures [171], CM [85], and AM [13] can provide in-depth knowledge on TO approaches, applications, issues, and manufacturing possibilities and constraints. As research continues, there is potential for the development of new techniques that can overcome these limitations and lead to the creation of more efficient, cost-effective, and environmentally sustainable structural components.

2.3 Conclusions

The literature review has provided valuable insights into the field of AM and optimisation procedures. In this chapter, many issues, advantages, drawbacks, and limitations of AM and optimisation procedures were discussed, and the most important remarks are listed below, which will serve as the basis for further developments in this thesis:

I. There are significant opportunities for innovation and advancement in the field of AM and optimisation procedures for concrete structures. While there are still limitations to 3DP technology for reinforced concrete systems, 3DCP has the potential to revolutionise the construction industry by enabling fast, economical, and environmentally sustainable building practices [6-7,45].

II. Strategies such as prestressing and fibre reinforcement can improve the ductility of printed concrete systems [57,62], but these approaches have not yet been tested at massive construction levels.

III. By enabling formwork-free construction, additive manufacturing and optimisation procedures make it possible to transform artistic expression into reality in a more efficient and sustainable way. Structural optimisation procedures ensure that the materials used in construction are used optimally, reducing waste and saving costs.

IV. Regular density-based optimisation procedures, such as SIMP, are limited in their ability to solve nonlinear problems due to the resulting low-density values that can cause an ill-conditioned stiffness matrix.

V. Nodal design variables with higher-order elements in TO offer significant advantages over element design variables. However, it is important to ensure proper energy regularisation to avoid islanding, which is a phenomenon where the optimisation algorithm converges to disconnected or isolated regions in the design space.

VI. The reliance of 3D printing technology on volumetric properties such as voxels can be seen as a limitation in the context of using density-based optimisation procedures. This is because density-based procedures typically yield 2D pixel designs and may result in impractical designs with 3D elements, limiting the full potential of 3D printing technology for the construction industry. Additionally, current optimisation techniques require post-processing efforts to be 3D printed, which can add complexity and time to the manufacturing process [56].

VII. Thickness as a geometric design variable can generate voids/holes by using a non-dimensional scaling parameter [139].

In light of the above conclusive remarks, it is evident that there is a significant gap between existing 3DCP and optimisation techniques. This gap is primarily due to the design variables and element classes used in the optimisation process, which can result in impractical designs, require rigorous post-processing techniques, and compromise the reliability of the optimisation solution for 3D printing.

To overcome these limitations, the next chapter of this thesis will introduce a new element that can characterise non-prismatic shapes using thickness as a design variable. By introducing this new element, the primary objective of this thesis will be achieved and will contribute to another objective of developing a new optimisation technique that contributes to the advancement of AM and optimisation procedures for concrete structures. This new technique aims to lead to a more innovative and sustainable built environment for future generations.

Chapter 3

Introduction to 2.5D Element

The goal of this thesis is to develop a tool that seamlessly connects architecture and structural design through optimisation, where optimised models can be 3D printed in a factory and assembled on-site, mimicking a prefab construction process. A common observation in architecture and 3DP is that both represent surfaces. However, as discussed in the previous chapter, optimisation techniques are limited to pixels using 2D elements and lead to impractical designs using 3D elements, requiring rigorous post-processing techniques. Another limitation is that existing methods use density as a design variable while it should be a geometric design variable to define or build a surface.

The solution to this problem exists in the literature in the form of the thickness design variable in the 2D analysis, which is capable of generating holes using a non-dimensional scaling parameter [139]. Additionally, using nodal design variables with higher-order elements is advantageous in TO [93-94]. Therefore, this chapter aims to develop an element that can characterise a surface with nodal thicknesses.

Flexural structural components, such as beams, are commonly designed for in-plane loading using plane stress assumptions. Under such loading conditions, there is little or no influence of out-of-plane stress on the component's integrity, as it is usually taken care of through measures such as diaphragms connecting steel or RC beams to form a grillage for a bridge superstructure. For such situations, which potentially represent the majority of design cases in practice, 2D plane stress assumptions are adequate. However, there is a question of stability in the third dimension if the optimised structure results in slender portions under compressive stress. This issue can be resolved by enforcing appropriate constraints.

While nodal thickness variables offer significant benefits for 3D printing the optimised structural designs, integrating them with 2D plane stress elements is not straightforward. This is because 2D plane stress elements are typically based on a unit thickness, which differs from the 3D volume represented by nodal thickness variables. One solution to this challenge is to degenerate a 3D element formulation based on 2D plane stress assumptions, resulting in what is known as the 2.5D element. This innovative approach allows for 3D geometric transformation while maintaining 2D planar transformation, offering exciting opportunities for optimising surface representation to 3D print.

In this thesis, a 2.5D element is formulated by degenerating the 3D serendipity element using a two-point integration rule, as illustrated in Fig. 3.1. The quadratic serendipity element is adapted to take advantage of higher-order elements that can partially avoid numerical instabilities in TO [73,93-94].

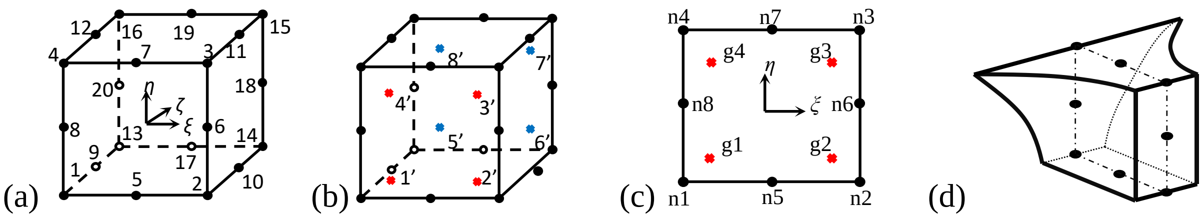

Figure 3.1: Degeneration of 3D serendipity element for 2.5D element formulation. (a)3D element; (b) Quadrature rule; (c) 2.5D planar transformation; (d) 2.5D variable nodal thickness

In Fig. 3.1, third-dimension ζ represents the thickness direction (z-direction), ξ and η represent the planar directions x and y, respectively, $1 - 20$ and n1 – n8 represent the node numbering, and 1' – 8' and g1' – g4', represent the sampling point numbering (Gaussian quadrature). Assuming,

I. no element distortion in planar directions, i.e., planar coordinates of the nodes along the thickness direction, remain the same (refer to Fig. 3.7);

II. nodal deformations across the thickness are equal;

III. plane stress assumptions remain valid, but the volume of an element is based on the nodal thickness; and

IV. quadrature rule is maintained throughout the process (e.g., two-point integration rule is used in this thesis, i.e., 2×2 for planar transformation, 2×2×2 for volume estimation).

Planar assumptions:

$$\begin{gathered}
\forall(i,j) \in \begin{cases} (\{1,9,13\}, n1) \\ (\{2,10,14\}, n2) \\ (\{3,11,15\}, n3) \\ (\{4,12,16\}, n4) \\ (\{5,17\}, n5) \\ (\{6,18\}, n6) \\ (\{7,19\}, n7) \\ (\{8,20\}, n8) \end{cases} : \begin{matrix} (x_i, y_i) = (x_j, y_j) \\ (u_i, v_i) = (u_j, v_j) \end{matrix} \\
\forall(i,j) \in \begin{cases} (1, n1) \\ (2, n2) \\ (3, n3) \\ (4, n4) \\ (5, n5) \\ (6, n6) \\ (7, n7) \\ (8, n8) \end{cases} : \begin{cases} z_i = t_j/2 \\ z_{i+12} = -t_j/2 \end{cases} \\
\forall i \in \{9,10,11,12\}: z_i = 0
\end{gathered} \tag{3.1}$$

Thin-member assumptions for in-plane loading:

$$\sigma_{zz} = \sigma_{xz} = \sigma_{yz} = 0 \tag{3.2}$$

Where (x_i,y_i,z_i) is the coordinate of the i^{th} node in the 3D element, and (x_j,y_j) and t_j are coordinate and thickness of the j^{th} node in the 2.5D element, respectively. (u_i,v_i)

and (u_j,v_j) represent the nodal deformations of i^{th} node in 3D and j^{th} node in 2.5D, respectively, while u and v are deformations in x and y directions, (i,j) sets in the Eq. (3.1) refer to the node numbering in Fig. 3.1.

The resulting shape functions of the 2.5D element are obtained based on the assumptions presented in Eq. (3.1) and are expressed as follows:

Geometry in a 3D serendipity element,

$$\alpha = \sum_{i=1}^{20} N_i^{3D} \alpha_i \tag{3.3}$$

Planar transformation in 2.5D element,

$$\alpha = \sum_{i=1}^{8} N_{ni}^{2.5D} \alpha_{ni} \tag{3.4}$$

By applying the assumptions in Eq. (3.1) to degenerate the 3D element, the shape functions for the 2.5D element can be obtained for planar transformation, as presented in Eq. (3.5).

$$\begin{gathered} N_{ni}^{2.5D} = N_i^{3D} + \beta N_{i+8}^{3D} + N_{i+12}^{3D} \\ \forall i \in Z_{[1,4],[13,16]}: N_i^{3D} \\ = \frac{1}{8}(1+\xi_i\xi)(1+\eta_i\eta)(1+\zeta_i\zeta)(\xi_i\xi+\eta_i\eta+\zeta_i\zeta-2) \\ \forall i \in \{5,7,17,19\}: N_i^{3D} = \frac{1}{4}(1-\xi^2)(1+\eta_i\eta)(1+\zeta_i\zeta) \\ \forall i \in \{6,8,18,20\}: N_i^{3D} = \frac{1}{4}(1+\xi_i\xi)(1-\eta^2)(1+\zeta_i\zeta) \\ \forall i \in \{9,10,11,12\}: N_i^{3D} = \frac{1}{4}(1+\xi_i\xi)(1+\eta_i\eta)(1-\zeta^2) \\ such\ that: \begin{cases} \forall i \in Z_{[1,4]}: \beta = 1 \\ \forall i \in Z_{[5,8]}: \beta = 0 \\ \xi,\eta,\zeta \in [-1,1] \end{cases} \end{gathered} \tag{3.5}$$

The evaluation of the elemental stiffness matrix is then performed as follows:

$$K_{e,j} = \left(\sum_{l=1}^{n_g} \sum_{m=1}^{n_g} \sum_{n=1}^{n_g} \underbrace{[B(\xi_l, \eta_m)]^T [D][B(\xi_l, \eta_m)]}_{2D} \underbrace{|J(\xi_l, \eta_m, \zeta_n)| w_l w_m w_n}_{3D} \right) \quad (3.6)$$

Where, α is a general representation for coordinates (x,y,z) or deformations (u,v), N_i^{3D} and $N_{ni}^{2.5D}$ are shape functions of i^{th} node in a 3D and 2.5D element, respectively, (ξ_i,η_i,ζ_i) is an isoparametric coordinate of the i^{th} node in an element, w_l,w_m,w_n are Gauss weights of the sample points (l,m,n).

The 2.5D shape functions formulated in this thesis share similarities with the 2D serendipity shape functions. The 2.5D (Eq. (3.4)) and 3D (Eq. (3.3)) shape functions generate strain energy and volumetric terms, respectively, to form the stiffness matrix for the 2.5D element, as illustrated in Eq. (3.6). Interestingly, similarities can also be observed between the proposed 2.5D element and shell elements with varying nodal thicknesses [172-176]. However, shell elements typically contain rotational degrees of freedom (DoF) in addition to translations and are characterised as either thick (6 DoFs) when considering drilling rotation or thin (5 DoFs) in other cases. In contrast, the proposed 2.5D element is limited to in-plane translational degrees of freedom. While thin shell elements with in-plane loading may yield similar results to the 2.5D element since out-of-plane stresses are absent, they are prone to locking and require more computational energy. The next section will evaluate the elements by comparison of the results obtained using the new element with those obtained using traditional finite element methods.

3.1 Element Stability and Accuracy

The 2.5D element is a novel formulation based on the serendipity method, presenting exciting opportunities to optimise surface representation for 3D printing. However, it's crucial to comprehend the element's capabilities and limitations before employing it further. In traditional finite element analysis, patch tests are conducted on new formulations to assess their behaviour and accuracy. Typically, a variety of loadings with discrete meshes and shapes are used to evaluate an element's performance and precision [177]. For example, patch tests can be performed with a cantilever or simply supported boundary conditions to understand the element's response under different loading scenarios [178].

Serendipity elements are known to be less susceptible to locking than other elements, and using more elements and reduced quadrature can enhance the accuracy of results [178-179]. However, it is crucial to exercise caution when using serendipity elements since their robustness is questionable in certain situations, such as:

I. Reduced quadrature, which can lead to possible spurious mode occurrence.

II. Non-linear problems, such as large displacement or contact analyses, can also result in spurious modes.

III. Using a single element, which leads to possible spurious mode occurrence.

IV. Distorted elements, which can also lead to inaccurate results.

In addition to these limitations, the 2.5D element developed using the serendipity method may be susceptible to out-of-plane distortion due to the nodal thickness variable. Therefore, it is recommended to test the behaviour of the 2.5D element for prismatic and non-prismatic shapes, which will provide a more comprehensive understanding of the element's behaviour. Unlike regular patch tests, such tests can help identify the potential out-of-plane distortion issues associated with the 2.5D element and provide insights into its behaviour under different conditions.

Two cases, as illustrated in Fig. 3.2, were studied to test the behaviour of the 2.5D element under different conditions. Case-I involved a prismatic linear varying thickness beam (trapezoidal beam) with a top surface load of 0.1 Pa, while Case-II involved a non-prismatic non-linear varying thickness beam with a top surface load of 0.16 Pa. Both cases had a maximum thickness of 0.1 m, an elastic modulus of 2.5 kPa, zero Poisson ratio, and simply supported boundary conditions. The whole material space lies in the prismatic domain of 1.0 m×0.1 m×0.1 m. It is worth noting that the material properties used in this chapter were selected for their simplicity and to avoid complex analytical calculations, and may not necessarily represent realistic values.

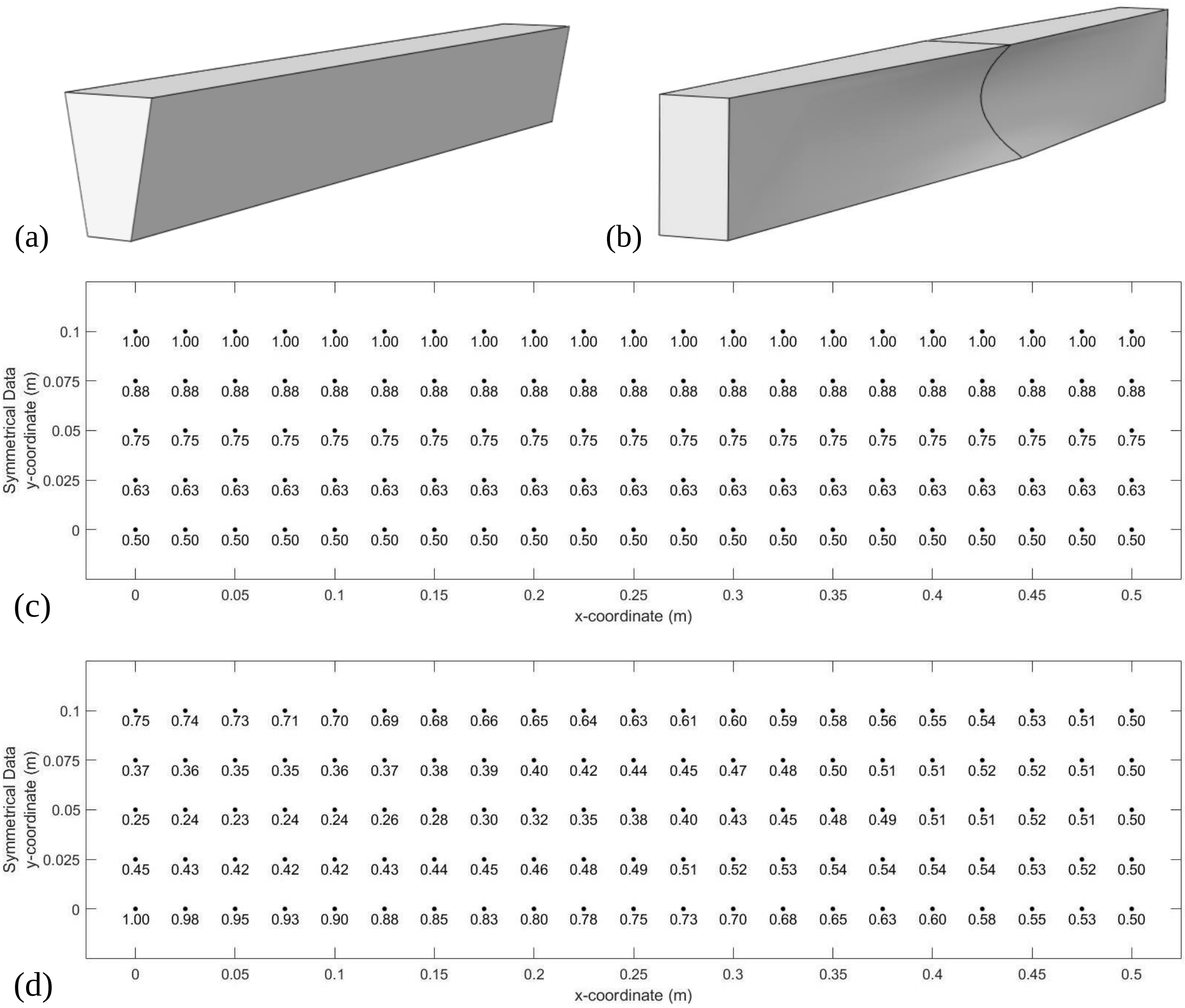

Figure 3.2: Geometric models and thickness data . (a) linear thickness model; (b) non-linear thickness model; (c) & (d) Surface data for cases I and II

The symmetrical surface data (factored thickness) for the two test cases are presented in Fig. 3.2(c) and Fig. 3.2(d), where planar coordinates (0,0) and (0.5,0.1) represent the bottom mid-span and the top right boundary of the beam, respectively. Nodal thicknesses are obtained by multiplying the surface data provided in Fig. 3.2 with the base thickness of 0.1 m. It is worth noting that the surface data is for the corner nodes, while mid-node thicknesses can be estimated as the average of two adjacent nodes and symmetrical data was provided to avoid a clumsy representation. The full-scale models of both cases in 2.5D and 3D will be analysed to compare the results. It is important to note that there will be a contrast in loading conditions, as 2.5D is limited to line loads, while 3D requires a surface load. Therefore, surface loads are converted to a uniformly varying load (UVL) to apply to the 2.5D models.

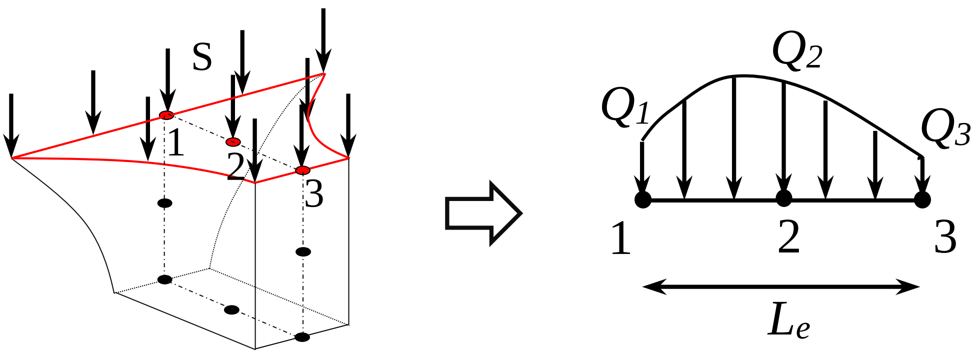

Figure 3.3: Surface load to UVL

Eq. (3.7) to Eq. (3.8) presents the conversion of the surface load S (highlighted as red in Fig. 3.3) acting on a 2.5D element to concentrated forces on edge nodes, assuming the edge as a linear element. Firstly, S is converted to UVL, and the UVL at any point on the edge of an element is given by the equation presented in Eq. (3.7), where Q_1, Q_2, and Q_3 are obtained by the product of S and corresponding nodal thicknesses t_1, t_2, and t_3, respectively.

$$Q = L_1Q_1 + L_2Q_2 + L_3Q_3 = [L_1 \quad L_2 \quad L_3]\begin{bmatrix} Q_1 \\ Q_2 \\ Q_3 \end{bmatrix} = L\left(S\begin{bmatrix} t_1 \\ t_2 \\ t_3 \end{bmatrix}\right) = L\,P \tag{3.7}$$

Next, the UVL at any point (Q) is converted to concentrated forces acting on the edge nodes, as presented in Eq. (3.8). These concentrated forces are then applied to the corresponding edge nodes of the 2.5D model.

$$\begin{gathered} [F] = \begin{bmatrix} F_1 \\ F_2 \\ F_3 \end{bmatrix} = \int_{-1}^{1} L^T L P \,{}^{\partial x}/_{\partial \xi}\, d\xi \\ x = L_1x_1 + L_2x_2 + L_3x_3 \\ F = \begin{bmatrix} 4 & 2 & -1 \\ 2 & 16 & 2 \\ -1 & 2 & 4 \end{bmatrix} P\,L_e/30 \end{gathered} \tag{3.8}$$

Here, F is the force vector of the element edge, S is the surface load, L_e is the edge length of the element, L is the shape function matrix of the quadratic three-noded line element, P is the UVL matrix.

By using the surface load to the UVL concept, both the 2.5D and 3D model results can be compared for a better understanding of the behaviour of the 2.5D element. To compare the results, 3D models of the two cases are built in ABAQUS 6.14, while 2.5D models are built in MATLAB. The 2.5D models are discretised with coarse (10×1) and fine meshes (40×4), while the 3D models are discretised with a fine mesh of 40×4×3 C3D20R elements. It is observed that the 3D models cannot be discretised using the above coarse mesh or single element in the thickness direction due to resulting instabilities. To provide a benchmark for the numerical models, an analytical solution based on 2D elasticity and Timoshenko beam solutions is provided for Case I in Appendix A, where 2D elasticity includes both stresses and deflection, while the Timoshenko solution is only provided for displacements. However, due to the non-linear thickness across the span, an analytical solution for Case II is too difficult to be given.

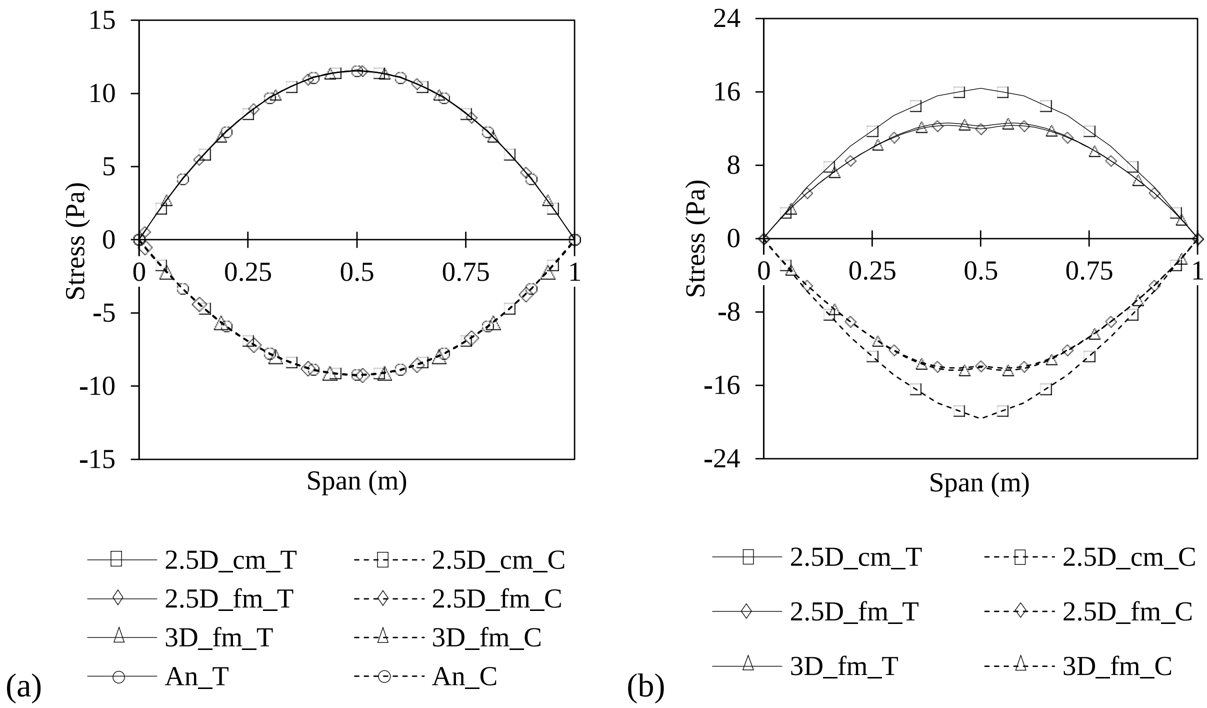

Figure 3.4: Flexural stresses at extreme fibres. (a) Case-I and (b) Case-II

To verify the elements accuracy, finite element results for extreme flexural stresses along the span and deflections at mid-span are compared to the analytical solutions. The flexural stresses extracted along the span after analysing the 2.5D, 3D and analytical models are presented in Fig. 3.4, where cm, fm, T, C, and An represent the short forms of coarse mesh, fine mesh, tension in bottom fibre, compression in top fibre, and analytical, respectively.

Table 3.1: Comparison of midspan downward deflections

Case	2.5D		3D	2D	Timoshenko
	cm	fm	fm	elasticity	
I ($\times 10^{-3}$ m)	8.791	8.813	8.816	8.804	8.814
II ($\times 10^{-3}$ m)	14.469	11.544	11.247	-	

In Tab. 3.1, midspan downward deflections for the 2.5D, 3D, and analytical models are provided, but relying solely on this data is not enough to validate an element's accuracy. Stress contours must also be observed to ensure that the element is behaving as expected and producing accurate results. In particular, the stress contours should be smooth and continuous across element boundaries and accurately capture stress concentrations in regions of high stress.

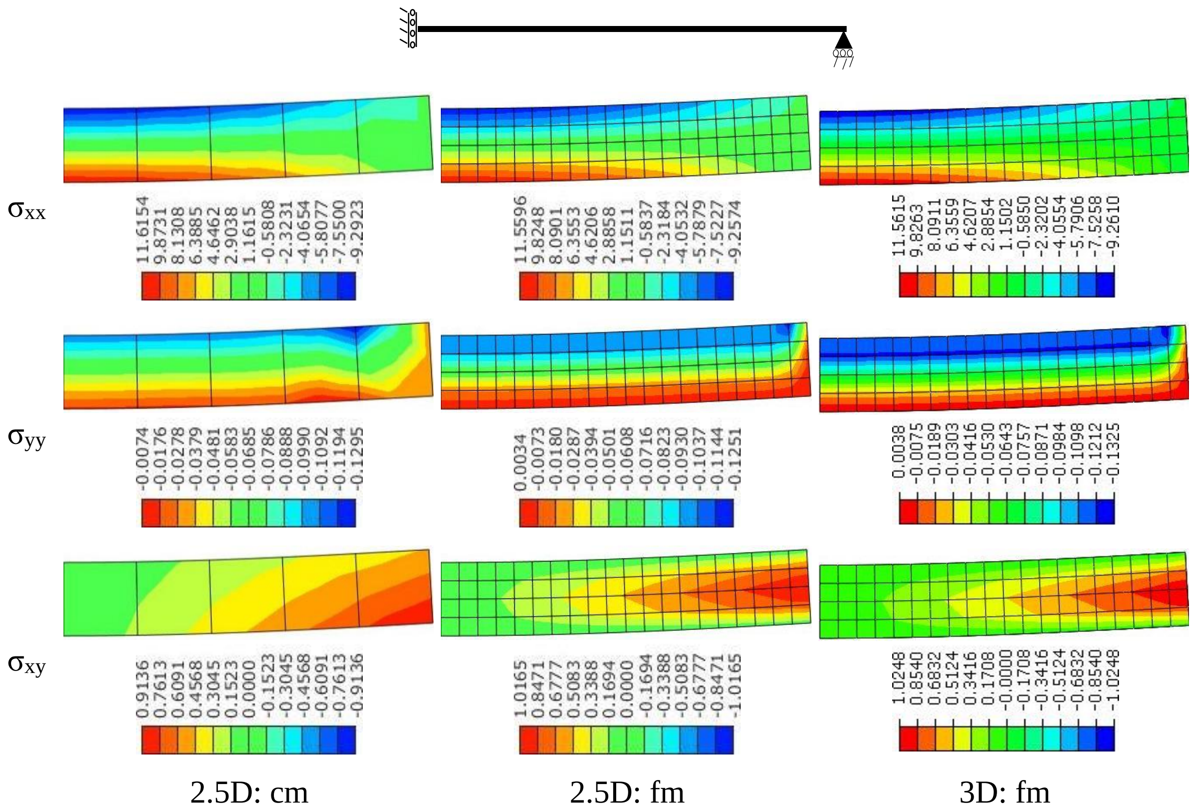

Figure 3.5: Deformed stress contours for prismatic beam

To visualise the stress contours, deformed stress contour plots (with deformations magnified by two times) for the prismatic and non-prismatic models of the right half of the beam are presented in Fig. 3.5 and Fig. 3.6, respectively. These plots show the recovered and smoothed stress distribution across the models, allowing for a visual comparison of the stress contours. This visual comparison is crucial to identify any potential issues with the element's formulation or implementation, such as spurious modes or inaccurate results under distorted conditions, which can then be addressed and resolved to ensure the accuracy and reliability of the element.

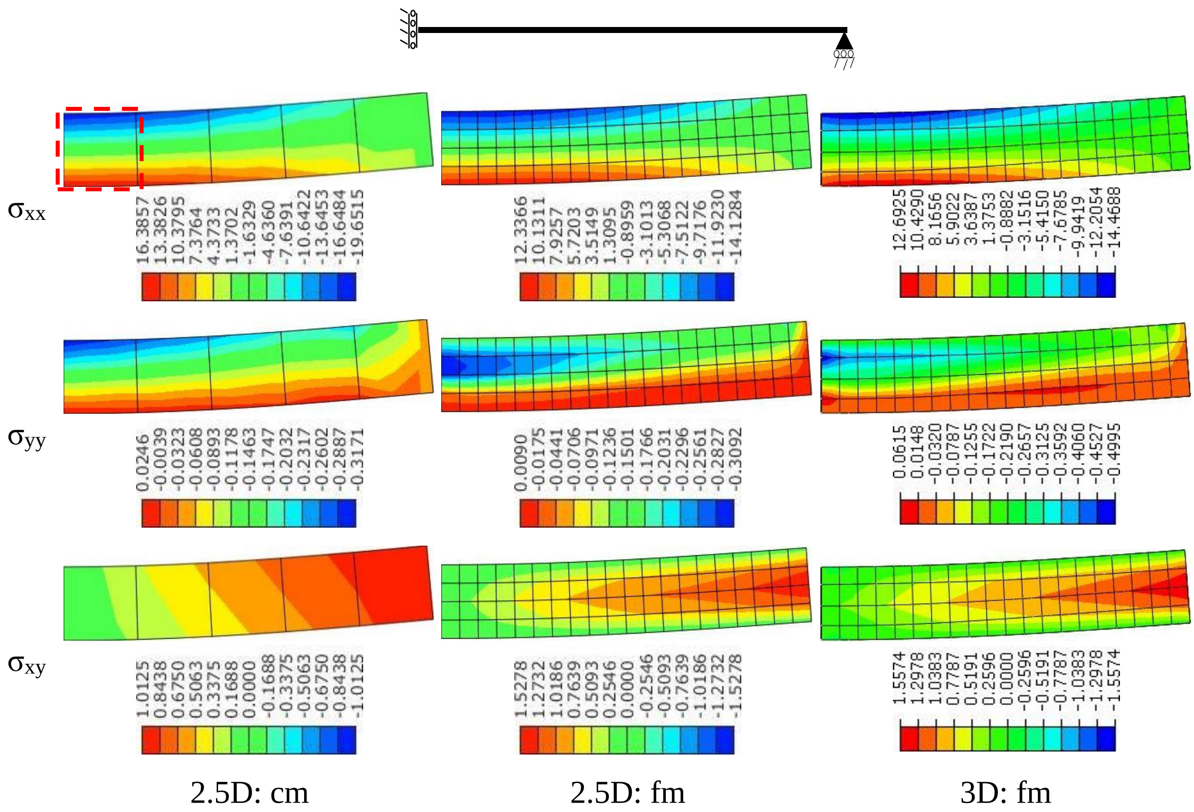

Figure 3.6: Deformed stress contours for non-prismatic beam

Overall, extreme fibre stresses, mid-span deflections and stress contour data are crucial in validating an element and ensuring its accuracy. By taking these multiple sets of data into account, informed decisions can be made with confidence when evaluating the performance of structural models.

3.2 The Computational Efficiency of the 2.5D Element

The results demonstrate that 2.5D elements can produce stable and accurate results for both prismatic and non-prismatic cases. However, it's important to note that a coarse mesh may produce unreliable results for extremely varying thicknesses, as observed in the non-prismatic case results. Although accuracy can be achieved with fewer elements, a coarse mesh may not be sufficient for accurate and reliable results in all cases.

For example, the comparison of extreme fibre flexural stresses along the span for the prismatic coarse mesh model are in total agreement, but this is not the case for the non-prismatic model. Coarse mesh extreme fibre stresses for non-prismatic cases are not in agreement, while fine mesh model results of 2.5D and 3D are in agreement. This is the first observation that the geometry of the beam and quantity of the elements are affecting the behaviour of a 2.5D element.

On the other hand, the midspan downward deflection results of the prismatic beam with the 2.5D element are in agreement with the 3D analysis and analytical results. In contrast, the non-prismatic coarse mesh model showed flexible results relative to its alternative model meshes. In general, coarse meshes yield stiffer results, as evidenced in the prismatic beam case.

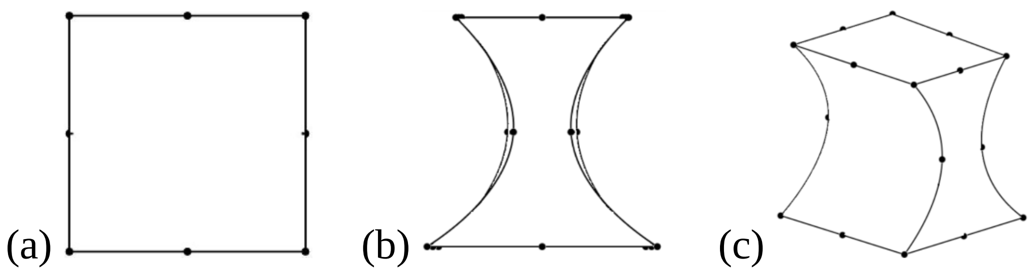

Figure 3.7: Element geometry at midspan of non-prismatic coarse model . (a) Front (+XY); (b) Side (+ZY) and (c) Isometric, views

Additionally, the geometry of the element at the midspan of the non-prismatic coarse mesh model (highlighted in Fig. 3.6) is extracted using surface data (in Fig. 3.2(d)) and presented in Fig. 3.7. The element's geometry is squeezed at mid-height relative to the top and bottom, indicating poor discretisation, which often leads to computationally inefficient results and is the cause for yielding flexible results for the non-prismatic coarse mesh model. The Jacobian is positive and stable in this case, despite the mesh quality and computational efficiency. Therefore, both stable Jacobian and mesh quality are equally important in achieving accurate results. However, stable Jacobian and mesh quality can only be achieved by avoiding the extreme thickness variation within the element. This is the second observation that the inaccurate behaviour of a 2.5D element can be commonly attributed to extreme thickness variation within the element.

The stress contours show no sign of stress concentration or spurious modes, but there is a considerable change in contours between coarse and fine mesh models, especially in the distribution of the shear stresses despite the model geometries. Here, it can be observed that even though coarse mesh models for prismatic cases are reliable in previous observations, there is a clear contradiction of shear stress contours. This suggests that, despite the complexity of geometry, discretisation should be performed in such a way that maximum stresses, deformations, and stress distribution are properly estimated to avoid inaccurate optimised shapes considering the continuum. Despite the coarse mesh results, 2.5D fine mesh model results are in total agreement with 3D and analytical results. It's worth noting that 2.5D models use a single element in the thickness direction, while 3D models were built with three elements. This clearly suggests that 2.5D elements, when used in a reasonable number, are as efficient as 3D elements.

These results suggest that while coarse meshes can yield stiffer results, they may not be reliable for extremely varying thicknesses, and finer meshes might be required to ensure accurate and stable results. Overall, the comparison of results obtained using 2.5D elements provides valuable insights into the element's behaviour and accuracy, highlighting the importance of stable Jacobian and mesh quality in achieving accurate results. It's also important to note that the 2.5D elements are different from traditional 2D or 3D elements, and their behaviour is greatly influenced by extreme thickness variation within the element. Therefore, to ensure accurate and reliable results, it's recommended to use more 2.5D elements to avoid extreme thickness variations, achieve greater mesh quality, and maintain a positive Jacobian.

In summary, the comparison of results obtained using 2.5D elements provides valuable insights into the element's behaviour and accuracy, which can be used to optimise mesh quality and stability for accurate and reliable results.

3.3 Remarks

This chapter successfully achieved one of the primary objectives of this thesis by introducing a new element. The 2.5D element introduced in this chapter is developed by degenerating a twenty-noded 3D serendipity element. The element estimates volume based on 3D geometric transformation, while strain energy is based on 2D planar transformation using a two-point Gauss rule. In this section, various remarks that were noted during the development and testing of this element are summarised.

I. One limitation of the element is that it is restricted to in-plane loading conditions, although the element's variable nodal thickness parameters help account for varying surface conditions.

II. The element's behaviour and accuracy are assessed through a combination of extreme fibre stresses, mid-span deflections, and stress contour data under different conditions.

III. Analytical solutions for the prismatic beam case are derived based on Airy's stress function and Timoshenko beam theory in Appendix A.

IV. The 2.5D models use a single element in the thickness direction and may exhibit squeezing behaviour when coarse meshes are used, especially for abruptly varying surface conditions.

V. The stress contour data visually compared the stresses and revealed that coarse meshes might yield inaccurate stress distributions, which may affect optimised designs. No signs of stress concentration or spurious modes were observed.

VI. The 2.5D element yields computationally efficient and stable solutions when relatively fine elements are used, and it can match the capabilities of 3D elements. The element is capable of adopting non-linear conditions, which further increases its versatility and applicability.

In summary, this chapter presents a thorough investigation of the 2.5D element, highlighting its strengths and limitations. Valuable insights into the behaviour and accuracy of 2.5D elements, which can help optimise mesh quality and stability for accurate and reliable results. The 2.5D element shows a promising approach for surface representation in architectural expression and 3DP, and further studies are needed to explore its full potential and limitations under different loading and geometric conditions.

The development of the 2.5D element presented in this chapter overcomes numerical limitations and opens up new possibilities for optimising thickness design variables in the field of topology optimisation. This breakthrough paves the way for achieving the second primary objective of this thesis: to develop an optimisation tool that creates surfaces inspired by the architectural expression for 3D printing. The upcoming chapter introduces a new thickness scaling strategy that leverages stiffness solutions obtained using 2.5D elements to achieve optimal designs.

Chapter 4

Introduction to Solid Isotropic Material with Thickness Penalisation

This chapter introduces an innovative optimisation methodology called Solid Isotropic Material with Thickness Penalisation (SIMTP) that aims to scale geometric variables for TO. SIMTP builds upon the well-known methods such as SIMP [16] and Kennedys DTO [139] but with significant improvements. The method penalises a dimensionless parameter called the thickness factor (TF) to scale the thickness at a point. One of the primary advantages of SIMTP is its formulation that frees the constitutive matrix from the design variable, allowing for easy incorporation of traditional non-linear FEM processes in the optimisation. However, non-linear analysis is not within the scope of the present thesis and will be addressed in future studies.

The use of 2.5D elements in the SIMTP methodology allows for numerical estimation of stiffness solutions based on the obtained scaled thicknesses, resulting in the combination termed 2.5D SIMTP. As discussed in the previous chapter, using 2.5D elements in TO offers numerous advantages, including stable Jacobian and mesh quality, which ensure a stable solution and practical designs during the optimisation process. These benefits extend to thickness variations. Thick and thin regions with extreme variations in thickness can lead to pathologies similar to those found in TO, such as checkerboards and thin member formations. These pathologies can affect surface continuity, leading to stress concentrations and reduced performance. Therefore, maintaining a stable Jacobian in 2.5D SIMTP is crucial to avoid numerical instabilities and ensure surface continuity in TO, even in the presence of extreme variations in thickness.

The following sections provide a detailed description of the SIMTP method and its formulation, highlighting its advantages and potential applications.

4.1 Definition of SIMTP

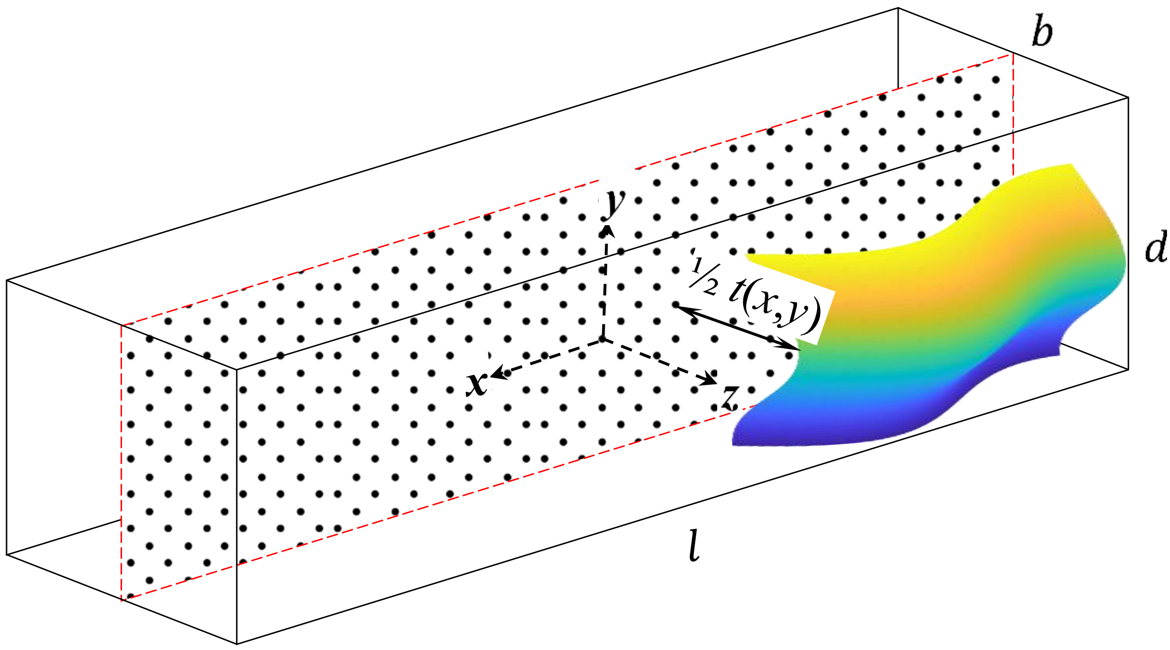

Figure 4.1: Boundary representation of a 3D solid body

SIMTP assumes a symmetrical material domain Ω^{m}, made up of a solid isotropic material, that lies within a prismatic design space Ω of dimensions $l \times b \times d$. The distribution of the material in a design space is represented by lumped point masses that can move only in the symmetrical plane, as highlighted in Fig. 4.1. The projection of a point mass (PM) at (x,y) to the material boundary Ω^{m} is defined as characteristic thickness $t(x,y)$. Initially, this boundary can be a parametric surface or an aesthetical and architectural expression. Under external or internal influences, such as deformations of a node in finite element space, t(x,y) becomes a continuous variable, allowing for a more accurate estimation of stiffness solutions. The continuity of t(x,y) ensures that the material boundary is represented effectively. The characteristic thickness t(x,y) can be defined as:

$$\forall(x,y) \in \Omega\colon t(x,y) = [f_{min} + f(x,y)^{p}(f_{max} - f_{min})]b$$

$$such\ that\colon \begin{cases} f(x,y) \in [0,1]^{R} \\ p \ \in \ R_{\geq 1} \\ \Omega^{m} \subseteq \Omega_{R^{3}} \end{cases} \qquad (4.1)$$

In the above equation, $f(x,y)$ is a dimensionless parameter called thickness factor (TF) and $f_{\max}$, $f_{\min}$ are maximum and minimum TFs. The parameter p is used to penalise intermediate TF values in order to avoid impractical geometries. When using an initial design candidate based on an architectural expression, a penalty of unit value can be used to obtain the TF values from Eq. (4.1). In case of a singularity in the mass system, such as a point mass with zero thickness, then the movement of the PM will be infinite under any infinitely smaller influence. This can lead to numerical instability and is therefore avoided in SIMTP by restricting the TF to positive unit interval values with a minimum thickness of $f_{\min} \times b$. A unit value of TF indicates a point mass with a total thickness of b, while zero is considered void. Penalising the TF does not change the dimensionality of the thickness, ensuring consistency and continuity.

In summary, SIMTP is a combination of SIMP and DTO, where a penalty is applied over a dimensionless parameter to generate holes and avoid exponential scaling of thickness while effectively parameterising the boundary surface within the practical limits of a design space. The dimensionless parameter data can also be used to draw pixels for image purposes, and the thickness values can be used to draw the surface or voxels for 3DP purposes. Therefore, SIMTP can produce both pixels and voxels, making it a valuable optimisation tool for image and 3DP applications.

The new thickness scaling function introduced in this section can be used with 2.5D elements to optimise a surface for 3DP purposes. The next section will discuss how thickness optimisation is performed in this context, building off the principles introduced by SIMTP.

4.2 Thickness Optimisation Problem

As previously mentioned, SIMTP solves the optimisation problem using the finite element (FE) approximation, where each node represents a PM and nodal thicknesses are evaluated as design candidates determined by sensitivity analysis to minimise compliance. The thickness of each node is adjusted iteratively until an optimal solution is found that satisfies the constraints. Sensitivity analysis is performed to assess the impact of thickness changes on the overall performance of the structure, which is critical in determining the optimal design. The next section will provide a more detailed explanation of minimum compliance, its relationship to the optimisation problem that is solved using 2.5D SIMTP, and how it is calculated and evaluated in practice.

4.2.1 Minimum Compliance

Minimum compliance is a crucial optimisation objective that aims to improve the performance of a structure while providing more efficient and cost-effective designs. In this thesis, it is achieved by minimising the strain energy, which represents the energy required to deform the structure under given load conditions. To achieve this objective, the thickness of each node is adjusted iteratively until an optimal thickness distribution is found that satisfies design constraints and minimises compliance. The optimisation problem based on the earlier discussion is formulated as follows:

$$min: C = F^T u = u^T K u$$

$$subject\ to: \begin{cases} Ku = F \\ V/V_o \leq V_r \\ 0 \leq\ f \leq\ 1 \end{cases}$$

$$K = \sum_{j \in N_e} K_{e,j} \tag{4.2}$$

$$V = \sum_{j \in N_e} V_{e,j}$$

In the above equation, the assembly of elemental stiffness matrices K and volume V is formed by summing the respective element, stiffness matrices $K_{e,j}$ and volumes $V_{e,j}$, for each j^{th} element belongs to a set of elements N_e. u is the nodal deformation matrix representing the movement of the point masses under external loads or body forces F subjected to boundary conditions, V and V_o are the volume of the total body mass at current and initial iterations, respectively, V_r is the volume ratio, f represents TF which is used as design candidates determined by sensitivity analysis to minimise compliance while satisfying the design constraints.

The following section discusses the sensitivity analysis, which is crucial in identifying the most effective design candidates for minimising compliance while satisfying the design constraints.

4.2.2 Sensitivity Analysis

Sensitivity analysis is a crucial aspect of TO, where changes in the objective function or constraints, such as strain energy and volume, are analysed concerning changes in design candidates. This information is then utilised to iteratively update the design variables until an optimised design is obtained by identifying and retaining the regions that contribute the most to stiffness while removing others.

In traditional TO, sensitivity analysis is performed at the element level. However, in this thesis, it is carried out at the nodal level since the design variables are nodal thicknesses. It must be understood that the nodes are non-integral variables in

FEM. Therefore, the energy of the element is lumped to the nodes, which requires an approximation of the thickness distribution. However, traditional shape function approximations can lead to negative thicknesses for higher-order elements [93-94]. As a result, Shepard interpolants [180] are used to approximate the thickness inside the element space, and the thickness at any point inside an element space (Ω_e) is interpreted as follows:

$$\forall (x,y) \in \Omega_e : t(x,y) = \sum_{i \in N_n, n_e} w_i t_i$$
$$w_i = \frac{1/((x-x_i)^2 + (y-y_i)^2)}{\sum_{i \in N_n, n_e} 1/((x-x_i)^2 + (y-y_i)^2)} \tag{4.3}$$

Here n_e is the set of nodes in an element, w_i is the inverse distance weight of the i^{th} node w.r.t. point (x,y), t_i is the thickness of the i^{th} node, and N_n is a set of nodes in the design domain. The most important aspect of sensitivity analysis in this thesis is estimating the sensitivities, such as the rate of change of compliance and volume, with respect to the nodal point thicknesses. Specifically, the rate of change of compliance is derived with respect to the TF as follows:

$$\forall i \in N_n : \partial C/\partial f_i = u^T \, \partial K/\partial f_i \, u$$
$$\partial K/\partial f_i = \sum_{j \in N_e} \partial K_{e,j}/\partial f_i \tag{4.4}$$

$\partial C/\partial f_i$ and $\partial K/\partial f_i$ are the rate of change of compliance and stiffness w.r.t. TF at node i that belongs to a set of nodes (N_n). The rate of change of global stiffness (K) is dependent on element stiffness, as shown in Eq. (4.4), and is evaluated as follows:

The elemental stiffness matrix in 2.5D is given by:

$$\forall j \in N_{\mathrm{e}}: K_{e,j} = \iiint_{\Omega_{\mathrm{e,j}}} (B(x,y)^T D B(x,y))\, dxdydz = \int g\left(x_{\Omega_{e,j}}, y_{\Omega_{e,j}}\right) dz \tag{4.5}$$

Assuming that the summation of change of thickness within the element space is equal to the change of thickness at the element centre and substituting thickness at element centre from Eq. (4.3) in Eq. (4.5),

$$\int g\left(x_{\Omega_{\mathrm{e,j}}}, y_{\Omega_{\mathrm{e,j}}}\right) dz = g\left(x_{\Omega_{e,j}}, y_{\Omega_{e,j}}\right) \left(\sum_{\substack{i \in N_n, n_{e,j} \\ j \in N_e}} w_{i,j} t_i \right) \tag{4.6}$$

Writing Eq. (4.1) in nodal thicknesses form and substituting in Eq. (4.6)

$$\forall i \in N_{\mathrm{n}}: t_i = \left[f_{min} + f_i^p (f_{max} - f_{min})\right] b$$

$$\begin{gathered} \forall i \in (N_{\mathrm{n}}, n_{e,j}), j \in N_{\mathrm{e}}: \partial K_{e,j} / \partial f_i \\ = g\left(x_{\Omega_{e,j}}, y_{\Omega_{e,j}}\right) w_{i,j} p f_i^{p-1} (f_{max} - f_{min}) b \end{gathered} \tag{4.7}$$

It is essential to compute the volumetric change along with the stiffness for sensitivity analysis. As mentioned earlier, the primary reason for penalising the stiffness values is to avoid intermediate design values. At the same time, the volumetric rate is evaluated based on absolute values (i.e., Eq. (4.1) with no penalty) such that design values having lower stiffness occupying relatively higher volume are strategically sized down. Thus, the gradient information successfully suppresses the intermediate thickness values. The rate of volume change at the nodal level is evaluated similarly to the stiffness.

Element volume for the varying thickness is given by:

$$\forall j \in N_{\mathrm{e}}: V_{e,j} = \iiint_{\Omega_{\mathrm{e,j}}} dxdydz = \int A\left(x_{\Omega_{e,j}}, y_{\Omega_{e,j}}\right) dz \tag{4.8}$$

Referring back to the assumption in Eq. (4.6) and re-writing the above equation:

$$\int A\left(x_{\Omega_{\mathrm{e,j}}}, y_{\Omega_{\mathrm{e,j}}}\right) dz = A\left(x_{\Omega_{e,j}}, y_{\Omega_{e,j}}\right)\left(\sum_{\substack{i \in N_n, n_{e,j} \\ j \in N_e}} w_{i,j} t_i\right) \tag{4.9}$$

Writing the thickness of a node from Eq. (4.1) without penalty and substituting it in Eq. (4.9) to obtain the rate of change of volume w.r.t. TF:

$$\forall i \in N_n : t_i = [f_{min} + f_i(f_{max} - f_{min})]b$$

$$\forall i \in N_{\mathrm{n}} : \partial V / \partial f_i = \sum_{j \in N_e} \partial V_{e,j} / \partial f_i \tag{4.10}$$

$$\forall i \in \left(N_{\mathrm{n}}, n_{e,j}\right), j \in N_{\mathrm{e}} : \partial V_{e,j} / \partial f_i = A\left(x_{\Omega_{e,j}}, y_{\Omega_{e,j}}\right) w_{i,j}(f_{max} - f_{min})b$$

Where t_i is the thickness of the i^{th} node, f_i is the TF of the i^{th} node, $g(x_{\Omega_{e,j}}, y_{\Omega_{e,j}})$ is the stiffness matrix of the j^{th} element ($\Omega_{e,j}$) with unit thickness, $n_{e,j}$ is the set of nodes of the j^{th} element, $w_{i,j}$ is the inverse distance weight of i^{th} node from the centre of the j^{th} element, $A(x_{\Omega_{e,j}}, y_{\Omega_{e,j}})$ is the area of the j^{th} element. It should be noted that SIMTP penalises the nodal design variable (i.e., TF). In contrast, other TO methods penalise element densities regardless of the design variable, including NDV methods.

The above sensitivities are used to update the design variables. However, this process alone may not provide a practical design and can result in unusual designs, often regarded as numerical instabilities in TO, as discussed earlier. Energy regularisation methods, such as filtering techniques, are commonly used to suppress these pathologies from occurring. The next section will discuss the significance of energy regularisation while using 2.5D SIMTP and how it can be used to obtain practical and structurally viable designs.

4.2.3 Energy Regularisation

In FEM, the Jacobian is the epicentre for most mesh-related instabilities, apart from the numerical instabilities of traditional TO. A primary advantage of 2.5D SIMTP is unifying all possible instabilities to the 3D Jacobian, except for those caused by material non-linearity. The 2.5D element presented in the previous chapter is seemingly stable and accurate until an unusual thickness gradient (out-of-plane distortion) appears in an element, causing the Jacobian illness (mapping from global coordinates to local coordinates). In this scenario, a Jacobian repair method is necessary to have a stable analysis. General practices in the literature to deal with heavily distorted elements include adjusting nodal positions or mesh refinement through Jacobian ratios [181], effectively maximising or relaxing the energy of an element.

Regularisation techniques [68-71,77-79,84] in TO work similarly to avoid unwanted material placement. Therefore, a general TO filter [70-71] is used as an energy regulator to filter the thicknesses, and its implementation at the nodal level is presented in Eq. (4.11) to Eq. (4.13). Fig. 4.2 illustrates the adopted filtering scheme, and Eq. (4.11) to Eq. (4.13) extend the derivatives in Eq. (4.7) and Eq. (4.10) based on the filtered/unfiltered TF.

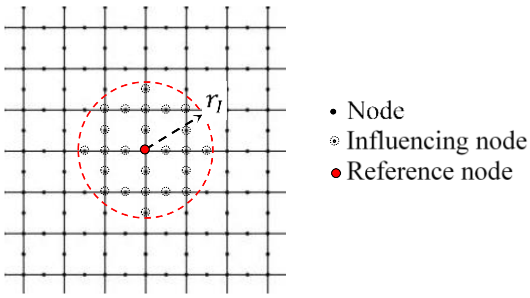

Figure 4.2: Energy regularisation

$$\begin{gathered}\forall i \in N_n: f_i = \sum_{k \in N_{I,i}} \hat{f}_k \phi_{i,k} \Big/ \sum_{k \in N_{I,i}} \phi_{i,k} \\ \forall k \in N_{I,i}: \phi_{i,k} = \left(r_{I,i} - r_{i,k}\right)/r_{I,i} \\ \forall k \notin N_{I,i}: \phi_{i,k} = 0\end{gathered} \tag{4.11}$$

Filtered TFs from Eq. (4.11) influence the sensitivity analysis (refer to Eq. (4.7) and Eq. (4.10)) accordingly

$$
\begin{gathered}
\forall i \in (N_{\mathrm{n}}, n_{e,j}), j \in N_{\mathrm{e}}, k \in N_{I,i}\colon \partial K_{e,j}/\partial \hat{f}_k = \left(\partial K_{e,j}/\partial f_i\right) \partial f_i/\partial \hat{f}_k \\
\forall i \in (N_{\mathrm{n}}, n_{e,j}), j \in N_{\mathrm{e}}, k \in N_{I,i}\colon \partial V_{e,j}/\partial \hat{f}_k = \left(\partial V_{e,j}/\partial f_i\right) \partial f_i/\partial \hat{f}_k \\
\forall i \in N_{\mathrm{n}}, k \in N_{I,i}\colon \partial f_i/\partial \hat{f}_k = \phi_{i,k} \Big/ \sum_{j \in N_{I,i}} \phi_{i,j}
\end{gathered} \tag{4.12}
$$

For un-filtered thickness

$$
\begin{gathered}
\forall i \in N_{\mathrm{n}}, k \in N_{I,i}, i = k\colon \partial f_i/\partial \hat{f}_k = 1 \\
\forall i \in N_{\mathrm{n}}, k \in N_{I,i}, i \neq k\colon \partial f_i/\partial \hat{f}_k = 0
\end{gathered} \tag{4.13}
$$

Where $r_{I,i}$ is the influence radius of the i^{th} node, $r_{i,k}$ is the distance of the k^{th} node from the i^{th} node, $\phi_{i,k}$ is the influence of the k^{th} node on the i^{th} node, $\hat{f}_k$ is the actual TF of the k^{th} node, $N_{I,i}$ is the set of influencing nodes of the i^{th} node, $\partial K_{e,j}/\partial \hat{f}_k$, $\partial V_{e,j}/\partial \hat{f}_k$, $\partial f_i/\partial \hat{f}_k$ is the rate of change of j^{th} element stiffness, j^{th} element volume, and scaled TF of i^{th} node, w.r.t. actual TF of k^{th} node, respectively.

Overall, this chapter has introduced a new optimisation tool called 2.5D SIMTP, which is an advancement of the widely used SIMP method. Although SIMP is an efficient optimisation method suitable for large-scale designs, it may not be suitable for designs with complex geometries or thickness variations. The 2.5D SIMTP method, on the other hand, incorporates 2.5D elements and a new thickness scaling function to provide more accurate stiffness solutions for designs with thickness variations and can handle complex geometries. Additionally, the tool can produce both pixels and voxels, which can be compared with 2D and 3D SIMP methods, respectively.

In the following section, a comparison of the pixels produced by 2.5D SIMTP and 2D SIMP using a few benchmark problems will be presented. This comparison will evaluate the accuracy, efficiency, and robustness of each method and provide insights into which method is best suited for a specific optimisation problem.

4.3 Comparison of Pixels

This section compares the results obtained from two optimisation methods, namely SIMTP using a 2.5D plane stress element and SIMP using a 2D plane stress element, for several benchmark problems with a unit thickness taken from the literature.

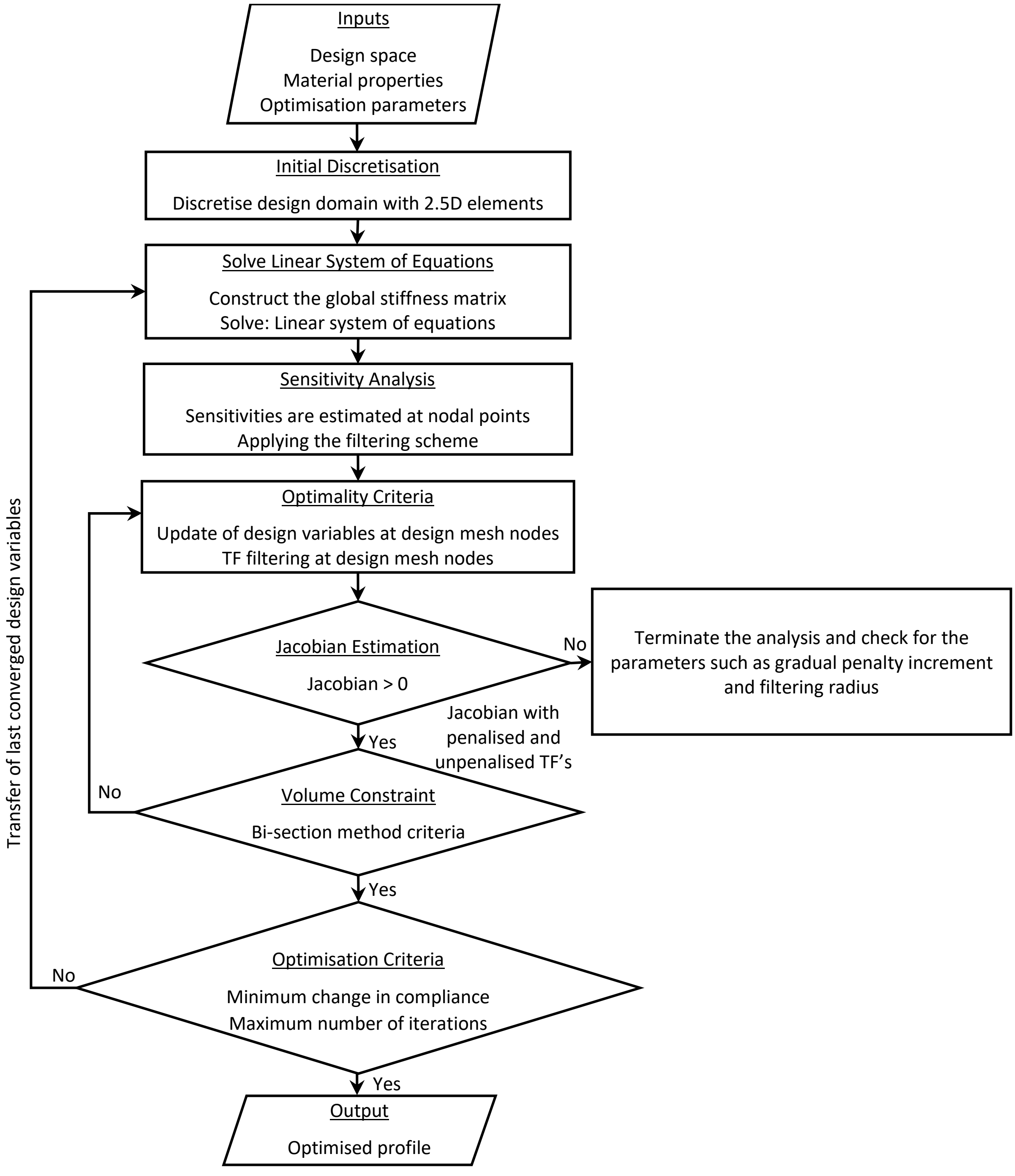

Figure 4.3: 2.5D SIMTP algorithm

All models were optimised for a 50% material occupancy for 150 iterations, and the analyses were performed on an Intel Xeon W-2155 processor with 64GB RAM. The OC method, as discussed in Andreassen et al. [182], was used to identify design variables that meet the volumetric constraint. Results presented in this section were obtained using a modified version of the top88 code [182] - the top211 MATLAB code, which includes 2D eight-noded elements and 2.5D elements using a two-point integration rule. The modified code also includes the SIMTP and SIMP TO methods, as well as an energy regularisation method. The algorithm employed in this study is presented in Fig. 4.3. For educational purposes, a copy of the code mentioned above is presented in Appendix B, along with examples to help users understand the implementation of the algorithm.

The benchmark problems explored in this section include cantilever, MBB, and L-beams, and their dimensions and material properties can be found in Fig. 4.4 [93,182]. While these problems were chosen to assess the stiffness solutions, efficiency, and robustness of the 2.5D SIMTP method compared to the 2D SIMP method, it is important to note that they may not represent real-life designs.

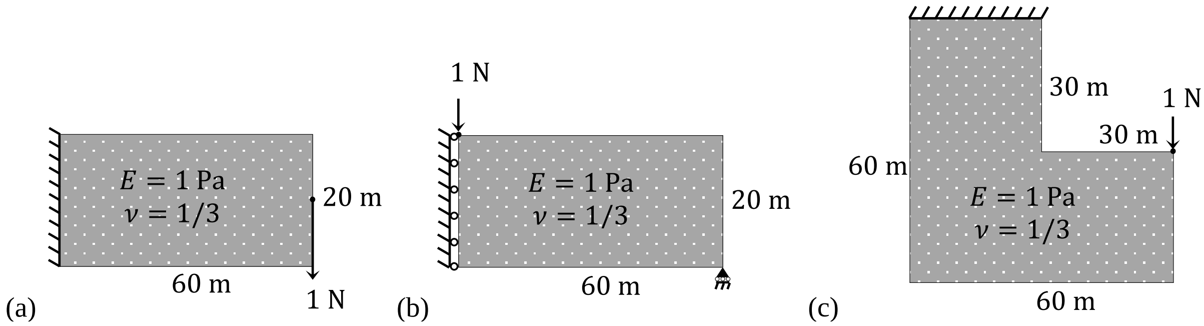

Figure 4.4: Design space. (a) Cantilever; (b) MBB and (c) L-beam

The primary objective of this study is to compare the shapes and resolutions of optimised profiles resulting from both 2.5D SIMTP and 2D SIMP. To achieve this, the section presents the results of a cantilever beam problem, summarised in Tab. 4.1. The nomenclature used in the present section: *O_X* and *t_X* are compliance and computational time of *X* (a method or case), e_z is the element size, r_z is the ratio of the radius (of influence) to e_z, Δp is the penalty increment per iteration. The computational time axis in the three-axis plots is displayed in the logarithmic scale (base 2).

The first two cases, C1 and C2, were compared with identical parameters, except for the initial threshold. The 2.5D SIMTP method required a higher initial threshold to ensure positive energy of the element, regardless of the regularisation method used (see lines 184 – 210 of top211). To determine the appropriate initial threshold, a parametric study was conducted by varying the TF at a single node while considering unit TF values at the rest of the nodes in an element, such that the Jacobian remains positive for the least TF values. The initial threshold value of 5% was determined based on this parametric study (see line 79 of top211).

Table 4.1: Cantilever beam results

Case	Beam Model	Opti. Method	e_z (m)	r_z	Initial Threshold (%)	Penalty			After 150 iterations	
						Min.	Max.	Δp	Compliance (N-m)	time (s)
C1	Cantilever	SIMTP	0.5	1.5	5	3	3	0	183	72
C2	Cantilever	SIMP	0.5	1.5	10^{-7}	3	3	0	190	41
C3	Cantilever	SIMTP	0.5	1.5	5	1	3	0.05	179	72
C4	Cantilever	SIMP	0.33	2.5	10^{-7}	3	3	0	190	88

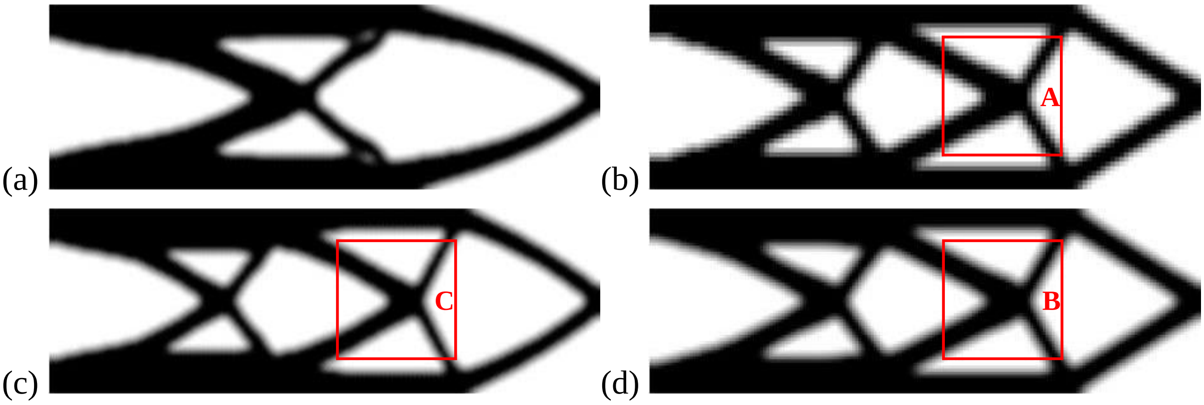

Figure 4.5: Pixels of cantilever beam. (a) C1; (b) C2; (c) C3 and (d) C4

Although using the same parameters, the optimised profiles of cases C1 and C2 in Fig. 4.5 exhibit distinct shape outcomes. The data for these cases from Tab. 4.1 indicates that SIMP has better computational efficiency, although SIMTP has a better stiffness solution. To achieve similar-shaped pixels, cases C3 and C4 were studied. In C3, the penalty increment was slowed down, while in C4, the mesh and influence radius parameters were modified. The results for these cases in Fig. 4.5 shows similar-shaped pixels, while the tabular data (see Tab. 4.1) reveals that SIMTP offered better computation time and stiffness solutions over SIMP. Furthermore, Fig. 4.6 compares the compliances and computational times of all the cases across the iterations, providing a comprehensive understanding of the performance of SIMP and SIMTP methods in terms of computational efficiency and compliance for different optimisation cases.

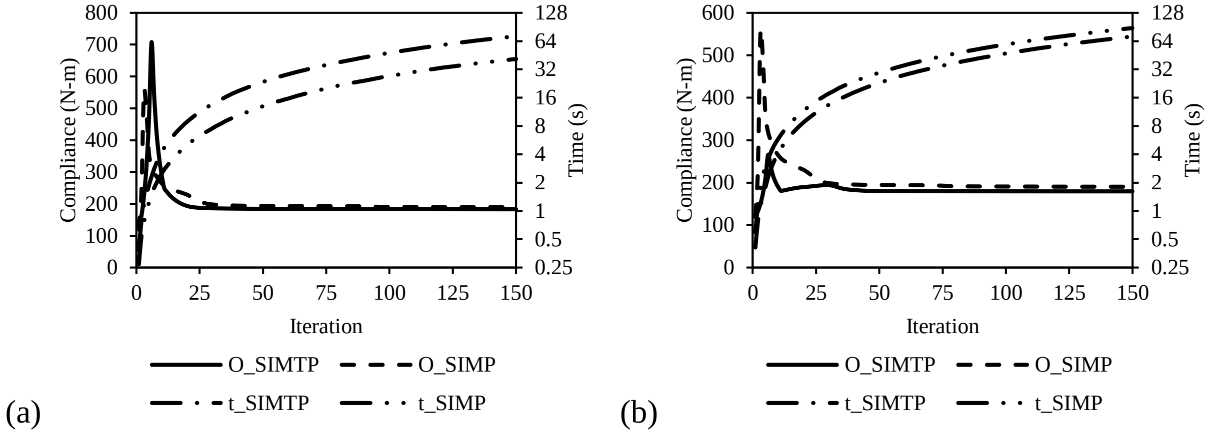

Figure 4.6: Cantilever beam - performance comparison. (a) C1 vs. C2: same parameters and (b) C3 vs. C4: similar pixels

As noted in Tab. 4.1 and Fig. 4.6, the 2.5D SIMTP method requires more computational effort than the 2D SIMP method while using the same discretisation. In 2.5D SIMTP, the volume is estimated based on the 3D Jacobian, which depends on the design variable, resulting in the repeated calling of the volume function during the bisection method (OC, see line 169 of top211). Additionally, computing the stiffness for every element is required in the 2.5D SIMTP method, unlike the SIMP method (see line 144 of top211). Therefore, the 2.5D SIMTP method requires more computational effort.

It is important to note that the computational efficiency of the 2D SIMP method in this section is due to the use of uniform element discretisation. The global stiffness matrix in SIMP is formed by assembling the resulting vector product of the element densities and stiffness of a single element (see [182]). However, the computational efficiency of the 2.5D SIMTP method is not affected by choice of uniform or non-uniform discretisation since it requires volume and stiffness computation for each element regardless of the discretisation.

Further, to compare the resolution of the optimised profiles obtained using SIMTP and SIMP methods, selected regions in Fig. 4.5 are magnified and presented in Fig. 4.7. Based on the current findings, the 2.5D SIMTP method appears to be more efficient and economical in producing high-resolution images, using only 80% of the computational efforts required by the 2D SIMP method to achieve a similar level of resolution. The SIMP method compromises resolution with less computational effort or requires greater computational effort to generate high-resolution images.

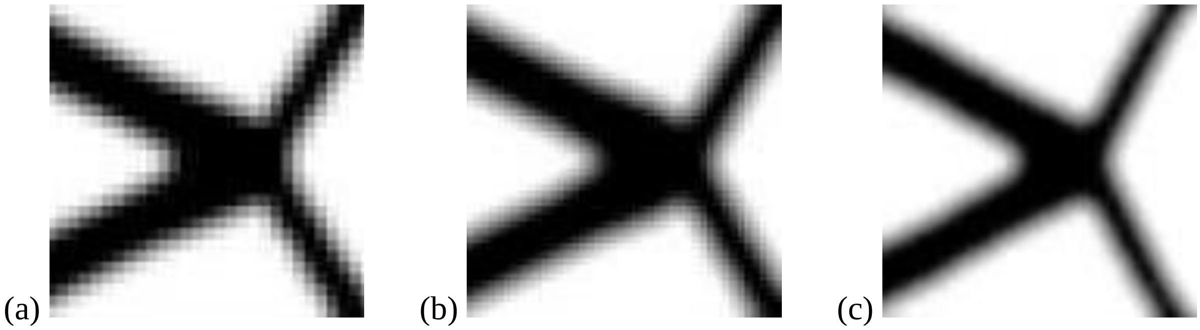

Figure 4.7: Magnified boundaries. (a) C2: region A; (b) C4: region B and (c) C3: region C

Table 4.2: MBB beam results

Case	Beam Model	Opti. Method	e_z (m)	r_z	Initial Threshold (%)	Penalty			After 150 iterations	
						Min.	Max.	Δp	Compliance (N-m)	time (s)
C5	MBB	SIMTP	0.5	1.5	5	3	3	0	204	72
C6	MBB	SIMP	0.5	1.5	5	3	3	0	199	42
C7	MBB	SIMTP	0.5	1.5	5	1	3	0.05	197	72
C8	MBB	SIMP	0.5	1.5	5	1	3	0.05	192	42

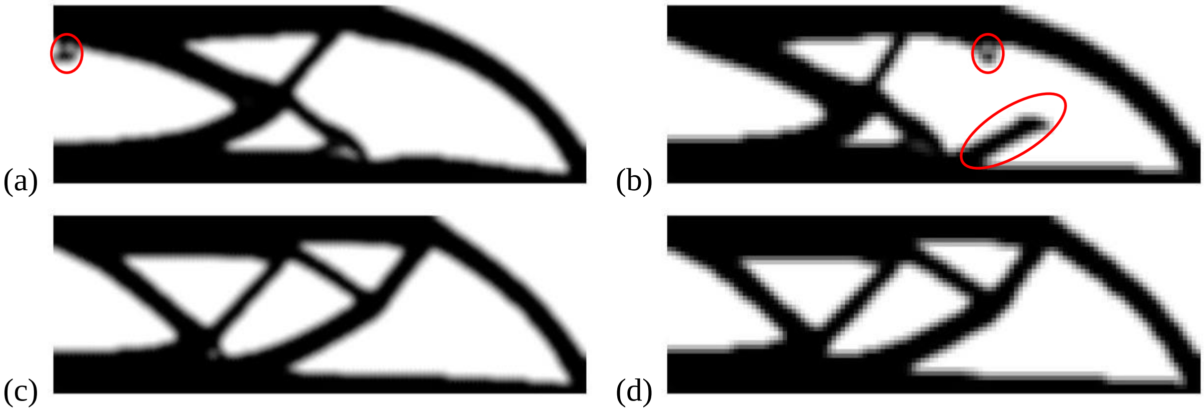

Figure 4.8: Pixels of MBB beam. (a) C5; (b) C6; (c) C7 and (d) C8

However, the 2.5D SIMTP method has a limitation that necessitates a higher initial threshold, which can result in the premature suppression of elements from the design. In contrast, the SIMP method includes the energy of these elements in the design, potentially leading to the premature suppression of elements when higher penalties are used, requiring a gradual penalty increment. To investigate this behaviour, MBB beam examples were studied using the SIMP method with the same initial threshold as SIMTP (i.e., 5%) for both aggressive and gradual penalties. The results are presented in Tab. 4.2 and Fig. 4.8 shows the optimised profiles, offering further insights into the strengths and limitations of these optimisation methods.

The results presented in Fig. 4.8 further reveal the presence of unwanted material distribution (highlighted in red) in both the 2.5D SIMTP and 2D SIMP methods when using aggressive penalty with a higher initial threshold. The unwanted material distribution in cases C5 and C6 may be attributed to the aggressive penalty since the higher penalty reduces the design values that are already low while values close to one remain the same, causing a greater reduction in compliance rates. An example of this can be seen in the performance plots of SIMTP with aggressive and gradual penalties shown in Fig. 4.6.

In SIMTP, an element with a sudden thickness variation and an aggressive penalty can cause a steeper compliance rate. Also, design variables are greatly influenced by the compliance rate, while the volume rate remains constant throughout the optimisation process (refer to line 137 of top211 code). Therefore, any adverse change in compliance rates within the element leads to the premature suppression of nodal thickness at the nodes with relatively lower thickness, while the higher thickness at neighbouring nodes appears as the unwanted thickness distribution.

However, similar shape profiles were obtained when using gradual penalty while the SIMP outcomes appeared pixelated. This suggests that a higher initial threshold can prematurely kill elements with aggressive penalties, and the SIMP method is no exception. Another observation is that the tabular data (see Tab. 4.2) showed that the SIMP method offers better stiffness solutions and computational efficiency, which has been previously discussed and attributed to uniform discretisation. Therefore, it is concluded that, based on the earlier comparisons, it is essential to use a higher initial threshold while using the 2.5D SIMTP method, and a gradual penalty is needed when using a higher initial threshold to avoid premature suppression of elements in both methods.

Through a comprehensive parametric study, it has been estimated that the 2.5D SIMTP method requires a gradual penalty increment in the range of 0.05 to 0.15

to achieve optimal results. This finding highlights the importance of carefully selecting the penalty increment value when using the SIMTP method for structural optimisation. By using a gradual penalty increment, it may be possible to prevent the premature killing of elements and produce high-resolution images with optimal computational efficiency.

Table 4.3: L- beam results

Case	Beam Model	Opti. Method	e_z (m)	r_z	Initial Threshold (%)	Penalty			After 150 iterations	
						Min.	Max.	Δp	Compliance (N-m)	time (s)
C9	L-beam	SIMTP	0.5	1.5	5	1	3	0.05	86	179
C10	L-beam	SIMP	0.5	1.5	10^{-7}	3	3	0.00	89	88

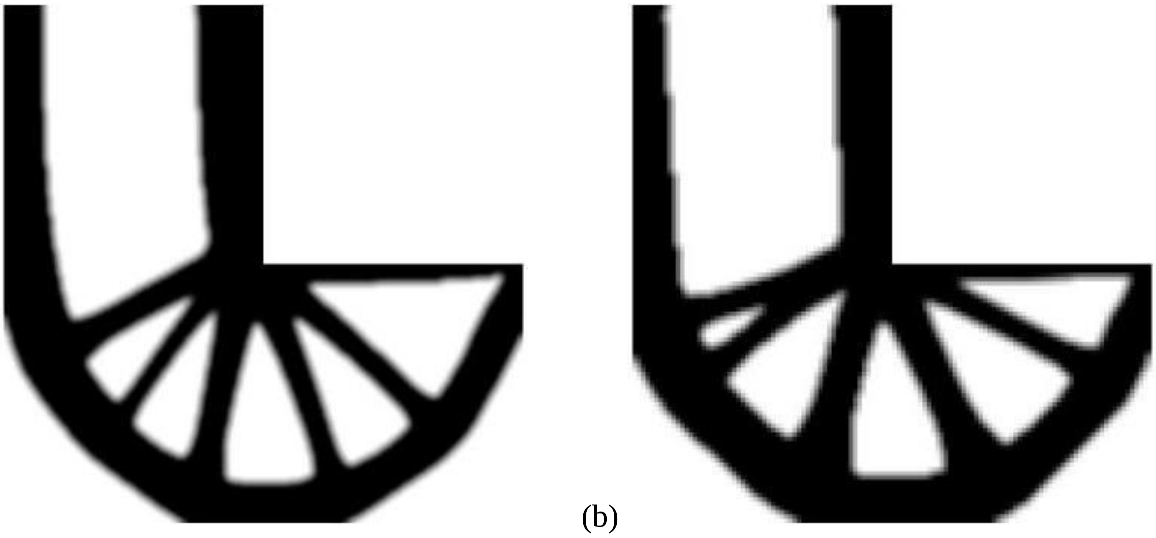

(a) (b)

Figure 4.9: Pixels of L- beam. (a) C9 and (b) C10

After a thorough analysis of the parameters that affect the outcomes of the 2.5D SIMTP method, an L-beam case was studied to compare the performances and shapes of both methods. In this study, C9 employs the SIMTP method with a higher threshold and a gradual penalty increment, while C10 uses the SIMP method with a relatively lower threshold and an aggressive penalty. The results and shape profiles of these cases are presented in Tab. 4.3 and Fig. 4.9. As expected, the SIMP method required half the computational time of the SIMTP method, with a higher number of elements relative to earlier beam cases (cantilever or MBB). Additionally, the SIMTP method produced high-resolution and better stiffness solutions, while the outcomes of the SIMP method appeared pixelated.

The trade-offs between computational efficiency and stiffness solutions highlight the strengths and limitations of the SIMP and SIMTP methods for solving optimisation problems. Based on the observations presented in this study, the SIMTP method is recommended for applications where high-resolution images are required, as it produces better stiffness solutions and high-resolution images, albeit with a higher computational cost. While the SIMP method can also produce high-resolution images, it often requires more computational effort to achieve the same level of resolution. Therefore, the SIMP method may be more suitable for scenarios where computational efficiency is a priority, as it can be used to quickly generate preliminary designs. However, it is important to carefully select the optimisation parameters based on the specific problem being solved to ensure that the chosen method produces the desired outcomes. Overall, the SIMP and SIMTP methods offer distinct advantages and limitations and can be used to solve a wide range of optimisation problems.

4.4 Remarks

This chapter presented a new thickness-scaling strategy called SIMTP and investigated its performance capabilities using 2.5D elements. To this end, various beam examples are explored, and the key aspects identified are listed below:

I. SIMTP uses a non-dimensional parameter, TF, to scale the nodal thickness of a 2.5D element, enabling the use of TF and thickness values to draw both pixels and voxels (or surfaces), respectively. However, this approach is limited to plane-stress problems with symmetrical geometry perpendicular to a loading plane.

II. The proposed approach enables seamless interaction between architectural and structural design by allowing the architectural expression of any surface to be provided as the initial design sample.

III. Achieving a stable Jacobian in 2.5D elements ensures numerical stability in SIMTP.

IV. A higher initial threshold of 5% is required to ensure a positive Jacobian in 2.5D SIMTP, while SIMP requires a very low value of 10^{-7}%. For initial thresholds of 5%, it is recommended to gradually increase the penalty from 0.05 to 0.15.

V. When the same discretisation is used, 2.5D SIMTP is more computationally expensive than 2D SIMP. The 2.5D SIMTP method produces high-resolution optimised profiles, while the 2D SIMP method requires a greater number of elements to achieve the same standard.

In summary, the SIMP and SIMTP methods offer unique advantages and limitations and can be applied to a diverse range of optimisation problems. The SIMTP method is recommended for applications where high-resolution images are required, while the SIMP method may be more suitable for scenarios where computational efficiency is a priority. Overall, SIMTP is an effective optimisation methodology that offers significant improvements over existing methods.

The next chapter explores the use of adaptive refinement with 2.5D SIMTP, which is essential to explore the possibilities of using threshold values as low as 10^{-3}, as this is not possible with uniform discretisation.

Chapter 5

Adaptive Refinement

In the preliminary investigation, 2.5D SIMTP showed unwanted thickness distribution with an aggressive penalty. Additionally, a general filtering scheme is necessary to regularise the energy and smooth the surface, which helps to maintain a stable Jacobian. In addition, an initial threshold of 5% is required to avoid negative Jacobian occurring from steep thickness gradients, and this threshold is relatively higher than the 10^{-7}% threshold used in 2D SIMP [182]. Although this is justified by comparing with the 50% display threshold of 3D SIMP [183], it is worth noting that an element with an initial threshold of 5% will be removed from the display, meaning that its contribution is disregarded for the design. However, this element's numerical significance is greater than the energy that is disregarded from the threshold of 10^{-7}%. Therefore, elements with a higher initial threshold may be prematurely removed, regardless of their ability to contribute to the design, resulting in a disruptive energy field in the design domain. The impact of this on optimised outcomes is yet to be fully explored.

This chapter explores the use of 2.5D SIMTP with an initial threshold as low as 10^{-3}, which is unachievable with uniform discretisation. To achieve this, quadtree adaptive mesh refinement is used to refine the elements with a higher thickness gradient (negative Jacobian). The adaptive refinement technique involves dividing the design domain into subdomains and applying a higher resolution to areas where the function values change rapidly. The adaptive refinement process is guided by the element-wise threshold values, which are computed based on the thickness gradient at Gaussian integration points. When the energy at one of these points is negative, the corresponding element is further refined. However, this refinement creates additional children elements, resulting in confirming and non-confirming nodes where the thicknesses are yet unknown. The following section discusses the refinement strategy and how the thicknesses are mapped to the newly formed nodes.

5.1 Refinement Strategy and Thickness Mapping

This section discusses refinement strategies for 2.5D elements, which have shape functions and interpolation properties similar to Q8 elements. Refinement strategies used for Q8 elements can also be used for 2.5D elements, which makes them a viable option for this study. There are many h-refinement and marking strategies available in the literature, along with open-source codes [184-194]. However, open-source refinement strategies for Q8 elements are limited in the literature.

To address this issue, the QrefineR implementation for Q4 elements developed by Funken and Schmidt [194] was modified to work with 2.5D elements using a 1-irregularity rule. A 1-irregular rule means that no more than one hanging node is allowed in an edge for a Q4 element. If introducing a new hanging node is inevitable, then the adjacent elements sharing the 1-irregular edge are refined first to convert 1-irregular edges to regular edges, maintaining 1-irregularity. An illustration of this is provided in Fig. 5.1, where element 1 is marked for refinement, resulting in three new elements and two 1-irregular edges shared by elements 2 and 4. Refining element 6 further leads to more than one hanging node in the earlier irregular edges; hence, elements 2 and 4 are refined before refining element 6.

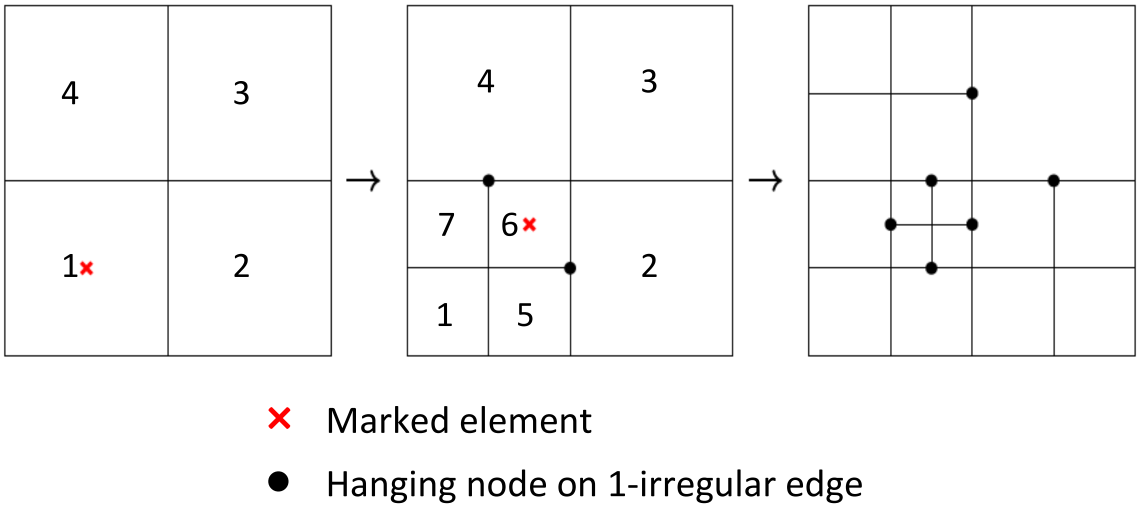

Figure 5.1: 1-Irregular rule for Q4 element[193]

Being 1-irregular can make it more difficult to generate a conforming mesh, but it is possible to generate conforming meshes from 1-irregular meshes using appropriate meshing techniques. However, conforming meshes, in case of refinement, are computationally more expensive than non-conforming meshes. In this chapter, quadtree refinement techniques are used, resulting in non-conforming meshes. Further details on QrefineR are available in the documentation of ameshref [193], along with an open-source package.

$$
\begin{gathered}
t_{17} = \sum_{i=1}^{4} \left(\frac{t_i}{12} + \frac{t_{i+4}}{6} \right) \\
\forall (i,j,k) \in \left\{ \begin{array}{l|l|l} (9,1,5) & (13,3,6) & (18,5,17) \\ (10,1,8) & (14,3,7) & (19,6,17) \\ (11,2,5) & (15,4,7) & (20,7,17) \\ (12,2,6) & (16,4,8) & (21,8,17) \end{array} \right. : t_i = \frac{t_j + t_k}{2}
\end{gathered} \tag{5.1}
$$

Quadtree refinement, which is a type of h-refinement, generates new nodes at every iteration, and a few nodes are left hanging. Since the 2.5D element is thickness-based, nodal thicknesses need to be mapped to newly born nodes after refinement. To achieve this mapping, a simple strategy is employed, which is presented in Eq. (5.1). The strategy involves estimating the thickness of the mid-node of the new children, such as node '17' in Fig. 5.2, using Shepard interpolants [180] on the thicknesses at parent nodes. Next, the thickness of the other children nodes is estimated by averaging the thicknesses at the adjacent nodes.

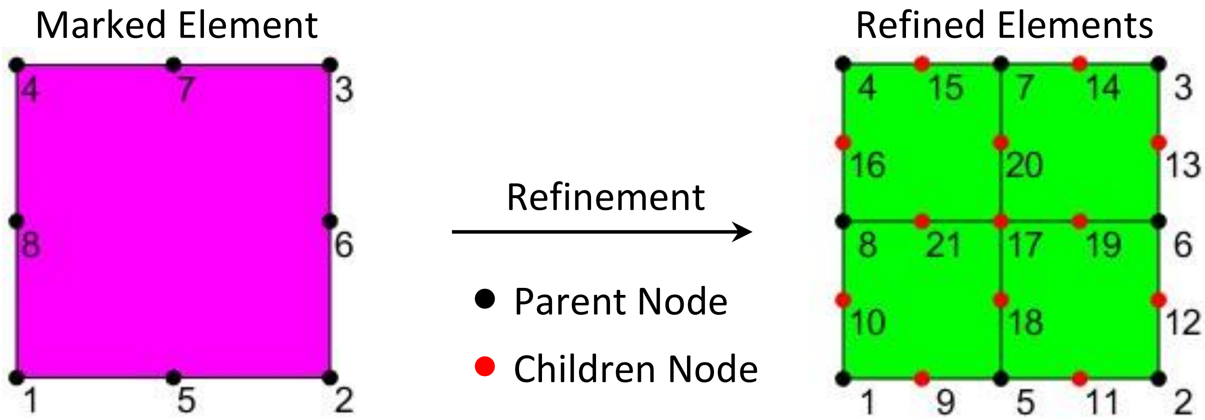

Figure 5.2: Element refinement - Parent and Children nodes

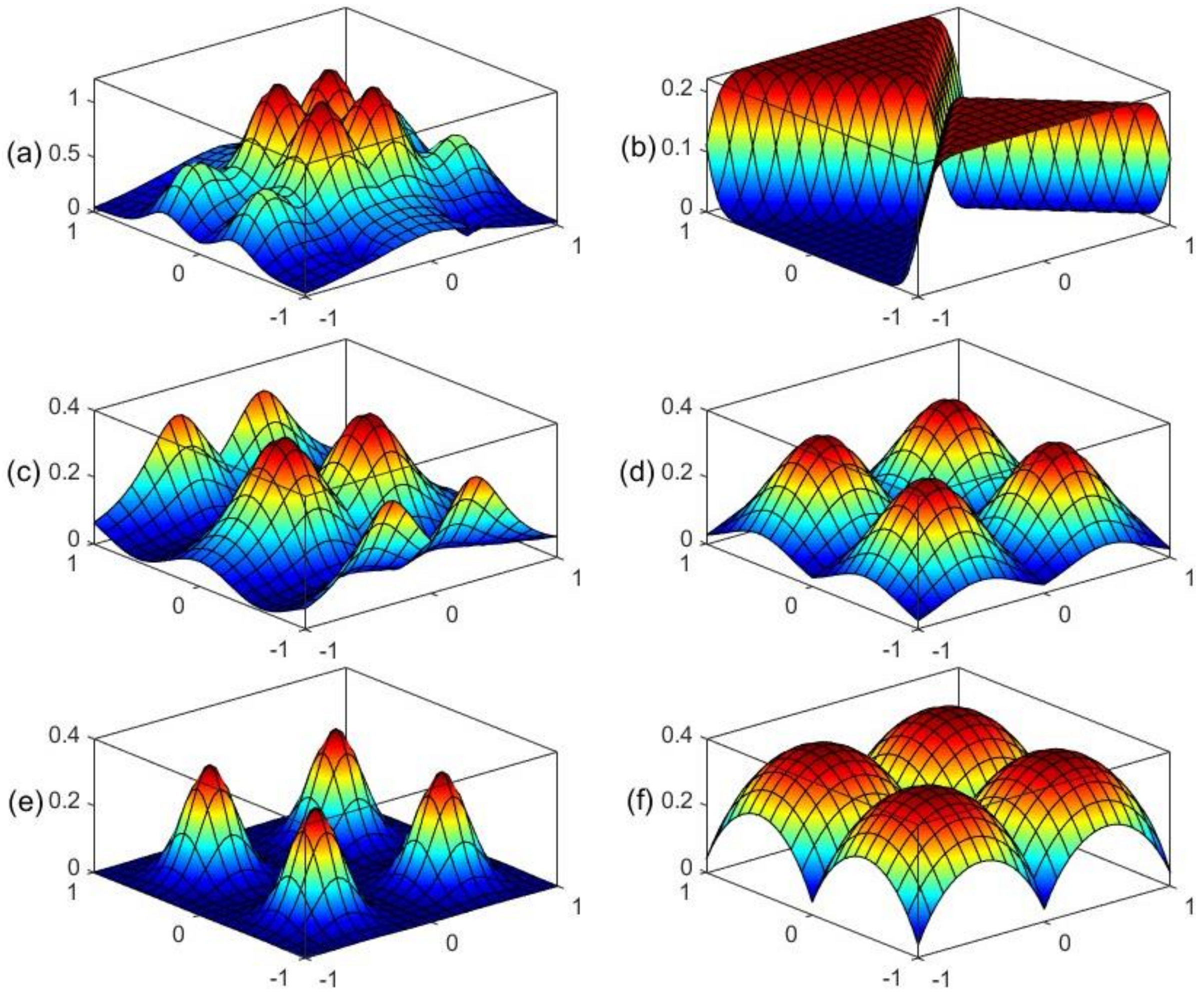

Figure 5.3: Surface plots of Franke's functions. (a) z_1; (b) z_2; (c) z_3; (d) z_4; (e) z_5 and (f) z_6

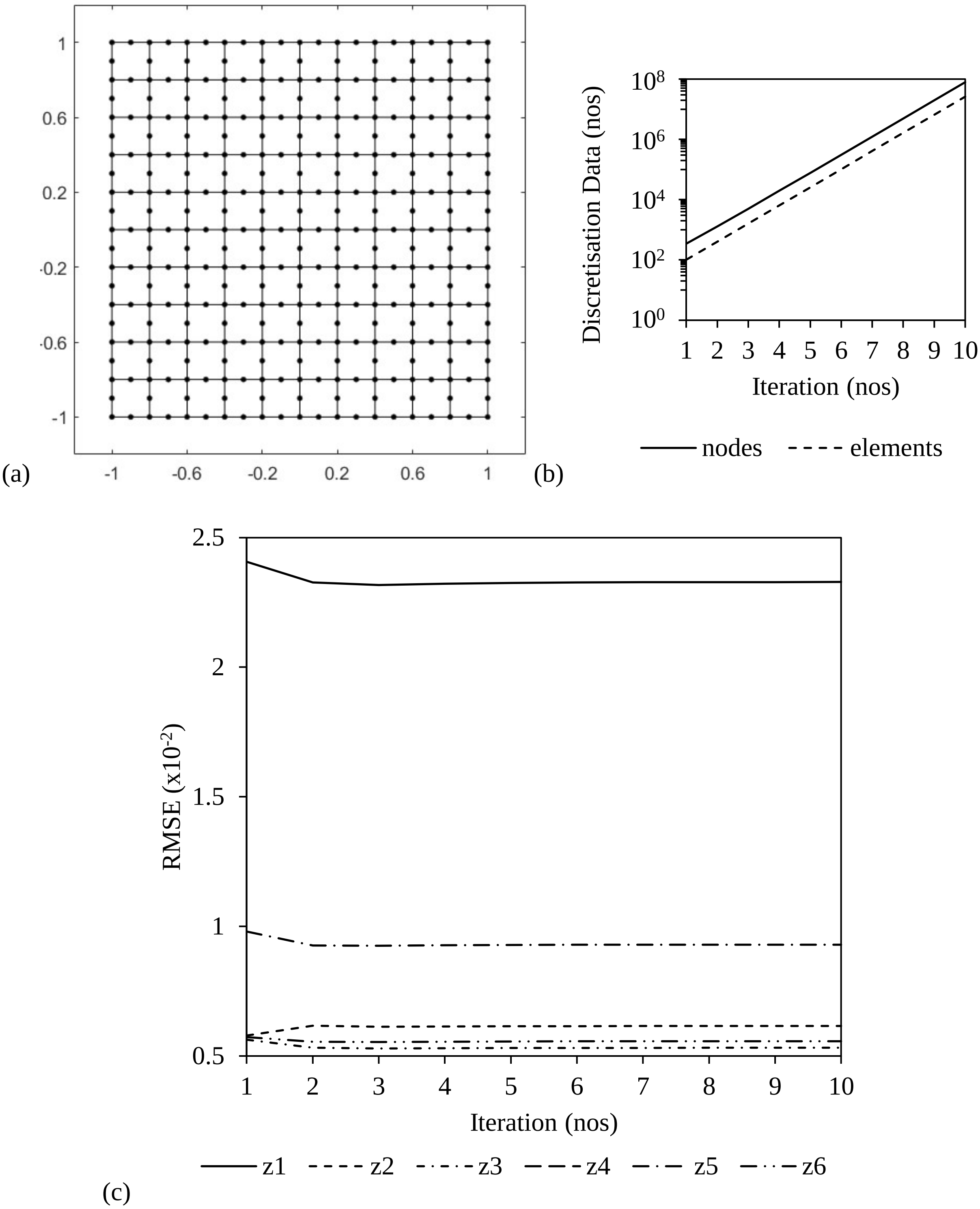

Figure 5.4: Thickness mapping and error estimate. (a) Parent mesh 10×10; (b) Discretisation growth over iterations and (c) RMSE for Frankes functions

The mapping process discussed above is tested with Franke's functions [195], as shown in Eq. (5.2) and Fig. 5.3. To estimate the errors that arise from the proposed thickness mapping in Eq. (5.1), a 10×10 parent mesh is chosen, as depicted in Fig. 5.4(a). To begin with, thickness values at the parent nodes are evaluated for the initial mesh, and then each parent element is refined ten times (see Fig. 5.4(b)). The errors at the children nodes are estimated from the exact thickness values obtained from Franke's functions. The RMSE of the new children nodes at each iteration for all testing functions are presented in Fig. 5.4(c). his plot shows that the employed thickness mapping is reliable in estimating the unknown values at children nodes with relatively low errors and can be used for thickness approximations during the optimisation process with adaptive refinement.

$$
\begin{aligned}
z_1 &= \begin{cases} 0.75e^{\left(-\frac{(9|x|-2)^2+(9|y|-2)^2}{4}\right)} + 0.75e^{\left(-\frac{(9|x|+1)^2}{49}-\frac{(9|y|+1)}{10}\right)} \\ + 0.50e^{\left(-\frac{(9|x|-7)^2+(9|y|-3)^2}{4}\right)} - 0.20e^{\left(-(9|x|-4)^2-(9|y|-7)^2\right)} \end{cases} \\
z_2 &= \frac{tanh(9|y|-9|x|)+1}{9} \\
z_3 &= \frac{1.25+cos(5.4|y|)}{6+6(3|x|-1)^2} \\
z_4 &= \frac{e^{\left(-5.0625\left((|x|-0.5)^2+(|y|-0.5)^2\right)\right)}}{3} \\
z_5 &= \frac{e^{\left(-20.25\left((|x|-0.5)^2+(|y|-0.5)^2\right)\right)}}{3} \\
z_6 &= \frac{\left(64-81((|x|-0.5)^2+(|y|-0.5)^2)\right)^{\frac{1}{2}}}{9} - 0.5
\end{aligned}
\tag{5.2}
$$

As previously mentioned, this section discussed refinement and thickness mapping strategies using the 1-irregular rule. It is known that the use of the 1-irregular rule with quadtree refinement can result in the presence of hanging nodes due to the non-conforming nature of the resulting meshes. In more detail, the following section discusses strategies for handling non-conforming meshes and hanging nodes resulting from refinement based on element marking.

5.2 Element Marking, Refinement and Treatment of Hanging Nodes

As discussed at the beginning of this chapter, the objective of this chapter is to explore 2.5D SIMTP with an initial thickness threshold as low as 10^{-3}. This causes high thickness variations within the element, resulting in negative energy. To address this, elements with negative Jacobians at any Gauss integration point are marked for refinement. The refinement procedure continues until all elements have positive Jacobians at all integration points. As previously discussed, the refinement strategy follows a 1-irregular rule. However, the 1-irregular rule in 2.5D elements results in two hanging nodes per irregular edge, unlike Q4 elements, as shown in Fig. 5.5.

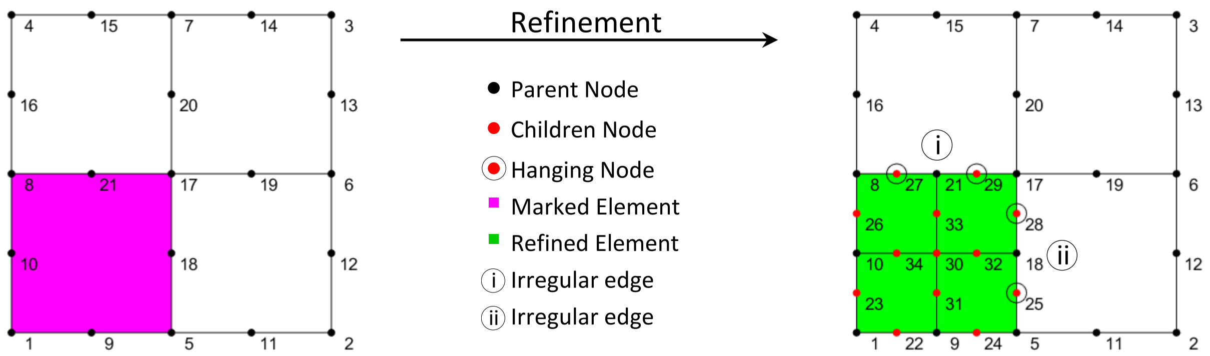

Figure 5.5: Refinement and hanging nodes

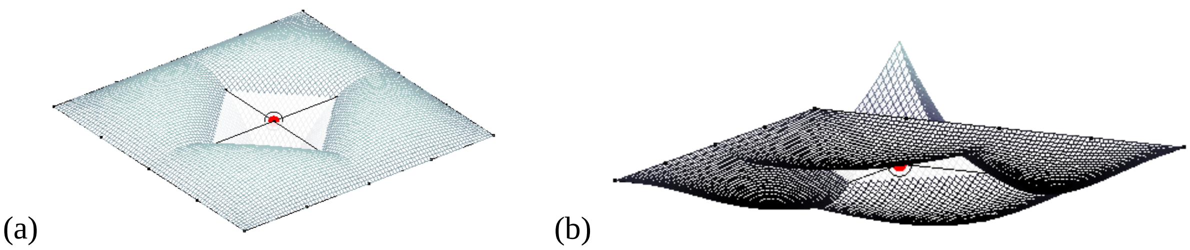

Figure 5.6: Continuous field

Regular FE analysis always contains conforming mesh nodes, resulting in a continuous energy field, as shown in Fig. 5.6. However, hanging nodes resulting from the adopted refinement process lead to non-conforming finite elements and discontinuous energy fields with regular shape functions, as shown in Fig. 5.7.

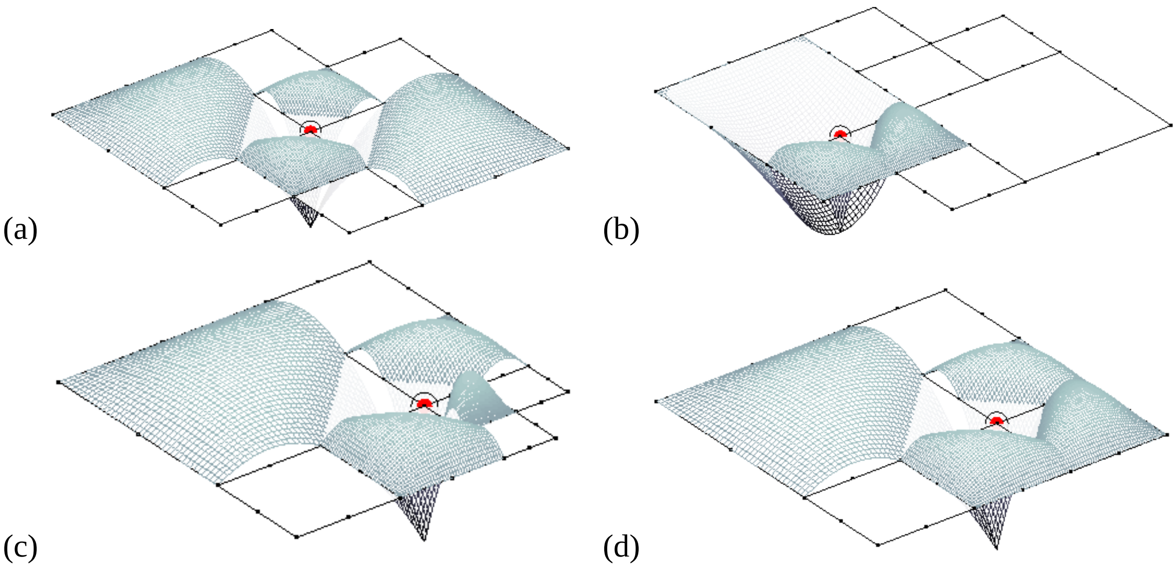

Figure 5.7: Discontinuous field

The discontinuous energy resulting from hanging nodes is dealt with in two ways. The first approach called the transition method [196], achieves a continuous energy field by obtaining conforming shape functions. However, this approach requires an extension of the quadrature rule, which increases the computation burden. In contrast, the constrained approximation [197-198] applies constraints on the degrees of freedom (DOFs) of hanging nodes. It is based on interpolation from adjacent conforming parent nodes lying on the corresponding irregular element's edge. Later, Lagrangian multipliers enforce the constraints on hanging nodes into FE solvers. However, other methods that are more accurate and efficient for specific problems are available in the literature [196,199-200], but they can be more complex and computationally costly due to their problem-specific efficiency, high element distortion, and discretisation errors. A detailed discussion on existing refinement schemes [196-200] can be found in [201], especially for the Q8 element in [202].

Based on the above discussion, constrained approximation is adopted in this chapter since it is easy to implement, less complicated, and can yield efficient results with low discretisation errors. As discussed earlier, the concept of the constraint approximation method is applied to 2.5D elements, and the constrained approximation is derived as follows:

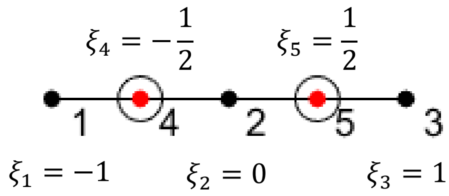

Figure 5.8: Irregular edge of a 2.5D element

A constraint equation for hanging nodes in the 2.5D element is evaluated based on the interpolation function, where the coefficients are estimated using the quadratic 1D shape functions of the parent nodes located on the irregular edge, as discussed for the Q8 element in Sarkar et al. [202]. Referring to Fig. 5.8, the constraint equation for hanging nodes 4 and 5 on an irregular edge connecting nodes 1, 2 and 3 is given by:

$$\forall i \in [4,5]: u_i = \sum_{j=1}^{3} L_{j,i} u_j$$
$$L_{1,i} = \frac{\xi_i(\xi_i - 1)}{2};\ L_{2,i} = (1 - \xi_i^2);\ L_{3,i} = \frac{\xi_i(\xi_i + 1)}{2} \tag{5.3}$$

By writing the constrained equations for all the hanging nodes and solving the traditional linear system of equations of FEM while enforcing Lagrangian multipliers, the resulting system of equations to be solved is derived as follows:

$$\forall i \in N_h, \forall j \in (\, N_n - N_i) :$$

Constraint equations : $$[0 \quad 1 \quad -L_{1,i} \quad -L_{2,i} \quad -L_{3,i}] \begin{bmatrix} u_j \\ u_i \\ u_{1,i} \\ u_{2,i} \\ u_{3,i} \end{bmatrix} = [c_i]u = 0$$

$$\forall i \in N_h: C_{eq} = [c_i]$$

(5.4)

Traditional Linear system of equations : $$Ku = F$$

Lagrangian multiplier approach : $$Ku + C_{eq}^T \lambda = F$$

Modified system of equations : $$\begin{bmatrix} K & C_{eq}^T \\ C_{eq} & 0 \end{bmatrix} \begin{bmatrix} u \\ \lambda \end{bmatrix} = \begin{bmatrix} F \\ 0 \end{bmatrix}$$

Where, c_i is constrained equation for hanging node i in a set of hanging nodes (N_h, for e.g., nodes 4 and 5 in Fig. 5.8), $L_{j,i}$ quadratic shape functions of j^{th} parent node in a set of parent nodes (N_i) of hanging node i, N_n is total set of nodes, C_{eq} is an assembly of constrained equations, λ is a Lagrangian multiplier, K is global stiffness matrix, u is deformation matrix and F is force matrix.

Overall, existing refinement strategies, element marking, and treatment of hanging nodes through constrained approximation are discussed and modified for 2.5D elements. The following section will implement the adaptive refinement technique discussed in the present section into 2.5D SIMTP, and the results of various beam cases explored using adaptive 2.5D SIMTP will be discussed.

5.3 Refinement Algorithm and Comparison of Pixels

Quadtree refinement can result in a higher number of elements, which increases the computational burden for FE analysis. When used in conjunction with optimisation processes, it can further impact computational costs. To avoid this, refinement is carried out on the analysis mesh while keeping the design mesh unchanged, with the same initial discretisation for both meshes. The design mesh is used for design parameterisation, thickness filtering, and pixel extraction. Guest and Genut [97] and Wang et al. [95] have also implemented a similar methodology, but they perform adaptive refinement on the design mesh while keeping the analysis mesh unchanged. Designing independently of the analysis mesh requires transferring key data, such as sensitivities, from the analysis mesh to the design mesh to perform design parameterisation on thickness values at design mesh nodes. This transfer of data can increase computational costs. To simplify this process, a straightforward method is adopted whereby the initial discretisation is the same as the design mesh, meaning that the initial parent nodes are located at the same location as the design mesh nodes. Refinement is then carried out on the analysis mesh using the technique introduced in earlier sections until a stable Jacobian is achieved.

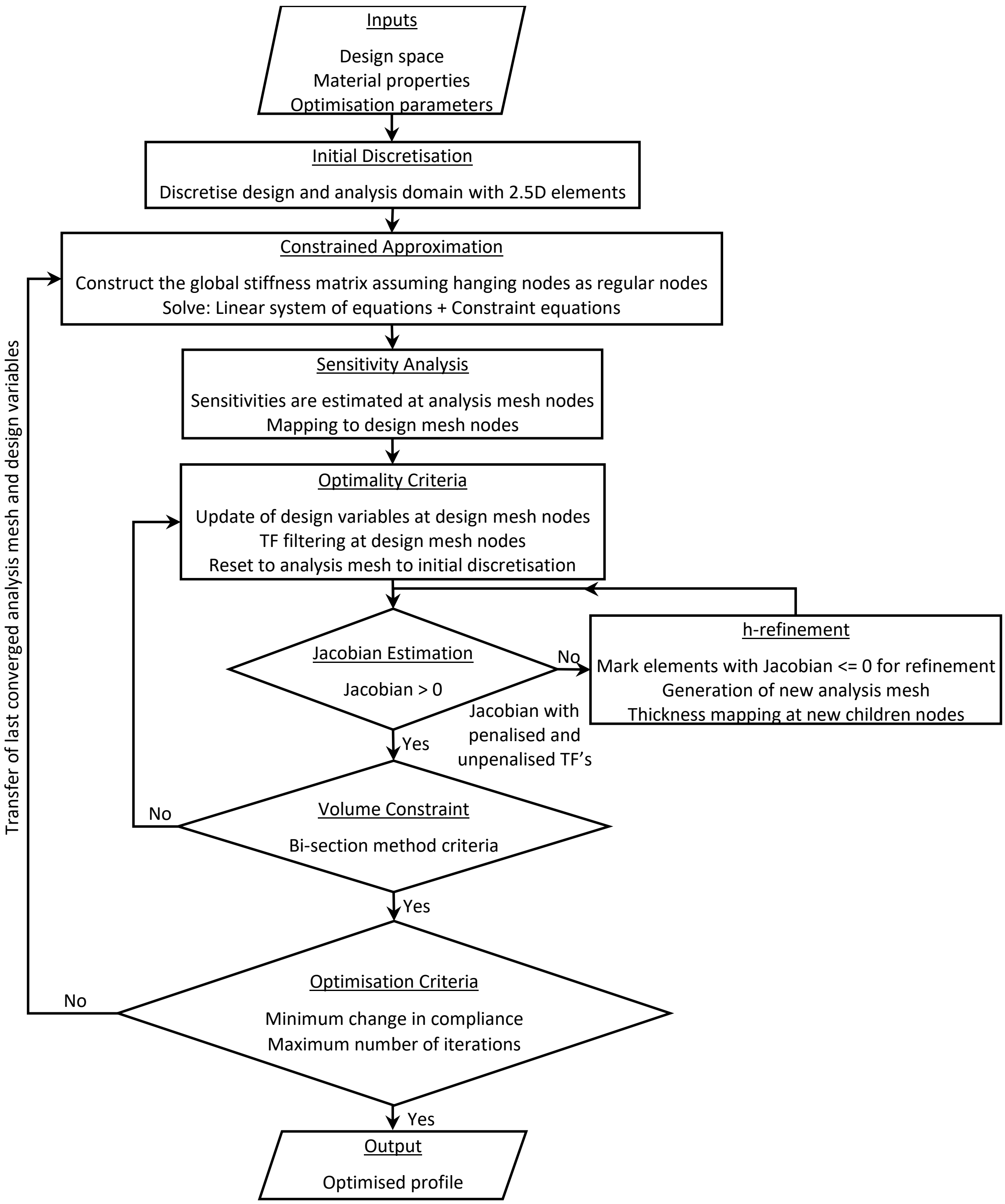

Figure 5.9: Adaptive 2.5D SIMTP algorithm

The thickness mapping method proposed in the previous section is used to estimate the thickness at children nodes for every refinement cycle. The design parameters are updated based on the filtered sensitivities of the initial parent nodes, and the design candidates are processed for thickness filtering, as discussed in the earlier chapter. The analysis mesh is then reset to its initial mesh, and this process is continued until the desired volume is achieved. The last converged analysis mesh is then used to estimate the energies, deformations, and sensitivities, with sensitivities of the parent nodes belonging to the initial analysis mesh directly associated with design mesh nodes. These sensitivities at design mesh nodes are again filtered and used for design parameterisation to obtain thickness values using the OC method. The process is continued until the desired outcomes are achieved. Adaptive 2.5D SIMTP optimisation is performed for 50 iterations since the adaptive procedures studied in this chapter require a lot of computation effort to carry out optimisation until 150 iterations (optimisation termination criteria in the previous chapter). Please refer to Fig. 5.9 for the optimisation and refinement algorithm used in this study. The MATLAB code that implements this algorithm with the 2.5D SIMTP metho introduced in the previous chapter is provided in Appendix C.

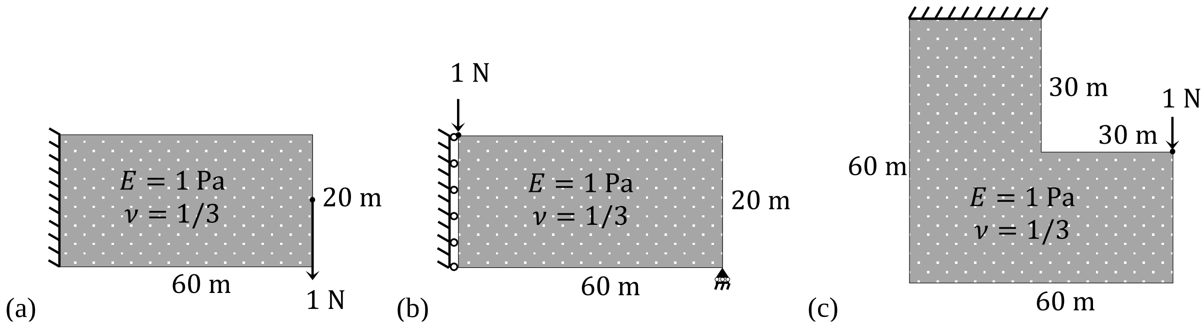

Figure 5.10: Design space. (a) Cantilever; (b) MBB and (c) L-beam

In this section, the same benchmark problems with unit thickness are used as in the previous chapter, and the optimised results obtained using adaptive 2.5D SIMTP are compared. All the models were optimised to 50% material occupancy, and the analyses were performed on the Intel Xeon W-2155 processor 3.3 GHz with 64GB RAM. Tab. 5.1 summarises the outcomes of the seven beam optimisation cases for the models presented in Fig. 5.10.

Table 5.1: Case studies, parameters, and outcomes

Case	Beam Model	Opt. Meth.	e_z (m)	r_z	In. Th. (%)	Penalty			After 50 iterations		
						Min.	Max.	Δp	Comp. (N-m)	time (s)	Ref.
C1	Cantilever	SIMTP	0.5	1.5	5	1	3	0.05	186	23	No
C2	Cantilever	SIMTP	0.5	0	0.1	3	3	0	263	6429	Yes
C3	Cantilever	SIMTP	0.5	1.5	0.1	3	3	0	194	91	Yes

C4	MBB	SIMTP	0.5	1.5	5	1	3	0.05	198	24	No
C5	MBB	SIMTP	0.5	1.5	0.1	3	3	0	210	89	Yes
C6	L-beam	SIMTP	0.5	1.5	5	1	3	0.05	87	58	No
C7	L-beam	SIMTP	0.5	1.5	0.1	3	3	0	89	254	Yes

Opt. Meth. – optimisation method; In. Th. – initial threshold; Min. – minimum; Max. – maximum; Comp. – compliance; Ref. – refinement

In the earlier chapter, it was concluded that a stable Jacobian in 2.5D elements ensures numerical stability in SIMTP, but it requires a higher initial threshold of 0.05 and thickness filtering to avoid negative energy elements. However, in this chapter, an adaptive refinement strategy is introduced to achieve initial thresholds as low as 10^{-3} to maintain a stable Jacobian. This raises an important question of whether 2.5D SIMTP is numerically stable when achieving a positive Jacobian. Therefore, three cases were studied that can ensure a stable Jacobian: C1 is based on the traditional 2.5D SIMTP parameters, which uses an unrefined mesh and filtered thicknesses, while C2 and C3 are based on the adaptive 2.5D SIMTP, which uses unfiltered and filtered thicknesses, respectively. Fig. 5.11 presents the optimised outcomes of these three cases along with the final refined analysis meshes of the cantilever beam.

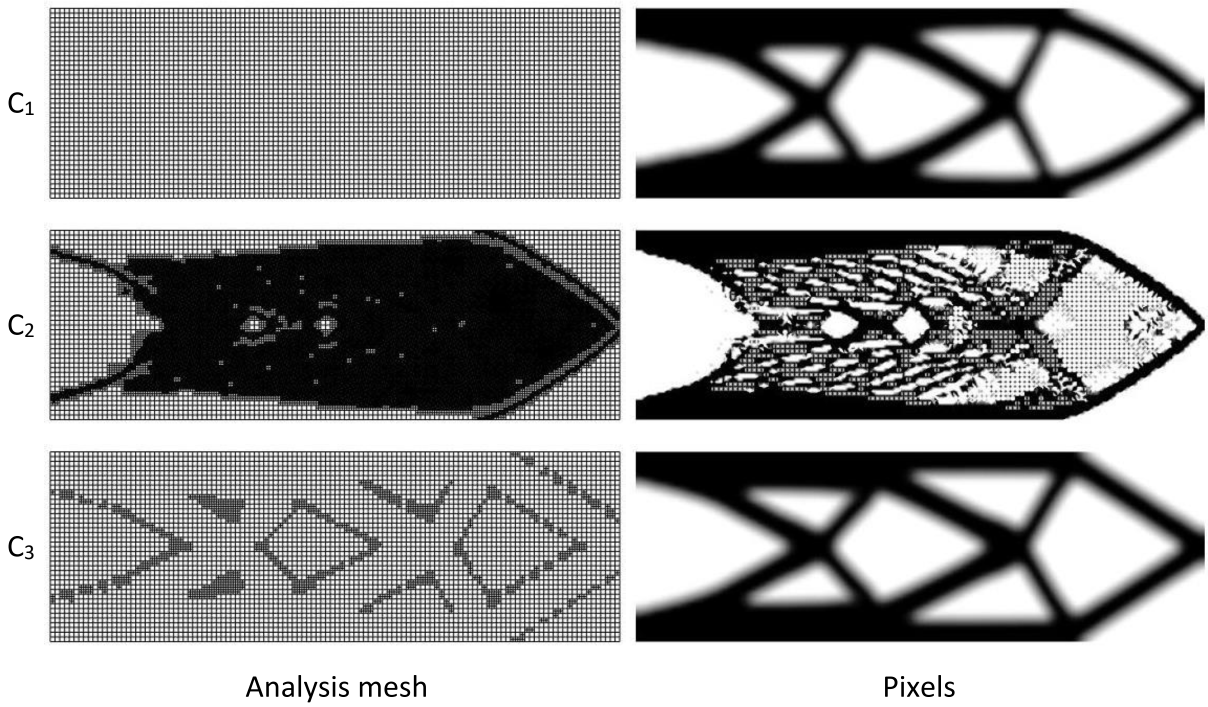

Figure 5.11: Comparison of adaptive meshes and pixels - cantilever beam

The results depicted in the above figures show an islanding phenomenon when thicknesses are unfiltered in C2 while it disappears after using filtering in C3. These observations suggest that 2.5D SIMTP alone is free from all TO pathologies except islanding. Additionally, Fig. 5.11 shows that the unfiltered case C2 used more refined elements compared to the filtered case C3. This shows that C2 struggled to achieve a stable Jacobian while C3 achieved it in fewer iterations, suggesting that filtering is necessary to speed up the process of stabilising the Jacobian during refinement. Moreover, by comparing the computational time and compliances from the data tabulated in Tab. 5.1, the unfiltered case C2 resulted in a high compliance design and used high computational energy relative to its alternative cases C1 and C3. To further understand the evolution of the stiffness solution and discretisation data across the iterations of these three cases, respective data is extracted and compared in Fig. 5.12.

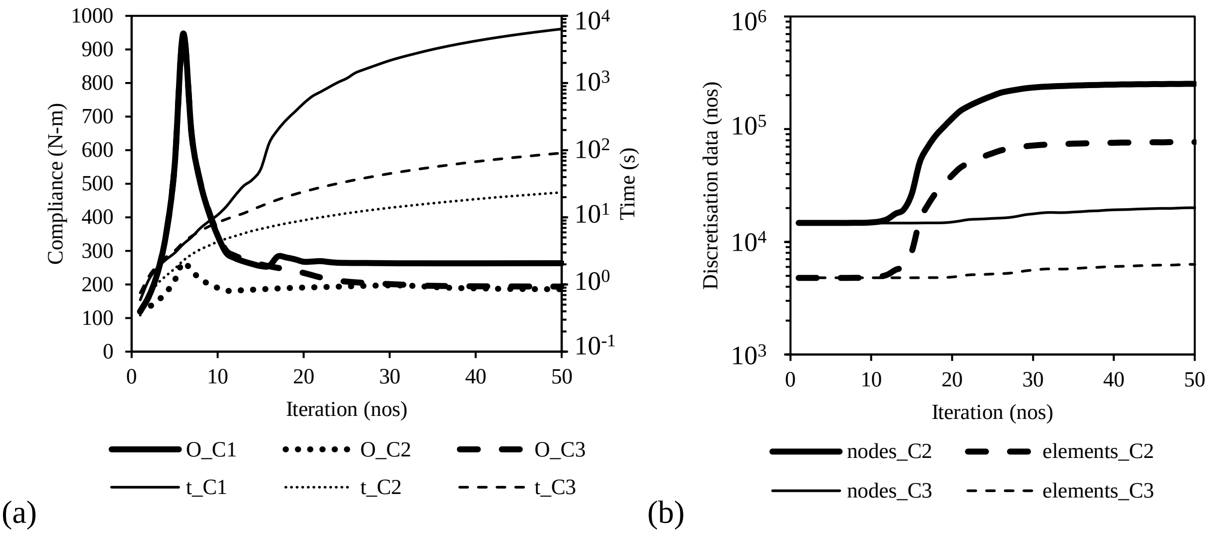

Figure 5.12: Comparison of performance and discretisation - cantilever beam . (a) Performance and (b) Discretisation data

The nomenclature used in the above figure is as follows: O_X and t_X are the compliance and computational time of case X, respectively. Both the computational time and discretisation data axes are displayed in a logarithmic scale (base 10). It can be observed that in cases C2 and C3, the growth of discretisation data across iterations is minimal until the tenth iteration, after which it begins to increase as compliance values start to decline (as shown in Fig. 5.12(a)). This indicates that material is being removed rapidly, resulting in sudden thickness variations. At this point, adaptive procedures are activated to address the issue by stabilising the Jacobian. Further to the previous observations, the above comparison shows the rapid growth of discretisation data in C2 over C3, again showing the significance of using thickness filtering (in C3). Therefore, the rest of the adaptive refinement cases, C5 and C7, are explored using filtered thicknesses. Also, the performance comparison plots show that there is a sudden increase in compliance values in C2 and C3 with aggressive penalties relative to C1 with a gradual penalty, which revalidates the relationship of compliance with the penalty, as stated in the previous chapter.

(a) (b)

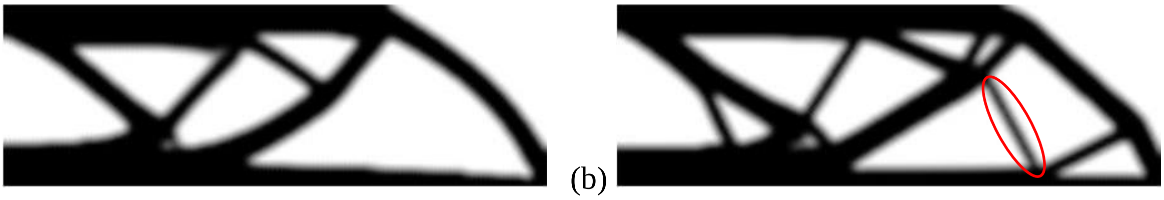

Figure 5.13: Pixels of MBB . (a) C4 and (b) C5

Further observations show that the pixels of cases C1 and C3 have similar shaped outcomes, while the tabular data in Tab. 5.1 reveals that the traditional 2.5D SIMTP case resulted in a better stiffness design (compliance value) and used lesser computational energy relative to its alternative cases C2 and C3. This suggests that despite the higher initial threshold and gradual penalty in the traditional way or lower initial threshold and adaptive refinement, they have an insignificant effect on optimised designs. Similar observations can be noticed in the MBB and L-beam cases, where traditional 2.5D cases C4 and C6 yielded better stiffness designs than their alternative adaptive refinement cases C5 and C7, respectively. The shape outcomes of these MBB and L-beam cases are presented in Fig. 5.13 and Fig. 5.14, respectively. Moreover, all the traditional approach cases (C2, C4, C6) used only 25% of the computational energy required by the adaptive 2.5D SIMTP cases (C3, C5, C7). These observations on stiffness designs and computational efficiency make the traditional approach reliable in yielding desired designs. Furthermore, thin member formations are observed, as highlighted in Fig. 5.13(b) of the MBB case using adaptive refinement, while this is not observed in the Cantilever and L-beam cases using adaptive refinement. However, the traditional 2.5D SIMTP is free from all these pathologies, making it a preferred approach for certain cases, especially when dealing with islanding and thin member formations.

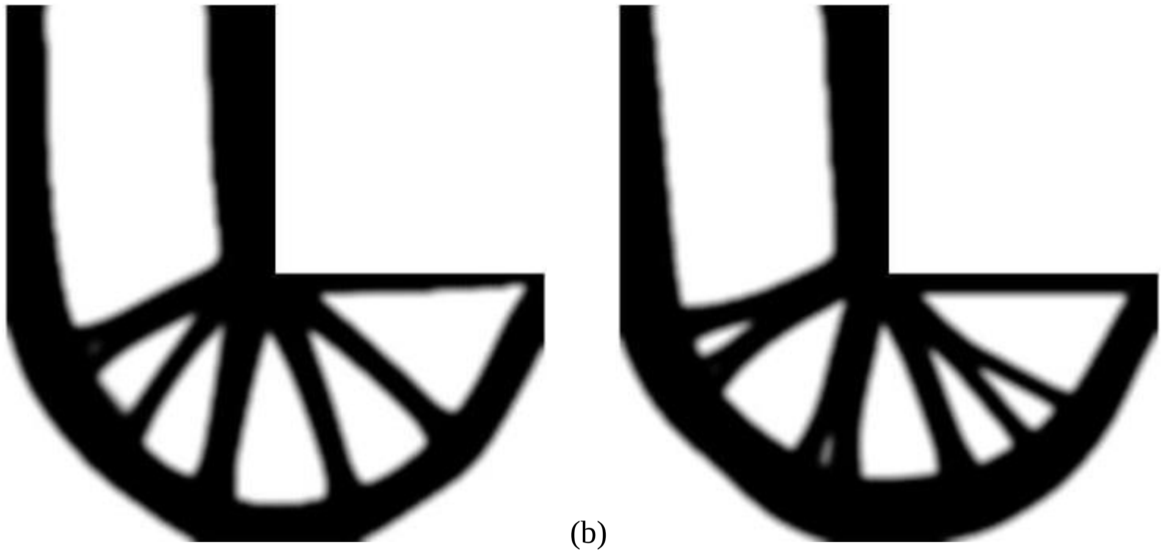

(a) (b)

Figure 5.14: Pixels of L- beam. (a) C6 and (b) C7

Overall, this section presented interesting outcomes of using adaptive refinement and provided valuable information on 2.5D SIMTP. The results highlighted the significance of using a higher initial threshold, gradual penalty, and thickness filtering in 2.5D SIMTP, which can improve the convergence and stability of the optimisation process. Moving to the next section sums up the important remarks noticed in this chapter.

5.4 Remarks

This chapter presented a successful introduction and development of an adaptive refinement strategy for 2.5D elements based on Jacobian estimations. The quadtree refinement technique is used with a 1-irregular rule, and FE analysis is performed on an analysis mesh separated from the design mesh, which is used for design parametrisation, thickness filtering, and pixel extraction. A simple thickness mapping technique based on Shepard interpolants is used to accurately evaluate thickness at the children's nodes, resulting in reliable approximations. The constrained approximation is used to solve the system of equations and to obtain the deformations at hanging nodes. Separate analysis and design meshes are used to reduce the computational burden of the optimisation process on refinement [95,97]. The adaptive 2.5D SIMTP results explored in this chapter provided valuable insights into the various aspects of the tool:

I. The implementation of an adaptive refinement process into the 2.5D SIMTP enabled an initial threshold as low as 10^{-3}, allowing for a more detailed analysis of the design space.

II. The explored beam examples demonstrated the importance of thickness filtering for achieving stable Jacobian, which is essential for preventing "islanding" and achieving practical designs.

III. "Islanding" is a phenomenon observed in the 2.5D SIMTP when thickness filtering is not performed in the refinement process, leading to impractical designs. However, the use of adaptive refinement with thickness filtering can prevent "islanding" and lead to more practical designs. In some cases, the use of thickness filtering may lead to thin member formations, highlighting the importance of careful design considerations and balancing structural performance with manufacturing feasibility.

IV. In comparison to adaptive refinement, the traditional 2.5D SIMTP approach, which employs a higher initial threshold and gradual penalty, can be a more reliable and efficient method for producing practical designs, especially when computational resources are limited and the design space is well understood.

The present and previous chapters have covered the performance capabilities, numerical benefits, and limitations of 2.5D SIMTP. The primary objective of this thesis is to develop an optimisation tool that seamlessly connects structural design, architectural expression, and manufacturing. To achieve this objective, the 2.5D SIMTP was created, which enables the use of the architectural expression as the initial design sample. However, to better understand the behaviour of 2.5D SIMTP under various conditions, the present and previous chapters focused on analysing beams with a unit thickness (2D) and compared pixels. Therefore, the following chapter will delve into the practical and true application of 2.5D SIMTP in managing the design evolution of a parametric surface expression and the manufacturing process. Furthermore, the chapter will compare the performance of 2.5D SIMTP to alternative 3D optimisation setups. Specifically, the chapter will present a comparison of voxels to demonstrate the effectiveness and efficiency of 2.5D SIMTP in handling non-prismatic geometries.

Chapter 6

Surface Fetching and 3D Printing

In traditional topology optimisation methods, density is often used as a design variable in 2D, resulting in pixelated outputs that do not take into account element or nodal variables. Although 2.5D SIMTP has been shown to produce high-resolution images in previous chapters, the beams explored are unit thickness problems, meaning that the outputs are still limited to pixels. However, pixels alone do not provide enough information for manufacturing optimised structural components. Therefore, in the case of SIMP, 3D optimisation is necessary to generate either voxels or STL outputs, while 2.5D SIMTP can produce either pixels or voxels (specifically surfaces) within the design space limits. This chapter explores the further capabilities of 2.5D SIMTP by (a) solving 3D problems and comparing them with alternative 3D optimisation methods and (b) 3D printing a beam prototype that was optimised using 2.5D SIMTP. The optimisation methodology in this chapter follows the same approach discussed in Chapter 4 but with the inclusion of thickness as a design variable. As shown in Fig. 6.1, “top211” (provided in Appendix B) was modified to incorporate thickness as a design variable, where "*th*" represents the model's thickness. This modification enables 2.5D SIMTP to optimise not only the topology but also the thickness of the beam, resulting in a more comprehensive optimisation process. The optimised design can then be 3D printed to produce a prototype.

(a)

```
18    V0=a*b;
43    V0=(a*b-c*d);
135   else,   dch=0.001;  dv1=repmat(ez*ez*w*(E0-Em),et,1);  dv=L(f(dv1'));
153   C=U'*K*U;dt=pn*(E0-Em)*xs(ep).^(pn-1).*w;
186   tp=(Em+xs(ep).^pn*(E0-Em));
199   tn=Em+xs(ep)*(E0-Em);
```

(b)

```
18    V0=a*b*th;
43    V0=(a*b-c*d)*th;
135   else,   dch=0.001;  dv1=repmat(ez*ez*w*(E0-Em)*th,et,1);  dv=L(f(dv1'));
153   C=U'*K*U;dt=pn*(E0-Em)*xs(ep).^(pn-1).*w*th;
186   tp=(Em+xs(ep).^pn*(E0-Em))*th;
199   tn=(Em+xs(ep)*(E0-Em))*th;
```

Figure 6.1: Modifications of top211 for non-prismatic surfaces. (a) Unit thickness and (b) Absolute thickness

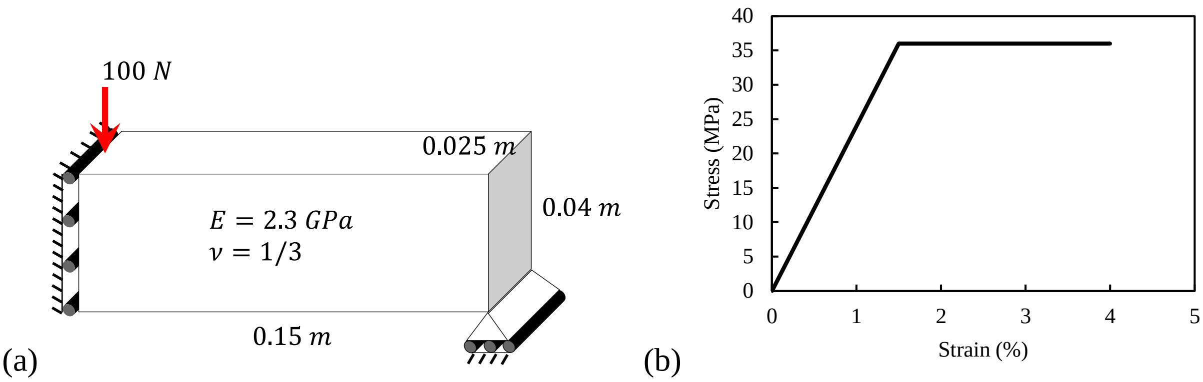

Figure 6.2: (a) Design space of beam prototype and (b) Stress-strain curve of ABS M30i

This chapter explores the MBB beam problem using 2.5D SIMTP and 3D SIMP. However, the design space of the beam and material properties are selected so that the prototype beam can be 3D printed in the PolyUs U3DP laboratory. The printer in this laboratory can only handle objects within a length range of 0.3 to 0.4 meters, and one of the readily available materials it uses is ABS M30i, a versatile and reliable material suitable for creating prototypes and manufacturing parts. It is worth mentioning that the optimisation model presented in this thesis is limited to elastic analysis. Considering these constraints, a simply supported beam with a span of 0.3 meters, a length-to-depth ratio of 7.5, and a width-to-depth ratio of 0.625 are selected to represent a practical design space. A load of 100 N is chosen such that it will limit the performance of the beam to the elastic range. A half model of this beam, along with ABS M30i material properties, is presented in Fig. 6.2. The following section explores various cases based on these inputs to compare the surfaces produced by 2.5D SIMTP and the voxels produced by 3D SIMP. Additionally, a surface fetching case is demonstrated to showcase how an architectural expression can be incorporated into the optimisation process as an initial design.

6.1 Comparison of Surface and Voxels

This section aims to explore the advantages of using 2.5D SIMTP over other 3D optimisation methods, such as SIMP. The optimisation process was conducted within the elastic range of ABS M30i material, and only the symmetric right half of the beam was modelled in 2.5D and 3D. Six case studies were conducted, with C1 to C2 being 2.5D SIMTP cases and C3 to C6 being 3D SIMP cases. These cases were designed to meet specific standards and logical comparisons: C1: A traditional 2.5D SIMTP case that begins with full material occupancy. A sufficient mesh size was used to avoid the pathologies of the 2.5D element. C2: A demonstration of surface fetching with 80% material occupancy. C3: Total number of degrees of freedom consistent with C1 and having a single element in the thickness direction. C4: Total number of degrees of freedom consistent with C1. C5: Element size consistence with C1 but having a single element in the thickness direction. C6: Element size consistence with C1.

It has been previously established that the development of the 2.5D element is based on a single element in the thickness direction. Therefore, cases C3 and C5 were studied with a single element in the thickness direction, which is consistent with the number of degrees of freedom and element size, respectively. Most importantly, cases C3 and C4 were investigated to compare computational standards, while C5 and C6 were analysed to compare the resolution of 3D SIMP with 2.5D SIMTP. Overall, these cases were logically organised to compare the various aspects of 2.5D SIMTP and 3D SIMP, particularly in terms of computational efficiency and optimised shapes.

Because the 2.5D element is based on the 3D serendipity element, 3D SIMP cases were analysed using twenty-noded serendipity elements. While any FE software, such as ABAQUS, can explore 3D SIMP cases, it is more logical to compare the results with a well-established 3D SIMP code, preferably on MATLAB. However, open-source optimisation tools based on the serendipity element are not readily available. As a result, the authors modified the top3d [183] optimisation tool to incorporate MBB beams and 3D serendipity elements, resulting in a 145-line MATLAB code, named "topMBB3D20N," which is provided in Appendix D for reference. Case C6 has a large number of nodes, which require substantial computational space and effort for direct matrix inversion. Therefore, lines 102 to 109 of the modified code introduce an iterative procedure to handle larger matrices.

Obtaining a 0-1 solution without intermediate values is a major challenge when using 3D SIMP. To address this issue, a display threshold is used in addition to the initial threshold. The initial threshold is part of the analysis, while the display threshold is used to omit elements from the display. The remaining elements are set to unit densities to generate boundary surfaces. In the 3D SIMP models, element densities less than 50% material occupancy were removed from the display, as suggested in top3d [183]. This display threshold is much higher than the combined initial and display thresholds of 2.5D SIMTP. However, after removing these intermediate elements, a smoothing function is necessary to construct the surface before converting it to an STL for manufacturing purposes. It is worth noting that the comparisons in this section were conducted without any post-processing techniques. As a result, the 3D SIMP outcomes are limited to unsmoothed voxels, which is why this section only compares them with the optimised surfaces from 2.5D SIMTP. Furthermore, the optimised surfaces obtained from 2.5D SIMTP are straightforward, implying that they do not require any additional techniques for surface construction or post-processing. The initial design candidates for cases C1 and C2, presented in Fig. 6.3, align with the definition and assumptions of the SIMTP, as discussed in the introductory chapter of SIMTP. Case C2 features a parametric surface as an initial design to demonstrate that any architectural expression of the surface can be incorporated into the optimisation process to yield stiffness solutions that meet the structural design criteria.

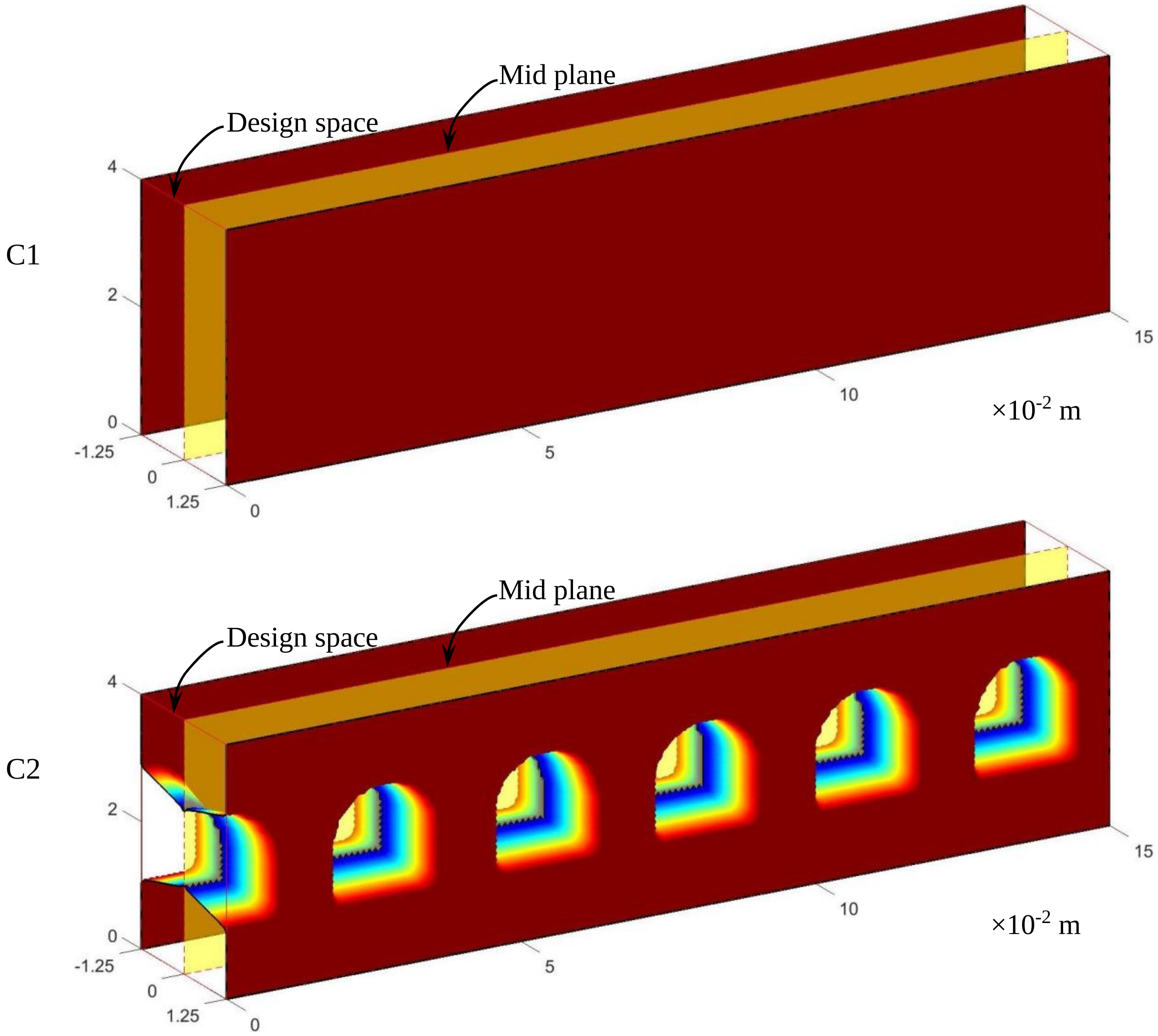

Figure 6.3: Initial design - flat and parametric surface

Tab. 6.1 presents the parameters and outcomes of the cases discussed above, which were optimised for 50% material occupancy using the OC method on an Intel Xeon W-2155 processor with 64GB RAM. Despite utilising a high-performance system, optimisation was only performed up to 50 iterations due to the considerable computational demand of the large models. It is worth noting that while previous chapters explored 2.5D SIMTP with a gradual penalty increment of 0.05, this chapter increased it to 0.075, which is within the proposed limits. This penalty increment was necessary to generate practical designs while taking into account changes in the size of the design space and a reduced number of iterations.

Table 6.1: Model discretisation, parameters, and outcomes

Opt. Meth.	e_z ($\times 10^{-2}$ m)	Nodes	Total Dofs	r_z	Th. (%)		Penalty			After 50 iterations	
					In.	Dp.	Min.	Max.	Δp	Comp. ($\times 10^{-2}$ N-m)	time (s)
C1 SIMTP	0.1	18,381	36,762	1.5	5	1	1	3	0.075	5.91	37
C2 SIMTP	0.1	18,381	36,762	1.5	5	1	1	3	0.075	6.11	39
C3 SIMP	0.19	12,116	36,348	1.5	10^{-7}	50	3	3	0	7.04	56
C4 SIMP	0.3825	13,232	39,696	1.5	10^{-7}	50	3	3	0	7.33	99
C5 SIMP	0.1	42,953	128,859	1.5	10^{-7}	50	3	3	0	6.49	NA
C6 SIMP	0.1	632,681	1,898,043	1.5	10^{-7}	50	3	3	0	5.68	NA

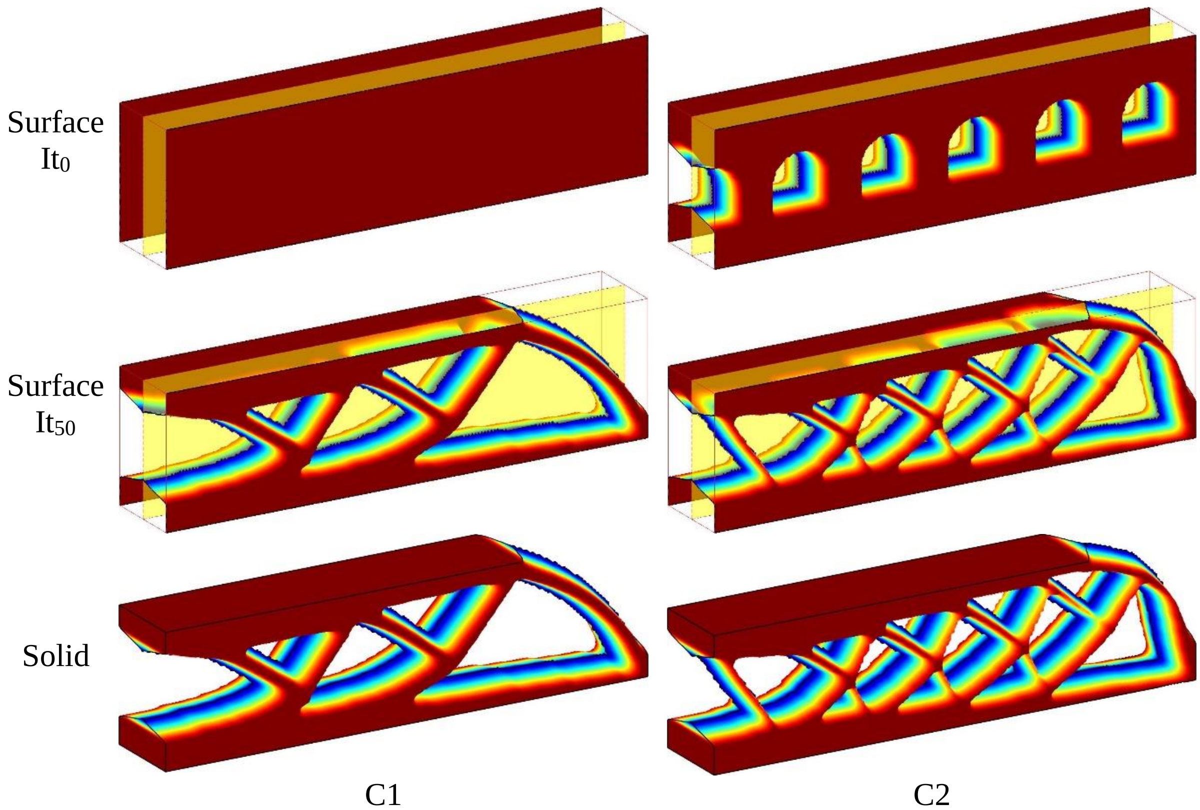

Figure 6.4: Solid volume from a surface boundary

The optimised surfaces of cases C1 and C2 are noteworthy, as depicted in Fig. 6.4. The figure displays the evolution of the surfaces after removing the parts below the set display threshold of 0.01 for full and 80% (surface fetching) occupancy cases after 50 iterations and highlights how these surfaces can be easily stitched at the boundaries to form solids for subsequent comparison with 3D SIMP shapes. Additionally, Fig. 6.6 illustrates the material occupancy across iterations, revealing that C1 and C2 achieved the occupancy criteria in six and four iterations, respectively.

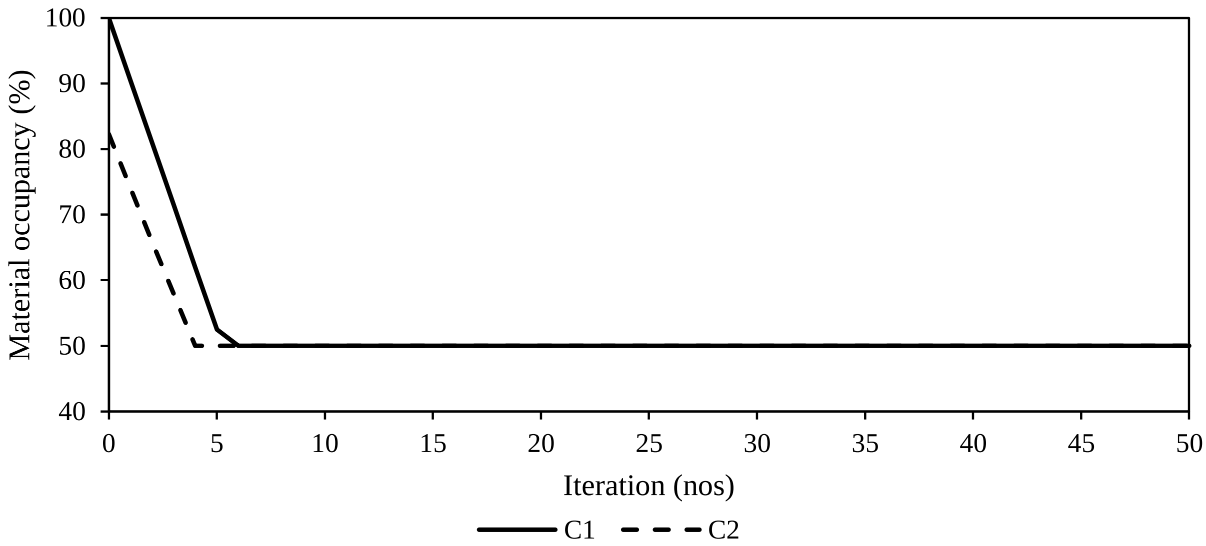

Figure 6.5: Comparison of material occupancy

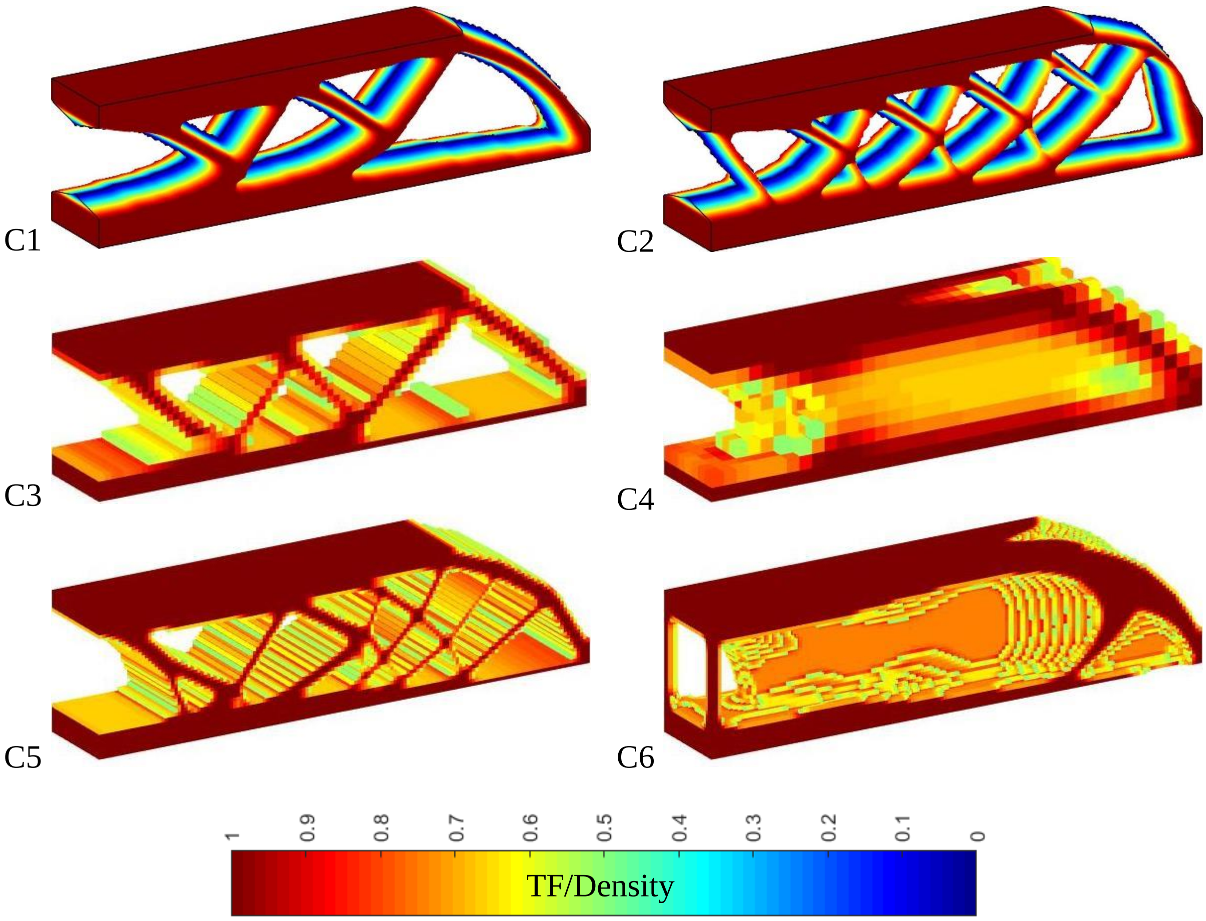

Figure 6.6: Optimised profiles

Fig. 6.6. This comparison has shown that the 2.5D SIMTP shapes have a better boundary description than 3D SIMP cases. The single-element 3D SIMP cases C3 and C5 demonstrate practical design scenarios, unlike the uniform coarse and fine mesh cases C4 and C6, which have resulted in impractical designs. These outcomes require further attention and rigorous post-processing using surface construction techniques to achieve practical shapes. The tabular data of compliances indicates that the 3D SIMP cases C3 to C5 have yielded high stiffness solutions compared to C1. Although C6 has recorded the lowest stiffness solution against its alternative cases, this is not the only criterion that makes the shape feasible. The optimised profiles of C3 and C5 are similar to C1 and C2, respectively. However, voxelised 3D SIMP cases exhibit bad and aesthetically unappealing voxels. The computational costs of cases C5 and C6 are not summarised in the tabular data since these cases are computationally expensive, making them unsuitable for comparison. Further observations of computational efficiency reveal that 2.5D SIMTP cases have exhibited superior performance over their alternative SIMP cases C3 and C4. Overall, the comparison indicates that 2.5D SIMTP has a significant edge over 3D SIMP in achieving high-resolution shapes while utilising significantly less computational effort than 3D SIMP cases C3 and C4. The 2.5D SIMTP cases C1 and C2 exhibit distinct shapes led by unique initial design candidates, with only slight differences in performance.

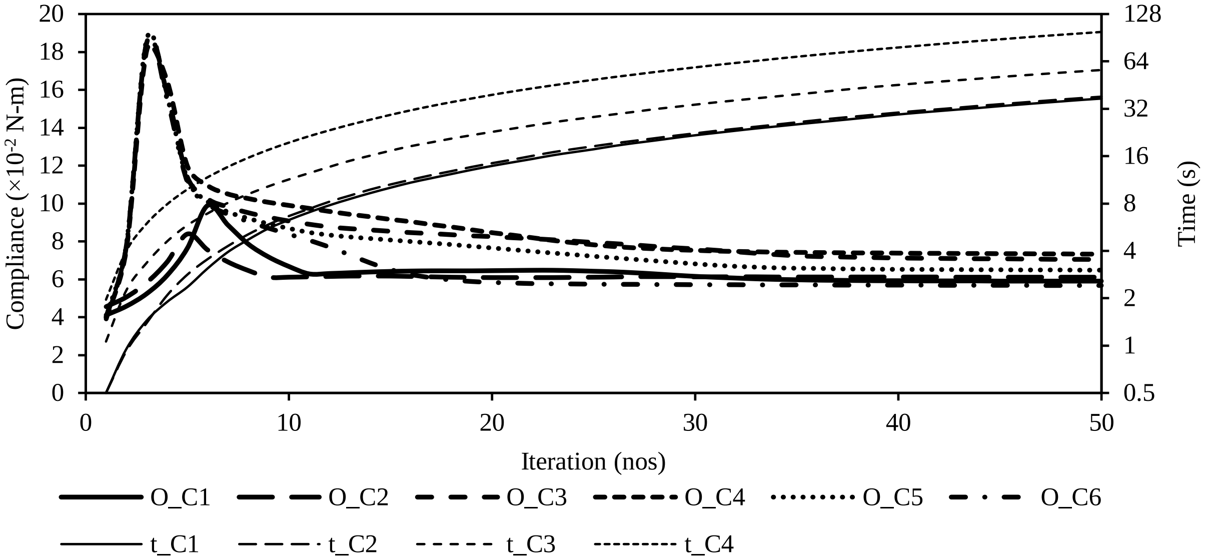

Figure 6.7: Performance comparison

The tabular observations are reinforced by comparing the stiffness solutions and computational time across the iterations, as depicted in Fig. 6.7. For clarity, only the computational costs of cases C1 to C4 are compared, while stiffness solutions are plotted for all cases. The figure uses the nomenclature O_X and t_X to represent the compliance and computational time of case X, respectively, and the computational time is plotted on a logarithmic scale of base 2 for better visualisation.

In summary, this section discussed the advantages of 2.5D SIMTP over 3D SIMP in terms of computational efficiency and practical designs for manufacturing purposes. While 2D SIMP is computationally efficient, it compromises resolution and requires design imagination to convert pixels into a manufacturable entity [56]. The various cases studied in this section are designed to accommodate both 2.5D and 3D optimisation cases by ensuring consistency in the number of degrees of freedom and discretisation, including the use of single and multiple elements in the thickness direction. However, 2.5D cases are limited to a single element due to their fundamental formulation, which restricts exploration with multiple thickness elements. Future research will aim to explore 2.5D cases with multiple thickness elements as an objective by refining modelling assumptions and addressing computational complexity to achieve this goal. It would be an interesting scenario if 2.5D cases could be explored with multiple thickness elements, as this approach could help to capture more realistic and accurate behaviour of structures that may have varying thicknesses or material properties in different directions.

The section also demonstrated a surface fetching case using 2.5D SIMTP, which is one of the aspirations of the tool discussed prior to its development. This demonstrates how an architectural vision can be integrated into structural design. However, a full scenario of this, considering practical construction aspects and limitations, is yet to be explored. The surface fetching case presented in this is just a model demonstration that will be extended to include practical scenarios in future studies.

In the full material occupancy and surface fetching cases, interesting and distinctive shapes were obtained, with the former resulting in a simple truss-like shape that is easy to manufacture and exhibits slightly better performance than the surface fetching case. Given its simple shape characteristics, the C1 shape outcome was selected for the prototype 3D printing using ABS M30i. In the upcoming section, a prototype printing of this beam will be demonstrated by providing details on the development process, such as STL and FE modelling, as well as the analysis and results obtained prior to printing.

6.2 Prototype 3D Printing

This section showcases a 3D printed model of the optimised shape of the C1 case from the previous section, printed using ABS M30i material. It has been emphasised multiple times previously that the optimisation tool used in this thesis is limited to elastic analysis. Although the design load on the beam cases demonstrated earlier was chosen carefully to remain within the elastic range of the material, it is crucial to test the shape beyond its design load to gain insights into its structural behaviour and robustness before manufacturing. Documenting this testing process is essential, even though the 3D printed case in this section is only for display purposes. In practical engineering applications, such testing must be conducted rigorously to check for ultimate and serviceability limit states, paving the way for cross-validating experimental performance with numerical procedures to ensure reliability in real-world use.

To perform ultimate strength analysis on the optimised shape of the C1 case, the solid body created in the previous section must be processed to contain the patch data required for FE modelling in ABAQUS. This is because non-linear numerical analysis is easier to perform on established platforms. Therefore, the boundary surface of the solid created in the previous section is examined for further processing, as shown in Fig. 6.8. The highlighted region is magnified, revealing kinks at the boundary lines due to the triangulation method used to represent the patch data.

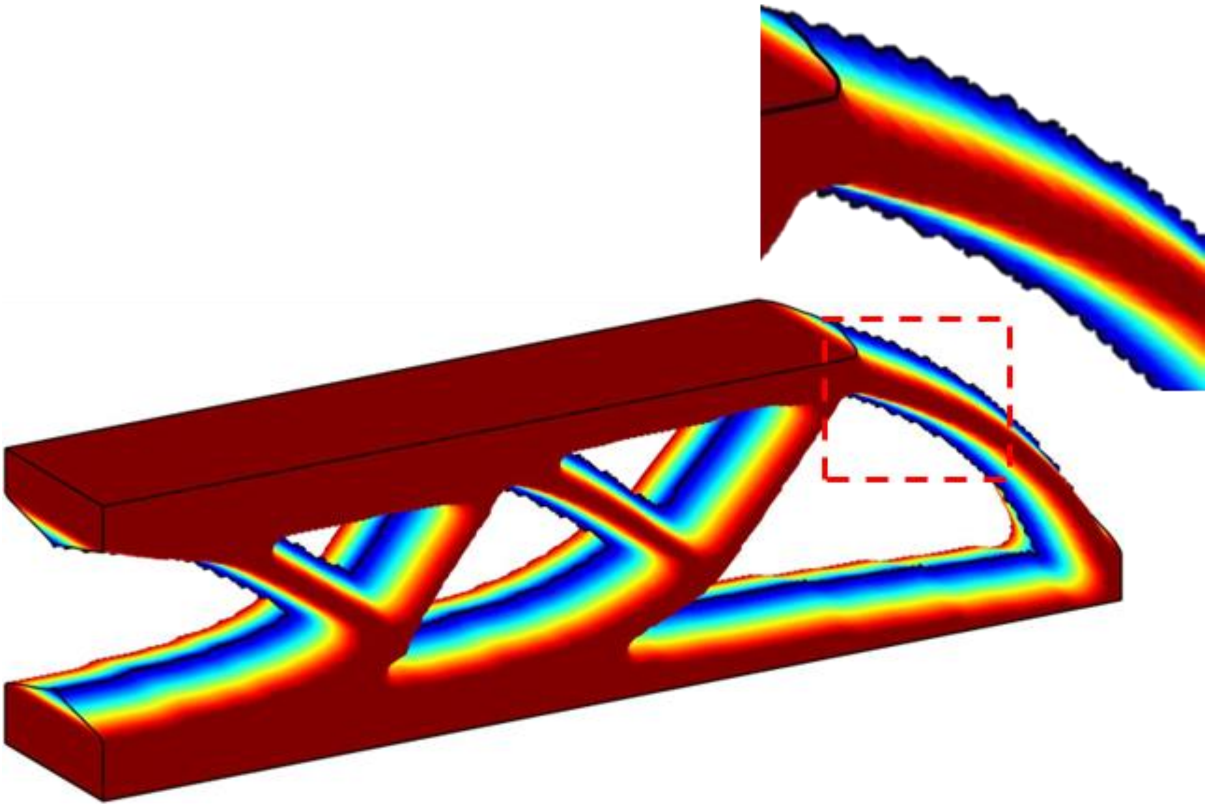

Figure 6.8: Surface boundary inspection

To eliminate the kinks highlighted in the previous figure, the solid model was converted into an STL file using an open-source MATLAB code called stlwrite [203]. The half-solid model was mirrored to create a full model, which was then processed to smooth out the kinks using the STL file format. This smoothed model is now suitable for use in finite element modelling, numerical analysis, and manufacturing applications. The solid (STL model) after smoothing from the above process is illustrated in Fig. 6.9.

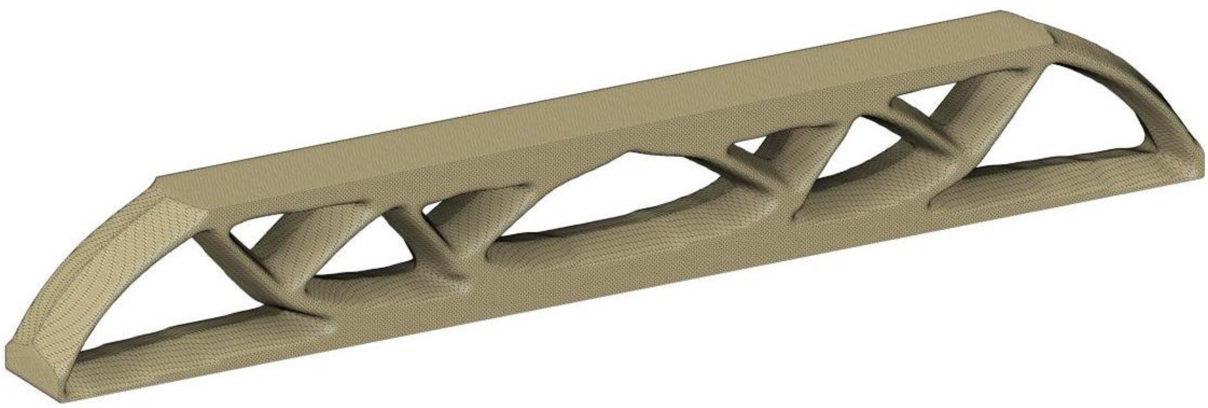

Figure 6.9: STL model of beam prototype

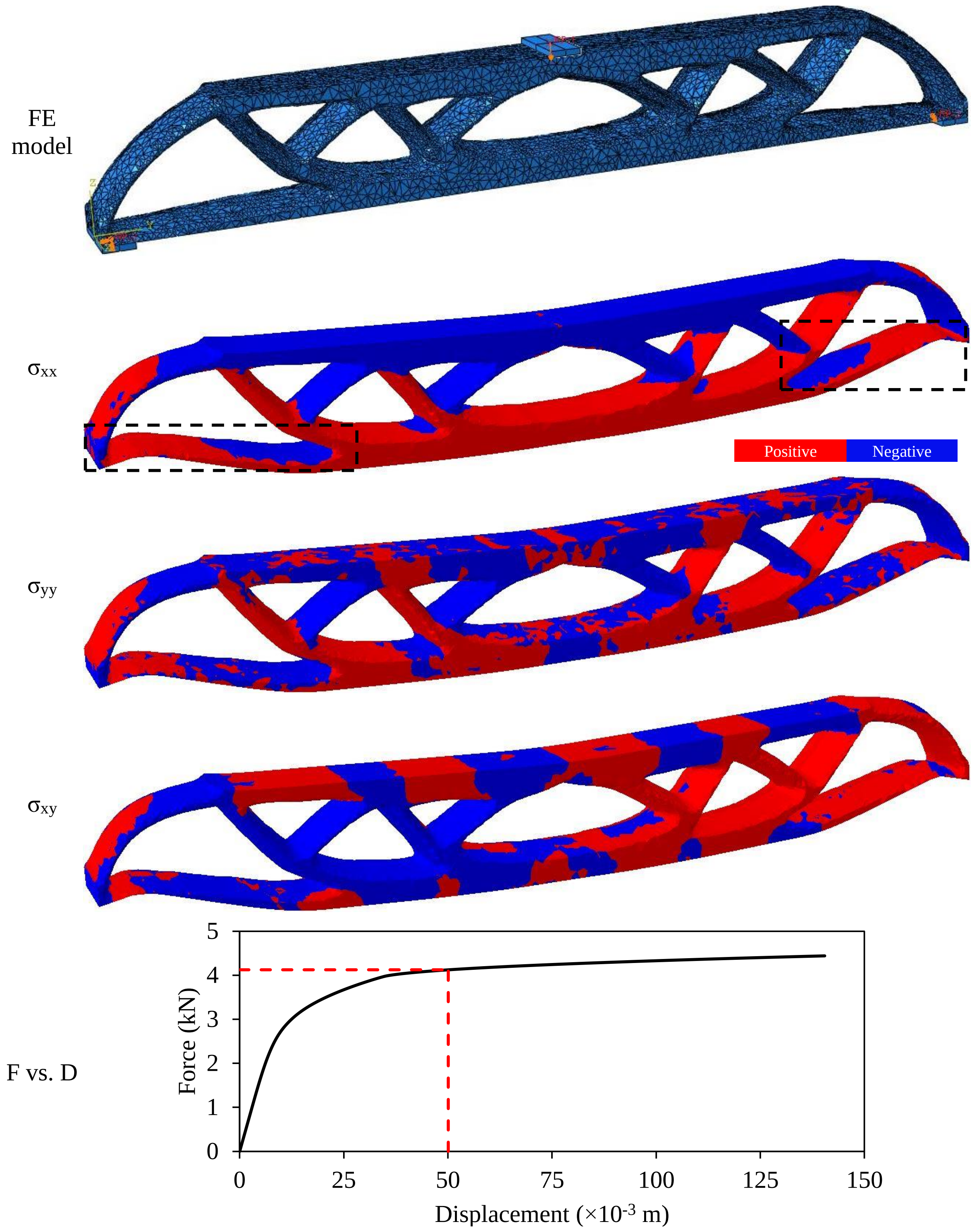

Figure 6.10: Ultimate displacement analysis and stresses

The solid model created from the smoothed STL file (in Fig. 6.9) was exported for FE modelling and ultimate displacement analysis using the non-linear material properties of ABS M30i, as described at the beginning of this chapter. The FE model and numerical analysis results, including stress contour outputs at a midspan deflection of 0.05m (50mm, one-sixth of the beam's span) and force-displacement data, are presented in Fig. 6.10. The force-displacement data shows that the optimised shape designed for 100 N falls within the elastic range of the material. However, the deformed stress contour data, magnified three times in the downward direction, reveals an unusual bending, as highlighted in the figure, which is unlikely for flexural members. This bending is due to the truss-type design of the beam, as the shear stress contour data shows a reversal of stresses in the highlighted region, which may be the reason for the local bending phenomenon.

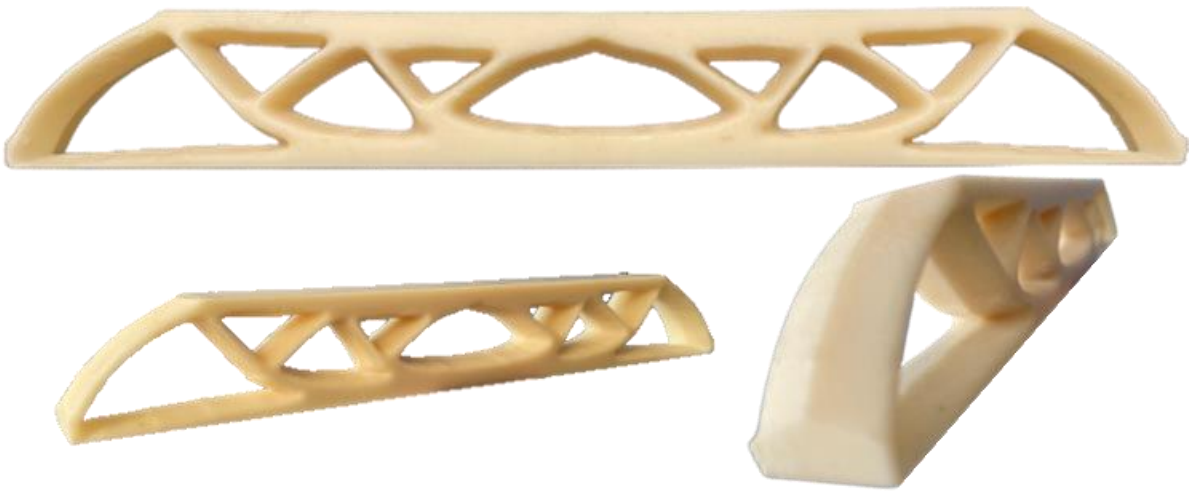

Figure 6.11: 3D printed beam prototype

The FE analysis results provided crucial insights into the optimised design of the beam, giving confidence that it is safe and reliable for manufacturing. To bring the design to life, the previously generated STL model was used to print a prototype model of the beam at the PolyUs U3DP laboratory using the ABS M30i material. The process was carefully documented, highlighting the various stages of the 2.5D SIMTP design optimisation process, from the initial design requirements to the design parameterisation, engineering analysis, and final manufacturing. The finished prototype, showcased in Fig. 6.11, is a testament to the success of the SIMTP design optimisation process, demonstrating how advanced tools and techniques can be used to create complex and high-performance structures. However, it is important to note that the tool and examples explored in this thesis are just a preliminary step in the process of creating real-life designs that consider all structural design and construction aspects. The ecosystem of the 2.5D SIMTP is illustrated in Fig. 6.12, providing a visual representation of the series of events involved in the design and manufacturing process.

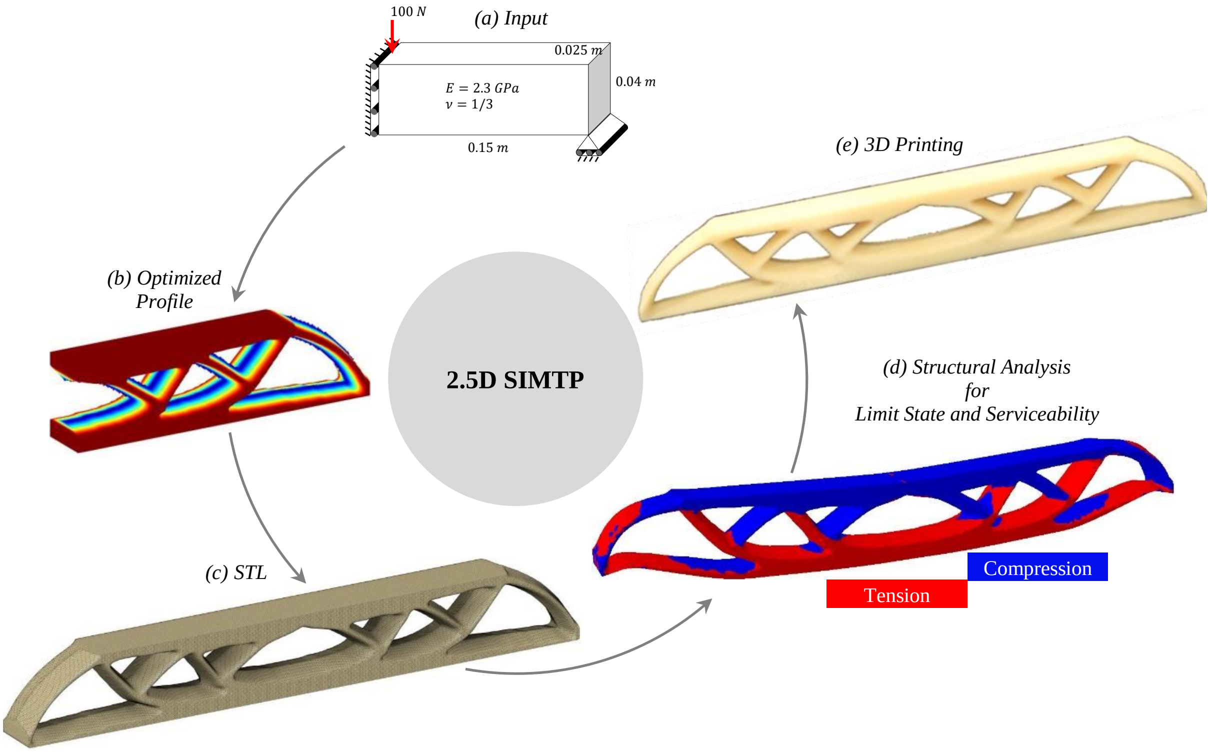

Figure 6.12: 2.5D SIMTPs ecosystem

This section has demonstrated the process of printing a prototype using an optimised model, which involves creating an STL file for FE modelling, analysis, and manufacturing. The successful completion of this step fulfils one of the objectives of the thesis. Additionally, significant observations and findings from this process are listed and will be discussed in the next section.

6.3 Remarks

This chapter has successfully demonstrated and achieved a part of the objectives set for this thesis. Despite the limitations and technical adjustments, the introduced 2.5D SIMTP has showcased the interaction of optimisation and manufacturing at a prototype level. While still in the theoretical stages, it is clear that architectural design can be considered as the initial design cycle, which is demonstrated through a surface fetching case. However, full-scale testing is yet to be explored, including non-linear dynamic analysis under various loading and material conditions, considering limit and ultimate state designs and serviceability scenarios. Additionally, full integration modelling of architecture expressions and optimisation is needed, along with full-scale building manufacturing. Despite the above shortcomings, there are some significant remarks to be made:

I. 2.5D SIMTP has a relatively low threshold requirement, which is negligible compared to the high threshold required by 3D SIMP. Additionally, 2.5D SIMTP requires less post-processing to obtain smooth surfaces for manufacturing compared to 3D SIMP.

II. Using a single element in the thickness direction of 2.5D SIMTP or 3D SIMP results in a truss-like design, while using multiple elements in 3D SIMP can lead to complicated designs that require rigorous post-processing.

III. 2.5D SIMTP has the ability to produce high-resolution pixels or voxels based on the design space limits. In contrast, 2D SIMP is limited to pixels that require design imagination, while 3D SIMP is limited to voxels that require rigorous post-processing techniques for manufacturing purposes.

IV. 2.5D SIMTP requires relatively less computation time than 3D SIMP to generate the 3D surface, and it also requires less effort for post-processing, making it a straightforward and efficient approach to structural design and optimisation.

This chapter has highlighted the potential benefits and limitations of 2.5D SIMTP, particularly in comparison to 3D SIMP methods. The tool has been shown to integrate architectural vision into structural design and has the potential to create unique and interesting shapes through material initial occupancy and surface fetching cases. However, the previous chapters have only explored benchmark problems using fictitious or non-construction materials to address potential issues and demonstrate the capabilities of 2.5D SIMTP.

Therefore, the use of 2.5D SIMTP with construction materials is an area that requires further exploration. Although the literature review has identified prestressing and fibre reinforcement as the best alternatives to ensure the ductility requirements of printed concrete structures, the rheology of fibre reinforcement in this context is yet to be explored. The next chapter will investigate the use of prestressing systems with 2.5D SIMTP to address this issue. Future studies will continue to expand on these findings and explore the potential for 2.5D SIMTP to be used in practical scenarios.

Chapter 7

Optimisation of Prestressed Concrete Beams

The previous chapter highlighted the potential benefits and limitations of 2.5D SIMTP in comparison to 3D SIMP methods, and it was noted that further exploration of 2.5D SIMTP with construction materials is needed. Prestressing and fibre reinforcement were identified as potential alternatives to ensure the ductility requirements of printed concrete structures based on the literature review [56]. Therefore, this chapter aims to demonstrate how 2.5D SIMTP can be used to optimise prestressed concrete beams.

Amir and Shakour [164] discussed interesting aspects of prestressed beam modelling and simultaneously optimised tendon layout and concrete topology. FE modelling is necessary to optimise a prestressed beam using optimisation techniques. Further, it is crucial for simulating the beam's material, loading, boundary, and interaction conditions. However, modelling prestressed beams differs from standard beams, as they require modelling techniques that reflect the active and passive stress states of the reinforcement. Specifically, stresses in passive reinforcement get activated after loading, while different modelling strategies are necessary for modelling the upward thrust and anchorage forces due to prestressing. There are several ways to represent these conditions, and the choice of modelling technique depends on the expected outcomes [204].

Previous research by Amir and Shakour [164] and Zhang et al. [14] has modelled prestressing force based on the principle of virtual work. The former estimated internal prestressing forces from the tendon geometry in a piecewise manner, while the latter built the tendon geometry using NURBS curves and estimated the internal forces from the tendon's curvature. The estimated forces at the tendon level were then transferred to the nearest concrete nodes using a mapping scheme. In [164], the anchorage force was applied as a concentrated external force, while in [14], it was applied as a distributed force to avoid stress concentration. The authors modelled the right symmetric half of the beams and provided sliding supports throughout the height of the beam.

The research by Amir and Shakour [164] inspired the "OptiBride" project [54], as discussed in the literature review. This chapter also takes inspiration from their work and includes a few more aspects to model prestressed beams for optimisation purposes. The prestressing scheme in this chapter is similar to the concept discussed earlier, with the tendon geometrically described through Bezier curves. The following section will discuss this scheme in more detail, including the idealisation of the tendon's geometry in the concrete domain and the transfer of prestress.

7.1 Tendon Geometry and Transfer of Prestress to Concrete

This section discusses various modelling aspects of prestressed beams, including concrete and tendon geometry, strategy for transferring prestressing forces to concrete, and loading and boundary conditions. As discussed earlier, the prestressing scheme employed in this chapter follows a similar concept, with the tendon geometrically described through Bezier curves.

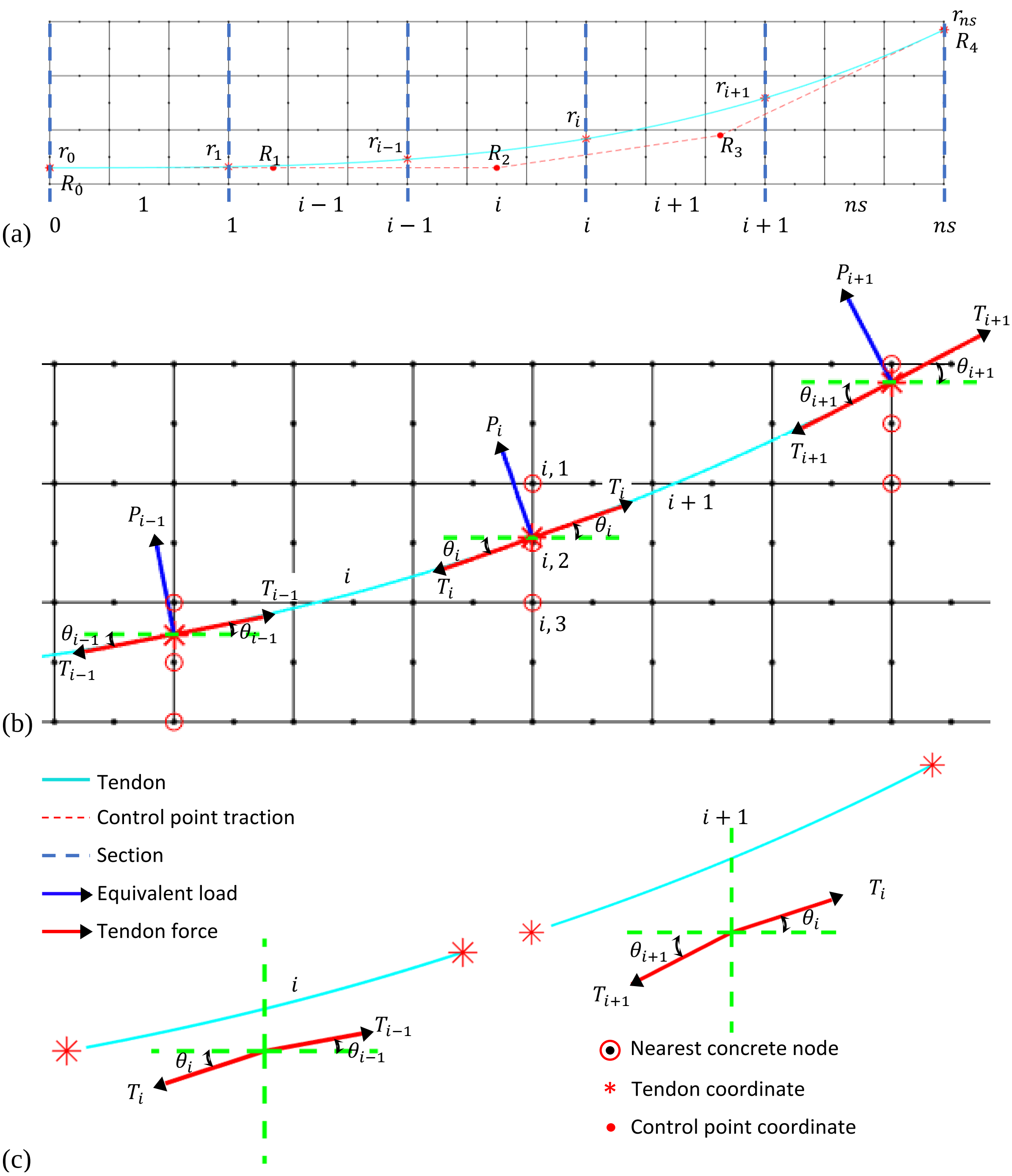

Figure 7.1: Transfer of prestress to concrete. (a) Tendon geometry; (b) Equivalent force; (c) Tendon forces

In Fig. 7.1, the tendon geometry using the Bezier definition was built using horizontally restricted control points. Geometrical coordinates of the tendon were extracted at the sections marked in Fig. 7.1(a), placed at every third element in the horizontal direction. It is important to note that the vertical position of tendon points will not exceed the extreme positions of control points, while control points move within the height excluding the nominal cover of the beam, thus positioning the tendon inside the concrete domain (refer to Fig. 7.2). The Bezier curve definition, presented in Eq. (7.1), is used for determining the coordinates and gradients of the tendon at any section. The gradient at a section is then used to estimate the equivalent force on the beam based on equilibrium conditions [205].

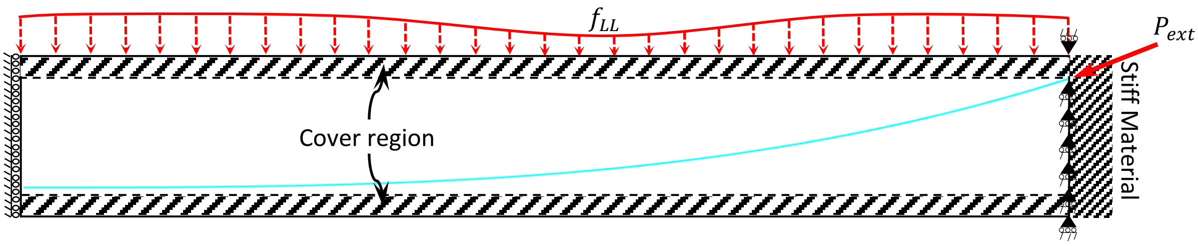

Figure 7.2: Modelling of prestressed beams

$$\begin{aligned}
&\forall i \in Z_{[0,ns]}: t_i = \frac{i}{ns} \\
&\forall i \in Z_{[0,ns]}: r_i = \sum_{j=0}^{nc-1} \binom{nc-1}{j} (1-t_i)^{nc-1-j} t_i^j R_j \\
&\forall i \in Z_{[0,ns]}: \frac{\partial r_i}{\partial t_i} = \tan\theta_i \\
&= (nc-1) \sum_{j=0}^{nc-2} \binom{nc-2}{j} (1-t_i)^{nc-2-j} t_i^j (R_{j+1} - R_j)
\end{aligned} \tag{7.1}$$

Fig. 7.1(b) and Fig. 7.1(c) depict the distribution of tendon force and equivalent concrete force. The equivalent force at the tendon point near i^{th} section is determined from the contribution of tendon forces from the i^{th} and $i+1^{th}$ segment. The difference in tendon forces in a segment is distributed to the nearest tendon points, and the equilibrium of these forces at the tendon points results in equivalent forces distributed to the nearest concrete nodes, as shown in Eq. (7.2). The anchorage forces are then applied as a concentrated force, and as shown in Fig. 7.2, a relatively stiff material is provided at the support edge to avoid stress concentration. Further sliding supports are provided throughout the height to simulate the anchoring effect [164]. The process of transferring prestress is easy to implement and does not require complex mapping processes, as seen in [14].

$$\forall i \in Z_{[0,ns]}:$$

$$\begin{cases} P_{x,i} = \frac{1}{2}(T_i \cos\theta_i - T_{i+1}\cos\theta_{i+1}) + \frac{1}{2}(T_{i-1}\cos\theta_{i-1} - T_i \cos\theta_i) \\ P_{y,i} = \frac{1}{2}(T_{i+1}\sin\theta_{i+1} - T_i \sin\theta_i) + \frac{1}{2}(T_i \sin\theta_i - T_{i-1}\sin\theta_{i-1}) \end{cases} \tag{7.2}$$

$$\forall i \in Z_{[0,ns]}: \begin{bmatrix} P_{i,1} \\ P_{i,2} \\ P_{i,3} \end{bmatrix} = \begin{bmatrix} L_1 \\ L_2 \\ L_3 \end{bmatrix} P_i$$

Where, ns is the number of segments, $\binom{nc-1}{j}$ is binomial coefficient, nc is number of control points, t_i is the scaling factor at i^{th} section, r_i is the tendon coordinate at i^{th} section, R_j is the j^{th} control point, θ_i is the gradient of the tendon at i^{th} section, P_i is the equivalent force at the i^{th} tendon coordinate, T_i is the tendon force at the i^{th} tendon coordinate, ($P_{i,1}$, $P_{i,2}$, $P_{i,3}$) are the equivalent forces at the i^{th} section concrete nodes, (L_1, L_2, L_3) are the shape functions of the quadratic three-noded line element. The following section will validate the modelling strategy for prestressed beams discussed so far, including the use of Bezier curves to describe the tendon geometry and the distribution of equivalent forces in the concrete domain.

7.2 Validation of the Modelling Strategy

To validate the efficiency of the prestressing modelling strategy discussed earlier, specifically the load transferring strategy, two simply supported beam examples are considered: (a) case I with an eccentric tendon and (b) case II with a linear tendon. The same beam used to assess the efficiency of the 2.5D element is used for validation purposes, with beam properties illustrated in Fig. 7.3. The beam has a size of 1 m × 0.1 m × 0.1 m and is subjected to a prestressing load of 1^{-3} N with an elastic modulus of 2.4 kPa and Poisson ratio set to zero. Only prestressing is applied to avoid complex calculations of analytical solutions. The symmetric right half of the beams is modelled using 20×4 2.5D elements, and the modelling results are compared with simple analytical calculations. These cases are simple to compare with analytical solutions, and thus there is no need to perform 3D analysis again. The goal is to validate the load-transferring strategy rather than test the elements themselves.

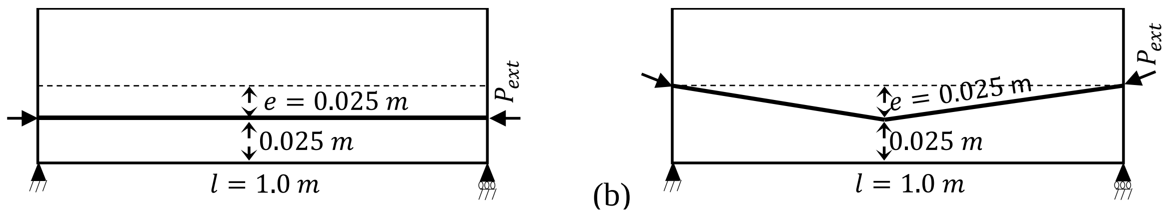

Figure 7.3: Beam properties. (a) case I; (b) case II

Table 7.1: Comparison of midspan upward deflections

Case	FEM	Analytical*
I (×10^{-4} m)	1.500	1.500*
II (×10^{-4} m)	1.025	1.024**

$*\delta = \frac{Pel^2}{8EI}$; shear deflection is zero (no variation in a moment)

$**\delta = \frac{P_{ext}el^2}{12EI} + \frac{kP_{ext}e}{AG}$; $k = 1.2$ [206]

Table 7.2: Comparison of top and bottom stresses at midspan

Case	FEM		Analytical*	
	Top	Bottom	Top	Bottom
I (×10^{-3} Pa)	50.030	250.150	50	250
II (×10^{-3} Pa)	47.821	262.918	50	250

$*\sigma = -\frac{P_{ext}}{A} \pm \frac{P_{ext}e}{Z}$

The results obtained from the mid-span for cases I and II are compared with analytical solutions. Tab. 7.1 compares the upward deflections of both cases with analytical calculations, while Tab. 7.2 compares the stresses at the top and bottom chords. It is worth noting that the deflections and stresses are in good agreement. The deviation of the recovered stresses from analytical solutions is observed to be higher for case II due to the upward thrust caused by the linear profile of the tendon that acts as a concentrated force at mid-span. However, this issue is minimal in the optimisation process because the first two control points (R0 and R1) are strategically located at the same height to ensure a smooth transition of the curve at mid-span, resulting in the absence of upward thrust. The recovered stress contours of the right half of the beams are presented in Fig. 7.4, and observations indicate no sign of stress concentration for normal stresses in the horizontal direction. However, the other stress contour data show signs of stress concentration, which is reasonable in the second case since the upward thrust caused by the linear tendon is a concentrated force at mid-span. In the first case, these stresses are negligible since the tendon is a straight layout with zero Poisson's ratio. The magnitude of these stresses is only 1% of the maximum horizontal stresses.

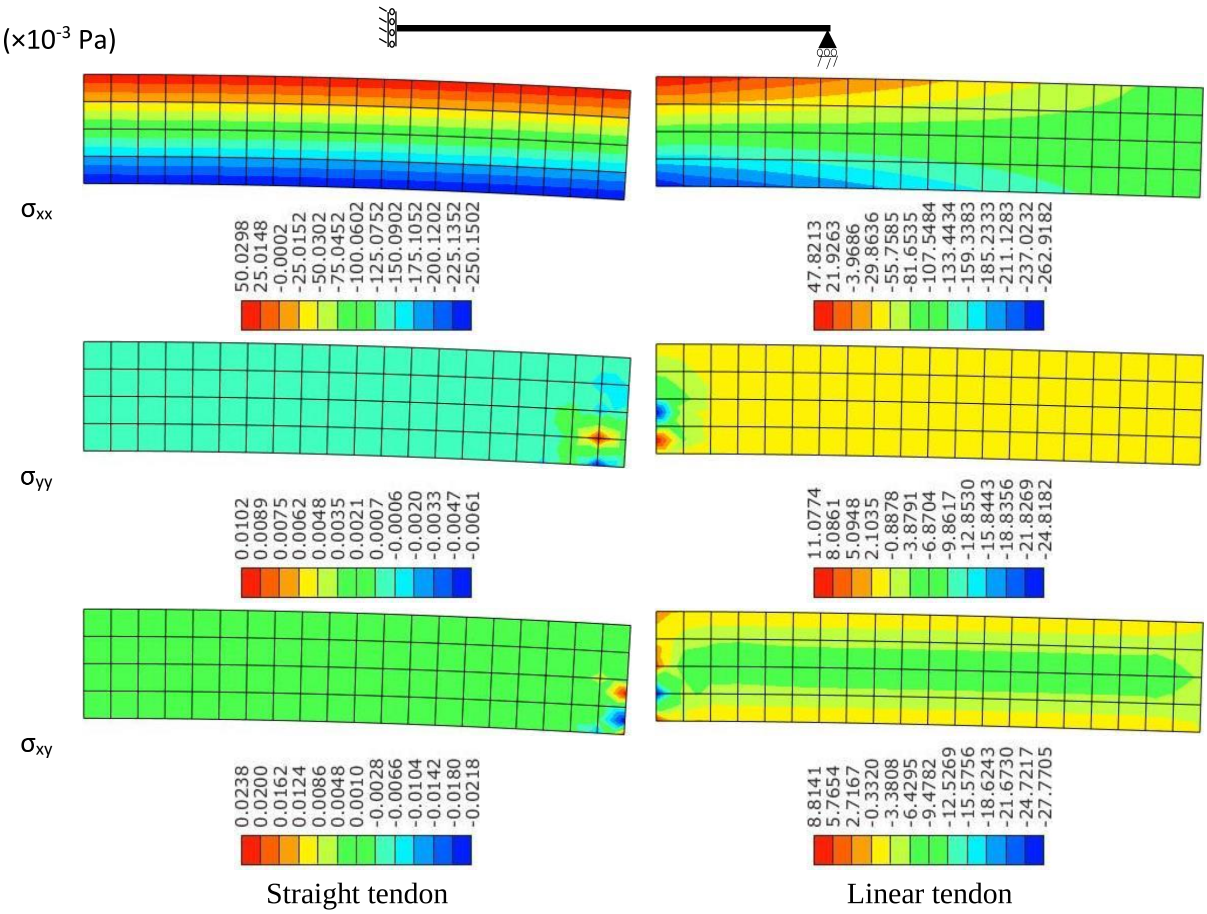

Figure 7.4: Recovered stress contours. (a) case I; (b) case II

This section has provided the basis for the interaction between tendon geometry and 2.5D elements, which has been validated through examples of simply supported beams. By using Bezier curves to describe the tendon geometry and distributing equivalent forces in the concrete domain, the method allows for accurate modelling of prestressed concrete beams. Building upon this interaction strategy, the following section will introduce a thickness optimisation formulation based on the 2.5D SIMTP. This formulation aims to optimise the thickness of prestressed concrete beams while simultaneously considering the layout of the tendon, as demonstrated in previous studies [14,164].

7.3 Optimisation Methodology

This section introduces a simultaneous optimisation methodology for tendon and concrete geometries using 2.5D SIMTP. The concrete geometry is discretised with 2.5D elements, while the tendon geometry is described using control points through the Bezier definition. In this approach, the tendon is not explicitly modelled as part of the finite element model, and its effect is simulated by estimating equivalent forces on the concrete. While a detailed modelling strategy may be necessary for the future, using equivalent forces to analyse prestressed concrete beams is currently efficient and easy to process [207].

The optimisation problems consist of nodal thicknesses and the vertical position of the control points as the design variables. The design variables are obtained based on the sensitivity analysis carried out at the nodal level with the objective of minimum compliance. A tendon to concrete filter [164] is used to obtain the sensitivities at the control points, and the control point locations are obtained based on the load balancing concept [208]. Another advantage of the tendon to concrete filter is to provide minimum cover to the tendon. As discussed in the previous section, the control point locations are used to obtain the equivalent forces on the concrete. The above sequence of events is iterated until the desired outcomes are achieved. The rest of this section covers the optimisation aspects and sequence of involved processes.

7.3.1 Energy Regularisation

As discussed earlier in the sections on 2.5D SIMTP traditional and adaptive processes, it was highlighted how thickness filtering is essential for achieving a positive volumetric integral in 2.5D elements, which is a primary concern for stable analysis. Thickness filtering in the prestressed beam optimisation problem is performed at the nodal level of the concrete domain. This filtering technique ensures that the thickness values remain physically meaningful and within a specified range during the optimisation process. The thickness filter is an essential component of the optimisation approach and helps to ensure accurate and stable results. The thickness filtering scheme adopted for optimising a prestressed beam is presented here in Eq. (7.3).

$$
\begin{gathered}
\forall i \in N_n : f_{r,i} = \sum_{k \in N_{I,i}} f_k \phi_{i,k} \Big/ \sum_{k \in N_{I,i}} \phi_{i,k} \\
\forall k \in N_{I,i} : \phi_{i,k} = \left(r_{I,i} - r_{i,k}\right) / r_{I,i} \\
\forall k \notin N_{I,i} : \phi_{i,k} = 0
\end{gathered}
\tag{7.3}
$$

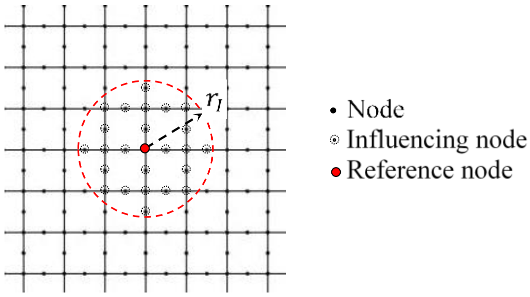

Figure 7.5: Filtering scheme

Where $r_{I,i}$ is the influence radius of the i^{th} node, $r_{i,k}$ is the distance of the k^{th} node from the i^{th} node, $\phi_{i,k}$ is the influence of the k^{th} node on the i^{th} node, $f_{r,i}$ is the regularised TF of the i^{th} node, f_k is the actual TF of the k^{th} node, $N_{I,i}$ is the set of influencing nodes of the i^{th} node.

Building upon the earlier discussion, it is important to note that the filtering technique discussed only regularises the concrete design variables and does not ensure that any material surrounds the tendon. To address this issue, the following section will introduce an alternative filtering technique that prevents the tendon from being exposed while also creating connectivity between design variables to enable the transfer of sensitivities.

7.3.2 Tendon to Concrete Filter

As mentioned earlier, the tendon to concrete filter provides minimum cover to the tendon by filtering the concrete nodal thicknesses surrounding the tendon. To achieve this, a super-gaussian function introduced in [164] is adopted and modified, as presented in Eq. (7.4).

$$\forall i \in N_{n,j}: f_{tc,i} = f_{r,i} + \left(1 - f_{r,i}\right)e^{-\frac{1}{2}\left(\frac{d_{i,j}}{\beta}\right)^{\mu}}$$

$$\forall i \in N_{n,j}: d_{i,j} = \frac{\left|\alpha_{i,j}\right|}{\widehat{\alpha}_j}$$

$$\alpha_{i,j} = \left(y_i - r_{y,j-1}\right)\left(r_{x,j} - r_{x,j-1}\right) - \left(x_i - r_{x,j-1}\right)\left(r_{y,j} - r_{y,j-1}\right) \tag{7.4}$$

$$\widehat{\alpha}_j = \sqrt{\left(r_{x,j} - r_{x,j-1}\right)^2 + \left(r_{y,j} - r_{y,j-1}\right)^2}$$

Where, $N_{n,j}$ is neighbourhood nodes of the j^{th} segment of the tendon, $f_{tc,i}$ is TF after tendon to concrete filter, $d_{i,j}$ is the shortest distance between i^{th} node to the j^{th} segment of the tendon, β is the length of the minimum cover, and μ is the sharpness of the function, (x_i,y_i) is i^{th} node coordinate, $(r_{x,j},r_{y,j})$ is j^{th} tendon point coordinate.

The significance of the above super-gaussian equation lies in its distance-based dependency between the concrete design variables and tendon points. However, calculating this distance between the tendon layout (Bezier definition) and concrete nodes can result in a complex power series problem. To overcome this, the tendon is idealised as piecewise lines, as illustrated in Fig. 7.6, and the shortest distance is calculated using the vector product. This approach takes into account the interdependency of the tendon points, concrete nodes, and concrete design variables, which facilitates the transfer of thickness-based solutions to the tendon points (at segment). This information provides the basis for control point regions based on the Bezier definition.

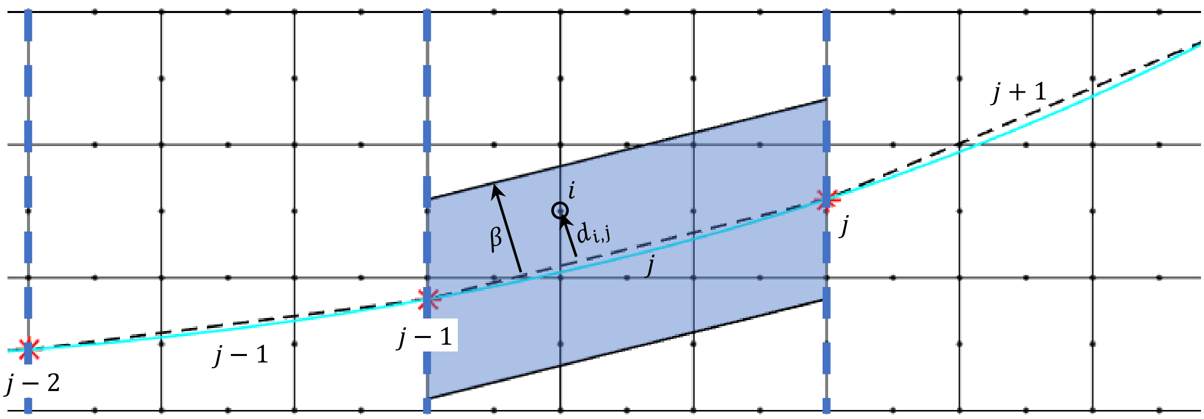

Figure 7.6: Tendon to concrete filter at the nodal level

By considering the interdependency between the variables allows for the transfer of solutions from the thickness-based design variables to the tendon points while ensuring that the tendon is adequately covered. This approach facilitates the simultaneous optimisation of the tendon layout and concrete domain using sensitivities of the concrete variables and tendon points.

However, the tendon to concrete filter, which was discussed in the previous section, is applied after the thickness filtering and can disrupt the concrete design domain. This requires further processing of the design variables, which can be achieved using morphological operators such as dilation and erosion. The next section will discuss how these morphological operators are used to address this issue and improve the stability of the optimisation approach.

7.3.3 Heaviside Filter with Morphological Operators

As mentioned earlier, this chapter draws inspiration from Amir and Shakour [164] work on optimising prestressed beams. In their study, a tendon to concrete filter was followed by a morphologically inspired Heaviside filter on element densities to obtain smooth void and solid profiles for prestressed beams. A better understanding of the application of morphological operators in topology optimisation is discussed in [209]. This paper highlights two morphological operators: dilated densities, which preserve volume, and eroded densities, which have the opposite effect.

Guest et al. [53] were the first to introduce the Heaviside projection based on nodal densities to topology optimisation, which was later extended to multiple-phase projection [96]. Multiple phase projection independently projects the solid and void phases to yield smooth boundaries of optimised profiles. Wang et al. [210] proposed a modified Heaviside projection method based on the hyperbolic tangent function to avoid conditional operations of the above projection methods, resulting in quicker and faster void/solid solutions. Lazarov et al. [211] introduced morphological operators to the above-modified Heaviside function, such that eroded densities contribute to stiffness design while dilated densities contribute to the volumetric design. More demonstrations and detailed discussions on the performance of morphologically operated Heaviside filters can be found in [14,164].

In this chapter, the same filtering technique is adopted using morphological operators, but it is modified for nodal thicknesses. However, in this case, the Heaviside filter is used not only to obtain void/solid solutions but also to stabilise the optimisation process from the disruptions caused after the tendon to concrete filtering. The modified Heaviside function for the tendon to concrete filter is presented here:

$$\begin{aligned} \forall i \in N_n\colon f_{ero,i} &= \frac{\tanh(\beta_{HS}\eta_{ero}) + \tanh\left(\beta_{HS}\left(f_{tc,i} - \eta_{ero}\right)\right)}{\tanh(\beta_{HS}\eta_{ero}) + \tanh\left(\beta_{HS}(1 - \eta_{ero})\right)} \\ \forall i \in N_n\colon f_{dil,i} &= \frac{\tanh(\beta_{HS}\eta_{dil}) + \tanh\left(\beta_{HS}\left(f_{tc,i} - \eta_{dil}\right)\right)}{\tanh(\beta_{HS}\eta_{dil}) + \tanh\left(\beta_{HS}(1 - \eta_{dil})\right)} \end{aligned} \tag{7.5}$$

Where, β_{HS} control the smoothness of the void-solid phase, $f_{ero,i}$ is the eroded TF of the i^{th} node, $f_{dil,i}$ is the dilated TF of the i^{th} node, η_{ero} and η_{dil} projection thresholds of eroded and dilated layouts.

Overall, this section provided a comprehensive discussion on the use of Heaviside projections and their advantages in the optimisation process. The introduction of morphological operators such as dilation and erosion changes the course of traditional SIMTP's thickness scaling function. These morphological operators are used to process the design variables and improve the efficiency and stability of the optimisation approach. The following section will discuss the new inclusions into the thickness scaling function based on these operators.

7.3.4 Thickness Scaling

The modified Heaviside filtering for TFs changes the approach for performing thickness scaling based on the morphological operators of erosion and dilation. Eroded thicknesses are used to evaluate stiffness design, while dilated thicknesses are used for volumetric estimations. In the present scenario, thickness scaling is performed at the nodal level on both eroded and dilated TFs, as presented in Eq.

(7.6). The scaled-eroded TFs are used for stiffness computations, while the scaled-dilated TFs are used for volumetric estimations.

$$\forall i \in N_n: th_{k,i} = \left[f_{min} + f_{ero,i}{}^{p}(f_{max} - f_{min})\right]b$$

$$\forall i \in N_n: th_{v,i} = \left[f_{min} + f_{dil,i}{}^{p}(f_{max} - f_{min})\right]b$$

$$such\ that: \begin{cases} f_{ero,i} \in [0,1]^{R} \\ f_{dil,i} \in [0,1]^{R} \\ p \ \in \ R_{\geq 1} \\ \Omega^{m} \subseteq \Omega_{R^3} \end{cases} \tag{7.6}$$

Where $th_{k,i}$, $th_{v,i}$ are i^{th} node thicknesses for stiffness and volume estimations, respectively and $f_{\max}$, $f_{\min}$ are maximum and minimum TFs.

The modifications made in this section, including the modified thickness scaling function, as well as previously discussed filtering procedures such as thickness filtering, tendon to concrete filter, and Heaviside filter, will alter the previously presented thickness optimisation procedure. These modifications enable the simultaneous optimisation of both the tendon layout and the concrete domain. The following section will discuss the updated procedure for optimising both the tendon layout and concrete domain, taking into account all of the modifications discussed so far.

7.3.5 Thickness Optimisation Problem

The objective of the current optimisation problem is to minimise the strain energy, as presented in Eq. (7.7).

$$\text{minimum compliance}: C = u^{T}Ku$$

$$subject\ to: \begin{cases} Ku = F = F_{LL} + F_{DL} + F_{P} \\ V/V_o \leq V_r \\ 0 \leq \ f \leq \ 1 \\ c_e \leq \ R_y \leq (d - c_e) \end{cases} \tag{7.7}$$

$$= \sum_{j \in N_e} K_{e,j}\,; V = \sum_{j \in N_e} V_{e,j}$$

Compliance and volume are sensitivities that impact the design variables while achieving the optimisation objective. While sensitivity analysis can be incorporated with limit-state design constraints [14], the present setup is currently limited to stiffness and volume sensitivities.

As previously discussed in the introductory chapter on 2.5D SIMTP, stiffness and volume rates are evaluated at the element level and then lumped to the nodes. It is important to note that the nodal thickness mapping inside the element with isoparametric shape functions may result in negative values [94]. To handle this issue, the thickness at any point inside an element space (Ω_e) is interpreted using Shepard interpolants [180] as follows,

$$\forall (x, y) \in \Omega_e \colon th(x, y) = \sum_{i \,\in\, n_e} w_i th_i$$

$$w_i = \frac{1/((x - x_i)^2 + (y - y_i)^2)}{\sum_{i \,\in\, n_e} 1/((x - x_i)^2 + (y - y_i)^2)} \tag{7.8}$$

Here concrete nodal thicknesses and tendon control points are the design variables. Obtaining sensitivities for nodal design candidates is straightforward, while sensitivities at tendon control points are obtained based on the dependency of thickness design variables on the geometrical points of the tendon, as discussed earlier. The estimation of sensitivities is as follows,

Nodal design variables: differentiating the compliance with the actual TF

$$\forall i \in N_n \colon \partial C/\partial f_i = u^T\, \partial K/\partial f_i\, u \tag{7.9}$$

$$\forall i \in N_{\mathrm{n}}, k \in N_{I,i}\colon \partial K/\partial f_i \ = \sum_{j\in N_e} \partial K_{e,j}/\partial f_i$$

$$= \sum_{j\in N_e} \frac{\partial K_{e,j}}{\partial f_{ero,i}} \frac{\partial f_{ero,i}}{\partial f_{tc,i}} \frac{\partial f_{tc,i}}{\partial f_{r,i}} \frac{\partial f_{r,i}}{\partial f_k}$$

$$\forall i \in (N_{\mathrm{n}}, n_{e,j}), j \in N_{\mathrm{e}}\colon \partial K_{e,j}/\partial f_{ero,i} = K_{e,j} w_{i,j} p f_{ero,i}^{p-1} (f_{max} - f_{min}) b$$

$$\forall i \in N_n\colon \frac{\partial f_{ero,i}}{\partial f_{tc,i}} = \frac{\beta_{HS}\left(1 - tanh\left(\beta_{HS}(f_{tc,i} - \eta_{ero})\right)^2\right)}{\tanh(\beta_{HS}\eta_{ero}) + \tanh\left(\beta_{HS}(1-\eta_{ero})\right)}$$

$$\forall i \in N_{n,j}\colon \frac{\partial f_{tc,i}}{\partial f_{r,i}} = 1 - e^{-\frac{1}{2}\left(\frac{d_{i,j}}{\beta}\right)^{\mu}}$$

$$\forall i \in N_{\mathrm{n}}, k \in N_{I,i}\colon \partial f_{r,i}/\partial f_k = \phi_{i,k} \Big/ \sum_{j\in N_{I,i}} \phi_{i,j}$$

Nodal design variables: differentiating the volume with the actual TF

$$\forall i \in N_{\mathrm{n}}, k \in N_{I,i}\colon$$

$$\partial V/\partial f_i \ = \sum_{j\in N_e} \partial V_{e,j}/\partial f_i \ = \sum_{j\in N_e} \frac{\partial V_{e,j}}{\partial f_{dil,i}} \frac{\partial f_{dil,i}}{\partial f_{tc,i}} \frac{\partial f_{tc,i}}{\partial f_{r,i}} \frac{\partial f_{r,i}}{\partial f_k}$$

$$\forall i \in (N_{\mathrm{n}}, n_{e,j}), j \in N_{\mathrm{e}}\colon \tag{7.10}$$

$$\partial V_{e,j}/\partial f_{ero,i} = A\left(x_{\Omega_{e,j}}, y_{\Omega_{e,j}}\right) w_{i,j} (f_{max} - f_{min}) b$$

$$\forall i \in N_n\colon \frac{\partial f_{dil,i}}{\partial f_{tc,i}} = \frac{\beta_{HS}\left(1 - tanh\left(\beta_{HS}(f_{tc,i} - \eta_{dil})\right)^2\right)}{\tanh(\beta_{HS}\eta_{dil}) + \tanh\left(\beta_{HS}(1-\eta_{dil})\right)}$$

Before introducing the sensitivities for the tendon design variables, it is important to note that the first two control point depths are set to the average of both points, as shown in Eq. (7.11) and illustrated in Fig. 7.7. This adjustment ensures a smooth variation of the tendon in a symmetrical region and eliminates any upward thrust, enabling the full integration of an eccentric prestress force to counteract the flexural stresses resulting from live and dead loads.

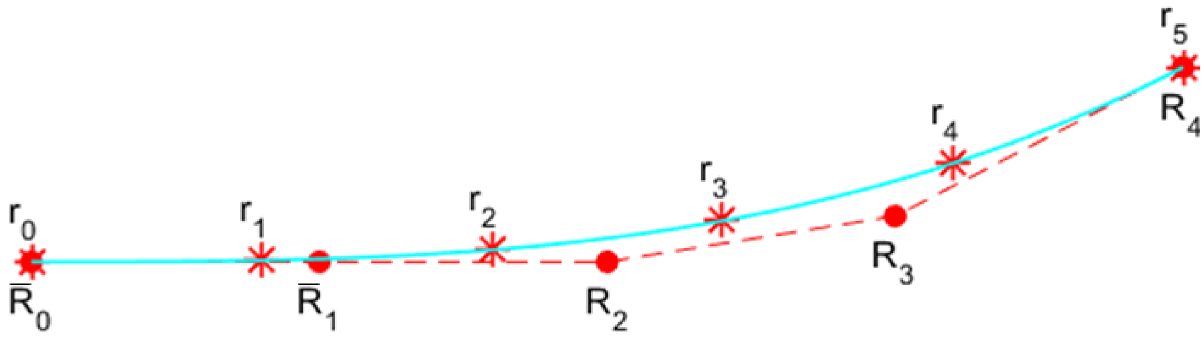

Figure 7.7: Tendon layout

$$\bar{R}_{y,0} = \bar{R}_{y,1} = \frac{(R_{y,0} + R_{y,1})}{2} \tag{7.11}$$

Load balancing [208] is applied in order to determine the sensitivities of the concrete nodes under the influence of a tendon segment, as shown in Fig. 7.6. The sum of these sensitivities gives the sensitivity at a tendon point, and the accumulated sensitivities at tendon points are then recalibrated at control points based on the Bezier definition. This leads to the sensitivity estimations as provided below:

Tendon design variables: differentiating compliance and volume with respect to tendon control point locations (vertical)

$$\forall k \in N_{nc}: \partial C_k / \partial R_{y,k} = \sum_{i \in [N_{n,j}, N_{n,j+1}]} \frac{\partial C_i}{\partial f_{ero,i}} \frac{\partial f_{ero,i}}{\partial f_{tc,i}} \frac{\partial f_{tc,i}}{\partial r_{y,j}} \frac{\partial r_{y,j}}{\partial \bar{R}_{y,k}} \frac{\partial \bar{R}_{y,k}}{\partial R_{y,k}}$$

$$\forall k \in [0,1]: \frac{\partial \bar{R}_{y,k}}{\partial R_{y,k}} = \frac{1}{2};\ \forall k \notin [0,1]: \frac{\partial \bar{R}_{y,k}}{\partial R_{y,k}} = 1 \tag{7.12}$$

$$\forall k \in N_{nc}: \partial V / \partial R_{y,k} = \sum_{i \in [N_{n,j}, N_{n,j+1}]} \frac{\partial V_i}{\partial f_{dil,i}} \frac{\partial f_{dil,i}}{\partial f_{tc,i}} \frac{\partial f_{tc,i}}{\partial r_{y,j}} \frac{\partial r_{y,j}}{\partial \bar{R}_{y,k}} \frac{\partial \bar{R}_{y,k}}{\partial R_{y,k}}$$

$$\forall i \in N_{n,j}: \frac{\partial f_{tc,i}}{\partial r_{y,j}} = -\mu\left(1 - f_{r,i}\right)\frac{1}{2}\left(\frac{d_{i,j}}{\beta}\right)^{\mu-1} e^{-\frac{1}{2}\left(\frac{d_{i,j}}{\beta}\right)^{\mu}} \frac{\partial d_{i,j}}{\partial r_{y,j}}$$

$$\forall i \in N_{n,j}: \frac{\partial d_{i,j}}{\partial r_{y,j}} = -\frac{\alpha_{i,j}\left(x_i - r_{x,j-1}\right)}{\left|\alpha_{i,j}\right|\widehat{\alpha}_j} - \frac{\left|\alpha_{i,j}\right|\left(r_{y,j} - r_{y,j-1}\right)}{\widehat{\alpha}_j^3}$$

$$\forall i \in N_{n,j+1}: \frac{\partial d_{i,j+1}}{\partial r_{y,j}} = \frac{\alpha_{i,j}\left(x_i - r_{x,j}\right)}{\left|\alpha_{i,j}\right|\widehat{\alpha}_j} + \frac{\left|\alpha_{i,j}\right|\left(r_{y,j} - r_{y,j-1}\right)}{\widehat{\alpha}_j^3}$$

$$\frac{\partial r_{y,j}}{\partial R_{y,k}} = \binom{nc-1}{k}\left(1 - t_j\right)^{nc-1-k} t_j^k$$

Where K is an assembly of elemental stiffness matrices corresponding to joint DoFs, u is nodal deformations matrix (movement of the point mass) under live loads (F_{LL}), body forces (F_{DL}) and prestressing forces (F_P), V is the volume of the total body mass for an obtained or a given set of TFs, V_o is the initial volume, V_r is the volume ratio limit, f is actual TF (nodal design variable), R_y is vertical coordinate of a control point (tendon design variable), N_{nc} set of control points, c_e is the effective cover of the tendon, $K_{e,j}$ is the j^{th} element stiffness matrix estimated based on scaled-eroded TFs, $V_{e,j}$ is j^{th} element volume estimated based on scaled-dilated TFs, th_i is the thickness of the i^{th} node, N_n and N_e are set of nodes and elements, $K_{e,j}$ is j^{th} element stiffness with unit thickness, $n_{e,j}$ is the set of nodes of the j^{th} element, $w_{i,j}$ is the inverse distance weight of i^{th} node from the centre of the j^{th} element, $A(x_{\Omega_{e,j}}, y_{\Omega_{e,j}})$ is the area of the j^{th} element, $R_{y,k}$ is the vertical position of the k^{th} control point.

In summary, the modifications and improvements made in this section to the 2.5D SIMTP approach have extended its capabilities for optimising prestressed concrete beam designs. This is a significant advancement in the field of prestressed concrete beam optimisation, as 2.5D SIMTP can offer both pixels and voxels, thus avoiding the limitation of design imagination to extend the pixels for manufacturing [54]. By simultaneously optimising both the tendon layout and concrete domain, and incorporating advanced modelling and filtering techniques, the new approach is used to explore various beam problems adopted from Amir and Shakour [164] and compared in the next section.

7.4 Prestressed Beam Design and Optimisation Results

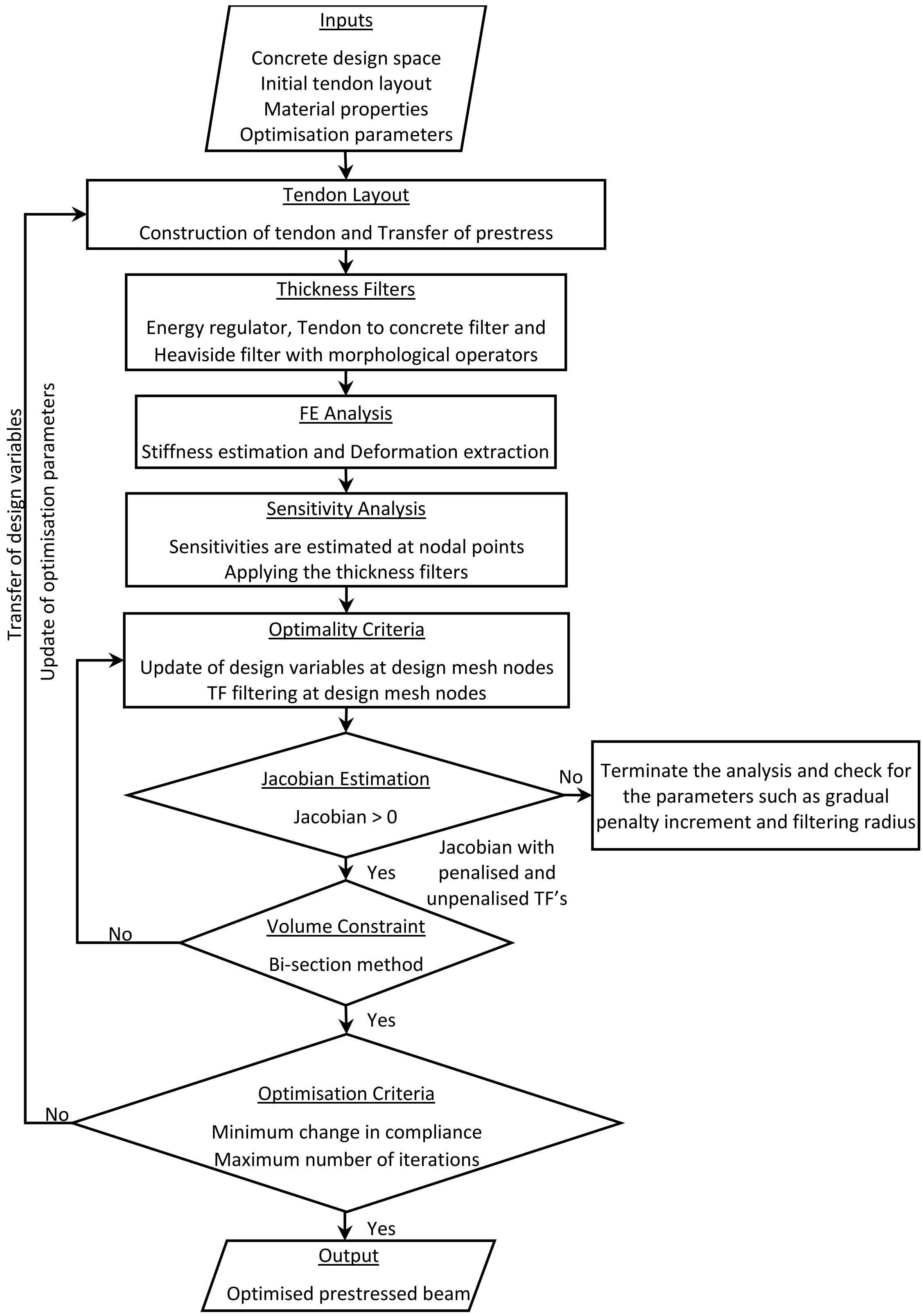

Figure 7.8: Prestressed beam optimisation algorithm

This section discusses various cases of prestressed beams (from [164]) optimised using the 2.5D SIMTP's optimisation methodology, which simultaneously optimises the tendon layout and concrete domains based on the methodology presented in the previous section. Additionally, a MATLAB code "topPSC" comprising 220 lines is provided in Appendix E, based on the optimisation algorithm shown in Fig. 7.8.

The design variables parameterisation for both tendon and concrete was performed using the OC method discussed in [182]. All analyses were carried out on the Intel Xeon W-2155 processor 3.3 GHz with 64GB RAM. The symmetrical half of the test cases studied and discussed in this section were discretised with 150×30 (for simply supported beams) and 240×30 2.5D (for multi-span beams) elements according to beam geometries. The optimisation parameter values used in the optimisation process are listed in Tab. 7.3.

Table 7.3: Prestressed beam optimisation parameters

Symbol	Value/Increment	Min	Max	Remarks
V_r	50%	-	-	Volume ratio
E	30 GPa	-	-	Modulus
ν	0.2	-	-	Poisson
rho	2400 kg/m^3	-	-	Concrete density
p	0.01	1	3	Penalty
nc	11			Control points for tendon
r_I	0.03 m	-	-	Influence radius
β	0.03 m	-	-	Cover length
μ	0.05	1	4	Sharpness
c_e	0.02	-	-	Effective cover
β_{HS}	0.01	1	8	Smoothness
η_{ero}	0.6	-	-	Erosion
η_{dil}	0.4	-	-	Dilation
mv_c	0.05	-	-	Move ratio for concrete until 30 iterations
mv_t	0.0052 m	-	-	Move ratio for tendon until 30 iterations
mv_c	0.1	-	-	Move ratio for concrete after 30 iterations
mv_t	2.6×10^{-5} m	-	-	Move ratio for tendon after 30 iterations
It_{max}	200	-	-	Maximum number of iterations

The optimisation methodology described previously is utilised to determine the optimal distribution of concrete material and to identify the appropriate tendon layout based on the load balancing concept. Initially, a set of initial tendon layouts is provided to the optimisation module for the simply supported beam model consisting of 150×30 elements. This model is subjected to a concentrated load of 10 N and a prestressing load of 40 N, as illustrated in Fig. 7.9, to understand the impact of load balancing. The resulting optimised profiles are compared in Fig. 7.10.

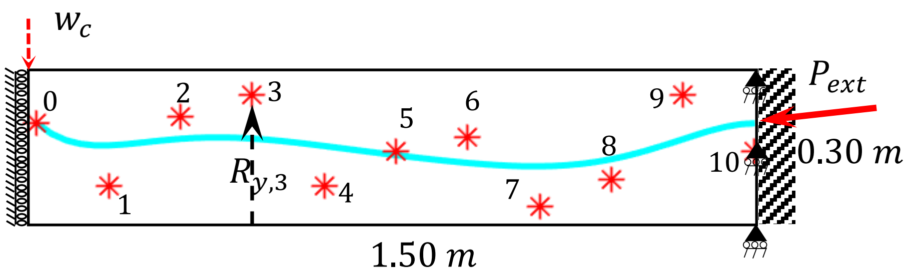

Figure 7.9: Beam properties for test case I

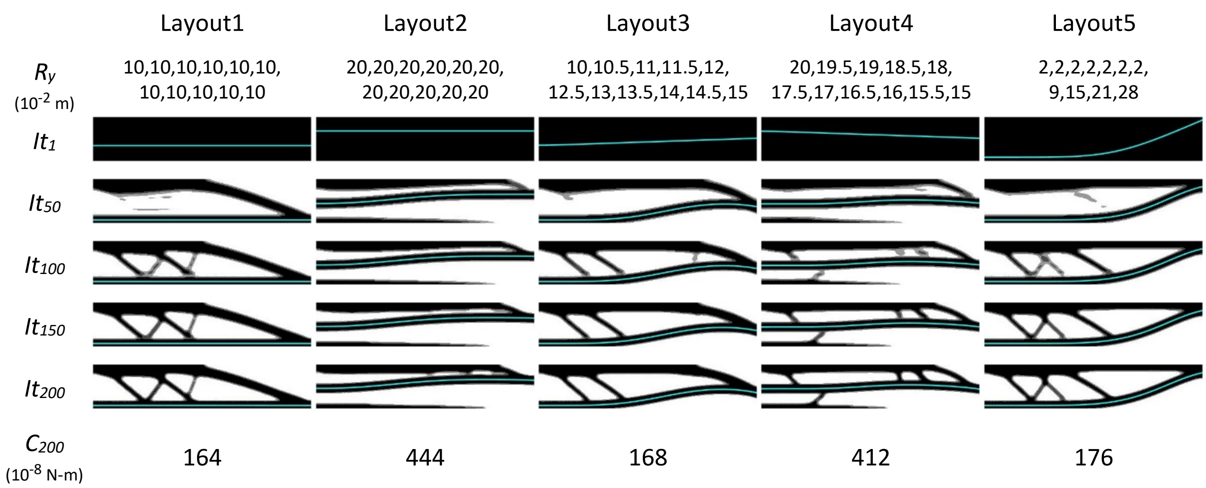

Figure 7.10: Tendon layout - comparison of optimised profiles

Tendon layouts 1 and 2 are eccentric profiles positioned below and above the neutral axis, respectively. Tendon layouts 3 and 4 are linear tendon profiles positioned below and above the neutral axis, respectively. Tendon layout 5 is a curved tendon profile that passes from below the neutral axis at midspan to above the neutral axis at supports. It is observed that the initial tendon layout has a significant impact on the optimised outcomes of the prestressed beams. Tendon layouts 3 and 5 have an upward thrust, resulting in a reasonably optimised profile. The optimised profiles of tendon layouts 2 and 4 are structurally unsatisfactory.

Tendon layouts 1 and 2 have resulted in a structurally viable optimised profile with the lowest compliance. However, it may not be feasible to have a varying top section for the integration of structural members. On the other hand, layout 5 has resulted in the lowest compliance next to layouts 1 and 2 while also being structurally feasible. It should be noted that the initial layout inputs should have an upward thrust or eccentric tendon below the neutral axis to obtain structurally sound profiles. This limitation of the proposed optimisation method highlights the importance of choosing a suitable tendon layout to achieve the desired outcomes. Therefore, layout 5 is selected for the rest of the beam cases to ensure that the desired structural requirements are met.

As discussed on many occasions, load balancing is used to identify the location of the tendon. The earlier parametric study on tendon layout has shown that it is effective when a suitable tendon layout is considered for the initial design. This raises an obvious question: what happens to the stiffness solutions and optimised designs when a beam is under/over prestressed? Therefore, test case I in Fig. 7.9 is further explored with varying concentrated and prestressing forces, and the results are summarised in Fig. 7.11. The observations showed that the higher the load to prestress, the more scattered the material distribution becomes, while a lower ratio leads to a more concentrated distribution.

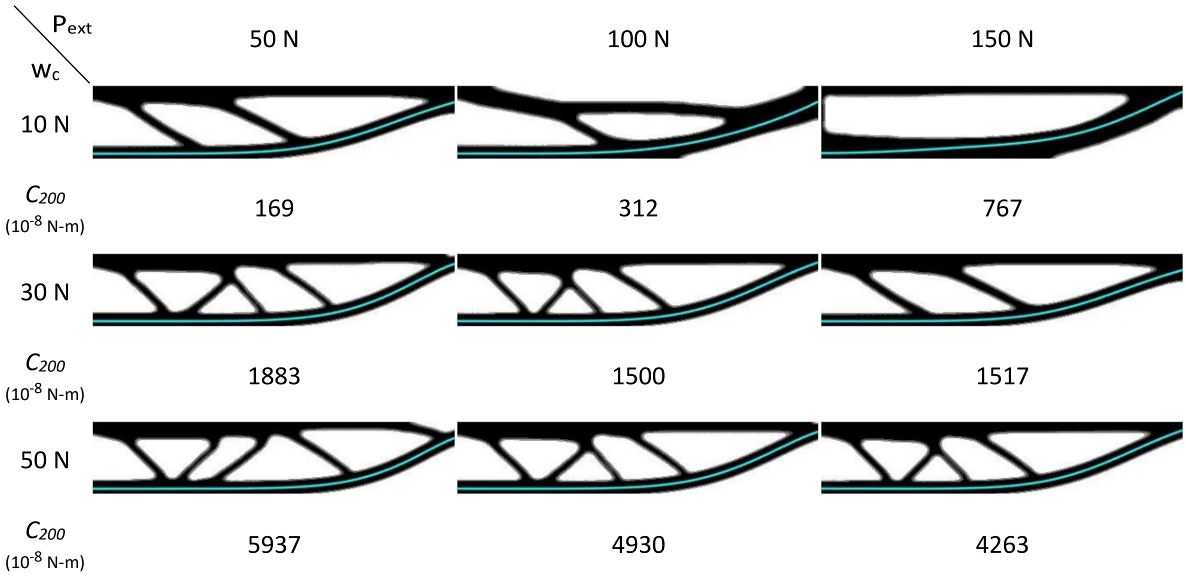

Figure 7.11: Load to prestress ratio - comparison of optimised profiles

Load ratios ($2w_c/P_{ext}$) ranging from 10% to 100% are explored, as shown in the above figure. It is observed that optimised profiles with a 60% load ratio resulted in better stiffness solutions. Furthermore, the optimised profiles are similar for the same load ratio, irrespective of the quantity. This suggests that the optimal counteractive efforts due to prestress are effective against the imposed loads. However, a relatively lower imposed load against higher prestress yielded unsatisfactory profiles with high compliances. This indicates that a suitable prestressing force is necessary to balance and counteract the resulting stresses from the imposed or dead loads.

The previous discussion emphasised the importance of selecting a suitable tendon profile and prestressing force in optimising prestressed beams. With these considerations in mind, three additional cases were explored under UDL, two of which were inspired by the work of Amir and Shakour [164]. To facilitate top chord loadings, the top four-element nodal TF values were always set to 1.0 for the UDL cases, irrespective of design parameterisation. The half models of these cases were examined, taking advantage of symmetry, and the optimised profiles were mirrored for visualisation and comparison purposes.

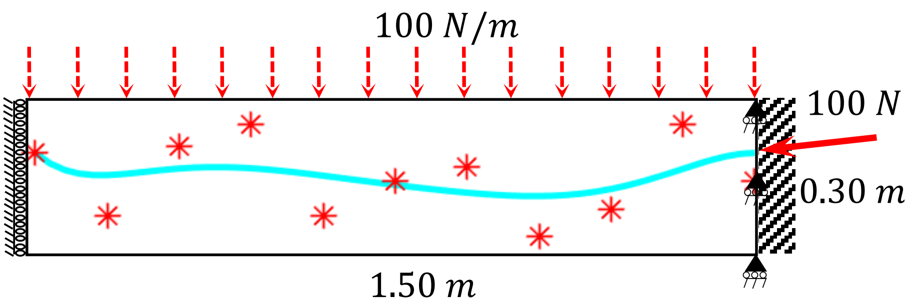

Figure 7.12: Case I with UDL

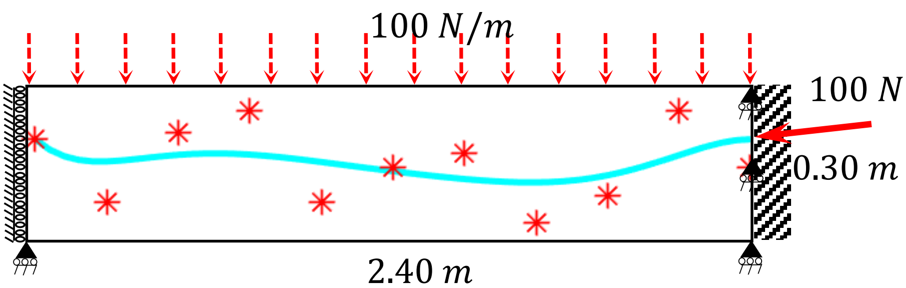

Figure 7.13: Beam properties for test case II

The first case, represented by UDL in Fig. 7.12, was optimised with 2.5D SIMTP and compared in Fig. 7.14. This is the same beam model that Amir and Shakour [164] optimised and was 3D printed by "OptiBridge" [54]. Similarly, a two-span beam, shown in Fig. 7.13, into 240×30 elements, and the optimised profiles were compared in Fig. 7.15.

Figure 7.14: Shape comparison of Case I with UDL . Top - 2.5D SIMTP and Bottom - Amir and Shakour [164]

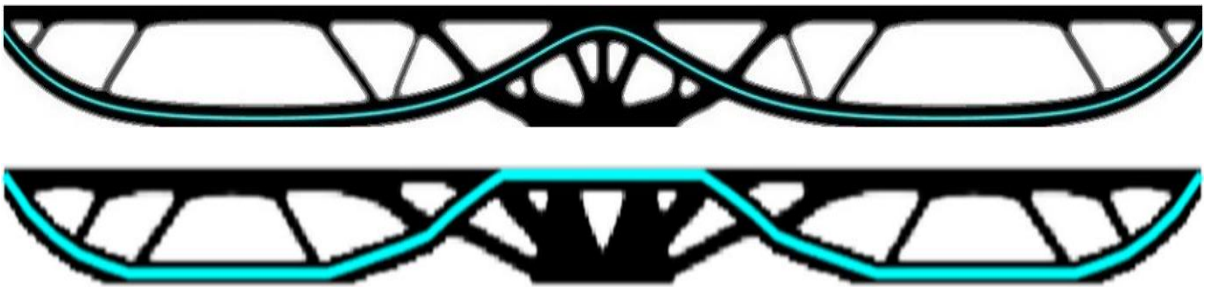

Figure 7.15: Shape comparison of Case II . Top - 2.5D SIMTP and Bottom - Amir and Shakour [164]

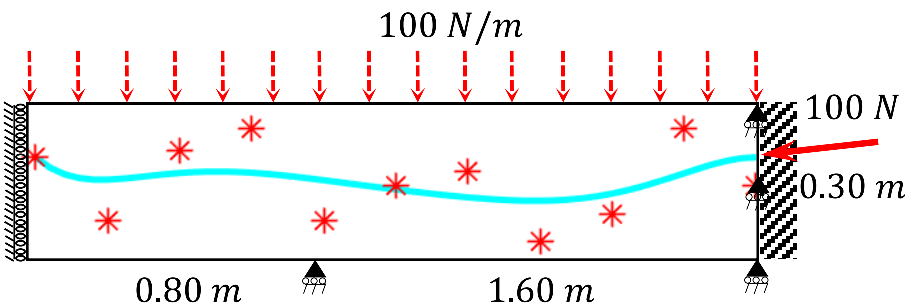

Figure 7.16: Case II with three-span

The comparison of optimised profiles with the work of Amir and Shakour [164] demonstrates that the prestressed beam profiles are consistent and in agreement with earlier findings. Additionally, the use of Bezier's definition of the tendon layout results in a smooth transition of the tendon, which differs from the piecewise linear approach used in Amir and Shakour's work. Also, these visual comparisons show that the 2.5D SIMTP's profiles have superior resolution despite using the same discretisation. Another beam problem, case II, with three spans shown in Fig.

7.16, was also optimised using 2.5D SIMTP, and the results are presented in Fig. 7.17.

Figure 7.17: Optimised three-span beam

All cases, including case I with UDL, case II, and case II with three spans, were explored with dead loads. The move ratio of the tendon (mv_t) was set to 0.0026 m for the two- and three-span models, and the optimised profiles were presented in Fig. 7.18. The density of the concrete was set to 2400 kg/m^3 and zero for cases with and without dead loads, respectively. It is worth noting that the dead load had a significant impact on the shape profiles of the beam. However, for practical applications, design loads are typically much greater than the self-weight of the beam, and the inclusion of self-weight would have minimal impact on the design. The load values chosen for this study were deliberately undervalued for dead loads to replicate the conditions used in the work of Amir and Shakour [164], enabling a direct comparison of our results with theirs.

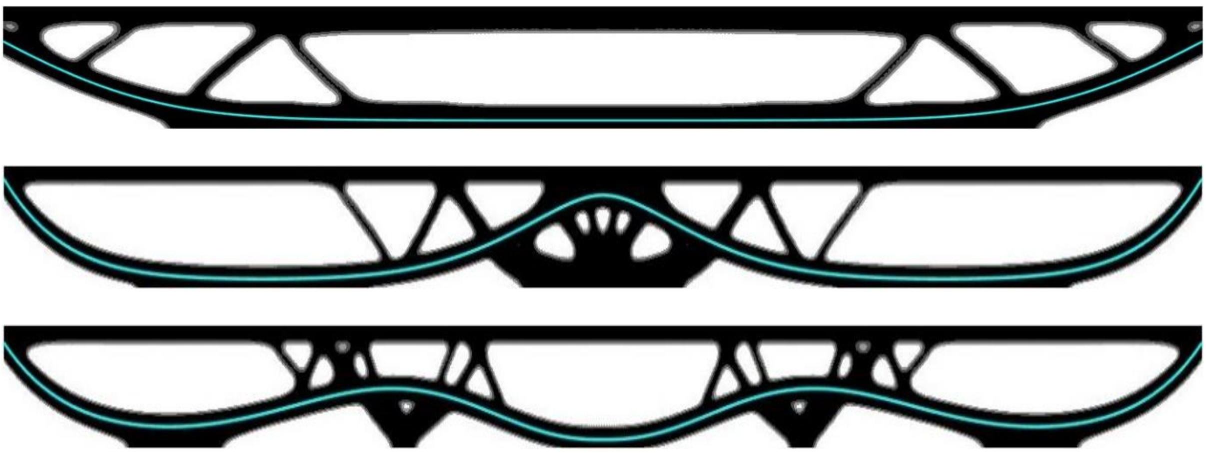

Figure 7.18: Optimised prestressed beams with UDL and dead loads

Thus far, the optimised results for prestressed beams have been unit thickness problems. These cases were optimised with a thickness of 0.225 m (thickness definition can be incorporated into "topPSC" similarly to "top211" discussed in the previous chapter) without dead loads, and the move ratio of the tendon (mv_t) was set back to 0.0052 m. These profiles are presented in Fig. 7.19. This demonstration specifically shows that 2.5D SIMTP can build surfaces for prestressed beams, thereby reducing the efforts of design imagination.

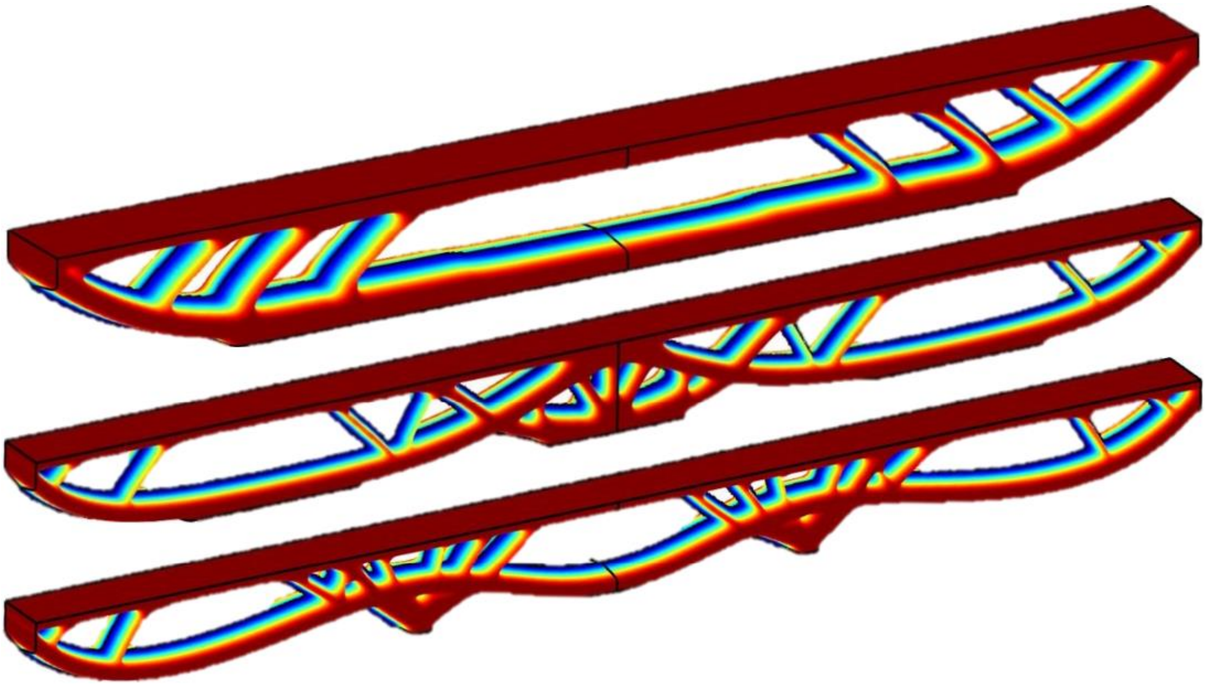

Figure 7.19: Surface optimisation - prestressed concrete beams

The findings presented in this section demonstrate the extended capabilities of 2.5D SIMTP in optimising prestressed beams while simultaneously designing the tendon layout and concrete domain. The exploration of various beam problems with different layouts, loading conditions, and spans provides valuable insights into the behaviour of prestressed beams and offers a starting point for designing 3D printed prestressed beams for various applications. However, it is important to note that the results presented in this chapter are based on linearly elastic models and should be interpreted with caution when considering their practical application. The following remarks will provide a more comprehensive discussion of the key points and contributions of the study, as well as its potential implications and limitations. By reflecting on the insights gained from this study, a deeper understanding of the capabilities and potential applications of 2.5D SIMTP in the design and optimisation of prestressed beams can be gained.

7.5 Remarks

This chapter extended the 2.5D SIMTP to design and optimise prestressed systems for concrete 3D printing, addressing practical constraints such as ductility provisions. The methodology incorporated tendon layout idealisation using Bezier definitions, prestressing modelling strategies based on the principle of virtual work, and various filtering techniques to simultaneously optimise the tendon and concrete geometry of prestressed beams. The results demonstrated the effectiveness of the methodology, with the initial tendon layout and prestressing force playing a significant role in the final design. Some important insights and contributions of this chapter are summarised here:

I. The prestressing strategy employed in this study produced reliable results, with equivalent tendon forces applied to the concrete geometry based on the principle of virtual work.

II. Bezier curve definitions for tendon geometry idealisation were effective in reducing the number of design variables by building the tendon layout with fewer control points.

III. The tendon to concrete filter adopted in this chapter played a crucial role in the optimisation process. By ensuring the material surrounding the tendon and creating dependencies that were part of the load balancing, the filter helped in designing the tendon layout.

IV. The extended capabilities of 2.5D SIMTP in optimising prestressed beams while simultaneously designing the tendon layout and concrete domain were demonstrated through various beam cases, exploring the pixels and surfaces of the optimised prestressed beam for these cases.

V. The results showed that the initial tendon layout greatly influences the final design, and a suitable prestressing force should be chosen to balance the applied loads; otherwise, the resulting profiles may be clumsy, impractical, and unappealing.

VI. The comparison of optimised profiles with the work of Amir and Shakour demonstrated consistency and agreement with their findings. Furthermore, the results showed that the designs produced by 2.5D SIMTP were of high quality compared to their findings.

As the final chapter of this thesis, this work provides valuable insights into the potential of 2.5D SIMTP in optimising prestressed beams and designing their tendon layout. The extended capabilities of 2.5D SIMTP demonstrated here to allow for simultaneous optimisation of both the tendon layout and the concrete domain. Engineers and researchers could use the findings presented in this chapter to optimise the design of various structural members, including prestressed beams. The exploration of various beam problems with different layouts, loading conditions, and spans provides valuable insights into the behaviour of prestressed beams under different conditions, allowing for more informed design decisions. The optimised profiles presented in this section could serve as a starting point for designing 3D printed prestressed beams for various applications, including in the construction of bridges, buildings, and other structures.

However, it is important to note that the results presented in this study are based on linearly elastic models. While these findings provide valuable insights into the behaviour of prestressed beams, it is essential to incorporate more practical design conditions and constraints into the model before implementing them in real-world applications. Such considerations might include material properties, safety standards, and construction methods. By doing so, engineers and researchers can ensure that the optimised profiles derived from 2.5D SIMTP are applicable to real-world scenarios and can be used to design and construct prestressed beams that meet the necessary requirements of safety, durability, and effectiveness.

The methodology developed in this study addresses practical constraints in the manufacturability of concrete systems through 3DP, and the results demonstrate the effectiveness of the approach. However, this work is far from complete, and future endeavours will continue to build on these findings and improve the practical application of 3D printed prestressed systems. The work presented in this thesis serves as a foundation for further research, development, and innovation in the field of 3D printed concrete structures through full-scale integration of architecture and structural engineering designs with practical limitations. The upcoming concluding chapter will summarise the key findings and impacts of this thesis's development on the innovative thickness optimisation tool that can efficiently retrieve and track the shapes of structural components and suggest areas for future research and development in the field.

Chapter 8

Conclusions and Future Work

This thesis is essentially a pilot project presenting a vision of transformational change to the construction industry. It shows the way forward towards a more sustainable future where most construction is automated and is part of a circular economy with greatly reduced carbon footprint and material wastage while also producing aesthetically pleasing and imaginative architecture. In addition to these major changes, construction automation can help reduce the demand for skilled tradesmen, whose average age in developed economies continues to increase, potentially presenting a severe challenge for traditional construction approaches in future. The global construction industry has grown from USD 9.5 trillion in 2014 to USD 11.4 trillion in 2019, with a compound annual growth rate of 3.71% from 2014 to 2019. These numbers are absolutely astronomical, and any disruptive new technology that envisions a transformational change in this industry, as this vision of this thesis does, will undoubtedly have an enormous impact if the concept can be proven and technical hurdles that would inevitably arise could be ironed out. One could not be more eloquent than Shakespeare in Julius Caesar to express the potential magnitude of the opportunity that beckons. There is a tide in the affairs of men. Which, taken at the flood, leads on to fortune. The proposed research has the potential to deliver a transformative impact on many aspects of the construction industry and on society in general, some of which are discussed below, followed by a number of suggested pathways that could be pursued to realise the impact.

Social impact: The largest single cost to sustaining a high quality of life and maximising the potential of humanity is that of civil infrastructure that is built through the age-old process of construction, which despite great technological leaps, remains essentially a chaotic, dirty, expensive and dangerous activity that is wasteful of energy and material resources. The vision of this thesis envisages future construction as largely an assembly exercise similar to current prefab and modular construction. However, with a key difference that enables all the advantages of prefab (cleaner, faster, more automated and less dangerous construction), with none of the disadvantages. Safer construction environments and rapid and more economical automated construction will undoubtedly have a significant social impact, however even more dramatic will be the impact on the "democratisation of architecture" where highly individualised and customised, grandiose and flamboyant architecture that has hitherto been the preserve of the elite would become affordable to ordinary citizens. The environment and ambience of towns and cities built using the proposed technologies and, in the manner described, will also benefit from increased civic pride among residents and reduced social problems and could potentially become areas of architectural and cultural heritage and tourism destinations.

Environmental and economic impact: In the face of climate change and as the world moves towards a circular economy where reducing the wastage of energy and material resources in construction is a major concern, the vision presented here could also make a major impact. High-end architecture constructed in the traditional manner usually wastes even more material and energy. The approach of automated prefabrication of structural components using AM can significantly reduce the volume of material used in construction through the optimised placement of material while delivering imaginative and exclusive architectural styles.

Research and academic impact: The innovative ideas presented here could potentially engender an entirely new field of research and education, involving collaborations between engineers, architects, mathematicians and social scientists and could potentially kick off a renaissance in architecture and construction by unlocking new opportunities in rethinking urbanism and urban regeneration. In addition to the research in exciting new architectural forms, the move towards automation in construction, as envisioned, could also inspire research into novel materials for constructing structural components through AM.

2.5D SIMTP introduced in this thesis is such an attempt to create an ecosystem of processes that involves architectures, structural engineers, and manufacturers under one roof. 2.5D SIMTP is studied under various conditions with interesting developments, and many observations were made during this process. Based on these observations, the following section is dedicated to outlining the merits and demerits of 2.5D SIMTP.

8.1 Conclusions

This thesis addresses several research questions and proposes innovative methods to optimise structural components while enhancing their functional and aesthetic properties. The study contributed to the development of a 2.5D SIMTP tool that bridges aesthetics, structural design, and manufacturing which is a significant contribution to achieving the research objectives of developing a new element that can accurately represent non-prismatic shapes and an innovative optimisation module that can efficiently retrieve and track the shapes of structural components. This has been achieved by a combination of literature review, mathematical and computational modelling, implementation, and evaluation using established engineering principles and testing methods.

Several conclusions can be drawn from addressing the research questions based on the methods presented in this thesis. Firstly, the novel 2.5D element developed in this study shows promising accuracy and efficiency in representing non-prismatic shapes for structural analysis under in-plane loading conditions. The 2.5D element uses a single element in the thickness direction, which may exhibit squeezing behaviour when coarse meshes are used, especially for abruptly varying surface conditions. Additionally, coarse meshes may yield inaccurate stress distributions, which can affect optimised designs. However, the 2.5D element yields computationally efficient and stable solutions when relatively fine elements are used and can match the capabilities of traditional 3D elements. Moreover, the element can adopt nonlinear conditions, increasing its versatility and applicability.

Secondly, the thesis also introduces an innovative optimisation module that addresses the limitations of traditional TO and generates optimised profiles for non-prismatic shapes. However, this approach is limited to plane-stress problems with geometry symmetrical to a loading plane. For flexural members such as beams, this limitation is adequate.

The stable Jacobian is crucial for avoiding general topology optimisation instabilities in 2.5D SIMTP. To achieve this, SIMTP uses a higher initial threshold compared to regular topology optimisation methods, which helps maintain a positive Jacobian in the 2.5D element. However, imposing an aggressive penalty can lead to unwanted thickness distribution, so it is recommended to use a gradual increment of the penalty between 0.05 and 0.15.

In comparison to 2D optimisation methods, 2.5D SIMTP produces high-resolution pixels using only 80% of the computational efforts required by 2D SIMP. This makes 2.5D SIMTP a practical and efficient option for structural design and optimisation when high-resolution pixels are necessary. However, if computational efficiency is a priority and high-resolution pixels are not necessary, 2D methods may be preferred.

The implementation of an adaptive refinement process into the 2.5D SIMTP tool has enabled an initial threshold as low as 10^{-3}, allowing for a more detailed analysis of the design space and providing valuable insights. The study highlights the importance of thickness filtering for achieving a stable Jacobian and practical designs in 2.5D SIMTP. In the absence of thickness filtering, a pathology called "islanding" can occur. However, adaptive refinement with thickness filtering may lead to the formation of thin members, emphasising the importance of careful design considerations and balancing structural performance with manufacturing feasibility.

In comparison to adaptive refinement, the traditional 2.5D SIMTP approach using a high threshold is a reliable and efficient method for yielding practical designs, particularly when computational resources are limited and the design space is well understood. In the majority of cases, traditional 2.5D SIMTP produces practical designs using only 25% of the computational efforts required by adaptive refinement.

The 2.5D SIMTP approach offers superior computational efficiency and optimised shapes, using only 60% of the resources required by 3D optimisation methods. This makes it a practical option for large-scale optimisation problems or situations where computational efficiency is a priority. Additionally, the approach can be complemented by 3D printing and surface fetching techniques to produce physical models of the optimised designs, allowing for the production of complex shapes and geometries for manufacturing purposes. The evaluation process demonstrated that the optimisation module was effective in generating optimised profiles that require minimal post-processing efforts to produce non-prismatic shapes. However, the use of single elements in the thickness direction can result in truss-like shapes, which is one limitation of 2.5D SIMTP.

Despite its limitations, the 2.5D SIMTP approach is not only computationally economical and efficient but also straightforward in producing high-resolution boundary surfaces, making it a promising alternative to traditional 3D optimisation methods. The approach's practical application was demonstrated by successfully 3D printing a prototype beam optimised using ABS M30i material, highlighting its potential for manufacturing purposes.

In addition to its computational efficiency, this study highlights how the 2.5D SIMTP approach can incorporate architectural expression into structural optimisation through surface fetching, as demonstrated in a trial implementation. However, further research is needed to explore the potential of other construction materials.

Traditional 3D concrete printing methods can limit the ductility requirements of printed concrete structures, which can be achieved by post-tensioning. To address this limitation, the 2.5D SIMTP approach was modified to optimise prestressed beams while simultaneously designing the tendon layout and concrete domain. The prestressing strategy employed in the study produced reliable results, with equivalent tendon forces applied to the concrete geometry based on the principle of virtual work.

The use of Bezier curve definitions for tendon geometry idealisation was effective in reducing the number of design variables by building the tendon layout with fewer control points. However, the results demonstrated that the initial tendon layout greatly influences the final design, and a suitable prestressing force should be chosen to balance the applied loads. Otherwise, the resulting profiles may be clumsy, impractical, and unappealing.

The comparison of optimised profiles with the work of Amir and Shakour demonstrated consistency and agreement with their findings. Furthermore, the results showed that the designs produced by 2.5D SIMTP were of high quality compared to their findings, demonstrating the potential of the approach for designing prestressed beams.

In summary, this thesis presents an innovative tool that integrates aesthetics, structural design, and manufacturing to improve the functional and aesthetic properties of structural components. The proposed approach efficiently retrieves and tracks the shapes of structural components, providing a reliable and efficient method for producing practical and optimised designs. The study offers valuable insights into the limitations and improvements of the SIMTP approach and 2.5D element.

The research demonstrates the potential of the approach in creating stable, computationally efficient, and high-resolution optimised designs for various structural problems. It is expected that the approach will bring significant technological changes to the construction industry. However, careful design considerations are necessary to balance structural performance with manufacturing feasibility, and the potential limitations of the approach must be taken into account.

Overall, the 2.5D SIMTP approach represents a significant advancement in the field of structural design and optimisation, and it has the potential to revolutionise the way building structures are designed in the future. For future implementations of this work, it is recommended to continue refining the approach to improve its capabilities and applicability to a wider range of structural problems.

8.2 Future Work

It should be noted that the demonstrated cases in the thesis are limited to elastic analysis, and the effects of material and geometric non-linearity are yet to be explored. Further research is needed to investigate the behaviour of the optimised designs under non-linear conditions and to develop appropriate design methodologies. While the results presented in the thesis are promising, it is important to consider the limitations and potential challenges of the 2.5D SIMTP approach. For example, the use of single elements in the thickness direction can result in truss-like shapes, and the approach's accuracy is limited to in-plane loading conditions. Future research will aim to explore 2.5D cases with multiple thickness elements as an objective by refining modelling assumptions and addressing computational complexity to achieve this goal. It would be an interesting scenario if 2.5D cases could be explored with multiple thickness elements, as this approach could help to capture more realistic and accurate behaviour of structures that may have varying thicknesses or material properties in different directions. Additionally, as mentioned earlier, the effects of material and geometric non-linearity on optimised designs need to be studied further. Self-weight has a noticeable impact on the optimal distribution of the material in prestressed systems. Further, several load combinations must be studied to understand the suitable design for serviceability and ultimate limit states. This process requires imposing further restrictions on deformation and stresses. Also, special care is required to eliminate thin, slender formations during optimisation, and this can only be achieved by imposing a length control. The authors look forward to implementing and incorporating the above ideas in future studies to bring the digitally fabricated optimised components into reality while meeting all the design requirements and practical engineering aspects.

In addition to the mechanical stiffness and strength aspects, achieving reliable ductility and tensile strength properties in homogenous materials used in 3D printing for fabricating structural components is likely to prove to be a major challenge. High-performance cementitious composites infused with fibres and prestressing perhaps hold the most promise in the short term and will be investigated, and considerably more research resources will need to be devoted to this area in future. Surface finishes of current 3D printed concrete are quite rough, and research will be needed to invent methodologies that can create more “finished” surfaces, perhaps also create surfaces with colours and textures (rather like textiles) as finishes, to take further inspiration from Antoni Gaudi, leading to a truly infinite range of architectural styles limited only by the designer’s imagination.

Based on the contents of this thesis, two funding proposals have been submitted while one was successful, and the other is under scrutiny. As an extension of the contents of this thesis, fibre-reinforced concrete systems are optimised for given conditions and will be manufactured in the coming year using funding from the Research Institute for Advanced Manufacturing (RIAM) based at PolyU.

References

[1] UnitedNationsEnvironmentProgramme. 2020 Global Status Report for Buildings and Construction: Towards a Zero-emission, Efficient and Resilient Buildings and Construction Sector. 15 December 2020 ed. www.worldgbc.org: Global Alliance for Buildings and Construction; 2020. p. 1-80. https://www.worldgbc.org/news-media/launch-2020-global-status-report-buildings-and-construction. Retrieved 19 January 2021

[2] Lam PTI, Chan EHW, Poon CS, Chau CK, Chun KP. Factors affecting the implementation of green specifications in construction. Journal of Environmental Management 2010;91:654-61. https://doi.org/10.1016/j.jenvman.2009.09.029

[3] Leiringer R, Gottlieb SC, Fang Y, Mo X. In search of sustainable construction: the role of building environmental assessment methods as policies enforcing green building. Construction Management and Economics 2022:1-19. https://doi.org/10.1080/01446193.2021.2021259

[4] Nie Y, Shi J, He Z, Zhang B, Peng Y, Lu J. Evaluation of high-volume fly ash (HVFA) concrete modified by metakaolin: Technical, economic and environmental analysis. Powder Technology 2022;397:117121. https://doi.org/10.1016/j.powtec.2022.117121

[5] De Schutter G, Lesage K, Mechtcherine V, Nerella VN, Habert G, Agusti-Juan I. Vision of 3D printing with concrete — Technical, economic and environmental potentials. Cement and Concrete Research 2018;112:25-36. https://doi.org/10.1016/j.cemconres.2018.06.001

[6] Zhang J, Wang J, Dong S, Yu X, Han B. A review of the current progress and application of 3D printed concrete. Composites Part A: Applied Science and Manufacturing 2019;125:105533. https://doi.org/10.1016/j.compositesa.2019.105533

[7] Weng Y, Li M, Ruan S, Wong TN, Tan MJ, Ow Yeong KL, et al. Comparative economic, environmental and productivity assessment of a concrete bathroom unit fabricated through 3D printing and a precast approach. Journal of Cleaner Production 2020;261:121245. https://doi.org/10.1016/j.jclepro.2020.121245

[8] Berman B. 3-D printing: The new industrial revolution. Business Horizons 2012;55:155-62. https://EconPapers.repec.org/RePEc:eee:bushor:v:55:y:2012:i:2:p:155-162.

[9] Lipson H, Kurman M. Fabricated: The new world of 3D printing: John Wiley & Sons; 2013. https://www.wiley.com/en-us/Fabricated%3A+The+New+World+of+3D+Printing-p-9781118350638.

[10] Feng P, Meng X, Chen J-F, Ye L. Mechanical properties of structures 3D printed with cementitious powders. Construction and Building Materials 2015;93:486-97. https://doi.org/10.1016/j.conbuildmat.2015.05.132

[11] Pedreschi R. The Engineer's Contribution to Contemporary Architecture: Eladio Dieste. Thomas Telford, London, UK 2000. https://doi.org/10.1680/edtectca.27725

[12] Candela F. Seven Structural Engineers: The Felix Candela Lectures. The Museum of Modern Art, New York, USA 2008.

[13] Plocher J, Panesar A. Review on design and structural optimisation in additive manufacturing: Towards next-generation lightweight structures. Materials & Design 2019;183:108164. https://doi.org/10.1016/j.matdes.2019.108164

[14] Zhang Z, Yarlagadda T, Zheng Y, Jiang L, Usmani A. Isogeometric analysis-based design of post-tensioned concrete beam towards construction-oriented topology optimisation. Structural and Multidisciplinary Optimisation 2021. https://doi.org/10.1007/s00158-021-03058-z

[15] Bendsøe MP, Kikuchi N. Generating optimal topologies in structural design using a homogenization method. Computer Methods in Applied Mechanics and Engineering 1988;71:197-224. https://doi.org/10.1016/0045-7825(88)90086-2

[16] Bendsøe MP. Optimal shape design as a material distribution problem. Structural optimisation 1989;1:193-202. https://doi.org/10.1007/BF01650949

[17] Zhou M, Rozvany GIN. The COC algorithm, Part II: Topological, geometrical and generalized shape optimisation. Computer Methods in Applied Mechanics and Engineering 1991;89:309-36. https://doi.org/10.1016/0045-7825(91)90046-9

[18] Rozvany GIN, Zhou M, Birker T. Generalized shape optimisation without homogenization. Structural Optimisation 1992;4:250. https://doi.org/10.1007/BF01742754

[19] Stolpe M, Svanberg K. An alternative interpolation scheme for minimum compliance topology optimisation. Structural and Multidisciplinary Optimisation 2001;22:116-24. https://doi.org/10.1007/s001580100129

[20] Bruns TE. A reevaluation of the SIMP method with filtering and an alternative formulation for solid–void topology optimisation. Structural and Multidisciplinary Optimisation 2005;30:428-36. https://doi.org/10.1007/s00158-005-0537-x

[21] Fuchs MB, Jiny S, Peleg N. The SRV constraint for 0/1 topological design. Structural and Multidisciplinary Optimisation 2005;30:320-6. https://doi.org/10.1007/s00158-005-0526-0

[22] Sethian JA, Wiegmann A. Structural Boundary Design via Level Set and Immersed Interface Methods. Journal of Computational Physics 2000;163:489-528. https://doi.org/10.1006/jcph.2000.6581

[23] Bourdin B, Chambolle A. Design-dependent loads in topology optimisation. ESAIM: COCV 2003;9:19-48. https://doi.org/10.1051/cocv:2002070

[24] Guo X, Zhang W, Zhong W. Doing Topology Optimisation Explicitly and Geometrically—A New Moving Morphable Components Based Framework. Journal of Applied Mechanics 2014;81. https://doi.org/10.1115/1.4027609

[25] Kobayashi MH. On a biologically inspired topology optimisation method. Communications in Nonlinear Science and Numerical Simulations 2010;15:787. https://doi.org/10.1016/j.cnsns.2009.04.014

[26] Xie YM, Steven GP. A simple evolutionary procedure for structural optimisation. Computers & Structures 1993;49:885-96. https://doi.org/10.1016/0045-7949(93)90035-C

[27] Buswell RA, Soar R, Gibb A, Thorpe A. Freeform Construction: Mega-scale Rapid Manufacturing for construction2007. https://doi.org/10.1016/j.autcon.2006.05.002

[28] Buswell RA, Soar RC, Gibb AGF, Thorpe A. Freeform Construction Application Research. Dordrecht: Springer Netherlands; 2006. p. 773-80. https://doi.org/10.1007/1-4020-4891-2_65. Retrieved

[29] Sungwoo L, Richard B, Philip J. V, Daniel P, Simon A, Xavier DK. Modelling curved-layered printing paths for fabricating large-scale construction components 2016. https://doi.org/10.1016/j.addma.2016.06.004

[30] Le TT, Austin SA, Lim S, Buswell RA, Gibb AGF, Thorpe T. Mix design and fresh properties for high-performance printing concrete. Materials and Structures 2012;45:1221-32. https://doi.org/10.1617/s11527-012-9828-z

[31] Papanek V, Fuller RB. Design for the real world: Thames and Hudson London; 1972.

[32] Kodama H. A scheme for three-dimensional display by automatic fabrication of three-dimensional model. IEICE Trans on Electronics 1981:237-41.

[33] Gao W, Zhang Y, Ramanujan D, Ramani K, Chen Y, Williams CB, et al. The status, challenges, and future of additive manufacturing in engineering. Computer-Aided Design 2015;69:65-89. https://doi.org/10.1016/j.cad.2015.04.001

[34] Hull CW. Apparatus for production of three-dimensional objects by stereolithography. Google Patents; 1986. Retrieved

[35] Crump SS. Apparatus and method for creating three-dimensional objects. Google Patents; 1992. Retrieved

[36] Lipsker D. Rapid prototyping. Google Patents; 2000. Retrieved

[37] Khoshevis B. Additive fabrication apparatus and method. Google Patents; 1996. Retrieved

[38] Doubrovski EL, Tsai EY, Dikovsky D, Geraedts JMP, Herr H, Oxman N. Voxel-based fabrication through material property mapping: A design method for bitmap printing. Computer-Aided Design 2015;60:3-13. https://doi.org/10.1016/j.cad.2014.05.010

[39] Persembe E, Parra-Cabrera C, Clasen C, Ameloot R. Binder-jetting 3D printer capable of voxel-based control over deposited ink volume, adaptive layer thickness, and selective multi-pass printing. Review of Scientific Instruments 2021;92:125106. https://doi.org/10.1063/5.0072715

[40] Otto IA, Capendale PE, Garcia JP, de Ruijter M, van Doremalen RFM, Castilho M, et al. Biofabrication of a shape-stable auricular structure for the reconstruction of ear deformities. Materials Today Bio 2021;9:100094. https://doi.org/10.1016/j.mtbio.2021.100094

[41] Gardiner J. Exploring the emerging design territory of construction 3D printing-project led architectural research. 2011. https://doi.org/10.13140/RG.2.2.11676.28807

[42] Deckard CR. Method and apparatus for producing parts by selective sintering. Google Patents; 1989. Retrieved

[43] Seibert J, Rynerson M. Solid free-form fabrication apparatus and method. Google Patents; 2009. Retrieved

[44] Rudenko A. Concrete 3D Castle completed 2014, August 25. http://www.totalkustom.com/3d-castle-completed.html. Retrieved January 10

[45] Sevenson B. Shanghai-based WinSun 3D Prints 6-Story Apartment Building and an Incredible Home. 3D Design, 3D Printing2015, January 18. https://3dprint.com/38144/3d-printed-apartment-building/. Retrieved

[46] Saunders S. 3D Printed Concrete Bridge in the Netherlands Officially Open to Cyclists. 3D Design, 3D Printing, 3D Printing Materials2017, October 18. https://3dprint.com/191375/3d-printed-concrete-bridge-open/. Retrieved

[47] Koslow T. Dubai's 3D Printed Office Building Officially Opened, Furnished By Bene. 3D Design, 3D Printing2016, August 17. https://3dprint.com/146273/dubai-office-furnished/. Retrieved

[48] Scott C. Chinese Construction Company 3D Prints an Entire Two-Story House On-Site in 45 Days. 3D Design, 3D Printers, 3D Printing Materials 2016, June 16. https://3dprint.com/138664/huashang-tengda-3d-print-house/. Retrieved

[49] MX3D. MX3D Bridge. 2018, October 20. https://mx3d.com/projects/bridge/. Retrieved

[50] Rudenko A. World's First 3D Printed Hotel Suite in the Philippines. 2015, December 15. http://www.totalkustom.com/. Retrieved

[51] Tay YWD, Panda B, Paul SC, Noor Mohamed NA, Tan MJ, Leong KF. 3D printing trends in building and construction industry: a review. Virtual and Physical Prototyping 2017;12:261-76. https://doi.org/10.1080/17452759.2017.1326724

[52] Menna C, Mata-Falcón J, Bos FP, Vantyghem G, Ferrara L, Asprone D, et al. Opportunities and challenges for structural engineering of digitally fabricated concrete. Cement and Concrete Research 2020;133:106079. https://doi.org/10.1016/j.cemconres.2020.106079

[53] Paolini A, Kollmannsberger S, Rank E. Additive manufacturing in construction: A review on processes, applications, and digital planning methods. Additive Manufacturing 2019;30:100894. https://doi.org/10.1016/j.addma.2019.100894

[54] OptiBridge: a topology optimised 3D-printed concrete bridge. Ghent, Belgium: Ghent University. https://www.ugent.be/ea/structural-engineering/en/research/projects/allprojects/optibridge2.htm. Retrieved 8 June 2022

[55] Ahmed Z, Wolfs R, Bos F, Salet T. A Framework for Large-Scale Structural Applications of 3D Printed Concrete: the Case of a 29 m Bridge in the Netherlands. Open Conference Proceedings 2022;1:5-19. https://doi.org/10.52825/ocp.v1i.74

[56] Vantyghem G, De Corte W, Shakour E, Amir O. 3D printing of a post-tensioned concrete girder designed by topology optimisation. Automation in Construction 2020;112:103084. https://doi.org/10.1016/j.autcon.2020.103084

[57] Salet TAM, Ahmed ZY, Bos FP, Laagland HLM. Design of a 3D printed concrete bridge by testing. Virtual and Physical Prototyping 2018;13:222-36. https://doi.org/10.1080/17452759.2018.1476064

[58] Asprone D, Auricchio F, Menna C, Mercuri V. 3D printing of reinforced concrete elements: Technology and design approach. Construction and Building Materials 2018;165:218-31. https://doi.org/10.1016/j.conbuildmat.2018.01.018

[59] Mechtcherine V, Nerella VN. Integration der Bewehrung beim 3D-Druck mit Beton. Beton- und Stahlbetonbau 2018;113:496-504. https://doi.org/10.1002/best.201800003

[60] Jipa M-A, Aghaei Meibodi M, Giesecke R, Shammas D, Leschok M, Bernhard M, et al. 3D-Printed Formwork for Prefabricated Concrete Slabs. Proceedings of 1st International Conference on 3D Construction Printing (3DcP), Melbourne, Australia, November 26-28, 2018: ETH Zurich, Digital Building Technologies (ITA); 2018. http://hdl.handle.net/20.500.11850/507716

[61] Rudenko A. World's First 3D Printed Hotel Suite in the Philippines. 2015, December 15. http://www.totalkustom.com/. Retrieved 8 June 2022

[62] Yang Y, Wu C, Liu Z, Wang H, Ren Q. Mechanical anisotropy of ultra-high performance fibre-reinforced concrete for 3D printing. Cement and Concrete Composites 2022;125:104310. https://doi.org/10.1016/j.cemconcomp.2021.104310

[63] Hambach M, Volkmer D. Properties of 3D-printed fiber-reinforced Portland cement paste. Cement and Concrete Composites 2017;79:62-70. https://doi.org/10.1016/j.cemconcomp.2017.02.001

[64] Panda B, Chandra Paul S, Jen Tan M. Anisotropic mechanical performance of 3D printed fiber reinforced sustainable construction material. Materials Letters 2017;209:146-9. https://doi.org/10.1016/j.matlet.2017.07.123

[65] Nematollahi B, Xia M, Sanjayan J, Vijay P. Effect of Type of Fiber on Inter-Layer Bond and Flexural Strengths of Extrusion-Based 3D Printed Geopolymer. Materials Science Forum 2018;939:155-62. https://doi.org/10.4028/www.scientific.net/MSF.939.155

[66] Bos FP, Bosco E, Salet TAM. Ductility of 3D printed concrete reinforced with short straight steel fibers. Virtual and Physical Prototyping 2019;14:160-74. https://doi.org/10.1080/17452759.2018.1548069

[67] Huang X, Xie YM. Bidirectional Evolutionary Topology Optimisation for Structures with Geometrical and Material Nonlinearities. AIAA Journal 2007;45:308-13. https://doi.org/10.2514/1.25046

[68] Sigmund O. Design of material structures using topology optimisation [Doctoral dissertation]: Technical University of Denmark Lyngby; 1994. https://www.researchgate.net/publication/261173987_Design_of_Material_Structures_Using_Topology_Optimisation

[69] Sigmund O, Petersson J. Numerical instabilities in topology optimisation: A survey on procedures dealing with checkerboards, mesh-dependencies and local minima. Structural optimisation 1998;16:68-75. https://doi.org/10.1007/BF01214002

[70] Bourdin B. Filters in topology optimisation. International Journal for Numerical Methods in Engineering 2001;50:2143-58. https://doi.org/10.1002/nme.116

[71] Bruns TE, Tortorelli DA. Topology optimisation of non-linear elastic structures and compliant mechanisms. Computer Methods in Applied Mechanics and Engineering 2001;190:3443-59. https://doi.org/10.1016/S0045-7825(00)00278-4

[72] Díaz A, Sigmund O. Checkerboard patterns in layout optimisation. Structural optimisation 1995;10:40-5. https://doi.org/10.1007/BF01743693

[73] Jog CS, Haber RB. Stability of finite element models for distributed-parameter optimisation and topology design. Computer Methods in Applied Mechanics and Engineering 1996;130:203-26. https://doi.org/10.1016/0045-7825(95)00928-0

[74] Guest JK, Prévost JH, Belytschko T. Achieving minimum length scale in topology optimisation using nodal design variables and projection functions. International Journal for Numerical Methods in Engineering 2004;61:238-54. https://doi.org/10.1002/nme.1064

[75] Jang G-W, Jeong JH, Kim YY, Sheen D, Park C, Kim M-N. Checkerboard-free topology optimisation using non-conforming finite elements. International Journal for Numerical Methods in Engineering 2003;57:1717-35. https://doi.org/10.1002/nme.738

[76] Jang G-W, Lee S, Kim YY, Sheen D. Topology optimisation using non-conforming finite elements: three-dimensional case. International Journal for Numerical Methods in Engineering 2005;63:859-75. https://doi.org/10.1002/nme.1302

[77] Haber RB, Jog CS, Bendsøe MP. A new approach to variable-topology shape design using a constraint on perimeter. Structural optimisation 1996;11:1-12. https://doi.org/10.1007/BF01279647

[78] Petersson J, Sigmund O. Slope constrained topology optimisation. International Journal for Numerical Methods in Engineering 1998;41:1417-34. https://doi.org/10.1002/(SICI)1097-0207(19980430)41:8<1417::AID-NME344>3.0.CO;2-N

[79] Zhou M, Shyy YK, Thomas HL. Checkerboard and minimum member size control in topology optimisation. Structural and Multidisciplinary Optimisation 2001;21:152-8. https://doi.org/10.1007/s001580050179

[80] Kobayashi M, Nishiwaki S, Izui K, Yoshimura M. An innovative design method for compliant mechanisms combining structural optimisations and designer creativity. Journal of Engineering Design 2009;20:125-54. https://doi.org/10.1080/09544820701565017

[81] Kogiso N, Ahn W, Nishiwaki S, Izui K, Yoshimura M. Robust Topology Optimisation for Compliant Mechanisms Considering Uncertainty of Applied Loads. Journal of Advanced Mechanical Design, Systems, and Manufacturing 2008;2:96. https://doi.org/10.1299/jamdsm.2.96

[82] Zhan J, Long L, Huang Z. Topology Optimisation of Thermally Actuated Compliant Mechanisms Using Node Design Variables. In: Zhang X, Wang N, Huang Y, editors. Mechanism and Machine Science. Singapore: Springer

Singapore; 2016. p. 667-75. https://doi.org/10.1007/978-981-10-2875-5_55. Retrieved

[83] Zhan J, Yang K, Huang Z. Topological Design of Hinge-Free Compliant Mechanisms Using the Node Design Variables Method. In: Zhang X, Liu H, Chen Z, Wang N, editors. Intelligent Robotics and Applications. Cham: Springer International Publishing; 2014. p. 567-75. https://doi.org/10.1007/978-3-319-13963-0_57. Retrieved

[84] Poulsen TA. A new scheme for imposing a minimum length scale in topology optimisation. International Journal for Numerical Methods in Engineering 2003;57:741-60. https://doi.org/10.1002/nme.694

[85] Zhu B, Zhang X, Zhang H, Liang J, Zang H, Li H, et al. Design of compliant mechanisms using continuum topology optimisation: A review. Mechanism and Machine Theory 2020;143:103622. https://doi.org/10.1016/j.mechmachtheory.2019.103622

[86] Kumar AV, Gossard DC. Synthesis of Optimal Shape and Topology of Structures. Journal of Mechanical Design 1996;118:68-74. https://doi.org/10.1115/1.2826858

[87] Hammer V. Checkmate? Nodal densities in topology optimisation. Proc II Max Planck Workshop on Engineering Design Optimisation, Dept of Mathematics, DTU, Denmark2001. Retrieved

[88] Bendsøe MP, Sigmund O. Topology optimisation by distribution of isotropic material. Topology Optimisation: Theory, Methods, and Applications. Berlin, Heidelberg: Springer Berlin Heidelberg; 2004. p. 1-69. https://doi.org/10.1007/978-3-662-05086-6_1

[89] Belytschko T, Xiao SP, Parimi C. Topology optimisation with implicit functions and regularization. International Journal for Numerical Methods in Engineering 2003;57:1177-96. https://doi.org/10.1002/nme.824

[90] Matsui K, Terada K. Continuous approximation of material distribution for topology optimisation. International Journal for Numerical Methods in Engineering 2004;59:1925-44. https://doi.org/10.1002/nme.945

[91] Rahmatalla SF, Swan CC. A Q4/Q4 continuum structural topology optimisation implementation. Structural and Multidisciplinary Optimisation 2004;27:130-5. https://doi.org/10.1007/s00158-003-0365-9

[92] Paulino GH, Le CH. A modified Q4/Q4 element for topology optimisation. Structural and Multidisciplinary Optimisation 2009;37:255-64. https://doi.org/10.1007/s00158-008-0228-5

[93] Kang Z, Wang Y. Structural topology optimisation based on non-local Shepard interpolation of density field. Computer Methods in Applied Mechanics and Engineering 2011;200:3515-25. https://doi.org/10.1016/j.cma.2011.09.001

[94] Kang Z, Wang Y. A nodal variable method of structural topology optimisation based on Shepard interpolant. International Journal for Numerical Methods in Engineering 2012;90:329-42. https://doi.org/10.1002/nme.3321

[95] Wang Y, Kang Z, He Q. An adaptive refinement approach for topology optimisation based on separated density field description. Computers & Structures 2013;117:10-22. https://doi.org/10.1016/j.compstruc.2012.11.004

[96] Guest JK. Topology optimisation with multiple phase projection. Computer Methods in Applied Mechanics and Engineering 2009;199:123-35. https://doi.org/10.1016/j.cma.2009.09.023

[97] Guest JK, Genut LCS. Reducing dimensionality in topology optimisation using adaptive design variable fields. International Journal for Numerical Methods in Engineering 2010;81:1019-45. https://doi.org/10.1002/nme.2724

[98] Nguyen TH, Paulino GH, Song J, Le CH. A computational paradigm for multiresolution topology optimisation (MTOP). Structural and Multidisciplinary Optimisation 2010;41:525-39. https://doi.org/10.1007/s00158-009-0443-8

[99] Almeida SRM, Paulino GH, Silva ECN. Layout and material gradation in topology optimisation of functionally graded structures: a global–local approach. Structural and Multidisciplinary Optimisation 2010;42:855-68. https://doi.org/10.1007/s00158-010-0514-x

[100] Areias P, Rodrigues HC, Rabczuk T. Coupled finite-element/topology optimisation of continua using the Newton-Raphson method. European Journal of Mechanics - A/Solids 2021;85:104117. https://doi.org/10.1016/j.euromechsol.2020.104117

[101] Wang H, Liu J, Wen G. An adaptive mesh-adjustment strategy for continuum topology optimisation to achieve manufacturable structural layout. International Journal for Numerical Methods in Engineering 2019;117:1304-22. https://doi.org/10.1002/nme.6001

[102] Wang Y-Q, He J-J, Luo Z, Kang Z. An adaptive method for high-resolution topology design. Acta Mechanica Sinica 2013;29:840-50. https://doi.org/10.1007/s10409-013-0084-4

[103] Liu Z, Korvink JG. Adaptive moving mesh level set method for structure topology optimisation. Engineering Optimisation 2008;40:529-58. https://doi.org/10.1080/03052150801985544

[104] Lambe AB, Czekanski A. Adaptive Topology Optimisation Using a Continuous Approximation of Material Distribution. ASME 2016 International Mechanical Engineering Congress and Exposition. Arizona, USA2016. https://doi.org/10.1115/imece2016-65537. Retrieved 5/23/2021

[105] Lambe AB, Czekanski A. Topology optimisation using a continuous density field and adaptive mesh refinement. International Journal for Numerical Methods in Engineering 2018;113:357-73. https://doi.org/10.1002/nme.5617

[106] Gao J, Xue H, Gao L, Luo Z. Topology optimisation for auxetic metamaterials based on isogeometric analysis. Computer Methods in Applied Mechanics and Engineering 2019;352:211-36. https://doi.org/10.1016/j.cma.2019.04.021

[107] Gao J, Luo Z, Xiao M, Gao L, Li P. A NURBS-based Multi-Material Interpolation (N-MMI) for isogeometric topology optimisation of structures. Applied Mathematical Modelling 2020;81:818-43. https://doi.org/10.1016/j.apm.2020.01.006

[108] Gao J, Gao L, Luo Z, Li P. Isogeometric topology optimisation for continuum structures using density distribution function. International Journal for Numerical Methods in Engineering 2019;119:991-1017. https://doi.org/10.1002/nme.6081

[109] Chi H, Pereira A, Menezes IFM, Paulino GH. Virtual element method (VEM)-based topology optimisation: an integrated framework. Structural and Multidisciplinary Optimisation 2020;62:1089-114. https://doi.org/10.1007/s00158-019-02268-w

[110] Cho S, Kwak J. Topology design optimisation of geometrically non-linear structures using meshfree method. Computer Methods in Applied Mechanics and Engineering 2006;195:5909-25. https://doi.org/10.1016/j.cma.2005.08.015

[111] Du Y, Luo Z, Tian Q, Chen L. Topology optimisation for thermo-mechanical compliant actuators using mesh-free methods. Engineering Optimisation 2009;41:753-72. https://doi.org/10.1080/03052150902834989

[112] Long K, Zuo Z, Zuberi RH. Study on parameters for topological variables field interpolated by moving least square approximation. Acta Mechanica

Solida Sinica 2009;22:180-8. https://doi.org/10.1016/S0894-9166(09)60103-8

[113] Luo Z, Zhang N, Wang Y, Gao W. Topology optimisation of structures using meshless density variable approximants. International Journal for Numerical Methods in Engineering 2013;93:443-64. https://doi.org/10.1002/nme.4394

[114] Zhang Y, Ge W, Tong X, Ye M. Topology optimisation of structures with coupled finite element – Element-free Galerkin method. Proceedings of the Institution of Mechanical Engineers, Part C: Journal of Mechanical Engineering Science 2018;232:731-45. https://doi.org/10.1177/0954406216688716

[115] Zhou JX, Zou W. Meshless approximation combined with implicit topology description for optimisation of continua. Structural and Multidisciplinary Optimisation 2008;36:347-53. https://doi.org/10.1007/s00158-007-0168-5

[116] Wang Y, Luo Z, Wu J, Zhang N. Topology optimisation of compliant mechanisms using element-free Galerkin method. Advances in Engineering Software 2015;85:61-72. https://doi.org/10.1016/j.advengsoft.2015.03.001

[117] Yang D, Liu H, Zhang W, Li S. Stress-constrained topology optimisation based on maximum stress measures. Computers & Structures 2018;198:23-39. https://doi.org/10.1016/j.compstruc.2018.01.008

[118] Zhu B, Zhang X, Li H, Liang J, Wang R, Li H, et al. An 89-line code for geometrically nonlinear topology optimisation written in FreeFEM. Structural and Multidisciplinary Optimisation 2021;63:1015-27. https://doi.org/10.1007/s00158-020-02733-x

[119] Zhao F. A nodal variable ESO (BESO) method for structural topology optimisation. Finite Elements in Analysis and Design 2014;86:34-40. https://doi.org/10.1016/j.finel.2014.03.012

[120] Du J, Olhoff N. Topological optimisation of continuum structures with design-dependent surface loading – Part I: new computational approach for 2D problems. Structural and Multidisciplinary Optimisation 2004;27:151-65. https://doi.org/10.1007/s00158-004-0379-y

[121] Du J, Olhoff N. Topological optimisation of continuum structures with design-dependent surface loading – Part II: algorithm and examples for 3D problems. Structural and Multidisciplinary Optimisation 2004;27:166-77. https://doi.org/10.1007/s00158-004-0380-5

[122] Carbonari RC, Silva ECN, Nishiwaki S. Topology optimisation applied to the design of multiactuated piezoelectric microtools. Smart Structures and

Materials 2004: Modeling, Signal Processing, and Control: International Society for Optics and Photonics; 2004. p. 277-88. https://doi.org/10.1117/12.538584. Retrieved

[123] Carbonari RC, Silva EC, Nishiwaki S. Optimum placement of piezoelectric material in piezoactuator design. Smart materials and structures 2007;16:207. https://doi.org/10.1088/0964-1726/16/1/025

[124] Wang H, Liu J, Wen G. An efficient multi-resolution topology optimisation scheme for stiffness maximization and stress minimization. Engineering Optimisation 2020:1-21. https://doi.org/10.1080/0305215X.2020.1853713

[125] Maute K, Ramm E. Adaptive techniques in topology optimisation. Proceedings of 5th Symposium on Multidisciplinary Analysis and Optimisation: American Institute of Aeronautics and Astronautics; 1994. https://arc.aiaa.org/doi/abs/10.2514/6.1994-4264

[126] Maute K, Ramm E. Adaptive topology optimisation. Structural optimisation 1995;10:100-12. https://doi.org/10.1007/BF01743537

[127] Maute K, Ramm E. Adaptive Topology Optimisation of Shell Structures. AIAA Journal 1997;35:1767-73. https://doi.org/10.2514/2.25

[128] Maute K, Schwarz S, Ramm E. Adaptive topology optimisation of elastoplastic structures. Structural optimisation 1998;15:81-91. https://doi.org/10.1007/BF01278493

[129] Kim JE, Jang G-W, Kim YY. Adaptive multiscale wavelet-Galerkin analysis for plane elasticity problems and its applications to multiscale topology design optimisation. International Journal of Solids and Structures 2003;40:6473-96. https://doi.org/10.1016/S0020-7683(03)00417-7

[130] Jang G-W, Kim JE, Kim YY. Multiscale Galerkin method using interpolation wavelets for two-dimensional elliptic problems in general domains. International Journal for Numerical Methods in Engineering 2004;59:225-53. https://doi.org/10.1002/nme.872

[131] Stainko R. An adaptive multilevel approach to the minimal compliance problem in topology optimisation. Communications in Numerical Methods in Engineering 2006;22:109-18. https://doi.org/10.1002/cnm.800

[132] Rossow MP, Taylor JE. A Finite Element Method for the Optimal Design of Variable Thickness Sheets. AIAA Journal 1973;11:1566-9. https://doi.org/10.2514/3.50631

[133] Bendsøe MP. Optimisation of structural topology, shape, and material. 1 ed: Springer; 1995. https://doi.org/10.1007/978-3-662-03115-5

[134] Li Q, Steven GP, Xie Y. Evolutionary thickness design with stiffness maximization and stress minimization criteria. International Journal for Numerical Methods in Engineering 2001;52:979-95. https://doi.org/10.1002/nme.241

[135] Li Q, Steven GP, Xie Y. Evolutionary structural optimisation for stress minimization problems by discrete thickness design. Computers & Structures 2000;78:769-80. https://doi.org/10.1016/S0045-7949(00)00057-2

[136] Li Q, Steven GP, Xie Y. A simple checkerboard suppression algorithm for evolutionary structural optimisation. Structural and Multidisciplinary Optimisation 2001;22:230-9. https://doi.org/10.1007/s001580100140

[137] Makrodimopoulos A, Bhaskar A, Keane AJ. A formulation of thickness optimisation for plane stress. Proceedings of 17th UK Conference on Computational Mechanics (ACME-UK) (05/04/09 - 07/04/09)2009. https://eprints.soton.ac.uk/69907/

[138] Makrodimopoulos A, Bhaskar A, Keane AJ. Second-order cone programming formulations for a class of problems in structural optimisation. Structural and Multidisciplinary Optimisation 2010;40:365. https://doi.org/10.1007/s00158-009-0376-2

[139] Kennedy GJ. Discrete thickness optimisation via piecewise constraint penalization. Structural and Multidisciplinary Optimisation 2015;51:1247-65. https://doi.org/10.1007/s00158-014-1210-z

[140] Kirsch U. Optimised prestressing by linear programming. International Journal for Numerical Methods in Engineering 1973;7:125-36. https://doi.org/10.1002/nme.1620070204

[141] Cohn MZ, MacRae AJ. Optimisation of Structural Concrete Beams. Journal of Structural Engineering 1984;110:1573-88. https://doi.org/10.1061/(ASCE)0733-9445(1984)110:7(1573)

[142] Quiroga AS, Arroyo MAU. Optimisation of prestressed concrete bridge decks. Computers & Structures 1991;41:553-9. https://doi.org/10.1016/0045-7949(91)90149-G

[143] Erbatur F, Zaid RA, Dahman NA. Optimisation and sensitivity of prestressed concrete beams. Computers & Structures 1992;45:881-6. https://doi.org/10.1016/0045-7949(92)90046-3

[144] Lounis Z, Cohn MZ. Multiobjective Optimisation of Prestressed Concrete Structures. Journal of Structural Engineering 1993;119:794-808. https://doi.org/10.1061/(ASCE)0733-9445(1993)119:3(794)

[145] Cohn MZ, Lounis Z. Optimum Limit Design of Continuous Prestressed Concrete Beams. Journal of Structural Engineering 1993;119:3551-70. https://doi.org/10.1061/(ASCE)0733-9445(1993)119:12(3551)

[146] Al-Gahtani AS, Al-Saadoun SS, Abul-Feilat EA. Design optimisation of continuous partially prestressed concrete beams. Computers & Structures 1995;55:365-70. https://doi.org/10.1016/0045-7949(94)00481-H

[147] Han SH, Adamu A, Karihaloo BL. MINIMUM COST DESIGN OF MULTISPAN PARTIALLY PRESTRESSED CONCRETE BEAMS USING DCOC. Engineering Optimisation 1996;26:35-59. https://doi.org/10.1080/03052159608941109

[148] Han SH, Adamu A, Karihaloo BL. Minimum cost design of multispan partially prestressed concrete T-beams using DCOC. Structural optimisation 1996;12:75-86. https://doi.org/10.1007/BF01196938

[149] Fontan AN, Diaz JM, Baldomir A, Hernandez S. Improved Optimisation Formulations for Launching Nose of Incrementally Launched Prestressed Concrete Bridges. Journal of Bridge Engineering 2011;16:461-70. https://doi.org/doi:10.1061/(ASCE)BE.1943-5592.0000169

[150] Barakat S, Kallas N, Taha MQ. Single objective reliability-based optimisation of prestressed concrete beams. Computers & Structures 2003;81:2501-12. https://doi.org/10.1016/S0045-7949(03)00305-5

[151] Barakat S, Bani-Hani K, Taha MQ. Multi-objective reliability-based optimisation of prestressed concrete beams. Structural Safety 2004;26:311-42. https://doi.org/10.1016/j.strusafe.2003.09.001

[152] Cagatay Ismail H, Dundar C, Aksogan O. Optimum design of prestressed concrete beams by a modified grid search method. Structural Engineering and Mechanics 2003;15:39-52. https://doi.org/10.12989/SEM.2003.15.1.039

[153] Aydın Z, Ayvaz Y. Optimum topology and shape design of prestressed concrete bridge girders using a genetic algorithm. Structural and Multidisciplinary Optimisation 2010;41:151-62. https://doi.org/10.1007/s00158-009-0404-2

[154] Aydın Z, Ayvaz Y. Overall cost optimisation of prestressed concrete bridge using genetic algorithm. KSCE Journal of Civil Engineering 2013;17:769-76. https://doi.org/10.1007/s12205-013-0355-4

[155] Quaranta G, Fiore A, Marano GC. Optimum design of prestressed concrete beams using constrained differential evolution algorithm. Structural and

Multidisciplinary Optimisation 2014;49:441-53. https://doi.org/10.1007/s00158-013-0979-5

[156] Dahman NA, Irhouma AH, Mousa AI, Saadideen WK, Allan MJ. Design optimisation and sensitivity analysis of simply supported prestressed concrete girders: A two dimensional non-linear paradigm. Journal of King Saud University - Engineering Sciences 2021. https://doi.org/10.1016/j.jksues.2021.02.006

[157] Nie J-G, Zhu Y-J, Tao M-X, Guo C-R, Li Y-X. Optimised Prestressed Continuous Composite Girder Bridges with Corrugated Steel Webs. Journal of Bridge Engineering 2017;22:04016121. https://doi.org/10.1061/(ASCE)BE.1943-5592.0000995

[158] Olhoff N, Taylor JE. On Structural Optimisation. Journal of Applied Mechanics 1983;50:1139-51. https://doi.org/10.1115/1.3167196

[159] Patnaik SN, Guptill JD, Berke L. Merits and limitations of optimality criteria method for structural optimisation. International Journal for Numerical Methods in Engineering 1995;38:3087-120. https://doi.org/10.1002/nme.1620381806

[160] Yin L, Yang W. Optimality criteria method for topology optimisation under multiple constraints. Computers & Structures 2001;79:1839-50. https://doi.org/10.1016/S0045-7949(01)00126-2

[161] Qing Quan Liang YMX, Grant PS. Generating Optimal Strut-and-Tie Models in Prestressed Concrete Beams by Performance-Based Optimisation. ACI Structural Journal;98. https://doi.org/10.14359/10191

[162] Eurviriyanukul S, Askes H. The equilibration of configurational forces in the tendon layout optimisation of pre-stressed concrete beams. Computers & Structures 2010;88:1412-8. https://doi.org/10.1016/j.compstruc.2008.08.007

[163] Eurviriyanukul S, Askes H. Tendon layout optimisation through configurational forces equilibration in plane stress analysis of prestressed concrete structures. Computers & Structures 2011;89:1673-80. https://doi.org/10.1016/j.compstruc.2011.04.011

[164] Amir O, Shakour E. Simultaneous shape and topology optimisation of prestressed concrete beams. Structural and Multidisciplinary Optimisation 2018;57:1831-43.

[165] Zhang Z, Yarlagadda T, Zheng Y, Jiang L, Usmani A. SourceCodeR.zip. 2021. https://doi.org/10.13140/RG.2.2.28117.91368. Retrieved 16 June 2022

[166] Sigmund O, Maute K. Topology optimisation approaches. Structural and Multidisciplinary Optimisation 2013;48:1031-55. https://doi.org/10.1007/s00158-013-0978-6

[167] Zegard T, Hartz C, Mazurek A, Baker WF. Advancing building engineering through structural and topology optimisation. Structural and Multidisciplinary Optimisation 2020;62:915-35. https://doi.org/10.1007/s00158-020-02506-6

[168] Rozvany GIN. A critical review of established methods of structural topology optimisation. Structural and Multidisciplinary Optimisation 2009;37:217-37. https://doi.org/10.1007/s00158-007-0217-0

[169] Deaton JD, Grandhi RV. A survey of structural and multidisciplinary continuum topology optimisation: post 2000. Structural and Multidisciplinary Optimisation 2014;49:1-38. https://doi.org/10.1007/s00158-013-0956-z

[170] Van Dijk NP, Maute K, Langelaar M, van Keulen F. Level-set methods for structural topology optimisation: a review. Structural and Multidisciplinary Optimisation 2013;48:437-72. https://doi.org/10.1007/s00158-013-0912-y

[171] Zhu J-H, Zhang W-H, Xia L. Topology Optimisation in Aircraft and Aerospace Structures Design. Archives of Computational Methods in Engineering 2016;23:595-622. https://doi.org/10.1007/s11831-015-9151-2

[172] Dvorkin EN, Bathe KJ. A continuum mechanics based four-node shell element for general non-linear analysis. Engineering Computations 1984;1:77-88. https://doi.org/10.1108/eb023562

[173] Shabana AA, Yakoub RY. Three Dimensional Absolute Nodal Coordinate Formulation for Beam Elements: Theory. Journal of Mechanical Design 2000;123:606-13. https://doi.org/10.1115/1.1410100

[174] Mikkola AM, Shabana AA. A Non-Incremental Finite Element Procedure for the Analysis of Large Deformation of Plates and Shells in Mechanical System Applications. Multibody System Dynamics 2003;9:283-309. https://doi.org/10.1023/A:1022950912782

[175] Abbas LK, Rui X, Hammoudi ZS. Plate/shell element of variable thickness based on the absolute nodal coordinate formulation. Proceedings of the Institution of Mechanical Engineers, Part K: Journal of Multi-body Dynamics 2010;224:127-41. https://doi.org/10.1243/14644193jmbd244

[176] Ko Y, Lee P-S, Bathe K-J. The MITC4+ shell element and its performance. Computers & Structures 2016;169:57-68. https://doi.org/10.1016/j.compstruc.2016.03.002

[177] Ai-Kah S, Yuqiu L, Song C. Development of eight-node quadrilateral membrane elements using the area coordinates method. Computational Mechanics 2000;25:376-84. https://doi.org/10.1007/s004660050484

[178] Zienkiewicz OC, Taylor RL, Zhu JZ. Chapter 8 - The Patch Test, Reduced Integration, and Nonconforming Elements. In: Zienkiewicz OC, Taylor RL, Zhu JZ, editors. The Finite Element Method: its Basis and Fundamentals (Seventh Edition). Oxford: Butterworth-Heinemann; 2013. p. 257-84. https://doi.org/10.1016/B978-1-85617-633-0.00008-3

[179] Bathe K-J. Finite element procedures: Klaus-Jurgen Bathe; 2006.

[180] Shepard D. A two-dimensional interpolation function for irregularly-spaced data. Proceedings of Proceedings of the 1968 23rd ACM national conference: Association for Computing Machinery; 1968. https://doi.org/10.1145/800186.810616

[181] Bucki M, Lobos C, Payan Y, Hitschfeld N. Jacobian-based repair method for finite element meshes after registration. Engineering with Computers 2011;27:285-97. https://doi.org/10.1007/s00366-010-0198-2

[182] Andreassen E, Clausen A, Schevenels M, Lazarov BS, Sigmund O. Efficient topology optimisation in MATLAB using 88 lines of code. Structural and Multidisciplinary Optimisation 2011;43:1-16. https://doi.org/10.1007/s00158-010-0594-7

[183] Liu K, Tovar A. An efficient 3D topology optimisation code written in Matlab. Structural and Multidisciplinary Optimisation 2014;50:1175-96. https://doi.org/10.1007/s00158-014-1107-x

[184] Dorfler W. A Convergent Adaptive Algorithm for Poisson's Equation. SIAM Journal on Numerical Analysis 1996;33:1106-24. http://www.jstor.org/stable/2158497.

[185] Alberty J, Carstensen C, Funken SA. Remarks around 50 lines of Matlab: short finite element implementation. Numerical Algorithms 1999;20:117-37. https://doi.org/10.1023/A:1019155918070

[186] Schneiders R. Algorithms for quadrilateral and hexahedral mesh generation. 2000. https://www.researchgate.net/publication/228740922_Algorithms_for_quadrilateral_and_hexahedral_mesh_generation.

[187] Bartels S, Carstensen C, Hecht A. P2Q2Iso2D=2D Isoparametric FEM in Matlab. Journal of Computational and Applied Mathematics 2006;192:219-50. https://doi.org/10.1016/j.cam.2005.04.032

[188] CHEN L. SHORT IMPLEMENTATION OF BISECTION IN MATLAB. Recent Advances in Computational Sciences 2008:318-32. https://doi.org/10.1142/9789812792389_0020

[189] Chen L. iFEM: an innovative finite element methods package in MATLAB. Preprint, University of Maryland 2008. https://www.math.uci.edu/~chenlong/Papers/iFEMpaper.pdf.

[190] Zhao X, Mao S, Shi Z. Adaptive Finite Element Methods on Quadrilateral Meshes without Hanging Nodes. SIAM Journal on Scientific Computing 2010;32:2099-120. https://doi.org/10.1137/090772022

[191] Funken S, Praetorius D, Wissgott P. Efficient implementation of adaptive P1-FEM in Matlab. Computational Methods in Applied Mathematics 2011;11:460-90. https://doi.org/10.2478/cmam-2011-0026

[192] Schneiders R. Mesh generation & grid generation on the web. www-users informatik rwthaachen de/∼ roberts/new_exampleshtml 2015.

[193] Funken S, Schmidt A. ameshref–Efficient implementation of adaptive mesh refinement in 2D. Software download at https://githubcom/aschmidtuulm/ameshref 2018.

[194] Funken SA, Schmidt A. Adaptive Mesh Refinement in 2D – An Efficient Implementation in Matlab. Computational Methods in Applied Mathematics 2020;20:459-79. https://doi.org/10.1515/cmam-2018-0220

[195] Franke R. A Critical Comparison of Some Methods for Interpolation of Scattered Data. 1979. http://hdl.handle.net/10945/35052. Retrieved

[196] Gupta AK. A finite element for transition from a fine to a coarse grid. International Journal for Numerical Methods in Engineering 1978;12:35-45. https://doi.org/10.1002/nme.1620120104

[197] Demkowicz L, Oden JT, Rachowicz W, Hardy O. Toward a universal h-p adaptive finite element strategy, part 1. Constrained approximation and data structure. Computer Methods in Applied Mechanics and Engineering 1989;77:79-112. https://doi.org/10.1016/0045-7825(89)90129-1

[198] Ainsworth M, Senior B. Aspects of an adaptive hp-finite element method: Adaptive strategy, conforming approximation and efficient solvers. Computer Methods in Applied Mechanics and Engineering 1997;150:65-87. https://doi.org/10.1016/S0045-7825(97)00101-1

[199] Sandhu JS, Liebowitz H. Examples of adaptive FEA in plasticity. Engineering Fracture Mechanics 1995;50:947-56. https://doi.org/10.1016/0013-7944(94)E0043-G

[200] Patil RU, Mishra BK, Singh IV. An adaptive multiscale phase field method for brittle fracture. Computer Methods in Applied Mechanics and Engineering 2018;329:254-88. https://doi.org/10.1016/j.cma.2017.09.021

[201] Fries T-P, Byfut A, Alizada A, Cheng KW, Schröder A. Hanging nodes and XFEM. International Journal for Numerical Methods in Engineering 2011;86:404-30. https://doi.org/10.1002/nme.3024

[202] Sarkar S, Singh IV, Mishra BK. Adaptive mesh refinement schemes for the localizing gradient damage method based on biquadratic-bilinear coupled-field elements. Engineering Fracture Mechanics 2020;223:106790. https://doi.org/10.1016/j.engfracmech.2019.106790

[203] Sven. stlwrite - write ASCII or Binary STL files. MATLAB Central File Exchange: MathWorks; 2021. https://www.mathworks.com/matlabcentral/fileexchange/20922-stlwrite-write-ascii-or-binary-stl-files. Retrieved December 8, 2021.

[204] Armstrong CG. Modelling requirements for finite-element analysis. Computer-Aided Design 1994;26:573-8. https://doi.org/10.1016/0010-4485(94)90088-4

[205] Robert BBM. Equivalent Load Method for Analyzing prestressed Concrete Structures. ACI Journal Proceedings 1952;48. https://doi.org/10.14359/11893

[206] Orosz I. Simplified method for calculating shear deflections of beams: US Department of Agriculture, Forest Service; 1970. https://www.fs.usda.gov/treesearch/pubs/5840.

[207] Oh BH, Jeon SJ. Limitations and realistic application of equivalent load methods in pre-stressed concrete structures. Magazine of Concrete Research 2002;54:223-31. https://doi.org/10.1680/macr.2002.54.3.223

[208] Lin TY. Load-Balancing Method for Design and Analysis of Prestressed Concrete Structures. ACI Journal Proceedings;60. https://doi.org/10.14359/7874

[209] Sigmund O. Morphology-based black and white filters for topology optimisation. Structural and Multidisciplinary Optimisation 2007;33:401-24. https://doi.org/10.1007/s00158-006-0087-x

[210] Wang F, Lazarov BS, Sigmund O. On projection methods, convergence and robust formulations in topology optimisation. Structural and Multidisciplinary Optimisation 2011;43:767-84. https://doi.org/10.1007/s00158-010-0602-y

[211] Lazarov BS, Wang F, Sigmund O. Length scale and manufacturability in density-based topology optimisation. Archive of Applied Mechanics 2016;86:189-218. https://doi.org/10.1007/s00419-015-1106-4

Appendix A

2D Elasticity Solution

In general, analytical solutions for 2D elasticity problems are derived based on the Airys stress function, and these solutions are limited to a constant width of a beam. However, case-I has linearly varying width across the span (trapezoidal beam), where general Airys stress function does not hold good. The analytical solution presented here is inspired by Airys stress function. The derived solution is limited to a simply supported trapezoidal beam assuming plane stress conditions.

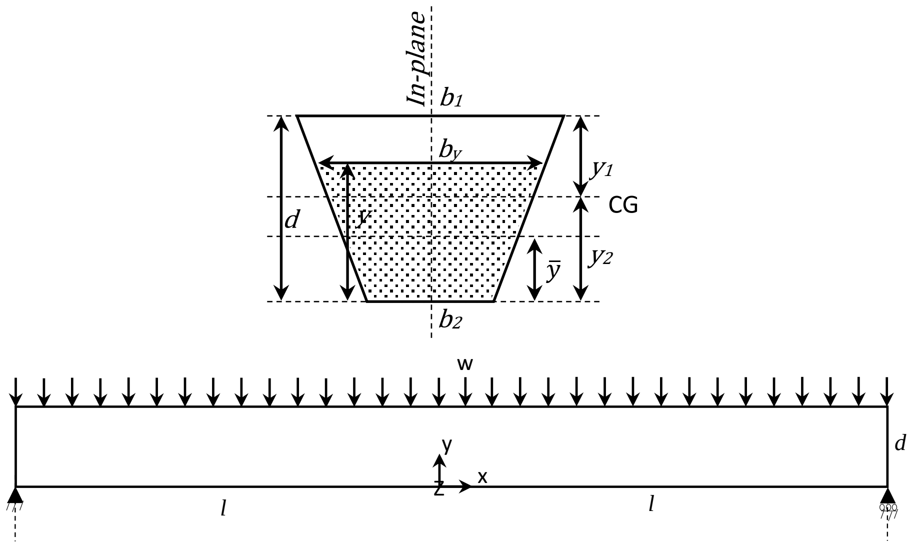

Stress equilibrium equations for a trapezoidal beam

$$\frac{\partial(\sigma_{xx}b_y)}{\partial x}+\frac{\partial(\sigma_{xy}b_y)}{\partial y}=0;\ \frac{\partial(\sigma_{xy}b_y)}{\partial x}+\frac{\partial(\sigma_{yy}b_y)}{\partial y}=0$$

Stresses should be of the following form in order to obey the above equilibrium equations

$$\sigma_{xx}=\frac{1}{b_y}\frac{\partial^2\phi}{\partial y^2};\ \sigma_{yy}=\frac{1}{b_y}\frac{\partial^2\phi}{\partial x^2};\ \sigma_{xy}=-\frac{1}{b_y}\frac{\partial^2\phi}{\partial x\partial y}$$

Stress, strain and displacement relationship (Poisson ratio is zero)

$$\varepsilon_{xx}=\frac{\partial u_x}{\partial x}=\frac{\sigma_{xx}}{E};\ \varepsilon_{yy}=\frac{\partial u_y}{\partial y}=\frac{\sigma_{yy}}{E};\ \varepsilon_{xy}=\frac{1}{2}\left(\frac{\partial u_x}{\partial y}+\frac{\partial u_y}{\partial x}\right)=\frac{\sigma_{xy}}{E}$$

Since strains are interdependent, they should satisfy the following compatibility equation

$$\frac{\partial^2\varepsilon_{xx}}{\partial y^2}+\frac{\partial^2\varepsilon_{yy}}{\partial x^2}=2\frac{\partial^2\varepsilon_{xy}}{\partial x\partial y}$$

Now substituting stress-strain relations and earlier assumed stress forms in the above compatibility equation, ϕ should satisfy the following criteria

$$b_y^2\left(\frac{\partial^4\phi}{\partial y^4}+\frac{\partial^4\phi}{\partial x^4}+2\frac{\partial^4\phi}{\partial x^2\partial y^2}\right)-2k_0b_y\left(\frac{\partial^3\phi}{\partial y^3}+\frac{\partial^3\phi}{\partial x^2\partial y}\right)+2k_0^2\frac{\partial^2\phi}{\partial y^2}=0$$

Any general function can satisfy the above equation, for example, $\phi=0$, but it has to satisfy the boundary conditions of case-I, which are as follows

Shear Stress at the top and bottom of the beam	:	$\sigma_{xy}(x,0)=0;\ \sigma_{xy}(x,d)=0$
Vertical Stress at the bottom of the beam	:	$\sigma_{yy}(x,0)=0$
Vertical Stress at the top of the beam	:	$\sigma_{yy}(x,d)=-\frac{w}{b_1}$

Axial force at ends : $\int_{-d}^{d} \sigma_{xx}(\pm l, y) b_y \, dy = 0$

Shear forces at ends : $\int_{-d}^{d} \sigma_{xy}(\pm l, y) \, b_y dy = \pm wl$

Moment at ends : $\int_{-d}^{d} \sigma_{xx}(\pm l, y) b_y y \, dy = 0$

Vertical deformation at both ends : $u_y(\pm l, 0) = 0$

Axial deformation at the left end : $u_x(-l, 0) = 0$

Assuming second to sixth-degree power series as a stress function since (1) criterion equation for ϕ is a fourth-order derivative; (2) width is a dependent variable; (3) stress components are second-order derivatives

$$\phi = \sum_{i=0}^{6} \sum_{j=0}^{6} \delta_{ij} C_{ij} x^i y^j$$

$$\delta_{ij} = \begin{cases} 1, & if \ 2 \le i + j \le 6 \\ 0, & otherwise \end{cases}$$

Considering the x-symmetry of the problem, ϕ should be an even function. Therefore, coefficients corresponding to the odd-order should be zero

$$\forall i \in [1,3,5], \forall j \in Z_{[0,6]}, 2 \le \ i + j \le 6: C_{ij} = 0$$

Now solving the above equations for ϕ satisfying the earlier stated criterion and boundary conditions

$$\phi = \sum_{j=2}^{6} \left(C_{0j} y^j \right) + \sum_{j=2}^{4} \left(C_{2j} x^2 y^j \right)$$

$$\sigma_{xx} = \frac{1}{b_y} \begin{pmatrix} 2C_{02} + 6C_{03}y + 12C_{04}y^2 + 20C_{05}y^3 \\ +30C_{06}y^4 + 2C_{22}x^2 + 6C_{23}x^2 y + 12C_{24}x^2 y^2 \end{pmatrix}$$

$$\sigma_{yy} = \frac{1}{b_y}(2C_{22}y^2 + 2C_{23}y^3 + 2C_{24}y^4);\ \sigma_{xy} = -\frac{1}{b_y}(4C_{22}xy + 6C_{23}xy^2 + 8C_{24}xy^3)$$

$$u_x = \frac{1}{Eb_y}\left(\begin{array}{c} 2C_{02}x + 6C_{03}xy + 12C_{04}xy^2 + 20C_{05}xy^3 + 30C_{06}xy^4 + \frac{2}{3}C_{22}x^3 \\ +2C_{23}x^3y + 4C_{24}x^3y^2 + a_1b_y \end{array}\right)$$

$$u_y = \frac{1}{Eb_y}\left(\frac{2}{3}C_{22}y^3 + \frac{1}{2}C_{23}y^4 + \frac{2}{5}C_{24}y^5 + g(x,y)\right)$$

$$\begin{bmatrix} 4k_0^2 & -12b_2k_0 & 24b_2^2 & 0 & 0 & 8b_2^2 & 0 & 0 \\ 0 & 0 & 0 & 120b_2^2 & 0 & 8b_2k_0 & 24b_2^2 & 0 \\ 0 & 0 & 0 & 120b_2k_0 & 360b_2^2 & 0 & 36b_2k_0 & 48b_2^2 \\ 0 & 0 & 0 & 0 & 0 & 4k_0^2 & -12b_2k_0 & 24b_2^2 \\ 0 & 0 & 0 & 0 & 0 & 4d & 6d^2 & 8d^3 \\ 0 & 0 & 0 & 0 & 0 & 2d & 2d^2 & 2d^3 \\ 2 & 3d & 4d^2 & 5d^3 & 6d^4 & 2l^2 & 3l^2d & 4l^2d^2 \\ 1 & 2d & 3d^2 & 4d^3 & 5d^4 & l^2 & 2l^2d & 3l^2d^2 \end{bmatrix} \begin{bmatrix} C_{02} \\ C_{03} \\ C_{04} \\ C_{05} \\ C_{06} \\ C_{22} \\ C_{23} \\ C_{24} \end{bmatrix} = \begin{bmatrix} 0 \\ 0 \\ 0 \\ 0 \\ 0 \\ -\frac{w}{d} \\ 0 \\ 0 \end{bmatrix}$$

$$g(x,y) = \left(\begin{array}{c} \frac{k_0}{b_y}\left(\begin{array}{c} C_{02}x^2 + 3C_{03}x^2y + 6C_{04}x^2y^2 + 10C_{05}x^2y^3 + 15C_{06}x^2y^4 \\ + \frac{C_{22}x^4}{6} + \frac{C_{23}x^4y}{2} + C_{24}x^4y^2 \end{array}\right) \\ -\left(\begin{array}{c} 4C_{22}x^2y + 6C_{23}x^2y^2 + 8C_{24}x^2y^3 + 3C_{03}x^2 + 12C_{04}x^2y \\ +30C_{05}x^2y^2 + 60C_{06}x^2y^3 + \frac{C_{23}x^4}{2} + 2C_{24}x^4y + a_2b_y \end{array}\right) \end{array}\right)$$

$$k_0 = \frac{b_1 - b_2}{d};\ a_1 = \frac{\left(2C_{02}l + \frac{2}{3}C_{22}l^3\right)}{b_2};\ a_2 = \frac{k_0\left(C_{02}l^2 + \frac{1}{6}C_{22}l^4\right) - b_2\left(3C_{03}l^2 + \frac{1}{2}C_{23}l^4\right)}{b_2^2}$$

For example, substituting the beam properties in u_y

$$b_1 = 0.1\ m;\ b_2 = 0.05\ m;\ d = 0.1\ m;\ l = 0.5\ m;\ E = 2.5\ kPa;$$

$$S = 0.1\ Pa;\ w = b_1S$$

$$u_y(0,0) = 8.804\ \times 10^{-3}\ m$$

Timoshenko beam solution

Further a Timoshenko beam deflection is also estimated using the following equation

$$U_y = \frac{5w(2l)^4}{384EI} + \frac{kw(2l)^2}{8AG}$$

Where 'k' is a factor generally obtained from the ratio of shearing stress at the centroid of a cross-section to average shear stress, which is 1.5 for rectangular/square cross-sections, however k here is estimated from Orosz's definition [206]. Orosz's definition is based on the variation of shear stress from top to bottom of the section while general calculation, as discussed earlier, is based on the shear stress at the centroid irrespective of stress profile.

$$k = \int_A \frac{S_y^2 A}{I^2 b_y^2} dA$$

$$\forall y \in [0, d] : \; S_y = \left(\frac{b_2 + b_y}{2}\right) y(y_2 - \overline{y})$$

$$\forall y \in [0, d] : \; \overline{y} = \frac{y}{3}\left(\frac{b_2 + 2b_y}{b_2 + b_y}\right)$$

$$\forall y \in [0, d] : \; b_y = b_2 + \frac{y}{d}(b_1 - b_2)$$

$$\forall y \in [0, d] : \; dA = b_y dy$$

$$I = \frac{d^3}{36}\left(\frac{b_1^2 + 4b_1 b_2 + b_2^2}{b_1 + b_2}\right)$$

$$y_1 = \frac{d}{3}\left(\frac{b_1 + 2b_2}{b_1 + b_2}\right)$$

$$y_2 = \frac{d}{3}\left(\frac{2b_1 + b_2}{b_1 + b_2}\right)$$

$$A = \frac{(b_1 + b_2)d}{2}$$

Assuming

$$y = \left(\frac{Y - b_2}{b_1 - b_2}\right) d$$

$$b_y = Y$$

$$dy = \frac{d}{b_1 - b_2} dY$$

$$y \in [0, d] \rightarrow Y \in [b_2, b_1]$$

Solving the integral

$$k = C\left(4d^2Y^6 + K_2^2 b_2 \log_e Y + \frac{K_3Y^5}{5} + \frac{K_4Y^4}{4} + \frac{K_5Y^3}{3} + \frac{K_6Y^2}{2} + K_7Y\right)\Bigg|_{b_2}^{b_1}$$

$$C = \frac{(b_1 + b_2)d^4}{72(b_1 - b_2)^5 I^2}$$

$$K_1 = 3y_2(b_1 - b_2) + b_2 d$$

$$K_2 = 3b_2 y_2 (b_1 - b_2) + b_2^2 d$$

$$K_3 = -4dk_{11} - 8b_2 d^2$$

$$K_4 = k_{11}^2 - 4dk_{12} + 4b_2^2 d^2 + 8b_2 k_{11} d$$

$$K_5 = 2k_{11}k_{12} - 4b_2^2 k_{11} d - 2k_{11}^2 b_2 + 8b_2 d k_{12}$$

$$K_6 = k_{12}^2 + k_{11}^2 b_2^2 - 4db_2^2 k_{12} - 4b_2 k_{11} k_{12}$$

$$K_7 = 2k_{11}k_{12}b_2^2 - 2b_2 k_{12}^2$$

Where, A - total area of cross-section; I - moment of area of cross-section; S_y - first moment of area of the section where the shear stress is desired; b_y - breadth at the point where shear stress is desired. Substituting the trapezoidal section properties in Oroszs definition, midspan deflection is estimated as

$$k = 1.202$$

$$U_y = 8.814 \times 10^{-3} \ m$$

Appendix B

Examples:

```
C1 : top211([60,20],0.5,-1,'mid',[1,1/3],'CB','SIMTP',0.5,3,1.5,2)
C2 : top211([60,20],0.5,-1,'mid',[1,1/3],'CB','SIMP',0.5,3,1.5,2)
C3 : top211([60,20],0.5,-1,'mid',[1,1/3],'CB','SIMTP',0.5,[1,0.05,3],1.5,2)
C4 : top211([60,20],1/3,-1,'mid',[1,1/3],'CB','SIMP',0.5,3,2.5,2)
C5 : top211([60,20],0.5,-1,'top',[1,1/3],'MBB','SIMTP',0.5,3,1.5,2)
C6 : top211([60,20],0.5,-1,'top',[1,1/3],'MBB','SIMP',0.5,3,1.5,2)
C7 : top211([60,20],0.5,-1,'top',[1,1/3],'MBB','SIMTP',0.5,[1,0.05,3],1.5,2)
C8 : top211([60,20],0.5,-1,'top',[1,1/3],'MBB','SIMP',0.5,[1,0.05,3],1.5,2)
C9 : top211([60,20,30,30],0.5,-1,'top',[1,1/3],'LB','SIMTP',0.5,[1,0.05,3],1.5,2)
C10: top211([60,60,30,30],0.5,-1,'top',[1,1/3],'LB','SIMP',0.5,3,1.5,2)
```

MATLAB top211 code:

```
%%%% AN 211 LINE TOPOLOGY OPTIMISATION CODE FOR 2.5D SIMTP May, 2021 %%%%
function top211(domain,ez,load,loc,matprop,prob,Opt,volfrac,penal,rmin,ft)
%% SHEPARD WEIGHTS
close all; w=[1/12*ones(1,4) 1/6*ones(1,4)];   f=@(x) reshape(x,[],1);
%% PROBLEM TYPE
if any(strcmpi(prob,{'CB','MBB'}))
    % Corner node coordinates for Cantilever beam(CB) or MBB beam
    a=domain(1);   b=domain(2);   nX1=round(a/ez);    nY1=round(b/ez);
    [aX,bY]=meshgrid(0:nX1,0:nY1);  ccX=aX*ez;  ccY=bY*ez;
    nc=(nX1+1)*(nY1+1); ns=reshape(1:nc,nY1+1,[]);
    cc=zeros(nc,2); cc(ns(:),:)=[ccX(:) ccY(:)];
    % Corner node topology
    c1=f(ns(1:end-1,1:end-1));  c2=f(ns(1:end-1,2:end));
    c3=f(ns(2:end,2:end));  c4=f(ns(2:end,1:end-1));
    % Loading element
    if strcmpi(loc,'mid')&&strcmpi(prob,'CB'),    le=(nX1-1)*nY1; end
    % Initial Volume
    V0=a*b;
elseif strcmpi(prob,'LB')
    % Corner node coordinates for L-beam
    a=domain(1);   b=domain(2);   c=domain(3);   d=domain(4);
    neX=round(a/ez);    neY=round(b/ez);
    ncX=round(c*neX/a); ndY=round(d*neY/b);
    nX1=neX-ncX;    nY1=neY-ndY;   nX2=ncX; nY2=nY1;    nX3=nX1; nY3=ndY;
    [X1,Y1]=meshgrid(0:nX1,0:nY1);  [X2,Y2]=meshgrid(1:nX2,0:nY2);
    [X3,Y3]=meshgrid(0:nX3,1:nY3);
```

```
        cX1=X1*ez;  cY1=Y1*ez;  cX2=(a-c)+X2*ez;    cY2=Y2*ez;
        cX3=X3*ez;  cY3=(b-d)+Y3*ez;
        N1=(nX1+1)*(nY1+1); N2=nX2*(nY2+1); N3=(nX3+1)*nY3;
        nc=N1+N2+N3;    cc=zeros(nc,2);
        n0=reshape(1:(N1+N3),nY1+nY3+1,[]); n1=n0(1:nY1+1,:);
        n2=N1+N3+reshape(1:N2,nY2+1,[]);    n3=n0(nY1+2:end,:);
        cc(n1(:),:)=[cX1(:) cY1(:)];    cc(n2(:),:)=[cX2(:) cY2(:)];
        cc(n3(:),:)=[cX3(:) cY3(:)];
        % Corner node topology
        c1=[f(n0(1:(nY1+nY3),1:end-1));n1(1:end-1,end);f(n2(1:end-1,1:end-1))];
        c2=[f(n0(1:(nY1+nY3),2:end));f(n2(1:end-1,:))];
        c3=[f(n0(2:end,2:end));f(n2(2:end,:))];
        c4=[f(n0(2:end,1:end-1));n1(2:end,end);f(n2(2:end,1:end-1))];
        % Loading element
        if strcmpi(loc,'mid'),  le=nX1*(nY1+nY3)+(nX2-1)*nY2;   end
        % Initial Volume
        V0=(a*b-c*d);
    end
    % Nodal coordinates of eight noded element and element topology arrangement
    ec=[c1 c2 c3 c4];   eds=reshape(ec(:,[1:4,2:4,1]),[],2);
    [en,~,ix]=unique(sort(eds,2),'rows');   em=reshape(ix,[],4)+size(cc,1);
    cm=(cc(en(:,1),:)+cc(en(:,2),:))/2; cd=[cc;cm]; ep=[ec em];
    %% DEFINE LOADS AND SUPPORTS
    et=size(ep,1);  nt=size(cd,1);   adfs=(1:2*nt)';   U=zeros(2*nt,1);
    if any(strcmpi(prob,{'CB','LB'}))
        if strcmpi(loc,'top'),  lid=2*nc;
        elseif strcmpi(loc,'mid')
            if rem(nY1,2),  eid=le+round(nY1/2);    lid=2*ep(eid,6);
            else,   eid=le+nY1/2;   lid=2*ep(eid,3);
            end
        else,   lid=2*(nc-nY1);
        end
        if strcmpi(prob,'CB'),    dfs=[(1:nY1+1)';   ep(1:nY1,8)];
        else,   dfs=[(1:nX1+1)'*(nY1+nY3+1);    ep((1:nX1)'*(nY1+nY3),7)];
        end
        fxdfs=sort([2*dfs-1;2*dfs]);
    elseif strcmpi(prob,'MBB')
        if strcmpi(loc,'top'),  lid=2*(nY1+1);
        elseif strcmpi(loc,'mid')
            if rem(nY1,2),  eid=round((nY1)/2);   lid=2*ep(eid,8);
            else,   eid=(nY1)/2;    lid=2*ep(eid,4);
            end
        elseif strcmpi(loc,'bot'),  lid=2;
        end
        fxdfs=sort([(2*[(1:nY1+1)'; ep(1:nY1,8)]-1);2*(nc-nY1)]);
    end
    F = sparse(lid,1,load,2*nt,1); fdfs=setdiff(adfs,fxdfs);
    %% MATERIAL PROPERTIES AND CONSTIUTIVE MATRIX
    if isempty(matprop), E=1000;  nu=0.3;
    elseif length(matprop)==1,    nu=0.3;
    else, E=matprop(1);   nu=matprop(2);
    end
    if strcmpi(Opt,'SIMTP'),   Em=0.05;   M=0;   else,   Em=1e-9;   M=1;   end
    E0=1; D=E/(1-nu^2)*[1 nu 0;nu 1 0;0 0 (1-nu)/2];
    %% PENALTY FUNCTION
    if length(penal)==1,    pl=penal;   dp=0;   ph=penal;
    elseif length(penal)==2,   dp=diff(penal)/100;   pl=penal(1);  ph=penal(2);
        if dp<0,    disp('check penalty limits');   return; end
    elseif length(penal)==3, pl=penal(1); dp=penal(2); ph=penal(3); ck=(ph-pl);
        if ck<0||dp>ck||dp<0, disp('check penalty limits');   return; end
    end
    %% STIFFNESS MATRIX
    % Preparing Jacobian
    dNr = [-0.6830,-0.2277,-0.1830,-0.0610,0.9107,0.3333,0.2440,-0.3333;-0.6830,-0.0610,-
0.1830,-0.2277,-0.3333,  0.2440,  0.3333,  0.9107;0.2277,  0.6830,  0.0610,  0.1830,-0.9107,
```

```
0.3333,-0.2440,-0.3333;-0.0610,-0.6830,-0.2277,-0.1830,-0.3333,       0.9107,       0.3333,
0.2440;0.1830,  0.0610,  0.6830,  0.2277,-0.2440,  0.3333,-0.9107,-0.3333;0.1830,  0.2277,
0.6830,  0.0610,-0.3333,-0.9107,  0.3333,-0.2440;-0.0610,-0.1830,-0.2277,-0.6830,  0.2440,
0.3333, 0.9107,-0.3333;0.2277, 0.1830, 0.0610, 0.6830,-0.3333,-0.2440, 0.3333,-0.9107];
    JTx=dNr*cd(ep(1,:),1);  JTy=dNr*cd(ep(1,:),2);
    JT(1:4:16,:)=JTx(1:2:end,:);    JT(3:4:16,:)=JTy(1:2:end,:);
    JT(2:4:16,:)=JTx(2:2:end,:);    JT(4:4:16,:)=JTy(2:2:end,:);
    JT=reshape(JT,2,2,4);   dJT=JT(1,1,:).*JT(2,2,:)-JT(1,2,:).*JT(2,1,:);
    % Preparing Strain Matrix and Stiffness matrix
    dN=zeros(2,8,4);
    for i=1:4,    ix=[2*i-1;2*i]; dN(:,:,i,:)=JT(:,:,i)\dNr(ix,:);    end
    B(1,1:2:16,:)=dN(1,:,:);    B(2,2:2:16,:)=dN(2,:,:);
    B(3,1:2:16,:)=dN(2,:,:);    B(3,2:2:16,:)=dN(1,:,:);
    K1=zeros(16,16,4,1);    K2=zeros(16,16,4,1);
    for i=1:4,  K1(:,:,i)=B(:,:,i)'*D*B(:,:,i); K2(:,:,i)=K1(:,:,i)*dJT(i); end
    KE = sum(K2,3);
    % Preparing 3D Jacobian data for SIMTP
    g=@(x) x(ep);   eX=g(cd(:,1));  eY=g(cd(:,2));
    if ~M
                  ds   =   [-0.4072,-0.311,-0.1796,-0.0129,0.7182,0.2629,0.1925,-0.2629,-
0.2629,0.2629,0.0704,-0.0704,-0.0129,-0.1796,-0.0739,0.0223,0.1925,0.0704,0.0516,-0.0704;-
0.4072,-0.0129,-0.1796,-0.311,-0.2629,0.1925,0.2629,0.7182,-0.2629,-0.0704,0.0704,0.2629,-
0.0129,0.0223,-0.0739,-0.1796,-0.0704,0.0516,0.0704,0.1925;-0.4072,-0.0129,0.0223,-0.0129,-
0.2629,-0.0704,-0.0704,-0.2629,0.7182,0.1925,0.0516,0.1925,-0.311,-0.1796,-0.0739,-
0.1796,0.2629,0.0704,0.0704,0.2629;0.311,0.4072,0.0129,0.1796,-0.7182,0.2629,-0.1925,-
0.2629,-0.2629,0.2629,0.0704,-0.0704,0.1796,0.0129,-0.0223,0.0739,-0.1925,0.0704,-0.0516,-
0.0704;-0.0129,-0.4072,-0.311,-0.1796,-0.2629,0.7182,0.2629,0.1925,-0.0704,-
0.2629,0.2629,0.0704,0.0223,-0.0129,-0.1796,-0.0739,-0.0704,0.1925,0.0704,0.0516;-0.0129,-
0.4072,-0.0129,0.0223,-0.2629,-0.2629,-0.0704,-0.0704,0.1925,0.7182,0.1925,0.0516,-0.1796,-
0.311,-0.1796,-0.0739,0.2629,0.2629,0.0704,0.0704;0.1796,0.0129,0.4072,0.311,-
0.1925,0.2629,-0.7182,-0.2629,-0.0704,0.0704,0.2629,-0.2629,0.0739,-0.0223,0.0129,0.1796,-
0.0516,0.0704,-0.1925,-0.0704;0.1796,0.311,0.4072,0.0129,-0.2629,-0.7182,0.2629,-0.1925,-
0.0704,-0.2629,0.2629,0.0704,0.0739,0.1796,0.0129,-0.0223,-0.0704,-0.1925,0.0704,-
0.0516;0.0223,-0.0129,-0.4072,-0.0129,-0.0704,-0.2629,-0.2629,-
0.0704,0.0516,0.1925,0.7182,0.1925,-0.0739,-0.1796,-0.311,-
0.1796,0.0704,0.2629,0.2629,0.0704;-0.0129,-0.1796,-0.311,-0.4072,0.1925,0.2629,0.7182,-
0.2629,-0.0704,0.0704,0.2629,-0.2629,0.0223,-0.0739,-0.1796,-0.0129,0.0516,0.0704,0.1925,-
0.0704;0.311,0.1796,0.0129,0.4072,-0.2629,-0.1925,0.2629,-0.7182,-0.2629,-
0.0704,0.0704,0.2629,0.1796,0.0739,-0.0223,0.0129,-0.0704,-0.0516,0.0704,-0.1925;-
0.0129,0.0223,-0.0129,-0.4072,-0.0704,-0.0704,-0.2629,-0.2629,0.1925,0.0516,0.1925,0.7182,-
0.1796,-0.0739,-0.1796,-0.311,0.0704,0.0704,0.2629,0.2629;-0.0129,-0.1796,-
0.0739,0.0223,0.1925,0.0704,0.0516,-0.0704,-0.2629,0.2629,0.0704,-0.0704,-0.4072,-0.311,-
0.1796,-0.0129,0.7182,0.2629,0.1925,-0.2629;-0.0129,0.0223,-0.0739,-0.1796,-
0.0704,0.0516,0.0704,0.1925,-0.2629,-0.0704,0.0704,0.2629,-0.4072,-0.0129,-0.1796,-0.311,-
0.2629,0.1925,0.2629,0.7182;0.311,0.1796,0.0739,0.1796,-0.2629,-0.0704,-0.0704,-0.2629,-
0.7182,-0.1925,-0.0516,-0.1925,0.4072,0.0129,-
0.0223,0.0129,0.2629,0.0704,0.0704,0.2629;0.1796,0.0129,-0.0223,0.0739,-0.1925,0.0704,-
0.0516,-0.0704,-0.2629,0.2629,0.0704,-0.0704,0.311,0.4072,0.0129,0.1796,-0.7182,0.2629,-
0.1925,-0.2629;0.0223,-0.0129,-0.1796,-0.0739,-0.0704,0.1925,0.0704,0.0516,-0.0704,-
0.2629,0.2629,0.0704,-0.0129,-0.4072,-0.311,-0.1796,-
0.2629,0.7182,0.2629,0.1925;0.1796,0.311,0.1796,0.0739,-0.2629,-0.2629,-0.0704,-0.0704,-
0.1925,-0.7182,-0.1925,-0.0516,0.0129,0.4072,0.0129,-
0.0223,0.2629,0.2629,0.0704,0.0704;0.0739,-0.0223,0.0129,0.1796,-0.0516,0.0704,-0.1925,-
0.0704,-0.0704,0.0704,0.2629,-0.2629,0.1796,0.0129,0.4072,0.311,-0.1925,0.2629,-0.7182,-
0.2629;0.0739,0.1796,0.0129,-0.0223,-0.0704,-0.1925,0.0704,-0.0516,-0.0704,-
0.2629,0.2629,0.0704,0.1796,0.311,0.4072,0.0129,-0.2629,-0.7182,0.2629,-
0.1925;0.0739,0.1796,0.311,0.1796,-0.0704,-0.2629,-0.2629,-0.0704,-0.0516,-0.1925,-0.7182,-
0.1925,-0.0223,0.0129,0.4072,0.0129,0.0704,0.2629,0.2629,0.0704;0.0223,-0.0739,-0.1796,-
0.0129,0.0516,0.0704,0.1925,-0.0704,-0.0704,0.0704,0.2629,-0.2629,-0.0129,-0.1796,-0.311,-
0.4072,0.1925,0.2629,0.7182,-0.2629;0.1796,0.0739,-0.0223,0.0129,-0.0704,-0.0516,0.0704,-
0.1925,-0.2629,-0.0704,0.0704,0.2629,0.311,0.1796,0.0129,0.4072,-0.2629,-0.1925,0.2629,-
0.7182;0.1796,0.0739,0.1796,0.311,-0.0704,-0.0704,-0.2629,-0.2629,-0.1925,-0.0516,-0.1925,-
0.7182,0.0129,-0.0223,0.0129,0.4072,0.0704,0.0704,0.2629,0.2629];
        X(:,1:8)=eX;    X(:,9:16)=repmat(eX(:,1:4),1,2);  X(:,17:20)=eX(:,5:8);
        Y(:,1:8)=eY;    Y(:,9:16)=repmat(eY(:,1:4),1,2);  Y(:,17:20)=eY(:,5:8);
```

```
    sx=ds*X';   sy=ds*Y';
    S(1:9:72,:)=sx(1:3:end,:);   S(2:9:72,:)=sx(2:3:end,:);
    S(3:9:72,:)=sx(3:3:end,:);  S(4:9:72,:)=sy(1:3:end,:);
    S(5:9:72,:)=sy(2:3:end,:);  S(6:9:72,:)=sy(3:3:end,:);
end
%% PREPARE FINITE ELEMENT ANALYSIS
emt=zeros(et,16);   emt(:,2:2:end)=ep*2;emt(:,1:2:end)=ep*2-1;
I=reshape(repmat((1:16),16,1),1,[]);    J=repmat(1:16,1,16);
iK=f(emt(:,I)');    jK=f(emt(:,J)');
%% PREPARE FILTER
if strcmpi(Opt,'SIMP')
    h=@(x) sum(x.*[-1/4*ones(1,4) 1/2*ones(1,4)],2);
    eXc=h(eX);  eYc=h(eY);  eC=[eXc eYc];
    x=ones(et,1);
else,   eC=cd;  x=ones(nt,1);
end
rmin = rmin+1e-3;
[Id,r]=rangesearch(eC,eC,rmin*ez);
w0=cell2mat(arrayfun(@(i) [i*ones(length(Id{i}),1) Id{i}' (rmin*ez -r{i})']...
    ,(1:length(eC))','un',0));
H=sparse(w0(:,1),w0(:,2),w0(:,3),max(w0(:,1)),max(w0(:,1)),nzmax(w0(:,3)));
Hs=sum(H,2);
%% INITIALIZE ITERATION
L=@(x) accumarray(f(ep'),x);    G=@(x) repmat(x,1,1,8,1);
xs=x;   lp=0;   lt=0;   ch=1;   maxloop=150;
if M,   dch=0.01;   dv=ones(et,1)*ez*ez;
else,   dch=0.001;  dv1=repmat(ez*ez*w*(E0-Em),et,1);  dv=L(f(dv1')); ft=2;
end
if ft~=1, dv(:)= H*(dv(:)./Hs); end, figure()
%% START ITERATION
while ch > dch && lp<maxloop
    %% PENALTY
    tic;    lp=lp+1;    pn=pl+dp*(lp-1);    if pn>ph,   pn=ph;  end
    %% FE-ANALYSIS
    if M,   sK=KE(:)*(Em+xs(:)'.^pn*(E0-Em));
    else,   sK=sum(K1.*J3d(),3);
    end
    K=sparse(iK,jK,sK(:));  K=(K+K')/2;
    U(fdfs)=K(fdfs,fdfs)\F(fdfs);
    %% OBJECTIVE FUNCTION AND SENSITIVITY ANALYSIS
    if M
        ce=sum((U(emt)*KE).*U(emt),2);  C=sum((Em+xs.^pn*(E0-Em)).*ce);
        dc=-pn*(E0-Em)*xs.^(pn-1).*ce;
    else
        C=U'*K*U;dt=pn*(E0-Em)*xs(ep).^(pn-1).*w;
        U1=G(reshape(U(emt)',[],1,1,et));
        U2=G(reshape(U(emt)',1,[],1,et));
        dK=KE.*reshape(dt',1,1,8,et);
        dc1=sum(sum(U1.*dK.*U2,1),2);   dc=-L(dc1(:));
    end
    %% FILTERING/MODIFICATION OF SENSITIVITIES
    if ft==1&&M,    dc(:)= H*(x(:).*dc(:))./Hs./max(1e-3,x(:));
    else,   dc(:)=H*(dc(:)./Hs);
    end
    %% OPTIMALITY CRITERIA UPDATE OF DESIGN VARIABLES
    l1=0;   l2=1e9; if M,   mv=0.2; else,   mv=0.1; end
    while (l2-l1)/(l1+l2)>1e-3
        lmd=0.5*(l2+l1);
        xnew=max(0,max(x-mv,min(1,min(x+mv,x.*sqrt(abs(dc)./dv/lmd)))));
        if ft==1,   xs=xnew;    else,   xs(:)=(H*xnew(:))./Hs;end
        V=vol();    Vr=V/V0;
        if Vr>volfrac,  l1=lmd; else,   l2=lmd; end
    end
    ch=max(abs(xnew(:)-x(:)));  x=xnew; lt=lt+toc;
    %% PRINT RESULTS
```

```
    pr='It.:%5i Obj.:%11.2f Vol.:%7.3f ch.:%7.3f t.:%7.2f Penal.:%7.2f\n';
    fprintf(pr,lp,C,Vr,ch,lt,pn);   delete(findobj('type', 'patch'));
    %% PLOT DENSITIES
    o=@(x,y,z) (repmat(linspace(x,y,z)',1,3));
    O=[o(0,0.1,100);o(0.1,0.3,150);o(0.3,0.5,200);o(0.5,1,650)];
    P=patch('Faces',ep(:,[1 5 2 6 3 7 4 8 1]),'Vertices',cd,'EdgeColor',...
        'none','FaceVertexCData',1-xs); caxis([0 1]);   daspect([1 1 0.1]);
    if M,   P.FaceColor='flat'; else,   P.FaceColor='interp';   end
    axis off;   colormap(O);   drawnow;
end
%% 3D JACOBIAN FOR PENALISED THICKNESS
function dJp=J3d()
    tp=(Em+xs(ep).^pn*(E0-Em));
    Zp(:,1:8)=-(tp)/2;  Zp(:,9:12)=0;   Zp(:,13:20)=(tp)/2;    sZp=ds*Zp';
    S(7:9:72,:)=sZp(1:3:end,:); S(8:9:72,:)=sZp(2:3:end,:);
    S(9:9:72,:)=sZp(3:3:end,:); s=reshape(S,3,3,8,et);
    dJp=s(1,1,:,:).*(s(2,2,:,:).*s(3,3,:,:)-s(3,2,:,:).*s(2,3,:,:))-...
        s(1,2,:,:).*(s(2,1,:,:).*s(3,3,:,:)-s(3,1,:,:).*s(2,3,:,:))+...
        s(1,3,:,:).*(s(2,1,:,:).*s(3,2,:,:)-s(3,1,:,:).*s(2,2,:,:));
    if find(dJp<10*eps, 1),   disp('Jacobian<0!');    return; end
    dJp=dJp(:,:,1:4,:)+dJp(:,:,5:8,:);
end
%% VOLUME CHANGES USING ACTUAL THICKNESS
function Vp=vol()
    if ~M
        tn=Em+xs(ep)*(E0-Em);
        Z(:,1:8)=-(tn)/2;   Z(:,9:12)=0;    Z(:,13:20)=(tn)/2;  sZ=ds*Z';
        S(7:9:72,:)=sZ(1:3:end,:);  S(8:9:72,:)=sZ(2:3:end,:);
        S(9:9:72,:)=sZ(3:3:end,:);  s=reshape(S,3,3,8,et);
        dJ=s(1,1,:,:).*(s(2,2,:,:).*s(3,3,:,:)-s(3,2,:,:).*s(2,3,:,:))-...
            s(1,2,:,:).*(s(2,1,:,:).*s(3,3,:,:)-s(3,1,:,:).*s(2,3,:,:))+...
            s(1,3,:,:).*(s(2,1,:,:).*s(3,2,:,:)-s(3,1,:,:).*s(2,2,:,:));
        if find(dJ<10*eps, 1), disp('Jacobian<0!');  return;  end
        Ve=f(sum(dJ,3));    Vp=sum(Ve);
    else, Vp=sum(xs(:))*ez*ez;
    end
end
end
%
%%%%%%%%%%%%%%%%%%%%%%%%%%%%%%%%%%%%%%%%%%%%%%%%%%%%%%%%%%%%%%%%%%%%%%%%%%%%%%
% 2.5D SIMTP code by Tejeswar YARLAGADDA                                     %
% PhD Student, BEEE, POLYU, HONGKONG                                         %
% This code is created and modified from top88, initially published by      %
% E. Andreassen, A. Clausen, M. Schevenels,B. S. Lazarov and O. Sigmund,    %
% Department of Solid  Mechanics,                                            %
% Technical University of Denmark,                                           %
% DK-2800 Lyngby, Denmark.                                                   %
% Please send your comments on SIMTP to: yarlagadda.tejeswar@gmail.com      %
% Please send your comments on SIMP to: sigmund@fam.dtu.dk                   %
%                                                                            %
% Email to yarlagadda.tejeswar@gmail.com for SIMTP code                      %
% The SIMP code is available at: http://www.topopt.dtu.dk                    %
%                                                                            %
% Disclaimer:                                                                %
% The authors reserve all rights but do not guaranty that the code is        %
% free from errors. Furthermore, we shall not be liable in any event         %
% caused by the use of the program.                                          %
%%%%%%%%%%%%%%%%%%%%%%%%%%%%%%%%%%%%%%%%%%%%%%%%%%%%%%%%%%%%%%%%%%%%%%%%%%%%%%
```

Appendix C

```
function SIMTPA(domain,ez,load,loc,matprop,prob,volfrac,penal)
%% SHEPARD WEIGHTS
close all; w=[1/12*ones(1,4) 1/6*ones(1,4)];   f=@(x) reshape(x,[],1);
%% PROBLEM TYPE
if any(strcmpi(prob,{'CB','MBB'}))
    % Corner node coordinates for Cantilever beam(CB) or MBB beam
    a=domain(1);   b=domain(2);   nX1=round(a/ez);    nY1=round(b/ez);
    [aX,bY]=meshgrid(0:nX1,0:nY1);  ccX=aX*ez;  ccY=bY*ez;
    nc=(nX1+1)*(nY1+1); ns=reshape(1:nc,nY1+1,[]);
    cc=zeros(nc,2); cc(ns(:),:)=[ccX(:) ccY(:)];
    % Corner node topology
    c1=f(ns(1:end-1,1:end-1));  c2=f(ns(1:end-1,2:end));
    c3=f(ns(2:end,2:end));  c4=f(ns(2:end,1:end-1));
    % Loading element
    if strcmpi(loc,'mid')&&strcmpi(prob,'CB'),    le=(nX1-1)*nY1; end
    % Initial Volume
    V0=a*b;
elseif strcmpi(prob,'LB')
    % Corner node coordinates for L-beam
    a=domain(1);   b=domain(2);   c=domain(3);   d=domain(4);
    neX=round(a/ez);    neY=round(b/ez);
    ncX=round(c*neX/a); ndY=round(d*neY/b);
    nX1=neX-ncX;    nY1=neY-ndY;   nX2=ncX; nY2=nY1;    nX3=nX1; nY3=ndY;
    [X1,Y1]=meshgrid(0:nX1,0:nY1);  [X2,Y2]=meshgrid(1:nX2,0:nY2);
    [X3,Y3]=meshgrid(0:nX3,1:nY3);
    cX1=X1*ez;  cY1=Y1*ez;  cX2=(a-c)+X2*ez;    cY2=Y2*ez;
    cX3=X3*ez;  cY3=(b-d)+Y3*ez;
    N1=(nX1+1)*(nY1+1); N2=nX2*(nY2+1); N3=(nX3+1)*nY3;
    nc=N1+N2+N3;    cc=zeros(nc,2);
    n0=reshape(1:(N1+N3),nY1+nY3+1,[]); n1=n0(1:nY1+1,:);
    n2=N1+N3+reshape(1:N2,nY2+1,[]);    n3=n0(nY1+2:end,:);
    cc(n1(:),:)=[cX1(:) cY1(:)];    cc(n2(:),:)=[cX2(:) cY2(:)];
    cc(n3(:),:)=[cX3(:) cY3(:)];
    % Corner node topology
    c1=[f(n0(1:(nY1+nY3),1:end-1));n1(1:end-1,end);f(n2(1:end-1,1:end-1))];
    c2=[f(n0(1:(nY1+nY3),2:end));f(n2(1:end-1,:))];
    c3=[f(n0(2:end,2:end));f(n2(2:end,:))];
    c4=[f(n0(2:end,1:end-1));n1(2:end,end);f(n2(2:end,1:end-1))];
    % Loading element
    if strcmpi(loc,'mid'),  le=nX1*(nY1+nY3)+(nX2-1)*nY2;   end
    % Initial Volume
    V0=(a*b-c*d);
end
```

```
% Nodal coordinates of eight noded element and element topology arrangement
ec=[c1 c2 c3 c4];   eds=reshape(ec(:,[1:4,2:4,1]),[],2);
[en,~,ix]=unique(sort(eds,2),'rows');   em=reshape(ix,[],4)+size(cc,1);
cm=(cc(en(:,1),:)+cc(en(:,2),:))/2; cd=[cc;cm]; ep=[ec em];
%% DEFINE LOADS AND SUPPORTS
nt=size(cd,1);
if any(strcmpi(prob,{'CB','LB'}))
    if strcmpi(loc,'top'),  lid=2*nc;
    elseif strcmpi(loc,'mid')
        if rem(nY1,2),  eid=le+round(nY1/2);    lid=2*ep(eid,6);
        else,   eid=le+nY1/2;   lid=2*ep(eid,3);
        end
    else,   lid=2*(nc-nY1);
    end, CL=1;
    if strcmpi(prob,'CB')
        ced=[(1:nY1)' ep(1:nY1,8);ep(1:nY1,8) (2:nY1+1)'];
    else
        ced=[(1:nX1)'*(nY1+nY3+1) ep((1:nX1)'*(nY1+nY3),7);...
            ep((1:nX1)'*(nY1+nY3),7) (2:nX1+1)'*(nY1+nY3+1)];
    end
elseif strcmpi(prob,'MBB')
    if strcmpi(loc,'top'),  lid=2*(nY1+1);
    elseif strcmpi(loc,'mid')
        if rem(nY1,2),  eid=round((nY1)/2);   lid=2*ep(eid,8);
        else,   eid=(nY1)/2;    lid=2*ep(eid,4);
        end
    elseif strcmpi(loc,'bot'),  lid=2;
    end
    ced=[(1:nY1)' ep(1:nY1,8);ep(1:nY1,8) (2:nY1+1)']; p0=2*(nc-nY1); CL=0;
end
%% MATERIAL PROPERTIES AND CONSTITUTIVE MATRIX
if isempty(matprop), E=1000;  nu=0.3;
elseif length(matprop)==1,    nu=0.3;
else, E=matprop(1);   nu=matprop(2);
end
Em=1e-3;    E0=1;
%% PENALTY FUNCTION
if length(penal)==1,    pl=penal;   dp=0;   ph=penal;
elseif length(penal)==2,   dp=diff(penal)/100;   pl=penal(1);  ph=penal(2);
    if dp<0,    disp('check penalty limits');   return; end
elseif length(penal)==3, pl=penal(1); dp=penal(2); ph=penal(3); ck=(ph-pl);
    if ck<0||dp>ck||dp<0, disp('check penalty limits');   return; end
end
%% INITIALIZE ITERATION
rmin = rmin+1e-3;
[Id,r]=rangesearch(cd,cd,rmin*ez);
w0=cell2mat(arrayfun(@(i) [i*ones(length(Id{i}),1) Id{i}' (rmin*ez-r{i})']...
    ,(1:nt)','un',0));
H=sparse(w0(:,1),w0(:,2),w0(:,3),max(w0(:,1)),max(w0(:,1)),nzmax(w0(:,3)));
Hs=sum(H,2);
x=ones(nt,1); xs=x; lp=0;   lt=0;   ch=1;   maxloop=50;    dch=0.001;
figure()
%% START ITERATION
while ch>dch && lp<maxloop
    %% PENALTY
    tic; ir=zeros(0,3); lp=lp+1; pn=pl+dp*(lp-1);
    if pn>ph, pn=ph; end
    if lp==1, [cdr,xsr,epr,ir,cedr,dJp,~,eX,eY]=refine(cd,xs,ep,ir,ced); end
    if CL,  fxdfs=unique(f([2*cedr-1;2*cedr]));
    else,   fxdfs=[unique(f(2*cedr-1));p0];
    end
    %% FE-ANALYSIS, OBJECTIVE FUNCTION AND SENSITIVITY ANALYSIS
    [K,dKe,dv]=Km(epr,eX,eY,E,nu,dJp,w,E0,Em,xsr,pn);
    U=slse(K,lid,load,fxdfs,ir,epr,cdr);
    %% UPDATE OF DESIGN VARIABLES
```

```
    et=size(epr,1); emt=zeros(et,16); emt(:,2:2:end)=epr*2;
    emt(:,1:2:end)=epr*2-1; U1=reshape(U(emt)',[],1,1,et);
    U2=permute(U1,[2,1,3,4]);
    C=U'*K*U;   dc1=sum(sum(U1.*dKe.*U2));
    id=reshape(epr',[],1); dc=accumarray(id,dc1(:));
    dcf=H*(dc(1:nt)./Hs); dvf= H*(dv(1:nt)./Hs);
    l1=0;   l2=1e9; mv=0.1;
    while (l2-l1)/(l1+l2)>1e-3
        lmd=0.5*(l2+l1);
        xnew=max(0,max(x-mv,min(1,min(x+mv,x.*sqrt(abs(dcf)./dvf/lmd)))));
        xs(:)=(H*xnew(:))./Hs; ir=zeros(0,3);
        [cdr,xsr,epr,ir,cedr,dJp,V,eX,eY]=refine(cd,xs,ep,ir,ced); Vr=V/V0;
        if Vr>volfrac,  l1=lmd; else,   l2=lmd; end
    end
    ch=max(abs(xnew(:)-x(:))); x=xnew; lt=lt+toc;
    %% PRINT RESULTS
    pr='It.:%5i Obj.:%11.2f Vol.:%7.3f ch.:%7.3f t.:%7.2f Penal.:%7.2f\n';
    fprintf(pr,lp,C,Vr,ch,lt,pn);   delete(findobj('type', 'patch'));
    %% PLOT DENSITIES
    o=@(x,y,z) (repmat(linspace(x,y,z)',1,3));
    O=[o(0,0.1,100);o(0.1,0.3,150);o(0.3,0.5,200);o(0.5,1,650)];
    patch('Faces',ep(:,[1 5 2 6 3 7 4 8 1]),'Vertices',[cd xs],'EdgeColor',...
        'none','FaceVertexCData',1-xs,'FaceColor','interp'); caxis([0 1]);
    daspect([1 1 0.1]);    axis off;   colormap(O);   drawnow;
end
%% REFINEMENT
function [cdr,xsr,epr,ir,cedr,dJp,V,eX,eY]=refine(cdr,xsr,epr,ir,cedr)
while 1
    g=@(x) x(epr); eX=g(cdr(:,1)); eY=g(cdr(:,2));
    [dJp,V,mk]=Jc(epr,eX,eY,E0,Em,xsr,pn);
    if mk~=0, [cdr,xsr,epr,ir,cedr]=Q8r(cdr,xsr,epr,ir,cedr,mk);
    else, break;
    end
end
end
end
```

```
function [dJp,Vp,mark]=Jc(ep,eX,eY,E0,Em,xs,pn)
%% INITIAL PARAMETERS
ds = [-0.4072,-0.311,-0.1796,-0.0129,0.7182,0.2629,0.1925,-0.2629,-
0.2629,0.2629,0.0704,-0.0704,-0.0129,-0.1796,-0.0739,0.0223,0.1925,0.0704,0.0516,-0.0704;-
0.4072,-0.0129,-0.1796,-0.311,-0.2629,0.1925,0.2629,0.7182,-0.2629,-0.0704,0.0704,0.2629,-
0.0129,0.0223,-0.0739,-0.1796,-0.0704,0.0516,0.0704,0.1925;-0.4072,-0.0129,0.0223,-0.0129,-
0.2629,-0.0704,-0.0704,-0.2629,0.7182,0.1925,0.0516,0.1925,-0.311,-0.1796,-0.0739,-
0.1796,0.2629,0.0704,0.0704,0.2629;0.311,0.4072,0.0129,0.1796,-0.7182,0.2629,-0.1925,-
0.2629,-0.2629,0.2629,0.0704,-0.0704,0.1796,0.0129,-0.0223,0.0739,-0.1925,0.0704,-0.0516,-
0.0704;-0.0129,-0.4072,-0.311,-0.1796,-0.2629,0.7182,0.2629,0.1925,-0.0704,-
0.2629,0.2629,0.0704,0.0223,-0.0129,-0.1796,-0.0739,-0.0704,0.1925,0.0704,0.0516;-0.0129,-
0.4072,-0.0129,0.0223,-0.2629,-0.2629,-0.0704,-0.0704,0.1925,0.7182,0.1925,0.0516,-0.1796,-
0.311,-0.1796,-0.0739,0.2629,0.2629,0.0704,0.0704;0.1796,0.0129,0.4072,0.311,-
0.1925,0.2629,-0.7182,-0.2629,-0.0704,0.0704,0.2629,-0.2629,0.0739,-0.0223,0.0129,0.1796,-
0.0516,0.0704,-0.1925,-0.0704;0.1796,0.311,0.4072,0.0129,-0.2629,-0.7182,0.2629,-0.1925,-
0.0704,-0.2629,0.2629,0.0704,0.0739,0.1796,0.0129,-0.0223,-0.0704,-0.1925,0.0704,-
0.0516;0.0223,-0.0129,-0.4072,-0.0129,-0.0704,-0.2629,-0.2629,-
0.0704,0.0516,0.1925,0.7182,0.1925,-0.0739,-0.1796,-0.311,-
0.1796,0.0704,0.2629,0.2629,0.0704;-0.0129,-0.1796,-0.311,-0.4072,0.1925,0.2629,0.7182,-
0.2629,-0.0704,0.0704,0.2629,-0.2629,0.0223,-0.0739,-0.1796,-0.0129,0.0516,0.0704,0.1925,-
0.0704;0.311,0.1796,0.0129,0.4072,-0.2629,-0.1925,0.2629,-0.7182,-0.2629,-
0.0704,0.0704,0.2629,0.1796,0.0739,-0.0223,0.0129,-0.0704,-0.0516,0.0704,-0.1925;-
0.0129,0.0223,-0.0129,-0.4072,-0.0704,-0.0704,-0.2629,-0.2629,0.1925,0.0516,0.1925,0.7182,-
0.1796,-0.0739,-0.1796,-0.311,0.0704,0.0704,0.2629,0.2629;-0.0129,-0.1796,-
0.0739,0.0223,0.1925,0.0704,0.0516,-0.0704,-0.2629,0.2629,0.0704,-0.0704,-0.4072,-0.311,-
0.1796,-0.0129,0.7182,0.2629,0.1925,-0.2629;-0.0129,0.0223,-0.0739,-0.1796,-
```

```
0.0704,0.0516,0.0704,0.1925,-0.2629,-0.0704,0.0704,0.2629,-0.4072,-0.0129,-0.1796,-0.311,-
0.2629,0.1925,0.2629,0.7182;0.311,0.1796,0.0739,0.1796,-0.2629,-0.0704,-0.0704,-0.2629,-
0.7182,-0.1925,-0.0516,-0.1925,0.4072,0.0129,-
0.0223,0.0129,0.2629,0.0704,0.0704,0.2629;0.1796,0.0129,-0.0223,0.0739,-0.1925,0.0704,-
0.0516,-0.0704,-0.2629,0.2629,0.0704,-0.0704,0.311,0.4072,0.0129,0.1796,-0.7182,0.2629,-
0.1925,-0.2629;0.0223,-0.0129,-0.1796,-0.0739,-0.0704,0.1925,0.0704,0.0516,-0.0704,-
0.2629,0.2629,0.0704,-0.0129,-0.4072,-0.311,-0.1796,-
0.2629,0.7182,0.2629,0.1925;0.1796,0.311,0.1796,0.0739,-0.2629,-0.2629,-0.0704,-0.0704,-
0.1925,-0.7182,-0.1925,-0.0516,0.0129,0.4072,0.0129,-
0.0223,0.2629,0.2629,0.0704,0.0704;0.0739,-0.0223,0.0129,0.1796,-0.0516,0.0704,-0.1925,-
0.0704,-0.0704,0.0704,0.2629,-0.2629,0.1796,0.0129,0.4072,0.311,-0.1925,0.2629,-0.7182,-
0.2629;0.0739,0.1796,0.0129,-0.0223,-0.0704,-0.1925,0.0704,-0.0516,-0.0704,-
0.2629,0.2629,0.0704,0.1796,0.311,0.4072,0.0129,-0.2629,-0.7182,0.2629,-
0.1925;0.0739,0.1796,0.311,0.1796,-0.0704,-0.2629,-0.2629,-0.0704,-0.0516,-0.1925,-0.7182,-
0.1925,-0.0223,0.0129,0.4072,0.0129,0.0704,0.2629,0.2629,0.0704;0.0223,-0.0739,-0.1796,-
0.0129,0.0516,0.0704,0.1925,-0.0704,-0.0704,0.0704,0.2629,-0.2629,-0.0129,-0.1796,-0.311,-
0.4072,0.1925,0.2629,0.7182,-0.2629;0.1796,0.0739,-0.0223,0.0129,-0.0704,-0.0516,0.0704,-
0.1925,-0.2629,-0.0704,0.0704,0.2629,0.311,0.1796,0.0129,0.4072,-0.2629,-0.1925,0.2629,-
0.7182;0.1796,0.0739,0.1796,0.311,-0.0704,-0.0704,-0.2629,-0.2629,-0.1925,-0.0516,-0.1925,-
0.7182,0.0129,-0.0223,0.0129,0.4072,0.0704,0.0704,0.2629,0.2629];
X(:,1:8)=eX;    X(:,9:16)=repmat(eX(:,1:4),1,2);  X(:,17:20)=eX(:,5:8);
Y(:,1:8)=eY;    Y(:,9:16)=repmat(eY(:,1:4),1,2);  Y(:,17:20)=eY(:,5:8);
sx=ds*X';   sy=ds*Y';
S(1:9:72,:)=sx(1:3:end,:);  S(2:9:72,:)=sx(2:3:end,:);
S(3:9:72,:)=sx(3:3:end,:);  S(4:9:72,:)=sy(1:3:end,:);
S(5:9:72,:)=sy(2:3:end,:);  S(6:9:72,:)=sy(3:3:end,:);
%% 3D JACOBIAN FOR PENALISED THICKNESS
tp=(Em+xs(ep).^pn*(E0-Em));
Zp(:,1:8)=-(tp)/2;  Zp(:,9:12)=0;   Zp(:,13:20)=(tp)/2;    sZp=ds*Zp';
S(7:9:72,:)=sZp(1:3:end,:); S(8:9:72,:)=sZp(2:3:end,:);
S(9:9:72,:)=sZp(3:3:end,:); s=reshape(S,3,3,8,size(ep,1));
dJp=s(1,1,:,:).*(s(2,2,:,:).*s(3,3,:,:)-s(3,2,:,:).*s(2,3,:,:))-...
    s(1,2,:,:).*(s(2,1,:,:).*s(3,3,:,:)-s(3,1,:,:).*s(2,3,:,:))+...
    s(1,3,:,:).*(s(2,1,:,:).*s(3,2,:,:)-s(3,1,:,:).*s(2,2,:,:));
m1=find(dJp<10*eps);
if isempty(m1), dJp=dJp(:,:,1:4,:)+dJp(:,:,5:8,:);
else,   m1=floor(m1/8)+1;   dJp=[];
end
%% VOLUME CHANGES USING ACTUAL THICKNESS
tn=Em+xs(ep)*(E0-Em);
Z(:,1:8)=-(tn)/2;   Z(:,9:12)=0;    Z(:,13:20)=(tn)/2;  sZ=ds*Z';
S(7:9:72,:)=sZ(1:3:end,:);  S(8:9:72,:)=sZ(2:3:end,:);
S(9:9:72,:)=sZ(3:3:end,:);  s=reshape(S,3,3,8,size(ep,1));
dJ=s(1,1,:,:).*(s(2,2,:,:).*s(3,3,:,:)-s(3,2,:,:).*s(2,3,:,:))-...
    s(1,2,:,:).*(s(2,1,:,:).*s(3,3,:,:)-s(3,1,:,:).*s(2,3,:,:))+...
    s(1,3,:,:).*(s(2,1,:,:).*s(3,2,:,:)-s(3,1,:,:).*s(2,2,:,:));
m2=find(dJ<10*eps);
if isempty(m2), Ve=sum(dJ,3);    Vp=sum(Ve(:));
else,   m2=floor(m2/8)+1;   Vp=[];
end
mark=union(m1,m2);
end
```

```
function [cd,tf,nep,ir,varargout]=Q8r(cd,tf,ep,ir,varargin)
    nE=size(ep,1);  mE=varargin{end};   nbe=nargin-5;
    %% Obtaining edge and boundary information
    e8=ep(:,[1,5,2,6,3,7,4,8]); be=cell(nbe,1);
    eg=[reshape(ir(:,[1:3,2:3,1]),[],2);reshape(e8(:,[1:8,2:8,1]),[],2)];
    pt=[3*size(ir,1),8*size(e8,1),zeros(1,nbe)];
    for j=1:nbe,   v=varargin{j};  pt(j+2)=size(v,1); eg=[eg;v];  end
    pt=cumsum(pt);    [en,~,ie]=unique(sort(eg,2),'rows');
    ire=reshape(ie(1:pt(1)),[],3);    ee=reshape(ie(pt(1)+1:pt(2)),[],8);
    for j=1:nbe,   be{j}=ie(pt(j+1)+1:pt(j+2));   end
```

```
    %% Finding and marking edges for quadtrees
    eN=zeros(1,size(en,1)); eN(ee(mE,:))=1; eN(ire(:,1))=1; k=1;
    while ~isempty(k)||~isempty(sp)
        me=eN(ee);
        k=find(sum(abs(me),2)<8&(sum(abs(me),2)>4|min(me,[],2)<0));
        [i,j]=find(~me(k,:));   eN(ee(k(i)+(j-1)*nE))=1;
        me=eN(ire); fg=ire(any(me(:,2:end),2),1);   sp=find(eN(fg)~=-1);
        eN(fg(sp))=-1;
    end
    %% New nodes for refined elements and boundaries
    eN(ire(:,1))=-1;    i=eN>0;    eN(i)=size(cd,1)+(1:nnz(i));
    cd(eN(i),:)=(cd(en(i,1),:)+cd(en(i,2),:))/2;
    tf(eN(i))=(tf(en(i,1))+tf(en(i,2)))/2;
    nbo=(nargout-4);    varargout=cell(nbo,1);
    for j=1:nbo
        bd=varargin{j};
        if ~isempty(bd)
            nN=eN(be{j})';    mEs=find(nN);
            if ~isempty(mEs)
                bd=[bd(~nN,:);bd(mEs,1),nN(mEs);nN(mEs),bd(mEs,2)];
            end
        end
        varargout{j}=bd;
    end
    eN(ire(:,1))=ir(:,3);   nN=reshape(eN(ee),[],8);
    rt=(nN~=0)*2.^(0:8-1)'; mb=(2^8)-1; none=rt<mb; r=rt==mb;  i=find(r);
    mN=zeros(nE,1); mN(i)=size(cd,1)+(1:length(i));
    cd=[cd;(cd(ep(i,1),:)+cd(ep(i,2),:)+cd(ep(i,3),:)+cd(ep(i,4),:))/4];
    tf=[tf;(tf(ep(i,1))+tf(ep(i,2))+tf(ep(i,3))+tf(ep(i,4)))/12+...
        (tf(ep(i,5))+tf(ep(i,6))+tf(ep(i,7))+tf(ep(i,8)))/6];
    mn=zeros(4*nE,1);   ii=[4*i-3,4*i-2,4*i-1,4*i]; ix=reshape(ii',[],1);
    jj=1:length(i); ii=[4*jj-3,4*jj-2,4*jj-1,4*jj]; jx=reshape(ii,[],1);
    mn(ix)=size(cd,1)+(1:4*length(i));  mn=reshape(mn,4,[])';
    mc=zeros(length(ix),2); tc=zeros(length(ix),1);
    mc(jx,:)=[(cd(ep(i,5),:)+cd(mN(i),:))/2;(cd(ep(i,6),:)+cd(mN(i),:))/2;...
        (cd(ep(i,7),:)+cd(mN(i),:))/2;(cd(ep(i,8),:)+cd(mN(i),:))/2];
    tc(jx,:)=[(tf(ep(i,5))+tf(mN(i)))/2;(tf(ep(i,6))+tf(mN(i)))/2;...
        (tf(ep(i,7))+tf(mN(i)))/2;(tf(ep(i,8))+tf(mN(i)))/2];
    cd=[cd;mc]; tf=[tf;tc];
    i=zeros(nE,1);  i(none)=1;  i(r)=4;    i=[1;1+cumsum(i)];
    %% New elements and topology
    nep=zeros(i(end)-1,8);  nep(i(none),:)=ep(none,:);
    nep([i(r),1+i(r),2+i(r),3+i(r)],:)=[ep(r,1),ep(r,5),mN(r),ep(r,8),...
        nN(r,1),mn(r,1),mn(r,4),nN(r,8);ep(r,5),ep(r,2),ep(r,6),mN(r),...
        nN(r,2),nN(r,3),mn(r,2),mn(r,1);mN(r),ep(r,6),ep(r,3),ep(r,7),...
        mn(r,2),nN(r,4),nN(r,5),mn(r,3);ep(r,8),mN(r),ep(r,7),ep(r,4),...
        mn(r,4),mn(r,3),nN(r,6),nN(r,7)];
    %% New 1-irregular data
    k=find(rt>0&rt<mb); [i,j,V]=find(nN(k,:));    edx=ee(k(i)+(j-1)*nE);
    ir=[en(edx,:),V(:)];  nN=reshape(eN(ire(:,2:3)),[],2);
    k=find(sum(nN,2)~=0);    [i,j,V]=find(nN(k,:));
    edx=ire(k(i)+(j-1+1)*size(ire,1));  ir=[ir;[en(edx(:),:),V(:)]];
end
```

```
function [K,dKe,dV]=Km(ep,eX,eY,E,nu,dJp,w,E0,Em,xs,pn)
%% 2D Jacobain
dNr = [-0.6830,-0.2277,-0.1830,-0.0610,0.9107,0.3333,0.2440,-0.3333;-0.6830,-0.0610,-
0.1830,-0.2277,-0.3333, 0.2440, 0.3333, 0.9107;0.2277, 0.6830, 0.0610, 0.1830,-0.9107,
0.3333,-0.2440,-0.3333;-0.0610,-0.6830,-0.2277,-0.1830,-0.3333, 0.9107, 0.3333,
0.2440;0.1830, 0.0610, 0.6830, 0.2277,-0.2440, 0.3333,-0.9107,-0.3333;0.1830, 0.2277,
0.6830, 0.0610,-0.3333,-0.9107, 0.3333,-0.2440;-0.0610,-0.1830,-0.2277,-0.6830, 0.2440,
0.3333, 0.9107,-0.3333;0.2277, 0.1830, 0.0610, 0.6830,-0.3333,-0.2440, 0.3333,-0.9107];
et=size(ep,1);  JTx=dNr*eX';  JTy=dNr*eY';
```

```
JT(1:4:16,:)=JTx(1:2:end,:);    JT(3:4:16,:)=JTy(1:2:end,:);
JT(2:4:16,:)=JTx(2:2:end,:);    JT(4:4:16,:)=JTy(2:2:end,:);
JT=reshape(JT,2,2,4,et);
dJT=JT(1,1,:,:).*JT(2,2,:,:)-JT(1,2,:,:).*JT(2,1,:,:);
IJT=[JT(2,2,:,:) -JT(1,2,:,:);-JT(2,1,:,:) JT(1,1,:,:)]./dJT;
dN=zeros(8,2,4,et);    f=@(x) sum(x,2); g=@(x) reshape(x,[],1);
for i=1:4,  j=[2*i-1;2*i];
    for k=1:2,  dN(:,k,i,:)=f(IJT(k,:,i,:).*dNr(j,:)'); end
end
dV=sum(dJT,3).*w*(E0-Em); dV=accumarray(g(ep'),dV(:));
%% Constitutive, Strain and Element Stiffness matrices
D=E/(1-nu^2)*[1 nu 0;nu 1 0;0 0 (1-nu)/2];
BT(1:2:16,1,:,:)=dN(:,1,:,:);   BT(2:2:16,2,:,:)=dN(:,2,:,:);
BT(1:2:16,3,:,:)=dN(:,2,:,:);   BT(2:2:16,3,:,:)=dN(:,1,:,:);
BTD=zeros(16,3,4,et);   Ke1=zeros(16,16,4,et);
for i=1:3,  BTD(:,i,:,:)=f(BT.*D(:,i)');    end
for i=1:16, Ke1(:,i,:,:)=f(BTD.*BT(i,:,:,:));    end
Ke=sum(Ke1.*dJp,3); dt=pn*(E0-Em)*xs(ep).^(pn-1).*w;
dKe=sum(Ke1.*dJT,3).*reshape(dt',1,1,8,et);
%% Assembly of global stiffness matrix
emt=zeros(et,16);   emt(:,2:2:end)=ep*2;emt(:,1:2:end)=ep*2-1;
I=reshape(repmat((1:16),16,1),1,[]);    J=repmat(1:16,1,16);
iK=g(emt(:,I)');    jK=g(emt(:,J)');
K=sparse(iK,jK,Ke(:),max(iK),max(iK),nzmax(Ke(:)));  K=(K+K')/2;
end
```

```
function d=slse(K,lid,load,fxdfs,ir,ep,cd)
%% Sorting Non-Confirming nodes
f=@(x) reshape(x',[],1);    hn=ir(:,3); mn=reshape(ep(:,5:8)',[],1);
cn=reshape(ir(:,1:2)',[],1);    [ni,~]=find(mn==cn');
eI=floor((ni-1)/4)+1;   nI=(ni-(eI-1)*4)*2; ie=ep(eI,[1 5 2 6 3 7 4 8 1]);
nH=length(nI);  ied=ie((1:nH)'+nH*[nI-2 nI-1 nI]);
fn=@(x,y) [x.*(x-1)/2.0 (1+x).*(1-x) x.*(1+x)/2.0];
EL=(sum((cd(ied(:,3),:)-cd(ied(:,1),:)).^2,2).^(1/2));
HL=(sum((cd(hn,:)-cd(ied(:,1),:)).^2,2).^(1/2));
xsi=2.0*HL./EL-1;   NF=bsxfun(fn,xsi,1);
%% Preparing Analysis
ik=2*repmat((1:nH)',1,4);   ik=f([ik-1 ik]);
jk=f([2*ied-1 2*hn-1 2*ied 2*hn]);
CV=f([-NF ones(nH,1) -NF ones(nH,1)]);  Z=sparse(2*nH,2*nH);
aldfs=size(K,1); C=sparse(ik,jk,CV,2*nH,aldfs,nzmax(CV));
KC=[K C';C Z]; F=sparse(lid,1,load,aldfs,1); FC=[F;zeros(2*nH,1)];
galdfs=size(KC,1); fdfs=setdiff((1:galdfs)',fxdfs); U=zeros(galdfs,1);
U(fdfs)=KC(fdfs,fdfs)\FC(fdfs);    d=U(1:aldfs);
end
```

Appendix D

Examples:

```
C3: topMBB3D20N([15,4,2.5],[0.19,2.5],-100,[230000,1/3],0.5,3,1.5,0)
C4: topMBB3D20N([15,4,2.5],0.3825,-100,[230000,1/3],0.5,3,1.5,0)
C5: topMBB3D20N([15,4,2.5],[0.1,2.5],-100,[230000,1/3],0.5,3,1.5,0)
C6: topMBB3D20N([15,4,2.5],0.1,-100,[230000,1/3],0.5,3,1.5,1,0)
```

MATLAB topMBB3D20N code:

```
function topMBB3D20N(domain,ez,load,matprop,volfrac,penal,rmin,itProc,alp)
%% MBB SETUP
% Planar direction setup for MBB beam
close all; dis=0;  f=@(x) reshape(x,[],1);
if length(ez)==1, ezX=ez; ezY=ez; ezZ=ez;
else, ezX=ez(1); ezY=ez(1); ezZ=ez(2);
end
a=domain(1);    b=domain(2);    c=domain(3);
nX1=round(a/ezX); nY1=round(b/ezY); nZ1=round(c/ezZ);
ezX=a/nX1; ezY=b/nY1; ezZ=c/nZ1; cZ=(-nZ1:nZ1)*ezZ/2;
[aX,bY]=meshgrid(0:nX1,0:nY1); ccX=aX*ezX;  ccY=bY*ezY; nc=(nX1+1)*(nY1+1);
ns=reshape(1:nc,nY1+1,[]); cc=zeros(nc,2); cc(ns(:),:)=[ccX(:) ccY(:)];
% planar (XY) topology and coordinates
c1=f(ns(1:end-1,1:end-1));  c2=f(ns(1:end-1,2:end));
c3=f(ns(2:end,2:end));  c4=f(ns(2:end,1:end-1));
ec=[c1 c2 c3 c4]; ed=reshape(ec(:,[1:4,2:4,1]),[],2);
[en,~,ix]=unique(sort(ed,2),'rows');
em=reshape(ix,[],4)+nc; cm=(cc(en(:,1),:)+cc(en(:,2),:))/2;
epP=[ec em]; cdP=[cc;cm]; ntP=nc+size(cm,1); etP=size(epP,1);
% Preparing 3D Topology
n1=f(repmat((1:ntP),1,1,nZ1+1)+reshape((0:nZ1)*(ntP+nc),1,1,nZ1+1));
n2=f(repmat((1:nc)+ntP,1,1,nZ1)+reshape((0:nZ1-1)*(ntP+nc),1,1,nZ1));
nt=max([n1;n2]);    cd=zeros(nt,3);
cd(n1,:)=[repmat(cdP,nZ1+1,1) f(repmat(cZ(1:2:end),ntP,1))];
cd(n2,:)=[repmat(cc,nZ1,1) f(repmat(cZ(2:2:end),nc,1))];
et=nX1*nY1*nZ1; ep=zeros(et,20);
epR=reshape(repmat((0:nZ1-1)*(ntP+nc),etP,1),[],1);
ep(:,1:8)=repmat(epP,nZ1,1)+epR; ep(:,9:12)=repmat(ec,nZ1,1)+epR+ntP;
ep(:,13:20)=repmat(epP,nZ1,1)+epR+ntP+nc;
% Initial Volume
V0=a*b*c;
%% DEFINE LOADS AND SUPPORTS
adfs=(1:3*nt)'; U=zeros(3*nt,1); lel=(1:etP:et)+(0:nY1-1)';
```

```
ln=unique(f(ep(lel(:),[1,4,8,9,12,13,16,20]))); rel=(etP:etP:et)+1-nY1;
rn=unique(f(ep(rel,[2,10,14])));
fxdfs=[3*ln-2;3*ln;3*rn-1]; fdfs=setdiff(adfs,fxdfs);
nlx=4; % Number of elements rows in x-direction for distributing load
we=repmat((nlx:-1:1)*load/(sum(1:nlx)*nZ1),nZ1,1);
we=we(:).*[-1/12*ones(1,4) 1/3*ones(1,4)]; lel=(0:nZ1-1)'*etP+nY1*(1:nlx);
lid=3*f(ep(lel,[4,3,15,16,7,11,19,12]))-1;
F=accumarray(lid,we(:),[3*nt,1],[],0,1);
%% MATERIAL PROPERTIES AND CONSTIUTIVE MATRIX
if isempty(matprop), E=1000;  nu=0.3;
elseif length(matprop)==1,    nu=0.3;
else, E=matprop(1);   nu=matprop(2);
end
D=E/(1+nu)/(1-2*nu)*[1-nu nu nu 0 0 0; nu 1-nu nu 0 0 0;...
    nu nu 1-nu 0 0 0; 0 0 0 (1-2*nu)/2 0 0; 0 0 0 0 (1-2*nu)/2 0;...
    0 0 0 0 0 (1-2*nu)/2]; E0 = 1; Em = 1e-9;
%% PENALTY FUNCTION
if length(penal)==1,    pl=penal;   dp=0;   ph=penal;
elseif length(penal)==2,   dp=diff(penal)/100;   pl=penal(1);  ph=penal(2);
    if dp<0,    disp('check penalty limits');   return; end
elseif length(penal)==3, pl=penal(1); dp=penal(2); ph=penal(3); ck=(ph-pl);
    if ck<0||dp>ck||dp<0, disp('check penalty limits');   return; end
end
%% STIFFNESS MATRIX
% Preparing Jacobian
           dNr    =    [-0.4072,-0.311,-0.1796,-0.0129,0.7182,0.2629,0.1925,-0.2629,-
0.2629,0.2629,0.0704,-0.0704,-0.0129,-0.1796,-0.0739,0.0223,0.1925,0.0704,0.0516,-0.0704;-
0.4072,-0.0129,-0.1796,-0.311,-0.2629,0.1925,0.2629,0.7182,-0.2629,-0.0704,0.0704,0.2629,-
0.0129,0.0223,-0.0739,-0.1796,-0.0704,0.0516,0.0704,0.1925;-0.4072,-0.0129,0.0223,-0.0129,-
0.2629,-0.0704,-0.0704,-0.2629,0.7182,0.1925,0.0516,0.1925,-0.311,-0.1796,-0.0739,-
0.1796,0.2629,0.0704,0.0704,0.2629;0.311,0.4072,0.0129,0.1796,-0.7182,0.2629,-0.1925,-
0.2629,-0.2629,0.2629,0.0704,-0.0704,0.1796,0.0129,-0.0223,0.0739,-0.1925,0.0704,-0.0516,-
0.0704;-0.0129,-0.4072,-0.311,-0.1796,-0.2629,0.7182,0.2629,0.1925,-0.0704,-
0.2629,0.2629,0.0704,0.0223,-0.0129,-0.1796,-0.0739,-0.0704,0.1925,0.0704,0.0516;-0.0129,-
0.4072,-0.0129,0.0223,-0.2629,-0.2629,-0.0704,-0.0704,0.1925,0.7182,0.1925,0.0516,-0.1796,-
0.311,-0.1796,-0.0739,0.2629,0.2629,0.0704,0.0704;0.1796,0.0129,0.4072,0.311,-
0.1925,0.2629,-0.7182,-0.2629,-0.0704,0.0704,0.2629,-0.2629,0.0739,-0.0223,0.0129,0.1796,-
0.0516,0.0704,-0.1925,-0.0704;0.1796,0.311,0.4072,0.0129,-0.2629,-0.7182,0.2629,-0.1925,-
0.0704,-0.2629,0.2629,0.0704,0.0739,0.1796,0.0129,-0.0223,-0.0704,-0.1925,0.0704,-
0.0516;0.0223,-0.0129,-0.4072,-0.0129,-0.0704,-0.2629,-0.2629,-
0.0704,0.0516,0.1925,0.7182,0.1925,-0.0739,-0.1796,-0.311,-
0.1796,0.0704,0.2629,0.2629,0.0704;-0.0129,-0.1796,-0.311,-0.4072,0.1925,0.2629,0.7182,-
0.2629,-0.0704,0.0704,0.2629,-0.2629,0.0223,-0.0739,-0.1796,-0.0129,0.0516,0.0704,0.1925,-
0.0704;0.311,0.1796,0.0129,0.4072,-0.2629,-0.1925,0.2629,-0.7182,-0.2629,-
0.0704,0.0704,0.2629,0.1796,0.0739,-0.0223,0.0129,-0.0704,-0.0516,0.0704,-0.1925;-
0.0129,0.0223,-0.0129,-0.4072,-0.0704,-0.0704,-0.2629,-0.2629,0.1925,0.0516,0.1925,0.7182,-
0.1796,-0.0739,-0.1796,-0.311,0.0704,0.0704,0.2629,0.2629;-0.0129,-0.1796,-
0.0739,0.0223,0.1925,0.0704,0.0516,-0.0704,-0.2629,0.2629,0.0704,-0.0704,-0.4072,-0.311,-
0.1796,-0.0129,0.7182,0.2629,0.1925,-0.2629;-0.0129,0.0223,-0.0739,-0.1796,-
0.0704,0.0516,0.0704,0.1925,-0.2629,-0.0704,0.0704,0.2629,-0.4072,-0.0129,-0.1796,-0.311,-
0.2629,0.1925,0.2629,0.7182;0.311,0.1796,0.0739,0.1796,-0.2629,-0.0704,-0.0704,-0.2629,-
0.7182,-0.1925,-0.0516,-0.1925,0.4072,0.0129,-
0.0223,0.0129,0.2629,0.0704,0.0704,0.2629;0.1796,0.0129,-0.0223,0.0739,-0.1925,0.0704,-
0.0516,-0.0704,-0.2629,0.2629,0.0704,-0.0704,0.311,0.4072,0.0129,0.1796,-0.7182,0.2629,-
0.1925,-0.2629;0.0223,-0.0129,-0.1796,-0.0739,-0.0704,0.1925,0.0704,0.0516,-0.0704,-
0.2629,0.2629,0.0704,-0.0129,-0.4072,-0.311,-0.1796,-
0.2629,0.7182,0.2629,0.1925;0.1796,0.311,0.1796,0.0739,-0.2629,-0.2629,-0.0704,-0.0704,-
0.1925,-0.7182,-0.1925,-0.0516,0.0129,0.4072,0.0129,-
0.0223,0.2629,0.2629,0.0704,0.0704;0.0739,-0.0223,0.0129,0.1796,-0.0516,0.0704,-0.1925,-
0.0704,-0.0704,0.0704,0.2629,-0.2629,0.1796,0.0129,0.4072,0.311,-0.1925,0.2629,-0.7182,-
0.2629;0.0739,0.1796,0.0129,-0.0223,-0.0704,-0.1925,0.0704,-0.0516,-0.0704,-
0.2629,0.2629,0.0704,0.1796,0.311,0.4072,0.0129,-0.2629,-0.7182,0.2629,-
0.1925;0.0739,0.1796,0.311,0.1796,-0.0704,-0.2629,-0.2629,-0.0704,-0.0516,-0.1925,-0.7182,-
0.1925,-0.0223,0.0129,0.4072,0.0129,0.0704,0.2629,0.2629,0.0704;0.0223,-0.0739,-0.1796,-
0.0129,0.0516,0.0704,0.1925,-0.0704,-0.0704,0.0704,0.2629,-0.2629,-0.0129,-0.1796,-0.311,-
```

```
0.4072,0.1925,0.2629,0.7182,-0.2629;0.1796,0.0739,-0.0223,0.0129,-0.0704,-0.0516,0.0704,-
0.1925,-0.2629,-0.0704,0.0704,0.2629,0.311,0.1796,0.0129,0.4072,-0.2629,-0.1925,0.2629,-
0.7182;0.1796,0.0739,0.1796,0.311,-0.0704,-0.0704,-0.2629,-0.2629,-0.1925,-0.0516,-0.1925,-
0.7182,0.0129,-0.0223,0.0129,0.4072,0.0704,0.0704,0.2629,0.2629];
JTx=dNr*cd(ep(1,:),1);  JTy=dNr*cd(ep(1,:),2);  JTz=dNr*cd(ep(1,:),3);
JT(1:9:72,:)=JTx(1:3:end,:);  JT(2:9:72,:)=JTx(2:3:end,:);
JT(3:9:72,:)=JTx(3:3:end,:);  JT(4:9:72,:)=JTy(1:3:end,:);
JT(5:9:72,:)=JTy(2:3:end,:);  JT(6:9:72,:)=JTy(3:3:end,:);
JT(7:9:72,:)=JTz(1:3:end,:);  JT(8:9:72,:)=JTz(2:3:end,:);
JT(9:9:72,:)=JTz(3:3:end,:);  JT=reshape(JT,3,3,8);
dJT=JT(1,1,:,:).*(JT(2,2,:,:).*JT(3,3,:,:)-JT(3,2,:,:).*JT(2,3,:,:))-...
    JT(1,2,:,:).*(JT(2,1,:,:).*JT(3,3,:,:)-JT(3,1,:,:).*JT(2,3,:,:))+...
    JT(1,3,:,:).*(JT(2,1,:,:).*JT(3,2,:,:)-JT(3,1,:,:).*JT(2,2,:,:));
% Preparing Strain Matrix and Stiffness matrix
dN=zeros(3,20,8);
for i=1:8,    ix=[3*i-2;3*i-1;3*i]; dN(:,:,i)=JT(:,:,i)\dNr(ix,:);    end
B(1,1:3:60,:)=dN(1,:,:); B(2,2:3:60,:)=dN(2,:,:); B(3,3:3:60,:)=dN(3,:,:);
B(4,1:3:60,:)=dN(2,:,:); B(4,2:3:60,:)=dN(1,:,:); B(5,2:3:60,:)=dN(3,:,:);
B(5,3:3:60,:)=dN(2,:,:); B(6,3:3:60,:)=dN(1,:,:); B(6,1:3:60,:)=dN(3,:,:);
K1=zeros(60,60,8,1); for i=1:8,  K1(:,:,i)=B(:,:,i)'*D*B(:,:,i)*dJT(i); end
KE = sum(K1,3);
%% PREPARE FINITE ELEMENT ANALYSIS AND FILTER
emt=zeros(et,60); emt(:,3:3:end)=ep*3; emt(:,2:3:end)=ep*3-1;
emt(:,1:3:end)=ep*3-2; I=reshape(repmat((1:60),60,1),1,[]);
J=repmat(1:60,1,60); iK=f(emt(:,I)'); jK=f(emt(:,J)');
g=@(x) x(ep); eX=g(cd(:,1)); eY=g(cd(:,2)); eZ=g(cd(:,3));
h=@(x) sum(x*1/4.*[-ones(1,4) ones(1,8) -ones(1,4) ones(1,4)],2);
eXc=h(eX);  eYc=h(eY);  eZc=h(eZ);  eC=[eXc eYc eZc];
rmin = (rmin+1e-3)*max(ezX,ezY); [Id,r]=rangesearch(eC,eC,rmin);
w0=cell2mat(arrayfun(@(i) [i*ones(length(Id{i}),1) Id{i}' (rmin-r{i})']...
    ,(1:length(eC))','un',0));
H=sparse(w0(:,1),w0(:,2),w0(:,3),max(w0(:,1)),max(w0(:,1)),nzmax(w0(:,3)));
Hs=sum(H,2);
x=ones(et,1); xs=x; lp=0;   lt=0;   ch=1;   maxloop=50;
% Linear system of equations Iterative parameters
Vr=sum(x)/et; xld=(a-cd(:,1)); xUy=load*xld.*(3*a^2-xld.^2)/(E*c*b^3);
% START ITERATION
dch=0.01;   dv=ones(et,1)*ezX*ezY*ezZ;  dv(:)= H*(dv(:)./Hs); ith=0.5;
figure()
%% START ITERATION
while ch > dch && lp<maxloop
    %% PENALTY
    tic;    lp=lp+1;    pn=pl+dp*(lp-1);    if pn>ph,   pn=ph;   end
    %% FE-ANALYSIS
    sK=KE(:)*(Em+xs(:)'.^pn*(E0-Em)); K=sparse(iK,jK,sK(:)); K=(K+K')/2;
  % Choose the procedure based on the specifications of the computer
    if itProc==1
      if nargin<9, alp=0.1; end
      % Iterative procedure for relatively large number of nodes
      K=K(fdfs,fdfs); ro=symrcm(K); xU=U; xU(2:3:end)=xUy/Vr;
      K=K(ro,ro); ro=fdfs(ro); Fs=F(ro); xUs=xU(ro);
        % Please change alp value > 0 if iterative procedure fails
      L=ichol(K,struct('type','ict','droptol',1e-3,'diagcomp',alp));
      xUs=pcg(K,Fs,1e-4,1000,L,L',xUs); U(ro)=xUs;
    else
      % Direct procedure
      U(fdfs)=K(fdfs,fdfs)\F(fdfs);
    end
    %% OBJECTIVE FUNCTION,SENSITIVITY ANALYSIS AND FILTERING/MODIFICATION
    ce=sum((U(emt)*KE).*U(emt),2);  C=sum((Em+xs.^pn*(E0-Em)).*ce);
    dc=-pn*(E0-Em)*xs.^(pn-1).*ce;
    dc(:)=H*(dc(:)./Hs);
    %% OPTIMALITY CRITERIA UPDATE OF DESIGN VARIABLES
    l1=0;   l2=1e9; mv=0.2;
    while (l2-l1)/(l1+l2)>1e-3
```

```
            lmd=0.5*(l2+l1);
            xnew=max(0,max(x-mv,min(1,min(x+mv,x.*sqrt(abs(dc)./dv/lmd)))));
            xs(:)=(H*xnew(:))./Hs; V=sum(xs(:))*ezX*ezY*ezZ; Vr=V/V0;
            if Vr>volfrac,  l1=lmd; else,   l2=lmd; end
        end
        ch=max(abs(xnew(:)-x(:)));  x=xnew; lt=lt+toc;
        %% PRINT RESULTS
        pr='It.:%5i Obj.:%11.2f Vol.:%7.3f ch.:%7.3f t.:%7.2f Penal.:%7.2f\n';
        fprintf(pr,lp,C,Vr,ch,lt,pn);
        %% DISPLAY DENSITIES
        if dis, mydisp(); end
    end
    mydisp();
    %% PLOT DENSITIES
    function mydisp()
        clf; xpl=(xs>ith);
      epl=ep(xpl,:); xP=reshape(repmat(xs(xpl)',6,1),[],1);
        P=patch('Faces',reshape(epl(:,[1 5 2 6 3 7 4 8 1 2 10 14 18 15 11 3 ...
            6 2 13 17 14 18 15 19 16 20 13 1 9 13 20 16 12 4 8 1 1 5 2 10 ...
            14 17 13 9 1 4 7 3 11 15 19 16 12 4])',9,[])','Vertices',...
            cd(:,[3,1,2]),'EdgeColor','none','FaceVertexCData',xP);
        caxis([0 1]); daspect([1 1 1]); P.FaceColor='flat';
        axis off; colormap(jet); view(60,20); set(gcf,'color','w'); drawnow;
    end
    end
    % ========================================================================
    % === This code was modified from top3d.m by Tejeswar Yarlagadda,      ===
    % === PhD Student, BEEE, POLYU, HONGKONG                               ===
    % === --------------------------------------------------------------- ===
    % === The top3d code is intended for educational purposes, and         ===
    % === the details and extensions can be found in the paper:            ===
    % === K. Liu and A. Tovar, "An efficient 3D topology optimisation code  ===
    % === written in Matlab", Struct Multidisc Optim,50(6):1175-1196, 2014, ===
    % === doi:10.1007/s00158-014-1107-x                                    ===
    % === Please send your suggestions and comments on top3d.m to:         ===
    % === kailiu@iupui.edu                                                 ===
    % === Please send your suggestions and comments on topMBB3D20N.m to:   ===
    % === yarlagadda.tejeswar@gmail.com                                    ===
    % === --------------------------------------------------------------- ===
    % === Disclaimer:                                                      ===
    % === The authors reserves all rights for the program.                 ===
    % === The code may be distributed and used for educational purposes.   ===
    % === The authors do not guarantee that the code is free from errors   ===
```

Appendix E

```
%%%% AN 220 LINE 2.5D SIMTP PRESTRESSING CODE FEBRUARY, 2022             %%%%
function topPSC(domain,ez,ld,ldtype,pf,niS,matprop,volfrac,penal,rmin)
%% SHEPARD WEIGHTS
close all; w=[1/12*ones(1,4) 1/6*ones(1,4)];   f=@(x) reshape(x,[],1);
%% MESH GENERATION
% Corner node coordinates for a Simply supported or Multiple support beam
a=domain(1); b=domain(2); nX=round(a/ez); nY=round(b/ez); cv=b/15;
if nX<=30, nX=30; ez=a/nX; nY=round(b/ez); end
[aX,bY]=meshgrid(0:nX,0:nY);  ccX=aX*ez;  ccY=bY*ez; nc=(nX+1)*(nY+1);
ns=reshape(1:nc,nY+1,[]); cc=zeros(nc,2); cc(ns(:),:)=[ccX(:) ccY(:)];
% Corner node topology
c1=f(ns(1:end-1,1:end-1));  c2=f(ns(1:end-1,2:end));
c3=f(ns(2:end,2:end));  c4=f(ns(2:end,1:end-1));
% Nodal coordinates of eight noded element and element topology arrangement
ec=[c1 c2 c3 c4];   eds=reshape(ec(:,[1:4,2:4,1]),[],2);
[en,~,ix]=unique(sort(eds,2),'rows');   em=reshape(ix,[],4)+size(cc,1);
cm=(cc(en(:,1),:)+cc(en(:,2),:))/2; cd=[cc;cm]; ep=[ec em];
% Stiff elements
et=size(ep,1);  nt=size(cd,1); epr=zeros(nY,8); nN=3*nY+2; nG=nt+nN;
epr(:,[1 8 4])=ep(et-nY+1:et,[2 6 3]); epr(:,[5 7])=(1:nY)'+nt+[0 1];
epr(:,[2 6 3])=(1:2:2*nY)'+nt+nY+1+[0 1 2];  eG=[ep;epr];
%% DEFINE LOADS AND SUPPORTS
adfs=(1:2*nG)'; UG=zeros(2*nG,1); F2=sparse(2*nN,1);
if strcmpi(ldtype,'con'), udl=0; F1=sparse(2*(nY+1),1,ld,2*nG,1);
elseif strcmpi(ldtype,'udl')
    udl=1; xid=unique(f(ep(nY*(1:nX)'-(0:3),:)));
    lid1=2*f((ep(nY*(1:nX),[3 4]))); lid2=2*f((ep(nY*(1:nX),7)));
    F1=(sparse(lid1,1,1/6,2*nG,1)+sparse(lid2,1,2/3,2*nG,1))*ld*ez;
else, disp('load type doesnot exist'); return;
end
iS=[]; rs=[(nc-nY:nc)';ep(et-nY+(1:nY),6)]; lS=[(1:nY+1)';ep(1:nY,8)];
if ~isempty(niS)
    iSs=2*a/(niS+1); iSX=(iSs:iSs:2*a-iSs)'-a; iSX(iSX<0)=[];
    iSY=zeros(length(iSX),1); iSn=unique(f(ep((0:nX-1)*nY+1,[1 5 2])));
    iSI=knnsearch(cd(iSn,:),[iSX iSY]); iS=iSn(iSI);
end
fxdfs=sort([(2*lS-1);2*[rs;iS]]); fdfs=setdiff(adfs,fxdfs);
%% PRESTRESSING AND BEZIER PARAMETERS
% Segmentation and Preparation of refinement of nodes
up=1; dj=zeros(nt,1); i1=dj; exd=dj; dV=dj; pec=([1:3:(nX-2) nX]-1)*nY+1;
nrN=length(pec); rN=zeros(nrN,2); pe=zeros(nrN,1); sL=zeros(nrN-1,1);
rN(:,1)=cd([ep(pec(1:end-1),1);ep(pec(end),2)],1); t=rN(:,1)/rN(end,1);
per=[pec(1:end-1)-1 et]; scn=[{zeros(0,1)};arrayfun(@(i) ...
```

```
    unique(ep((1:nY)'+per(i+1),[1 4 8])),(1:nrN-2)','un',0)];
sn=arrayfun(@(i) setdiff(unique(ep(per(i)+1:(per(i+1)),:)),...
    scn{i}),(1:nrN-1)','un',0); si=cell2mat(sn);
sz=cell2mat(arrayfun(@(i) i*ones(length(sn{i}),1),(1:nrN-1)','un',0));
szz=[sz;sz+1]; InC=[cd(1:nY+1,2) [cd(2:nY+1,2);cd(nY+1,2)+1e-3]];
% Intial tendon limits, Bezier points, coeffecients and Derivatives
y0=cv; ym=b-cv; y=[y0*ones(10,1);ym]; nP=length(y);
if isempty(iS), y(end-4+(1:3))=[0.3;0.5;0.7]*b;
else
    iSx=cd(iS,1)'; tx=linspace(0,a,nP)';
    [ti,~]=find((iSx-tx(1:end-1)>=0)&(tx(2:end)-iSx>0)); y(ti+(0:1)')=ym;
end
nd=nP-1; ii=0:1:nd; jj=ii(1:end-1); ys=y;
z=arrayfun(@(i) nchoosek(nd,i),ii); dz=arrayfun(@(i) nchoosek(nd-1,i),jj);
zt=z.*((1-t).^(nd-ii)).*(t.^ii);    dzt=dz.*((1-t).^(nd-1-jj)).*(t.^jj);
rN(:,2)=zt*ys; Px=linspace(0,rN(end,1),nP)'; dPx=diff(Px); TV=zeros(nrN,2);
TV(:,1)=nd*dzt*dPx; NF=@(x,y) [x.*(x-1)/2.0 (1+x).*(1-x) x.*(1+x)/2.0];
%% MATERIAL PROPERTIES AND CONSTIUTIVE MATRIX
if isempty(matprop), E=1000; nu=0.3; dm=0;
elseif length(matprop)==1, E=matprop(1); nu=0.3; dm=0;
elseif length(matprop)==2, E=matprop(1); nu=matprop(2); dm=0;
else, E=matprop(1); nu=matprop(2); dm=matprop(3);
end
Em=0.02; E0=1;    D=E/(1-nu^2)*[1 nu 0;nu 1 0;0 0 (1-nu)/2]; gr=-9.81;
%% PENALTY FUNCTION
if length(penal)==1,    pl=penal;    dp=0;    ph=penal;
elseif length(penal)==2,    dp=diff(penal)/100;    pl=penal(1);   ph=penal(2);
    if dp<0,    disp('check penalty limits');    return; end
elseif length(penal)==3, pl=penal(1); dp=penal(2); ph=penal(3); ck=(ph-pl);
    if ck<0||dp>ck||dp<0, disp('check penalty limits');    return; end
end
%% STIFFNESS MATRIX
% Preparing Jacobian
N=[0.0962 -0.1667 -0.0962 -0.1667 0.5258 0.1409 0.1409 0.5258;-0.1667 0.0962 -0.1667
-0.0962 0.5258 0.5258 0.1409 0.1409;-0.0962 -0.1667 0.0962 -0.1667 0.1409 0.5258 0.5258
0.1409;-0.1667 -0.0962 -0.1667 0.0962 0.1409 0.1409 0.5258 0.5258];
dNr=[-0.6830,-0.2277,-0.1830,-0.0610,0.9107,0.3333,0.2440,-0.3333;-0.6830,-0.0610,-
0.1830,-0.2277,-0.3333, 0.2440, 0.3333, 0.9107;0.2277, 0.6830, 0.0610, 0.1830,-0.9107,
0.3333,-0.2440,-0.3333;-0.0610,-0.6830,-0.2277,-0.1830,-0.3333, 0.9107, 0.3333,
0.2440;0.1830, 0.0610, 0.6830, 0.2277,-0.2440, 0.3333,-0.9107,-0.3333;0.1830, 0.2277,
0.6830, 0.0610,-0.3333,-0.9107, 0.3333,-0.2440;-0.0610,-0.1830,-0.2277,-0.6830, 0.2440,
0.3333, 0.9107,-0.3333;0.2277, 0.1830, 0.0610, 0.6830,-0.3333,-0.2440, 0.3333,-0.9107];
JTx=dNr*cd(ep(1,:),1);  JTy=dNr*cd(ep(1,:),2);
JT(1:4:16,:)=JTx(1:2:end,:);    JT(3:4:16,:)=JTy(1:2:end,:);
JT(2:4:16,:)=JTx(2:2:end,:);    JT(4:4:16,:)=JTy(2:2:end,:);
JT=reshape(JT,2,2,4);   dJT=JT(1,1,:).*JT(2,2,:)-JT(1,2,:).*JT(2,1,:);
% Preparing Strain Matrix and Stiffness matrix
dN=zeros(2,8,4);
for i=1:4,    ix=[2*i-1;2*i]; dN(:,:,i,:)=JT(:,:,i)\dNr(ix,:);    end
B(1,1:2:16,:)=dN(1,:,:);    B(2,2:2:16,:)=dN(2,:,:);
B(3,1:2:16,:)=dN(2,:,:);    B(3,2:2:16,:)=dN(1,:,:);
K1=zeros(16,16,4,1);    K2=zeros(16,16,4,1);
for i=1:4,  K1(:,:,i)=B(:,:,i)'*D*B(:,:,i); K2(:,:,i)=K1(:,:,i)*dJT(i); end
KE = sum(K2,3); J2=zeros(1,1,4,nY);
% Preparing 3D Jacobian data for SIMTP
g=@(x) x(ep);   cX=cd(:,1); cY=cd(:,2); eX=g(cX);  eY=g(cY);
ds=[-0.4072,-0.311,-0.1796,-0.0129,0.7182,0.2629,0.1925,-0.2629,-
0.2629,0.2629,0.0704,-0.0704,-0.0129,-0.1796,-0.0739,0.0223,0.1925,0.0704,0.0516,-0.0704;-
0.4072,-0.0129,-0.1796,-0.311,-0.2629,0.1925,0.2629,0.7182,-0.2629,-0.0704,0.0704,0.2629,-
0.0129,0.0223,-0.0739,-0.1796,-0.0704,0.0516,0.0704,0.1925;-0.4072,-0.0129,0.0223,-0.0129,-
0.2629,-0.0704,-0.0704,-0.2629,0.7182,0.1925,0.0516,0.1925,-0.311,-0.1796,-0.0739,-
0.1796,0.2629,0.0704,0.0704,0.2629;0.311,0.4072,0.0129,0.1796,-0.7182,0.2629,-0.1925,-
0.2629,-0.2629,0.2629,0.0704,-0.0704,0.1796,0.0129,-0.0223,0.0739,-0.1925,0.0704,-0.0516,-
0.0704;-0.0129,-0.4072,-0.311,-0.1796,-0.2629,0.7182,0.2629,0.1925,-0.0704,-
0.2629,0.2629,0.0704,0.0223,-0.0129,-0.1796,-0.0739,-0.0704,0.1925,0.0704,0.0516;-0.0129,-
```

```
0.4072,-0.0129,0.0223,-0.2629,-0.2629,-0.0704,-0.0704,0.1925,0.7182,0.1925,0.0516,-0.1796,-
0.311,-0.1796,-0.0739,0.2629,0.2629,0.0704,0.0704;0.1796,0.0129,0.4072,0.311,-
0.1925,0.2629,-0.7182,-0.2629,-0.0704,0.0704,0.2629,-0.2629,0.0739,-0.0223,0.0129,0.1796,-
0.0516,0.0704,-0.1925,-0.0704;0.1796,0.311,0.4072,0.0129,-0.2629,-0.7182,0.2629,-0.1925,-
0.0704,-0.2629,0.2629,0.0704,0.0739,0.1796,0.0129,-0.0223,-0.0704,-0.1925,0.0704,-
0.0516;0.0223,-0.0129,-0.4072,-0.0129,-0.0704,-0.2629,-0.2629,-
0.0704,0.0516,0.1925,0.7182,0.1925,-0.0739,-0.1796,-0.311,-
0.1796,0.0704,0.2629,0.2629,0.0704;-0.0129,-0.1796,-0.311,-0.4072,0.1925,0.2629,0.7182,-
0.2629,-0.0704,0.0704,0.2629,-0.2629,0.0223,-0.0739,-0.1796,-0.0129,0.0516,0.0704,0.1925,-
0.0704;0.311,0.1796,0.0129,0.4072,-0.2629,-0.1925,0.2629,-0.7182,-0.2629,-
0.0704,0.0704,0.2629,0.1796,0.0739,-0.0223,0.0129,-0.0704,-0.0516,0.0704,-0.1925;-
0.0129,0.0223,-0.0129,-0.4072,-0.0704,-0.0704,-0.2629,-0.2629,0.1925,0.0516,0.1925,0.7182,-
0.1796,-0.0739,-0.1796,-0.311,0.0704,0.0704,0.2629,0.2629;-0.0129,-0.1796,-
0.0739,0.0223,0.1925,0.0704,0.0516,-0.0704,-0.2629,0.2629,0.0704,-0.0704,-0.4072,-0.311,-
0.1796,-0.0129,0.7182,0.2629,0.1925,-0.2629;-0.0129,0.0223,-0.0739,-0.1796,-
0.0704,0.0516,0.0704,0.1925,-0.2629,-0.0704,0.0704,0.2629,-0.4072,-0.0129,-0.1796,-0.311,-
0.2629,0.1925,0.2629,0.7182;0.311,0.1796,0.0739,0.1796,-0.2629,-0.0704,-0.0704,-0.2629,-
0.7182,-0.1925,-0.0516,-0.1925,0.4072,0.0129,-
0.0223,0.0129,0.2629,0.0704,0.0704,0.2629;0.1796,0.0129,-0.0223,0.0739,-0.1925,0.0704,-
0.0516,-0.0704,-0.2629,0.2629,0.0704,-0.0704,0.311,0.4072,0.0129,0.1796,-0.7182,0.2629,-
0.1925,-0.2629;0.0223,-0.0129,-0.1796,-0.0739,-0.0704,0.1925,0.0704,0.0516,-0.0704,-
0.2629,0.2629,0.0704,-0.0129,-0.4072,-0.311,-0.1796,-
0.2629,0.7182,0.2629,0.1925;0.1796,0.311,0.1796,0.0739,-0.2629,-0.2629,-0.0704,-0.0704,-
0.1925,-0.7182,-0.1925,-0.0516,0.0129,0.4072,0.0129,-
0.0223,0.2629,0.2629,0.0704,0.0704;0.0739,-0.0223,0.0129,0.1796,-0.0516,0.0704,-0.1925,-
0.0704,-0.0704,0.0704,0.2629,-0.2629,0.1796,0.0129,0.4072,0.311,-0.1925,0.2629,-0.7182,-
0.2629;0.0739,0.1796,0.0129,-0.0223,-0.0704,-0.1925,0.0704,-0.0516,-0.0704,-
0.2629,0.2629,0.0704,0.1796,0.311,0.4072,0.0129,-0.2629,-0.7182,0.2629,-
0.1925;0.0739,0.1796,0.311,0.1796,-0.0704,-0.2629,-0.2629,-0.0704,-0.0516,-0.1925,-0.7182,-
0.1925,-0.0223,0.0129,0.4072,0.0129,0.0704,0.2629,0.2629,0.0704;0.0223,-0.0739,-0.1796,-
0.0129,0.0516,0.0704,0.1925,-0.0704,-0.0704,0.0704,0.2629,-0.2629,-0.0129,-0.1796,-0.311,-
0.4072,0.1925,0.2629,0.7182,-0.2629;0.1796,0.0739,-0.0223,0.0129,-0.0704,-0.0516,0.0704,-
0.1925,-0.2629,-0.0704,0.0704,0.2629,0.311,0.1796,0.0129,0.4072,-0.2629,-0.1925,0.2629,-
0.7182;0.1796,0.0739,0.1796,0.311,-0.0704,-0.0704,-0.2629,-0.2629,-0.1925,-0.0516,-0.1925,-
0.7182,0.0129,-0.0223,0.0129,0.4072,0.0704,0.0704,0.2629,0.2629];
X(:,1:8)=eX;    X(:,9:16)=repmat(eX(:,1:4),1,2);  X(:,17:20)=eX(:,5:8);
Y(:,1:8)=eY;    Y(:,9:16)=repmat(eY(:,1:4),1,2);  Y(:,17:20)=eY(:,5:8);
sx=ds*X';   sy=ds*Y';
S(1:9:72,:)=sx(1:3:end,:);  S(2:9:72,:)=sx(2:3:end,:);
S(3:9:72,:)=sx(3:3:end,:);  S(4:9:72,:)=sy(1:3:end,:);
S(5:9:72,:)=sy(2:3:end,:);  S(6:9:72,:)=sy(3:3:end,:);
%% PREPARE FINITE ELEMENT ANALYSIS
emt=zeros(et+nY,16); emt(:,2:2:end)=eG*2;emt(:,1:2:end)=eG*2-1;
I=reshape(repmat((1:16),16,1),1,[]); J=repmat(1:16,1,16);
iG=f(emt(:,I)'); jG=f(emt(:,J)'); iK=f(emt(1:et,I)'); jK=f(emt(1:et,J)');
%% PREPARE FILTER
rmin = rmin+1e-6; bphil1=rmin*ez; bphil=min(b/3,max([bphil1,cv,3.0*ez]));
[Id,r]=rangesearch(cd,cd,bphil1);
w0=cell2mat(arrayfun(@(i) [i*ones(length(Id{i}),1) Id{i}' (bphil1-r{i})']...
    ,(1:nt)','un',0));
H=sparse(w0(:,1),w0(:,2),w0(:,3),max(w0(:,1)),max(w0(:,1)),nzmax(w0(:,3)));
Hs=sum(H,2);
%% INITIALIZE ITERATION
L=@(x) accumarray(f(ep'),x);    G=@(x) repmat(x,1,1,8,1);
x=ones(nt,1); x=TCf(x); xs=x; x2=x; lp=0; lt=0; ch=1; maxloop=100;
dch=0.001;  dv1=repmat(ez*ez*w*(E0-Em),et,1);  dv2=L(f(dv1'));
hs=1; er=0.6; dl=0.4; pn=pl; figure();
% Initial Volume
[V0,J3]=vol();
%% START ITERATION
while ch > dch && lp<maxloop
    %% PENALTY
    tic; lp=lp+1;
    if lp>1, up=min(4,up+0.05); hs=min(8,hs+0.01); pn=min(ph,pn+dp); end
    %% FE-ANALYSIS
```

```
        J1=J3d(); J2(:,:,[1 4 2 3],:)=repmat(J1(:,:,2:3,et-nY+1:et),[1 1 2 1]);
        sK1=sum(K1.*J1,3); sK2=1e3*sum(K1.*J2,3); K=sparse(iK,jK,sK1(:));
        KG=sparse(iG,jG,[sK1(:);sK2(:)]); K=(K+K')/2; KG=(KG+KG')/2;
        F3=sparse(2*f(ep'),1,f(sum(N.*reshape(J3,4,1,1,[]),1))*dm*gr,2*nt,1);
        F=F1+[Bzr();F2]+[F3;F2]; UG(fdfs)=KG(fdfs,fdfs)\F(fdfs);
        %% OBJECTIVE FUNCTION AND SENSITIVITY ANALYSIS
        U=UG(1:2*nt,1); C=U'*K*U; dt=pn*(E0-Em)*xs(ep).^(pn-1).*w;
        U0=U(emt(1:et,:))'; U1=G(reshape(U0,[],1,1,et));
        U2=G(reshape(U0,1,[],1,et)); dK=KE.*reshape(dt',1,1,8,et);
        dc1=sum(sum(U1.*dK.*U2,1),2); dc2=-L(dc1(:));
        %% FILTERING/MODIFICATION OF SENSITIVITIES
        [dx,ddj,dyri]=dTC();
        dc3=hs*dc2(:).*(1-(tanh(hs*(x2-er))).^2)/(tanh(hs*er)+tanh(hs*(1-er)));
        dv3=hs*dv2(:).*(1-(tanh(hs*(x2-dl))).^2)/(tanh(hs*dl)+tanh(hs*(1-dl)));
        dc4=dc3.*ddj; dc5=repmat(dc4(si),2,1).*dyri; dc6=accumarray(szz,dc5);
        dv4=dv3.*ddj; dv5=repmat(dv4(si),2,1).*dyri; dv6=accumarray(szz,dv5);
        dc7=dc3.*dx; dcx=H*(dc7(:)./Hs); dcy=zt'*dc6; dcy(1:2)=mean(dcy(1:2));
        dv7=dv3.*dx; dvx=H*(dv7(:)./Hs); dvy=zt'*dv6; dvy(1:2)=mean(dvy(1:2));
        %% OPTIMALITY CRITERIA UPDATE OF DESIGN VARIABLES
        l1=0;   l2=1e9; dy=ym-y0;
        if lp<=25, mv1=0.05; mv2=0.02*dy; else, mv1=0.1; mv2=0.0001*dy; end
        while (l2-l1)/(l1+l2)>1e-3
         lmd=0.5*(l2+l1);
         xnw=max(0,max(x-mv1,min(1,min(x+mv1,x.*sqrt(abs(dcx)./dvx/lmd)))));
         if udl, xnw(xid)=1; end
         ynw=max(y0,max(y-mv2,min(ym,min(y+mv2,y.*sqrt(abs(dcy./dvy)/lmd)))));
         ys=ynw; ys(1:2)=mean(ys(1:2));
         x1=(H*xnw(:))./Hs; rN(:,2)=zt*ys; x2=TCf(x1);
         xs(:)=(tanh(hs*dl)+tanh(hs*(x2(:)-dl)))/(tanh(hs*dl)+tanh(hs*(1-dl)));
         [V,J3]=vol(); Vr=V/V0; if Vr>volfrac,  l1=lmd; else,   l2=lmd; end
        end
        xs(:)=(tanh(hs*er)+tanh(hs*(x2(:)-er)))/(tanh(hs*er)+tanh(hs*(1-er)));
        ch=max([abs(xnw(:)-x(:));abs(ynw-y)/dy]); x=xnw; lt=lt+toc; y=ynw;
        %% PRINT RESULTS
        pr='It.:%5i Obj.:%11.2f Vol.:%7.3f ch.:%7.3f t.:%7.2f Penal.:%7.2f upre.:%7.2f bhs.:%7.2f\n';
        fprintf(pr,lp,C*1e8,Vr,ch,lt,pn,up,hs);
        %% PLOT DENSITIES
        clf; set(gcf,'color','w'); colormap(repmat([0 0.3 0.6 1]',[1,3]));
        P=patch('Faces',ep(:,[1 5 2 6 3 7 4 8 1]),'Vertices',cd,'EdgeColor',...
            'none','FaceVertexCData',1-xs);
        P1=patch('Faces',ep(:,[1 5 2 6 3 7 4 8 1]),'Vertices',...
            [-cd(:,1) cd(:,2)],'EdgeColor','none','FaceVertexCData',1-xs);
        caxis([0 1]); daspect([1 1 0.1]); axis off; hold on;
        plot(rN(:,1),rN(:,2),'c','linewidth',3);
        plot(-rN(:,1),rN(:,2),'c','linewidth',3);
        P.FaceColor='interp'; P1.FaceColor='interp'; drawnow; hold off;
    end
    %% 3D JACOBIAN FOR PENALIZED THICKNESS
    function dJp=J3d()
        tp=(Em+xs(ep).^pn*(E0-Em));
        Zp(:,1:8)=-(tp)/2;  Zp(:,9:12)=0;   Zp(:,13:20)=(tp)/2;    sZp=ds*Zp';
        S(7:9:72,:)=sZp(1:3:end,:); S(8:9:72,:)=sZp(2:3:end,:);
        S(9:9:72,:)=sZp(3:3:end,:); s=reshape(S,3,3,8,et);
        dJp=s(1,1,:,:).*(s(2,2,:,:).*s(3,3,:,:)-s(3,2,:,:).*s(2,3,:,:))-...
            s(1,2,:,:).*(s(2,1,:,:).*s(3,3,:,:)-s(3,1,:,:).*s(2,3,:,:))+...
            s(1,3,:,:).*(s(2,1,:,:).*s(3,2,:,:)-s(3,1,:,:).*s(2,2,:,:));
        if find(dJp<10*eps, 1),   disp('Jacobian<0!');    return; end
        dJp=dJp(:,:,1:4,:)+dJp(:,:,5:8,:);
    end
    %% VOLUME CHANGES USING ACTUAL THICKNESS
    function [Vp,dJ]=vol()
        tn=Em+xs(ep)*(E0-Em);
        Z(:,1:8)=-(tn)/2;   Z(:,9:12)=0;    Z(:,13:20)=(tn)/2;  sZ=ds*Z';
        S(7:9:72,:)=sZ(1:3:end,:);  S(8:9:72,:)=sZ(2:3:end,:);
```

```matlab
    S(9:9:72,:)=sZ(3:3:end,:);  s=reshape(S,3,3,8,et);
    dJ=s(1,1,:,:).*(s(2,2,:,:).*s(3,3,:,:)-s(3,2,:,:).*s(2,3,:,:))-...
        s(1,2,:,:).*(s(2,1,:,:).*s(3,3,:,:)-s(3,1,:,:).*s(2,3,:,:))+...
        s(1,3,:,:).*(s(2,1,:,:).*s(3,2,:,:)-s(3,1,:,:).*s(2,2,:,:));
    if find(dJ<10*eps, 1), disp('Jacobian<0!');  return;  end
    dJ=dJ(:,:,1:4,:)+dJ(:,:,5:8,:); Ve=f(sum(dJ,3)); Vp=sum(Ve);
end
%% BEZIER CURVE FINDING COMPONENTS
function fP=Bzr()
    % Bezier Curve, Tangential vectors, Components and Intersections
    dPy=diff(ys); TV(:,2)=nd*dzt*dPy; Hyp=sum(TV.^2,2).^(1/2); h=TV./Hyp;
    yr=rN(:,2)'; [ei,~]=find((yr-InC(:,1)>=0)&(InC(:,2)-yr)>0);
    ei(ei==(nY+1))=nY; pe=pec'+ei-1; xi=2*(yr'-InC(ei,1))/ez-1;
    % Prestressing Components and distribution
    Nd=bsxfun(NF,xi,1); tP=[h(1,:);0.5*diff([-h(:,1) h(:,2)]);-h(end,:)];
    Pc=tP(1:end-1,:)+tP(2:end,:); Pdx=Nd.*Pc(:,1); Pdy=Nd.*Pc(:,2);
    Pdn=[ep(pe(1:end-1),[1 8 4]);ep(pe(end),[2 6 3])];
    fP=sparse([2*Pdn(:)-1;2*Pdn(:)],1,[Pdx(:);Pdy(:)]*pf,2*nt,1);
end
%% TENDON CONCRETE FILTER AND DERIVATIVES
function xc=TCf(xx)
    sV=rN(2:end,:)-rN(1:end-1,:); sL=sum(sV.^2,2).^(1/2);
    dV=diff((cd(si,:)-rN(sz,:)).*sV(sz,[2 1]),1,2); dj(si)=abs(dV)./sL(sz);
    i1=-0.5*(dj/bphil).^up; exd=exp(i1); xc=xx+(1-xx).*exd;
end
function [dx,ddj,dyri]=dTC()
    dx=1-exd; ddj=up*(1-x).*exd.*i1./dj; ddj(dj==0)=0; C1=dV./abs(dV);
    C1(isnan(C1))=0; C2=C1.*(cd(si,1)-rN(sz+1,1))./sL(sz);
    C3=abs(dV).*(rN(sz+1,2)-rN(sz,2))./(sL(sz).^3);
    C4=-C1.*(cd(si,1)-rN(sz,1))./sL(sz);
    dyi1=C2+C3; dyi2=C4-C3; dyri=[dyi1;dyi2];
end
end
% Examples
% topPSC([1.50,.30],0.01,-10,'con',20,0,[3e10,0.2,0],0.5,[1,0.01,3],2.0)
% topPSC([1.50,.30],0.01,-100,'udl',100,0,[3e10,0.2,0],0.5,[1,0.01,3],2.0)
% topPSC([1.50,.30],0.01,-100,'udl',100,0,[3e10,0.2,2400],0.5,[1,0.01,3],2.0)
% topPSC([2.40,.30],0.01,-100,'udl',100,1,[3e10,0.2,0],0.5,[1,0.01,3],2.0)
% topPSC([2.40,.30],0.01,-100,'udl',100,1,[3e10,0.2,2400],0.5,[1,0.01,3],2.0)
% topPSC([2.40,.30],0.01,-100,'udl',100,2,[3e10,0.2,0],0.5,[1,0.01,3],2.0)
% topPSC([2.40,.30],0.01,-100,'udl',100,2,[3e10,0.2,2400],0.5,[1,0.01,3],2.0)
%%%%%%%%%%%%%%%%%%%%%%%%%%%%%%%%%%%%%%%%%%%%%%%%%%%%%%%%%%%%%%%%%%%%%%%%%%%%
% 2.5D SIMTP code for optimising prestressed beams by Tejeswar YARLAGADDA  %
% PhD Student, BEEE, POLYU, HONGKONG                                      %
% Email to yarlagadda.tejeswar@gmail.com for the   code                   %
%                                                                         %
% Disclaimer:                                                             %
% The authors reserve all rights but do not guaranty that the code is     %
% free from errors. Furthermore, we shall not be liable in any event      %
% caused by the use of the program.                                       %
%%%%%%%%%%%%%%%%%%%%%%%%%%%%%%%%%%%%%%%%%%%%%%%%%%%%%%%%%%%%%%%%%%%%%%%%%%%%
```